

EXTENDING THE IN-MEDIUM SIMILARITY RENORMALIZATION GROUP TO
NUCLEAR MATTER WITH NOVEL INSIGHTS ON UNITARY COUPLED-CLUSTER
THEORY

By

Omokuyani Chibuzor Udiani

A DISSERTATION

Submitted to
Michigan State University
in partial fulfillment of the requirements
for the degree of

Physics — Doctor of Philosophy
Computational Mathematics, Science and Engineering — Dual Major

2024

ABSTRACT

The nuclear matter equation-of-state (NM-EOS) determines the stability and bulk properties of nuclear matter, and is thus, directly linked to astrophysical phenomena—e.g. neutron star physics. Moreover, a tightly constrained NM-EOS opens an avenue to test and improve nuclear force models. The NM-EOS is therefore, of great interest to the physics community. Recent advances in *ab initio* nuclear theory have led to an explosion of nuclear forces amenable to many-body methods—which scale polynomially in time. Some of such methods include Many-Body Perturbation Theory (MBPT), and nonperturbative approaches: In-Medium Similarity Renormalization Group (IMSRG), and Coupled-Cluster theory (CC). Unlike MBPT and CC, the IMSRG has *not* been applied to study NM-EOS with realistic nucleon forces. Therefore, we apply the IMSRG to calculate NM-EOS using multiple realistic forces. To accomplish this goal, we develop a state-of-the-art, high-performant nuclear matter IMSRG program with access to a multitude of two and three-body nuclear forces. We compare NM-EOS obtained from MBPT, IMSRG, and CC to benchmark the methods. And we observe disparities between the methods in symmetric nuclear matter that are due to non-perturbative physics. IMSRG NM-EOS computations are done at scale, and are therefore, *highly* computationally demanding. Consequently, we introduce novel ideas to accelerate IMSRG computations using Unitary Coupled-Cluster (UCC)-inspired IMSRG generators, and Shanks and Padé IMSRG extrapolators. We realize that approximate UCC solutions can be used as IMSRG generators. And, viewing UCC as a nonlinear commutator inversion problem, we realize that UCC amplitudes are given by a generalized Born series—so long the series converges. Using these developments, we introduce three IMSRG generators named “Born,” “UCC-Born,” and “Carinae.” Using the novel generators, we sometimes observe 2–4X IMSRG speedup, particularly when the IMSRG is slowly convergent.

I dedicate this work to my loving family: **Dayo, Eunice, Oyita, Ivy, Anise, Tiolu, Iyanu, and Carly**. Moreover, I dedicate this work to the mentors I have been very fortunate to encounter: **Melanie Caldwell,¹ Donald Fear, Michelle Kim, Ireneo Abadejos, Dr. Hoon Hong, Dr. Erin Banks and Dr. Hans Hallen**.

Everyone listed has been integral to my development as a person and academic. They showed me kindness and gave me guidance at my times of most need. This work truly is an extension of these people. Thank you so much.

¹Who passed away in 2018

ACKNOWLEDGMENTS

My family including loving father **Dayo** & mother **Eunice Udiani**, supportive brothers **Oyita & Anise Udiani**, & patient and devoted partner **Carly “Carl” Fox & H.B.** the kitty;

Therapist **Marsha Carolan**;

Long time friends **Dr. Melvin “Melonhead” Thomas, Henil Patel**

Friends **Mike “Quiznos” Quiñonez**, **Robert “Roberto” Branson**, **Alex Baez**, **Dr. Pierre Nzabahimana**, **Dr. Felix Ndayisabye**, **Dr. Avik Sarkar**, **Dr. Nick Valverde**, (soon-to-be Dr.) **Gabriel Given**, **Dr. Jacob Watkins**, **Elizabeth Deliyski**, **Paulette Stenzel, J.D.**, **Dr. Ágnes Mócsy**, **Dr. Pablo Giuliani**, & **Jennifer Torrez-Favreau**;

I would like to also thank collaborators (Soon-to-be Dr.) **Kang Yu**, **Dr. Christian Drischler**, & **Dr. Justin Lietz**;

Professors and mentors **Dr. Scott Bogner**, **Dr. Heiko Hergert**, **Dr. Morten Jensen**, **Dr. Scott Pratt**, **Dr. Vladimir Zelevinsky**, **Dr. Filomena Nunes**, & **Dr. Kirsten Tollefson**.

Songs that got me through grad school: “Road Song”—*Tigran Hamasyan*, “Alkaline” and “Say That You Will”—*Sleep Token*, “Is It Really You?”—*Loathe X Sleep Token*, “We Live in a Strange World,” “The Mara Effect, Pt. 3,” and “Eternal Blue”—*Spiritbox*, “Tempting Time” and “CAFO”—*Animals As Leaders*, “Luck as a Constant”—*Periphery*, “Blame Brett”—*The Beaches*, “John Madden”—*Chief Keef*, “No Time for Caution”—*Hans Zimmer*, “Luz Y Cielo”—*Mestis*, “Cages”—*Tesseract*, “Clockworks”—*Meshuggah*, “Before Lights Out”—*Hiroeyuki Sawano*, “GIANT GREEN DESTRUCTION”—*The Ogre Packet Slammers*, “If It Means A Lot To You”—*A Day To Remember*, “Lady Maria of the Astral

Clocktower”—*Yuka Kitamura et al.*, “r a u m”—*Jakub Zytecki*, “Love After Love”—*Jóhann Jóhannsson*

Development of this project was made possible through funding from the National Science Foundation via grants PHY-2310020 and PHY-2013047 and the NSCL Graduate Fellowship. This work was supported in part by Michigan State University through computational resources provided by the Institute for Cyber-Enabled Research (ICER).

I greatly thank **Dr. Heiko Hergert** for his kindness, guidance, technical help, and many fruitful and interesting conversations.

I would like to thank **Dr. Christian Drischler**, **Dr. Gaute Hagen**, and **Dr. Sam Novario** for providing MBPT and CC nuclear matter results to make comparisons with IMSRG.

TABLE OF CONTENTS

LIST OF SYMBOLS	viii
LIST OF ABBREVIATIONS	ix
Chapter 1. Background and Introduction	1
1.1 Importance of the Nuclear Matter Equation-of-State	1
1.2 Recent Advances in <i>Ab Initio</i> Nuclear Theory	1
1.3 Thesis Outline	2
Chapter 2. IMSRG Theory for Nuclear Matter	3
2.1 SRG Theory	4
2.2 IMSRG Theory	6
2.2.1 Flow Implementation	8
2.2.2 Magnus Expansion	10
2.3 Modeling Infinite Nuclear Matter in a Cubic Box	15
2.3.1 Single-Particle Basis	15
2.3.2 Two- and Three-Particle Bases	19
2.3.3 Errors Due to Finite Size and Incomplete Basis Sets	20
2.4 Conclusion	21
Chapter 3. Nuclear Matter IMSRG Program	22
3.1 SCKY-IMSRG Program Output	23
3.2 Big <i>Data</i> Management: Parsing IMSRG Outputs	28
3.3 Nuclear Forces	28
3.4 SCKY-IMSRG Program Hierarchy	29
3.5 High-Performance Optimizations	38
3.5.1 Performance Results	39
3.6 Concluding Remarks with Perspectives	49
Chapter 4. Nuclear Matter Equation-of-State	51
4.1 Results	55
4.2 Discussion	72
4.3 Conclusion	74
4.4 Outlook	76
Chapter 5. UCC-Inspired IMSRG Generators	78
5.1 Motivation	79
5.2 Assumptions	80
5.3 Magnus-IMSRG Convergence Acceleration	81
5.4 Unitary Coupled-Cluster Theory	83
5.5 Linearized UCC	84
5.6 Commutator Inversion via Born Series	85

5.7	Regulating the Born Series	90
5.8	Preconditioning the Born Series	93
5.9	Born Generator	94
5.10	UCC-Born Generator	95
5.11	Carinae Generator	96
5.12	Results	98
5.13	A Few Remarks	108
5.14	Summary	108
5.15	Perspectives	109
Chapter 6. IMSRG Post-Processors		111
6.1	Shanks Transformation	112
6.2	Padé Approximant	112
6.3	Results	113
6.4	Discussion	120
6.5	Conclusion and Perspectives	120
Chapter 7. Closing Remarks		122
7.1	Summary	122
7.2	Outlook	124
BIBLIOGRAPHY		126
APPENDIX A. Generalized Baker-Campbell-Hausdorff Formula		130
APPENDIX B. Fourier Transform of Local Two-Body Force in a Box		133
APPENDIX C. Minnesota Potential in a Finite Box		140
APPENDIX D. One Pion Exchange Interaction in a Finite Box		147
APPENDIX E. Partial Wave Expansion for Two-Body Forces		153
APPENDIX F. Optimized Particle-hole Transformation		161
APPENDIX G. Properties of Born Series Adjoints		166
APPENDIX H. MBPT Expressed in Terms of IMSRG Commutators		168
H.1	MBPT Truncation for UCC-Inspired Generators	175
APPENDIX I. UCC Renormalized Hamiltonian Ansatz		176

LIST OF SYMBOLS

- N, Z, A – Number of neutrons, protons, and nucleons ($A = N + Z$), respectively
- H – A -body operator representing the nuclear Hamiltonian
- H^{RG} – A -body operator representing a renormalized nuclear Hamiltonian
- E – Rank zero-body component of H (energy)
- f – Rank one-body component of H
- Γ – Rank two-body component of H
- W – Rank three-body component of H
- Δ – Green’s A -body operator used in perturbation theory (often called an energy denominator)
- η – Approximate A -body diagonalizer to H
- Ω – Approximate A -body diagonalizer to H *specifically* from the Magnus expansion
- s – Dimensionless flow parameter in IMSRG
- ds – Step-size in s
- $: a^\dagger \dots a :$ – Normal-ordered product of creation and annihilation operators
- $[\Omega, H]$ – Commutator between Ω and H
- n_p – Occupation status in single-particle state (orbital) p such that $0 \leq n_p \leq 1$
- $\bar{n}_p = 1 - n_p$
- p, q, r, s, t, u – Subscript labels for generic orbitals in the Fermi vacuum $|\Phi\rangle$
- a, b, c, d – Subscript labels for unoccupied orbitals in the Fermi vacuum $|\Phi\rangle$
- i, j, k, l – Subscript labels for occupied orbitals in the Fermi vacuum $|\Phi\rangle$
- $_{abij}$ – Subscript labels for off-diagonal sector of the two-body component of an A -body operator.²
- H_{od} – Off-diagonal sector of H

²We only do ground state energy (zero temperature) calculations in this work.

LIST OF ABBREVIATIONS

FRIB – Facility for Rare Isotope Beams³

ICER – Institute for Cyber-Enabled Research⁴

χ -EFT – Chiral Effective Field Theory

DD3NF – Density-Dependent three-body Nuclear Forces

SRG – Similarity Renormalization Group

IMSRG – In-Medium Similarity Renormalization Group

IMSRG(2)/IMSRG(3) – IMSRG with operators truncated at the two-/three-body level

Magnus-IMSRG – Magnus expansion formulation of the IMSRG

CC – Coupled-Cluster theory

UCC – Unitary Coupled-Cluster theory

MBPT – Many-Body Perturbation Theory

BCH – Baker-Campbell-Hausdorff formula

NM-EOS – Nuclear matter equation-of-state

PNM – Pure Neutron Matter

SNM – Symmetric Nuclear Matter

OPE – One Pion Exchange potential

N2LO_{opt} – Optimized potential at next-to-next-to leading-order (NNLO) of χ -EFT⁵

RHS/LHS – Right/left-hand side of any equation

H.c. – Hermitian conjugate

od – Off-diagonal sector(s) of a body-operator or an A -body operator

³Located at Michigan State University

⁴Located at Michigan State University

⁵NNLO is sometimes referred to as N2LO.

Chapter 1. Background and Introduction

“Everything is fine!”

—Periphery

1.1 Importance of the Nuclear Matter Equation-of-State

The nuclear matter equation-of-state (NM-EOS) is given by $E(\rho)/A$ where $E(\rho)$ is the total energy of a system containing $A \rightarrow \infty$ interacting nucleons confined in a $\mathcal{V} \rightarrow \infty$ volume at density ρ . It determines the stability and bulk properties of nuclear matter, such as its response to gravitational compression. Consequently, the NM-EOS is directly linked to astrophysical phenomena—e.g. neutron star physics [1–3]. And it is indicative of possible new states of ultra-compressed matter [1–3]. Moreover, a tightly constrained NM-EOS allows the testing and improvement of nuclear force models [4–6]. There are known deficiencies in χ -EFT in heavy nuclei (overbinding with radii that are too small) that are linked to poor nuclear saturation [6].

1.2 Recent Advances in *Ab Initio* Nuclear Theory

Ab initio nuclear theory predicts properties of nuclear systems using the most fundamental building blocks that are accessible to theorists [7]. Recent advancements in *ab initio* nuclear theory have led to an explosion of two- and three-body nuclear forces from Chiral Effective Field Theory (χ -EFT) that can be used by many-body methods to compute observables in nuclear systems [1, 4, 8, 9]. Some of such methods include Many-Body Perturbation Theory (MBPT), and nonperturbative approaches: In-Medium Similarity Renormalization Group

(IMSRG) and Coupled-Cluster theory (CC). These many-body methods scale polynomially in time, and consequently, have been used to target heavy nuclei [10–12]. Unlike MBPT and CC, the IMSRG has *not* been applied to study NM-EOS with realistic nucleon forces. Therefore, the application of the IMSRG in nuclear matter is still in its infancy.

1.3 Thesis Outline

We introduce the IMSRG in Chapter 2, and detail how it can be applied to study an infinite lattice of nuclear matter. We subsequently introduce the computer program in Chapter 3 that is used to perform all nuclear matter IMSRG calculations in this work. And we show the program’s performance capabilities. In Chapter 4, we calculate and exhibit various NM-EOS using three chiral forces. Observing the large runtimes needed to obtain NM-EOS using the IMSRG at scale, we then look towards developing techniques to accelerate IMSRG computations. In Chapter 5, we introduce novel physics-motivated techniques to accelerate IMSRG computations. And, we apply known data driven methods in Chapter 6, to extrapolate converged IMSRG energies. This thesis is accompanied by a graphic presentation located in the supplemental materials. The graphic presentation offers visual explanations of the ideas in this work, which may enhance the reader’s understanding. Therefore, we employ the reader to seek it according to their preference.

Chapter 2. IMSRG Theory for Nuclear Matter

*“Sometimes you have to be
willing to accept ‘good
enough’”*

—Scott K. Bogner

The In-Medium Similarity Renormalization Group (IMSRG) is a powerful computational tool that has been used to calculate nuclear structure observables for a wide range of finite nuclei starting from realistic inter-nucleon forces [10,11,13–15]. However, prior to the present work, the IMSRG had never been adapted to carry out large-scale EOS calculations of infinite nuclear matter starting from realistic Hamiltonians—it had only been used to perform small, proof-of-principle calculations of pure neutron matter with the aged and godforsaken Minnesota two-nucleon potential [16,17].¹ In this work, we develop a nuclear matter IMSRG program built from the ground up to be performant and thus, usable for large-scale calculations using modern chiral two- and three-nucleon forces. In this chapter, we describe the basic formalism of the IMSRG, and how it can be extended and applied to carry out microscopic EOS calculations of nuclear matter as well as other infinite homogeneous many-body systems such as the electron gas.

¹We jest, and hope that the Minnesota force, which has served its role well as a highly simplified (and hence only semi-realistic) model, is without offense.

2.1 SRG Theory

The Similarity Renormalization Group (SRG) is the al-Qa'idah (foundation) of the IMSRG. The SRG performs a sequence of continuous unitary transformations on a given Hamiltonian to construct unitarily equivalent Hamiltonians with desired properties determined by the transformations' generators. Simply stated, the SRG enables the shaping or manipulation of a given Hamiltonian while preserving its eigenvalues.² Consider a bare interaction^{3,4}

$$H = \sum_{pq} T_{pq} a_p^\dagger a_q + \frac{1}{(2!)^2} \sum_{pqrs} V_{pqrs}^{(2)} a_p^\dagger a_q^\dagger a_s a_r + \frac{1}{(3!)^2} \sum_{pqrst} V_{pqrst}^{(3)} a_p^\dagger a_q^\dagger a_r^\dagger a_u a_t a_s. \quad (2.1)$$

H is an A -body operator that is truncated at the three-body level. And $V^{(2)}$ and $V^{(3)}$ are anti-symmetrized body-operators. Notice that H is normal-ordered relative to the true vacuum, i.e. $\langle 0|H|0\rangle = 0$.

The SRG transforms H via

$$H(s) = U(s)H(0)U(s)^\dagger \quad (2.2a)$$

$$U(s=0) \equiv \mathbb{1} \implies H(s=0) = H \quad (2.2b)$$

$$U(s)U(s)^\dagger = U(s)^\dagger U(s) = \mathbb{1} \quad (2.2c)$$

$$\eta(s) \equiv \frac{dU(s)}{ds}U(s)^\dagger = -\eta(s)^\dagger \quad (2.2d)$$

$$\frac{dH(s)}{ds} = [\eta(s), H(s)] \quad (2.2e)$$

²Unitarity in the SRG and IMSRG are theoretically guaranteed. However, approximations within each method—such as many-body truncations for computational feasibility—can break unitarity.

³The two-body and higher-body ranks of H in Eq. (2.1) are typically determined from Chiral Effective Field Theory (χ -EFT) [18].

⁴The p, \dots, u subscripts in Eq. (2.1) label single-particle states.

[19]. Eq. (2.2e) is commonly referred to as the “flow equation.” s is a continuous parameter that labels the stage of the SRG evolution.⁵ And $\eta(s)$ is an anti-Hermitian A -body operator ($\eta(s) = -\eta^\dagger(s)$) that is also truncated at the three-body level. $\eta(s)$ is called the generator of the SRG since it implicitly defines the SRG transformation [20]. Let $H(s) = H_d(s) + H_{od}(s)$, where $H_d(s)$ and $H_{od}(s)$ denote the diagonal and off-diagonal sectors of $H(s)$, respectively.⁶ The SRG is typically used to diagonalize H . To that end, $\eta(s)$ is chosen via perturbative analysis of Eq. (2.2e) such that $\lim_{s \rightarrow \infty} H_{od}(s) = 0$. The SRG evolution is then iterated until $\frac{dH(s)}{ds} = 0$. Some notable generators include the White, Imaginary-time, and Wegner generators [20].

Although we truncated H at the three-body level, Eq. (2.2e)’s commutator induces many-body forces above the three-body level in $\frac{dH(s)}{ds}$. If there are A particles in the system of interest, $\frac{dH(s)}{ds}$ will contain operator ranks up to the A -body level. These induced higher-body operators are not only computationally troublesome to handle, but can also have important effects on the convergence and unitarity of the SRG in many-body systems [19]. Therefore, we are motivated to find alternatives that avoid the explicit handling of such induced higher-body operators. This leads us to the IMSRG, which we turn to next.

⁵The flow parameter s , should not be confused with the generic single-particle index s —since the latter will always be shown as a subscript.

⁶In the matrix formulation of the SRG, $H_d(s)$ and $H_{od}(s)$ correspond to the conventional definition of diagonal and off-diagonal matrices of H in a given basis, respectively [19]. In this work, the notions of “diagonal” and “off-diagonal” are kept general. This is convenient when we employ the minimal decoupling scheme in Subsection 2.2.2.

2.2 IMSRG Theory

The IMSRG improves on the SRG by rewriting $H = H(0)$ *exactly* into a normal-ordered form, based on a Hartree-Fock reference state—called the Fermi vacuum $|\Phi\rangle$ [20].⁷

$$H = E + \sum_{pq} f_{pq} : a_p^\dagger a_q : + \frac{1}{4} \sum_{pqrs} \Gamma_{pqrs} : a_p^\dagger a_q^\dagger a_s a_r : \quad (2.3a)$$

$$+ \frac{1}{36} \sum_{pqrst} W_{pqrst} : a_p^\dagger a_q^\dagger a_r^\dagger a_u a_t a_s :$$

$$E = \sum_q T_{qq} n_q + \frac{1}{2} \sum_{qr} V_{qrqr}^{(2)} n_q n_r + \frac{1}{6} \sum_{qrs} V_{qrsqrs}^{(3)} n_q n_r n_s \quad (2.3b)$$

$$f_{pq} = T_{pq} + \sum_r V_{prqr}^{(2)} n_r + \frac{1}{2} \sum_{rs} V_{prsqrs}^{(3)} n_r n_s \quad (2.3c)$$

$$\Gamma_{pqrs} = V_{pqrs}^{(2)} + \sum_t V_{pqrst}^{(3)} n_t \quad (2.3d)$$

$$W_{pqrst} = V_{pqrst}^{(3)} \quad \forall pqrst. \quad (2.3e)$$

$: a^\dagger a^\dagger \dots aa :$ denotes the normal-ordered form of $a^\dagger a^\dagger \dots aa$ with respect to $|\Phi\rangle$, such that $\langle \Phi | : a^\dagger a^\dagger \dots aa : | \Phi \rangle = 0$. And $n_p = \theta(\epsilon_{\text{Fermi}} - \epsilon_p)$ is the occupation of the p th single-particle state with energy ϵ_p embedded in $|\Phi\rangle$ with energy ϵ_{Fermi} . Since H is normal-ordered relative to $|\Phi\rangle$, $H(s)$ and $\eta(s)$ are likewise normal-ordered relative to $|\Phi\rangle$.⁸ Therefore, the commutator in Eq. (2.2e) is written to act on normal-ordered operators using Wick's theorem [10, 15, 19–21]. In conclusion, the IMSRG solves Eq. (2.2e) using a commutator that acts on normal-ordered operators $H(s)$ and $\eta(s)$ [10].

By rewriting H into a normal-ordered form in Eq. (2.3), we propagate terms from T ,

⁷When modeling infinite nuclear matter, $f_{ia} = f_{ai} = 0$ is guaranteed in Eq. (2.3c) due to momentum conservation seen in Eqs. (2.15) and (2.17). Therefore, Hartree-Fock conditions on f are automatically satisfied [19].

⁸See Eqs. (2.4a–2.4c).

$V^{(2)}$, and $V^{(3)}$ into their respective lower operator ranks of H . This is the appeal of normal-ordering. If the target wavefunction $|\Psi\rangle$, of H is approximated well by $|\Phi\rangle$, we can truncate induced high-body forces while mitigating the violation of unitarity. Simply stated—for example, the IMSRG allows the inclusion of three-body forces without explicitly evolving three-body operators [15, 19].

In this work, we utilize the IMSRG(2) scheme—meaning that *all* IMSRG operators and induced commutators are truncated at the two-body level. The IMSRG(2) truncation is employed because the computational cost needed to store and evolve three-body operators at scale is *immense*. Additionally, we utilize two normal-ordering truncation schemes denoted “normal-ordered 2NF” and “normal-ordered 3NF.” Within the normal-ordered 2NF scheme, H is truncated at the two-body level by assuming $V^{(3)} = 0$ in Eq. (2.3). Within the normal-ordered 3NF scheme, $V^{(3)}$ is preserved in Eqs.(2.3b)–(2.3e). Consequent to the IMSRG(2) truncation, W is however, discarded in Eq. (2.3a). Thus, we render the $V^{(3)}$ dependence in W , inconsistent with the $V^{(3)}$ dependence in E , f , and Γ . Hence, the IMSRG(2) + normal-ordered 3NF scheme certainly violates unitarity. Despite this drawback, three-body correlations are still propagated to the lower operator ranks E , f , and Γ .

The IMSRG(2) scales roughly as N_{orbitals}^6 , where N_{orbitals} is the number of single-particle orbitals. The next level of truncation, the IMSRG(3), is intractable for large scale problems as it scales as N_{orbitals}^9 . However, recently Stroberg, Morris and He introduced an approximate IMSRG(3) scheme that captures the dominant three-body correlations and only scales as N_{orbitals}^7 [22]. Going forward, insights from Stroberg *et al.* [22] will likely improve the handling of three-body correlations in this work. Lastly, note that the IMSRG(2) + normal-ordered 3NF scheme can also be called the IMSRG(2) with density-dependent three-body

nuclear forces (DD3NF).⁹

2.2.1 Flow Implementation

Within both normal-ordered 2NF and 3NF IMSRG(2) schemes, $H(s)$, $\frac{dH(s)}{ds}$, and $\eta(s)$ are given by¹⁰

$$H(s) = E(s) + \underbrace{\sum_{pq} f_{pq}(s) : a_p^\dagger a_q :}_{f(s)} + \frac{1}{4} \underbrace{\sum_{pqrs} \Gamma_{pqrs}(s) : a_p^\dagger a_q^\dagger a_s a_r :}_{\Gamma(s)} \quad (2.4a)$$

$$\frac{dH(s)}{ds} = \frac{dE(s)}{ds} + \sum_{pq} \frac{df_{pq}(s)}{ds} : a_p^\dagger a_q : + \frac{1}{4} \sum_{pqrs} \frac{d\Gamma_{pqrs}(s)}{ds} : a_p^\dagger a_q^\dagger a_s a_r : \quad (2.4b)$$

$$\eta(s) = \text{scalar} + \sum_{pq} \eta_{pq}(s) : a_p^\dagger a_q : + \frac{1}{4} \sum_{pqrs} \eta_{pqrs}(s) : a_p^\dagger a_q^\dagger a_s a_r : . \quad (2.4c)$$

Utilizing Eqs. (2.2e, 2.4a–2.4c), and derived expressions for commutators of normal-ordered operators from Hergert *et al.* [10], a set of coupled differential equations for the individual body-operator components of $\frac{dH(s)}{ds}$ —i.e. $\frac{dE(s)}{ds}$, $\frac{df(s)}{ds}$, and $\frac{d\Gamma(s)}{ds}$ —called “flow equations,”

⁹In Eqs.(2.3b)–(2.3d), $V^{(3)}$ enters E , f , and Γ with occupation factors (density matrices).

¹⁰The zero-body component of $\eta(s)$ does not affect the dynamics of the IMSRG. Since it has no physical relevance, it is usually neglected.

can be derived [10, 15, 19, 20].¹¹

$$\frac{dE}{ds} = \sum_{pq} (n_q - n_r) \times \eta_{pq} f_{qp} + \frac{1}{2} \sum_{pqrs} n_p n_q \bar{n}_r \bar{n}_s \times \eta_{pqrs} \Gamma_{rspq} \quad (2.5a)$$

$$\frac{df_{pq}}{ds} = \sum_r (1 + P_{pq}) \times \eta_{pr} f_{rq} + \sum_{rs} (n_r - n_s) \times (\eta_{rs} \Gamma_{sprq} - f_{rs} \eta_{sprq}) \quad (2.5b)$$

$$+ \frac{1}{2} \sum_{rst} (n_r n_s \bar{n}_t + \bar{n}_r \bar{n}_s n_t) \times (1 + P_{pq}) \times \eta_{tprs} \Gamma_{rstq} \quad (2.5c)$$

$$\begin{aligned} \frac{d\Gamma_{pqrs}}{ds} &= \sum_t (1 - P_{pq}) \times (\eta_{pt} \Gamma_{tqrs} - f_{pt} \eta_{tqrs}) \\ &\quad - \sum_t (1 - P_{rs}) \times (\eta_{tr} \Gamma_{pqts} - f_{tr} \eta_{pqts}) \\ &\quad + \frac{1}{2} \sum_{tu} (1 - n_t - n_u) \times (\eta_{pqtu} \Gamma_{turs} - \Gamma_{pqtu} \eta_{turs}) \\ &\quad - \sum_{tu} (n_t - n_u) \times (1 - P_{pq}) \times (1 - P_{rs}) \times \eta_{uqts} \Gamma_{tpur} . \end{aligned}$$

Note that the flow parameter s , is suppressed in Eq. (2.5) for brevity. The permutation operators P_{pq} and P_{rs} , exchange indices on their operand; e.g., $P_{pq} \times \eta_{uqts} \Gamma_{tpur} \equiv \eta_{upts} \Gamma_{tqur}$. And $\bar{n}_p \equiv 1 - n_p$.

In this work, we chose to instead solve the flow implementation of the IMSRG directly in Eq. (2.2e)'s form, on the condition that $\eta(s)$ and $H(s)$ are normal-ordered relative to $|\Phi\rangle$. Thus, we let our highly optimized commutators handle the tensor contractions between the body-operator components of $\eta(s)$ and $H(s)$ seen in the RHS of Eq. (2.5) (see Listing 3.1).

The flow equation is numerically integrated with high-order adaptive ordinary differential equation solvers to preserve the unitary equivalence between H and $H(s)$. Such high-order solvers require the storage of multiple solution vectors calculated at different step sizes. The flow implementation of the IMSRG can therefore be memory expensive, especially in large

¹¹Heinz *et al.* [15] notably corrected some expressions of three-body commutators from Hergert *et al.* [10].

systems [20]. And the flow equations can become stiff when using potentials with a hard core [19]. Lastly, the flow equation was specifically engineered to evolve $H(s)$. Therefore, we must simultaneously evolve other operators beyond $H(s)$ to obtain observables beyond energies [20]. This is prohibitively expensive since the IMSRG solution vector doubles in size for each additional operator that is evolved. Observables beyond $E(s)$ may converge at different time scales than $E(s)$. This would introduce complications in our performance tuning of the IMSRG, since we would like to avoid storing and evolving operators for observables that are effectively converged. We look towards the Magnus expansion to cure some of these aforementioned ailments.

2.2.2 Magnus Expansion

We seek to describe the Magnus formulation of the IMSRG, denoted “Magnus-IMSRG,” which bypasses some issues of the IMSRG flow implementation [20]. Multiplying both sides of Eq. (2.2d) with $U(s)$, the SRG/IMSRG dynamics can be rewritten

$$\eta(s)U(s) = \frac{dU(s)}{ds}. \quad (2.6)$$

If the Magnus expansion is convergent, one can write $U(s) = e^{\Omega(s)}$ where $\Omega(s) = -\Omega(s)^\dagger$ and $\Omega(0) \equiv 0$. And $\Omega(s)$ is obtained by numerically integrating the Magnus series [20]:

$$\Omega(s) = \sum_{pq} \Omega_{pq}(s) : a_p^\dagger a_q : + \frac{1}{4} \sum_{pqrs} \Omega_{pqrs}(s) : a_p^\dagger a_q^\dagger a_s a_r : \quad (2.7a)$$

$$\frac{d\Omega(s)}{ds} = \sum_{m=0}^{\infty} \frac{b_m}{m!} [\Omega(s), \eta(s)]^{(m)} \quad (2.7b)$$

$$[\Omega(s), \eta(s)]^{(m)} \equiv \left[\Omega(s), [\Omega(s), \eta(s)]^{(m-1)} \right], \quad \forall m > 0 \quad (2.7c)$$

$$[\Omega(s), \eta(s)]^{(0)} \equiv \eta(s), \quad (2.7d)$$

where b_m are Bernoulli numbers of the 1st-kind. Eq. (2.7b) can be integrated with a 1st-order Euler solver with the benefit of $H(s)$ being unitarily equivalent to H , regardless of errors incurred in $\Omega(s)$ [20].¹² And the unitary transformed Hamiltonian $H(s)$, is given by the Baker-Campbell-Hausdorff (BCH) formula

$$H(s) = e^{\Omega(s)} \underbrace{H(0)}_H e^{-\Omega(s)} = \sum_{m=0}^{\infty} \frac{1}{m!} [\Omega(s), H(0)]^{(m)}. \quad (2.8)$$

In this work, we utilize the minimal decoupling scheme detailed by Jensen *et al.* [19] to eliminate all one-particle-one-hole (1p1h) excitations $|\Phi_i^a\rangle$, and 2p2h excitations $|\Phi_{ij}^{ab}\rangle$, generated by H acting once on $|\Phi\rangle$.¹³ We work in the single reference picture [19]; and the

¹²While a nice feature, the built-in unitarity of the Magnus-IMSRG does not permit arbitrarily large errors in $\Omega(s)$. This may yield divergent calculations of $H(s)$ that are although unitary, but do not yield physically meaningful observables.

¹³Although we describe the minimal decoupling scheme in this subsection, its use is not restricted to the Magnus-IMSRG. It can also be applied to the flow implementation of the IMSRG [19].

off-diagonal sectors of $H(s)$ are given by

$$H_{od}(s) = \sum_{ai} \langle \Phi | H(s) | \Phi_i^a \rangle : a_a^\dagger a_i : + \frac{1}{4} \sum_{abij} \langle \Phi | H(s) | \Phi_{ij}^{ab} \rangle : a_a^\dagger a_b^\dagger a_j a_i : + \text{H.c.} \quad (2.9)$$

where ‘‘H.c.’’ denotes the Hermitian conjugate of the first two terms in Eq. (2.9). Note that $\langle \Phi | H(s) | \Phi_i^a \rangle = 0$ in infinite nuclear matter—due to momentum conservation seen in Eqs. (2.15) and (2.17) in conjunction with Eq. (2.3c).¹⁴ Therefore, $|\Phi\rangle$ is a Hartree-Fock reference state. Figure 2.1 illustrates that so long the ground state wavefunction $|\Psi_{g.s}\rangle$, of H is approximated well by $|\Phi\rangle$, we can obtain the ground state energy of H by employing the minimal decoupling scheme. Consequently,

$$|\Psi_{g.s}\rangle = \lim_{s \rightarrow \infty} e^{-\Omega(s)} |\Phi\rangle. \quad (2.10)$$

If the Magnus-IMSRG is convergent—i.e. $\lim_{s \rightarrow \infty} H_{od}(s) = 0$, we take the scalar component of $\lim_{s \rightarrow \infty} H(s)$ as the ground state energy of H

$$\begin{aligned} E_{g.s} &\equiv \langle \Psi_{g.s} | H | \Psi_{g.s} \rangle = \lim_{s \rightarrow \infty} \langle \Phi | e^{\Omega(s)} H e^{-\Omega(s)} | \Phi \rangle \\ &= \langle \Phi | \lim_{s \rightarrow \infty} H(s) | \Phi \rangle = \left\{ \lim_{s \rightarrow \infty} H(s) \right\}_{0\text{-body}} = \lim_{s \rightarrow \infty} E(s). \end{aligned} \quad (2.11)$$

Therefore, $E(s)$ approximates $E_{g.s}$; and $\lim_{s \rightarrow \infty} E(s)$ is the ground state energy of H . For brevity in this work, we sometimes employ the notation: $E(\infty) \equiv \lim_{s \rightarrow \infty} E(s)$.

Figure 2.2 shows iterative IMSRG(2) approximations of the ground state energy. And the zero temperature ($T = 0$) equation-of-state (EOS) is taken as the converged IMSRG ground state energy per particle $E(\infty)/A$, over various particle densities ρ . Figure 2.2

¹⁴The flow equations also preserve momentum conservation.

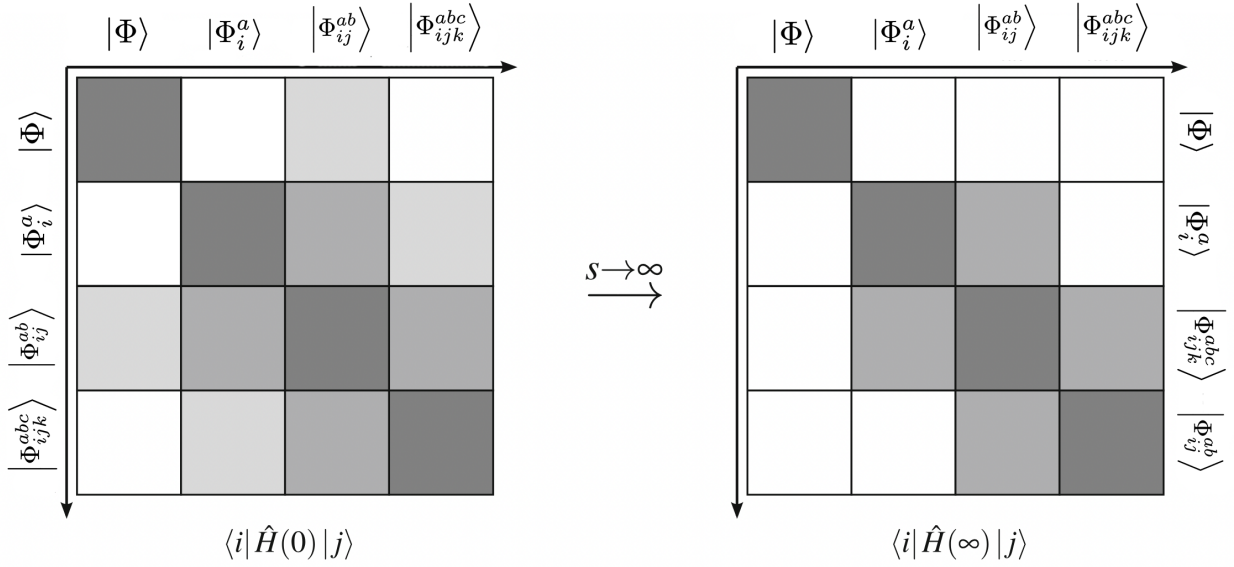


Figure 2.1: Schematic of the ground state decoupling of H carried out by the IMSRG(2) within the single-reference context. H is represented in a basis spanned by Slater determinant $|\Phi\rangle$, and its particle-hole excitations $|\Phi_{i,\dots}^a\rangle$. In the limit of $s \rightarrow \infty$, the IMSRG(2) eliminates the coupling of $|\Phi\rangle$ to $|\Phi_i^a\rangle$ and $|\Phi_{ij}^{ab}\rangle$ through H . Since H is truncated at the two-body level in Eq. (2.4a), it can generate at most $2p2h$ excitations by acting once on $|\Phi\rangle$. Consequently, the ground state energy of H is given by $\langle \Phi | \lim_{s \rightarrow \infty} H(s) | \Phi \rangle$. This figure is obtained courtesy of Jensen *et al.* [19].

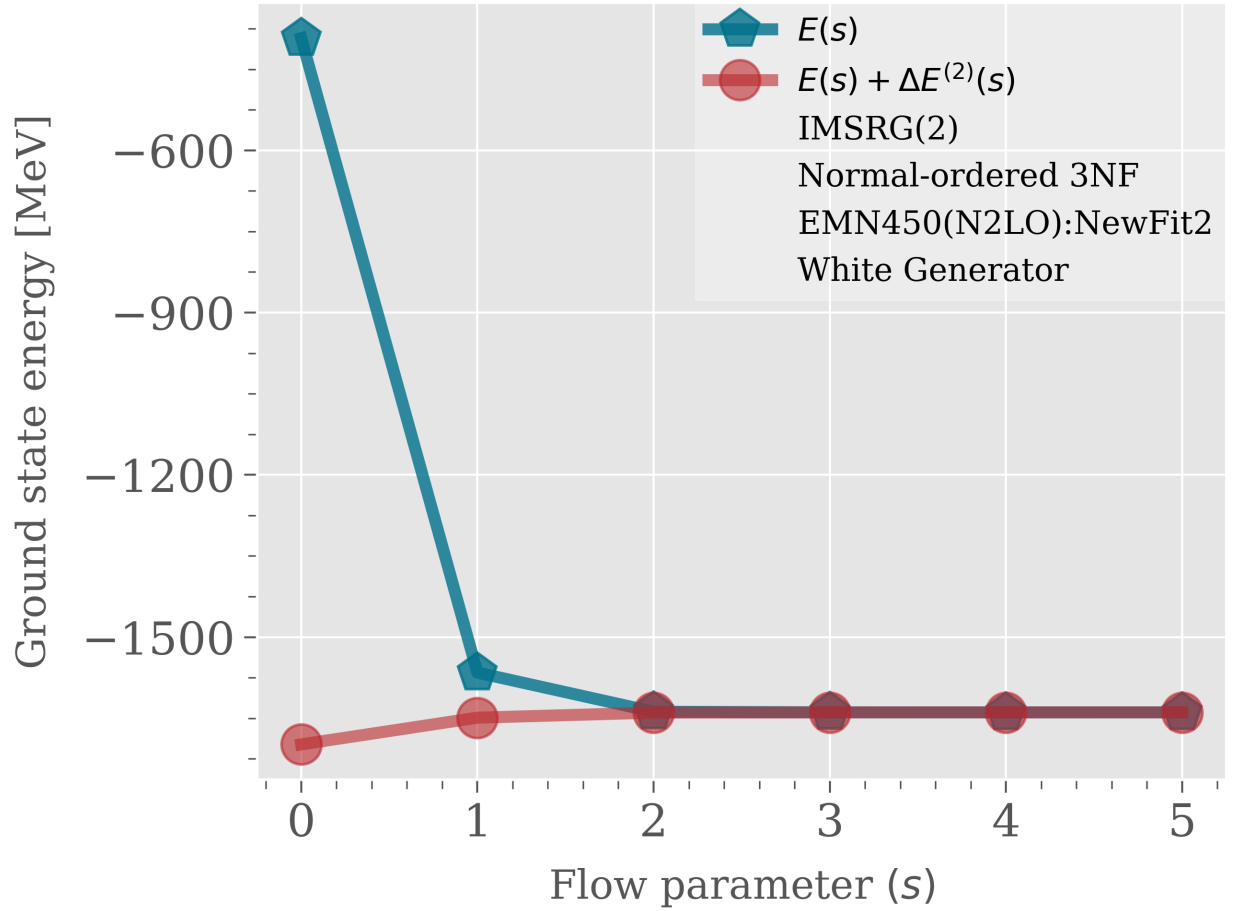


Figure 2.2: Iterative IMSRG(2) approximations to the ground state energy of H for symmetric $N = Z = 66$ nuclear matter at density $\rho = 0.11 \text{ fm}^{-3}$. This calculation is done in a model space of size $N_{\text{orbitals}} = 3700$. We include MBPT(2) correlations $\Delta E^{(2)}(s)$. Notice that $\lim_{s \rightarrow \infty} \Delta E^{(2)}(s) = 0$. Therefore, the IMSRG obviates MBPT(2) correlations as it converges in s .

includes 2nd-order Many-Body Perturbation Theory (MBPT) correlations from $H(s)$ to demonstrate that the IMSRG eliminates said correlations in the limit of $s \rightarrow \infty$. Therefore, the IMSRG generates a unitary equivalent $H(\infty)$, to H , such that 2nd-order MBPT on $H(\infty)$ is converged [10].

We utilize the Magnus-IMSRG in this work due to its many appealing features.¹⁵ By using a 1st-order Euler solver, the Magnus-IMSRG bypasses the needed storage of multiple solution vectors used by high-order solvers [20]. Once $\lim_{s \rightarrow \infty} \Omega(s)$ is computed, it permits unitary transformations to obtain observables of interest beyond energies [20]. Lastly, similarities between the Magnus-IMSRG and Unitary Coupled-Cluster theory (UCC) inspire novel IMSRG generators seen in Chapter 5 of this work.

2.3 Modeling Infinite Nuclear Matter in a Cubic Box

All operators in this work are represented within an infinite matter basis. In this section, we describe the single-, two-, and three-particle bases—which comprise the infinite matter basis.

2.3.1 Single-Particle Basis

We model nuclear matter following the work of Jensen *et al.* [19]. All calculations in this work are performed in a finite 3-dimensional box of volume $\mathcal{V} = \mathcal{L}^3$ [fm³] with periodic boundary conditions, containing N identical neutrons and Z identical protons.¹⁶ The density of particles in the box is given by $\rho = A/\mathcal{V}$ [fm⁻³], where $A = N + Z$. The single-particle

¹⁵All IMSRG results in this work are procured using the Magnus-IMSRG formulation.

¹⁶We use periodic boundary conditions to model an infinite system. Also, \mathcal{L} denotes the box-size.

basis is composed of normalized plane wave states:

$$\psi_{\vec{k}, \sigma_z, \tau_z}(\vec{r}) = \frac{e^{-i\vec{k}\cdot\vec{r}}}{\sqrt{\mathcal{V}}} \times \underbrace{|\sigma_z\rangle \times |\tau_z\rangle}_{\langle \vec{k} | \vec{r} \rangle}, \quad (2.12)$$

$$|\sigma_z = 1\rangle = |\uparrow\rangle, \quad |\sigma_z = 0\rangle = |\downarrow\rangle,$$

$$|\tau_z = 1\rangle = |\uparrow\rangle, \quad |\tau_z = 0\rangle = |\downarrow\rangle,$$

$$\vec{k} = \frac{2\pi}{\mathcal{L}} \vec{n}, \quad \|\vec{n}\|^2 \leq N_{\max}, \quad \vec{n} \in \mathbb{Z}^3.$$

$|\sigma_z\rangle$, and $|\tau_z\rangle$ are spin and isospin projection states on the z -axis. $\tau_z = 1$ labels proton states, while $\tau_z = 0$ labels neutron states. And $N_{\max} \geq 0$ is a proxy for the upper-bound of momenta \vec{k} , in the basis. We work in spin unpolarized systems; therefore, each orbital is at least 2-fold degenerate. Our basis is also isospin unpolarized, so long $\min(N, Z) > 0$. If $\min(N, Z) = 0$, we can work in an isospin polarized basis—if we can guarantee that all body-operators built on top of the basis will conserve total charge. By storing only isospin polarized orbitals, we reduce the overall basis size by a factor of 2. Furthermore, each orbital $\psi_{\vec{k}, \sigma_z, \tau_z}(\vec{r})$, has an associated kinetic energy $\epsilon_{\vec{k}, \sigma_z, \tau_z}$, dependent on the nucleon mass m_{τ_z}

$$\epsilon_{\vec{k}, \sigma_z, \tau_z} = \frac{(\hbar c)^2}{2m_{\tau_z}} \vec{k} \cdot \vec{k}. \quad (2.13)$$

$m_{\tau_z=1} = 938.272$ MeV, and $m_{\tau_z=0} = 939.565$ MeV. And each orbital $\psi_{\vec{k}, \sigma_z, \tau_z}(\vec{r})$, has an associated occupation number $\text{Occ}_{\vec{k}, \sigma_z, \tau_z}$ —which measures the number of particles located in its respective orbital. This work is done at zero temperature; therefore, the occupation of all orbitals is binary.

N_{\max} is used to truncate the size of the single-particle basis into a closed shell structure.¹⁷ A shell is a collection of orbitals with the same kinetic energies. Every shell has an associated modevector \vec{n}_{Shell} such that $\|\vec{n}_{\text{Shell}}\|^2 \leq N_{\max}$. We choose to either completely fill each shell with particles, or leave each shell empty. This is done to model the wavefunction when it is believed to have a closed shell structure. N and Z are magic numbers with sample values: 0, 2, 14, 38, 54, 66, 114, 162, 186, 246, 294, 342, 358, 406, 502, 514, \dots ¹⁸ And, the total number of single-particle states in the basis is denoted N_{orbitals} . We include an example single-particle basis in Table 2.1. Notice, we fill our basis such that all nucleons sit in orbitals with the lowest possible energies consistent with the Pauli exclusion principle. This is done to model the ground state wavefunction. Thus, the basis contains baked-in information regarding the overall system’s wavefunction.

Table 2.1: Single-particle basis with $N_{\text{orbitals}} = 76$ containing $N = 2$ and $Z = 14$ nucleons in a box sized $\mathcal{L} = 4.308 \text{ fm}$ at density $\rho = 0.20 \text{ fm}^{-3}$.

Index	Occ	n_x	n_y	n_z	σ_z	τ_z	$k \text{ [fm}^{-1}\text{]}$	$\epsilon \text{ [MeV]}$
0	1	0	0	0	$\downarrow\uparrow$	\downarrow	0.000	0.000
2	1	0	0	0	$\downarrow\uparrow$	\uparrow	0.000	0.000
4	1	-1	0	0	$\downarrow\uparrow$	\uparrow	1.458	44.121
6	1	0	-1	0	$\downarrow\uparrow$	\uparrow	1.458	44.121
8	1	0	0	-1	$\downarrow\uparrow$	\uparrow	1.458	44.121
10	1	0	0	1	$\downarrow\uparrow$	\uparrow	1.458	44.121
12	1	0	1	0	$\downarrow\uparrow$	\uparrow	1.458	44.121
14	1	1	0	0	$\downarrow\uparrow$	\uparrow	1.458	44.121

¹⁷Practically, we must truncate the number of orbitals in our basis. This introduces artifacts in our many-body calculations that we try to minimize using a large number of orbitals.

¹⁸Practically, we must truncate the number of particles in our basis. This introduces finite-size artifacts in our many-body calculations. See Subsection 2.3.3 for how we address this issue.

Table 2.1 (cont'd)								
Index	Occ	n_x	n_y	n_z	σ_z	τ_z	k [fm ⁻¹]	ϵ [MeV]
16	0	-1	-1	0	↓↑	↑	2.062	88.242
18	0	-1	0	-1	↓↑	↑	2.062	88.242
20	0	-1	0	1	↓↑	↑	2.062	88.242
22	0	-1	1	0	↓↑	↑	2.062	88.242
24	0	0	-1	-1	↓↑	↑	2.062	88.242
26	0	0	-1	1	↓↑	↑	2.062	88.242
28	0	0	1	-1	↓↑	↑	2.062	88.242
30	0	0	1	1	↓↑	↑	2.062	88.242
32	0	1	-1	0	↓↑	↑	2.062	88.242
34	0	1	0	-1	↓↑	↑	2.062	88.242
36	0	1	0	1	↓↑	↑	2.062	88.242
38	0	1	1	0	↓↑	↑	2.062	88.242
40	0	-1	0	0	↓↑	↓	1.458	44.060
42	0	0	-1	0	↓↑	↓	1.458	44.060
44	0	0	0	-1	↓↑	↓	1.458	44.060
46	0	0	0	1	↓↑	↓	1.458	44.060
48	0	0	1	0	↓↑	↓	1.458	44.060
50	0	1	0	0	↓↑	↓	1.458	44.060
52	0	-1	-1	0	↓↑	↓	2.062	88.121
54	0	-1	0	-1	↓↑	↓	2.062	88.121
56	0	-1	0	1	↓↑	↓	2.062	88.121
58	0	-1	1	0	↓↑	↓	2.062	88.121
60	0	0	-1	-1	↓↑	↓	2.062	88.121

Table 2.1 (cont'd)								
Index	Occ	n_x	n_y	n_z	σ_z	τ_z	k [fm ⁻¹]	ϵ [MeV]
62	0	0	-1	1	$\downarrow\uparrow$	\downarrow	2.062	88.121
64	0	0	1	-1	$\downarrow\uparrow$	\downarrow	2.062	88.121
66	0	0	1	1	$\downarrow\uparrow$	\downarrow	2.062	88.121
68	0	1	-1	0	$\downarrow\uparrow$	\downarrow	2.062	88.121
70	0	1	0	-1	$\downarrow\uparrow$	\downarrow	2.062	88.121
72	0	1	0	1	$\downarrow\uparrow$	\downarrow	2.062	88.121
74	0	1	1	0	$\downarrow\uparrow$	\downarrow	2.062	88.121

2.3.2 Two- and Three-Particle Bases

The two- and three-particle bases are subsequently built on top of the single-particle basis. The two-particle basis stores all tuples $(p, q) \forall pq$, and categorizes them into blocks that conserve symmetries of the two-body Hamiltonian. Particularly, two-particle blocks contain two-particle states (p, q) and (r, s) such that

$$(\tau_z)_p + (\tau_z)_q = (\tau_z)_r + (\tau_z)_s, \quad (2.14)$$

$$\vec{k}_p + \vec{k}_q = \vec{k}_r + \vec{k}_s \quad \forall pqr. \quad (2.15)$$

Likewise, the three-particle basis stores all triples $(p, q, r) \forall pqr$, and categorizes them into blocks that conserve symmetries of the three-body Hamiltonian. Particularly, three-particle

blocks contain three-particle states (p, q, r) and (s, t, u) such that

$$(\tau_z)_p + (\tau_z)_q + (\tau_z)_r = (\tau_z)_s + (\tau_z)_t + (\tau_z)_u, \quad (2.16)$$

$$\vec{k}_p + \vec{k}_q + \vec{k}_r = \vec{k}_s + \vec{k}_t + \vec{k}_u \quad \forall pqrstu. \quad (2.17)$$

The two- and three-particle blocks are then used to create block matrices of two- and three-body operators seen in Chapter 3.¹⁹ The two- and three-particle bases also store metadata such as the numbers and locations of two- and three-particle states for our IMSRG program's administration.

2.3.3 Errors Due to Finite Size and Incomplete Basis Sets

To obtain many-body quantities that are free from finite size and incomplete basis set artifacts, we must approach the thermodynamic and complete basis set limit [23]. Approaching the thermodynamic limit requires the use of a sufficiently large number of particles at fixed particle density. Likewise, approaching the complete basis set limit requires the use of a sufficiently large number of single-particle orbitals. IMSRG calculations with large particle numbers and basis sizes are computationally expensive. Therefore, we must balance the need to maximize particle numbers and basis sizes, with constraints from our available computational resources. Although we do not study how finite size and finite basis errors affect equation-of-state calculations in this work, we take reasonable measures to reduce such errors. Equations-of-state are computed in Chapter 4 using $A = 66$ and $A = 132$ in pure neutron and symmetric matter, respectively. This is done following Hagen *et al.*'s observation that finite size artifacts are particularly small in pure $N = 66$ neutron and sym-

¹⁹The single-particle basis is also used to create one-body operators composed of one matrix block with shape $N_{\text{orbitals}} \times N_{\text{orbitals}}$.

metric $N = Z = 66$ matter [23].²⁰ Moreover, we perform IMSRG calculations with large values of N_{orbitals} , such that results are obtained within days, using < 1 terabyte memory consumption.

2.4 Conclusion

We model an infinite lattice of nuclear matter, by placing nucleons in a finite-sized box with periodic boundary conditions. This finite box contains states which form the basis of our calculations. Nuclear Hamiltonians are thus, represented within the infinite matter basis, and diagonalized using the IMSRG to extract ground state energies of nuclear matter. Therefore, we can obtain zero temperature nuclear equations-of-state, by computing ground state energies that are normalized to the number of nucleons in our model—over various nucleon densities. In the following chapter, we describe the IMSRG program that is used to extract nuclear equations-of-state.

²⁰We only utilize periodic boundary conditions in this work. Following insights from Hagen *et al.*, it might be lucrative to implement twist-averaged boundary conditions—to further reduce finite size effects [23]. We also have the computational horsepower to perform $A \sim 1000$ IMSRG(2) calculations—which have significantly less finite size effects than their $A \sim 132$ counterparts [23]. However, we believe such calculations might require significantly more orbitals than their $A \sim 132$ counterparts—to sufficiently reduce incomplete basis set artifacts. Thus, we consider $A \sim 1000$ EOS calculations in this work to be preliminary.

Chapter 3. Nuclear Matter IMSRG Program

“You think too much. Why

not go do something?”

—Donald Fear

We need high performant and reliable codes to achieve our physics objectives. Therefore, we have developed a C++ IMSRG program (dubbed “SCKY-IMSRG”) that calculates ground state energies of nuclear matter with the following features:¹

1. Carefully designed—verbose, unit-tested, and sufficiently general for future needs
2. Compatible with various proton fractions Z/A , and extendable to other systems (e.g. finite nuclei, e^- gas)
3. Based on Eigen C++ library with BLAS, Intel MKL, OpenMP multi-threading, and The Message Passing Interface (MPI) support²
4. Optimized for high-performance calculations: ~ 10 hour runtime and < 1 terabyte memory consumption for $A = 132$ and $N_{\text{orbitals}} \sim 3700$, without three-body forces
5. Integrated with a variety of chiral forces from Drischler *et al.* [1], including density-dependent three-body forces
6. Equipped with canonical and novel generators from Chapter 5
7. Equipped with Shanks + Padé extrapolators from Chapter 6
8. Modernized with automated data compilation—file parsing for plots

We detail the most salient components of the SCKY-IMSRG in this chapter.

¹The name SCKY-IMSRG is chosen as a homage to the founders of this project: Yani Udiani, Kang Yu, Christian Drischler and Scott Bogner; and the incredible journey we took to complete it.

²Although available, MPI is not used in this project. Our MPI implementation in the SCKY-IMSRG assumes that all nodes store *all* IMSRG operators. Given the high memory demands needed just to do a single large-scale IMSRG calculation on *one* node, the use of MPI with multiple nodes is intractable in this project.

3.1 SCKY-IMSRG Program Output

We include a sample program output below:³

```
cmd: ./imsrg -N 66 -Z 0 -gen born -rho 0.12 -numshells 1
hostname: Urmum
date (month/day/year): 10/08/2024 : 15:04:23
Warning: EOS_NNPWBASEPATH hasn't been set.
Warning: EOS_NNEFFPWBASEPATH hasn't been set.
+++++
overall configuration
+++++

N.....66
Z.....0
numShells.....1
rho.....0.12
temperature.....0

ConserveTz.....1
usePH.....1
boxDimension.....3
ds.....1
ODE_threshold.....1e-06
useSCKYTrunc.....0
saveMISCResults.....0
noIMSRG.....0

bornOrder.....5
genRefOrder.....14
genTargOrder.....14
generator_choice.....6
imsrgRunConfig.....0
```

³One might wonder why MBPT *before* the IMSRG starts differs from MBPT at $s = 0$. This is because we employ a generalized form of MBPT during the IMSRG seen in Appendix H—which depends on the chosen IMSRG generator. Standard MBPT can be restored using White’s generator.

imsrgSolver.....0
useSCKYInteraction.....1
interaction.....OptimizedN2LO

[NOTIFICATION]: Anti-symmetrized components of all BodyOps will be omitted.

----- SINGLE PARTICLE BASIS INFO -----

Neutron number (N): 66
Proton number (Z): 0
Total particle number (A): 66
Neutron fraction (xn): 1
Proton fraction (xp): 0

[NOTIFICATION]: Only storing neutron containing orbitals.

[ACTION]: Generating and populating single particle states (SPS)...

[SUCCESS!]: The single particle basis (SPB) has been constructed.

[UNIT SYSTEM]: Length[fm], Density[fm⁻³], Momentum[fm⁻¹], Mass/Energy[MeV]

[NOTIFICATION]: Using SPB composed of plane waves in a 3-D box with periodic boundary conditions.

Number of shells above max(N,Z) occupied orbits (numShells): 1

SPS obtained using box cutoff: $n_x^2 + n_y^2 + n_z^2 \leq n_{max}$

Number of single particle states (numSPS): 114

Box size (L): 8.19321271 [fm]

Particle density (A/L³): 0.12000000 [fm⁻³]

Neutron fermi momentum (kfn): 1.53375374 [fm⁻¹], 302.65099380 [MeV]

Momentum cutoff (kmax): 1.71478881 [fm⁻¹], 338.37409780 [MeV]

Modevector cutoff: 2 1 0

[NOTIFICATION]: All 66 fermions have the lowest possible kinetic energies consistent with the exclusion principle.

[NOTIFICATION]: When handling: Two Particle Basis.

The 2-particle basis has been successfully constructed!

Number of stored physical 2-particle states: 6441

Number of blocks in the 2-particle basis: 341

Time taken to create standard basis --- 18.669 --- milliseconds.

[NOTIFICATION]: When handling: A-Body Operator: H

This 0.003973 [GB] HamiltonianOp is populating itself up to at most the 2-Body level.

Time taken to populate HamiltonianOp --- 135.176 --- milliseconds.

[NOTIFICATION]: When handling: A-Body Operator: H

This ABodyOp is normal ordering itself at the 2-Body level.

Time taken to normal order ABodyOp --- 0.378 --- milliseconds.

[NOTIFICATION]: When handling: A-Body Operator: H

Measuring how much this ABodyOp deviates from its stated hermiticity.

$||H[0]-H[0]^{\dagger}|| = 0.000000000000$

$||H[1]-H[1]^{\dagger}|| = 0.000000000000$

$||H[2]-H[2]^{\dagger}|| = 0.000000000000$

$||H-H^{\dagger}|| = 0.000000000000$

[NOTIFICATION]: When handling: A-Body Operator: H

Printing available norms over this ABodyOp's differing sectors.

$||H[0]|| = 892.54185704$

$||H[1]|| = 316.91701542$, $||H[1]_{ai}|| = 0.00000000$, $||H[1]_{(p!=q)}|| = 0.00000000$

$||H[2]|| = 415.26158947$, $||H[2]_{abij}|| = 111.54291337$, $||H[2]_{abcj+ijka}|| = 258.75293935$,

$||H[2]_{iajb}|| = 204.29038345$, $||H[2]_{abcd}|| = 98.37469423$, $||H[2]_{ijkl}|| = 204.04690958$

[NOTIFICATION]: When handling: MBPT solver.

Doing many body perturbation theory up to 3rd order.

$E_{\{Reference\}} / A = (13.52336147, 0.00000000)$

$dE2 / A = (-0.35265909, -0.00000000)$

$dE3 / A = (0.07796819, -0.00000000)$

$E_{\{Correlation\}} / A = (-0.27469090, -0.00000000)$

$(E_{\{Reference\}} + dE2) / A = (13.17070238, -0.00000000)$

$(E_{\{Reference\}} + dE) / A = (13.24867057, -0.00000000)$

Time taken to do MBPT --- 55.860 --- milliseconds.

[NOTIFICATION]: When handling commutator routine.

Constructing particle-hole basis.

Time taken to construct the particle-hole basis --- 40.622 --- milliseconds.

Using mirror block symmetry in particle-hole commutators.

[NOTIFICATION]: When handling: A-Body Operator: Eta

Generating Born generator.

Born series order: 5

[NOTIFICATION]: When handling: IMSRG ODE Solver.

All 10 needed A-Body operators have been created costing a total 0.043906 [GB].

Time taken to construct operators and commutator --- 208.859 --- milliseconds.

Initiating IMSRG(2) evolution...

Flow (s)	E/A	(E+DE2)/A	(E+DE2+DE3)/A	Shanks(1)	Pade	Eta[2]	Gammaod
0.00000000	13.52336147	13.22700538	13.26500506	13.22700538	13.22700538	1.52374776	111.54291337
1.00000000	13.23030104	13.23009147	13.23008626	13.23009147	13.23009219	0.05139831	2.33940529
2.00000000	13.23011774	13.23011762	13.23011761	13.23011785	13.23011785	0.00134170	0.04758731

Correlation energy per particle: -0.29324373

Nonperturbativity (smaller is better): 0.40019827

Time taken to perform IMSRG transformations --- 913.521 --- milliseconds.

[NOTIFICATION]: When handling commutator routine.

Printing any existing performance statistics:

Commute(): 35 calls | <duration> = 25.6995 milliseconds | total duration = 899.4820 milliseconds

Commute1_1_0(): 16 calls | 0.0288 % of total duration

Commute1_1_1(): 16 calls | 2.2612 % of total duration

Commute1_2_2(): 32 calls | 0.9749 % of total duration

Commute2_2_0(): 32 calls | 0.1937 % of total duration

Commute2_2_1(): 26 calls | 31.1108 % of total duration

Commute2_2_2(): 29 calls | 65.0163 % of total duration
Commute2_2_2_Ladder(): 29 calls | 48.4970 % of total duration
Commute2_2_2_Ladder()'s DotProd(): 29 calls | 47.5244 % of total duration
Commute2_2_2_Ladder()'s hermitize: 29 calls | 0.4340 % of total duration
Commute2_2_2_PH(): 29 calls | 16.5101 % of total duration
Commute2_2_2_PH()'s DotProd(): 29 calls | 13.9360 % of total duration
PH-Transform: 29 calls | 1.0833 % of total duration
PH-Inverse Transform: 29 calls | 1.4822 % of total duration
Anti-Symmetrization: 26 calls | 0.0002 % of total duration
BornSeriesCommute(): 10 out of 35 Commute() calls | 35.6947 % of total duration
MBPT(2) Commute(): 6 out of 35 Commute() calls | 0.0481 % of total duration
MBPT(3) Commute(): 3 out of 35 Commute() calls | 3.7414 % of total duration
There were 2 Anti-Hermitian commute calls.
There were 33 Hermitian commute calls.
Operators for approximate particle-hole cost a total 0.00824678 [GB].

[NOTIFICATION]: When handling: Rank 2-Body Operator: 1st Internal Commutator Temporary

Printing distribution of blocks:

There are a total of 235337 matrix elements.

There are 24 blocks shaped (1, 1)

There are 60 blocks shaped (4, 4)

There are 72 blocks shaped (8, 8)

There are 6 blocks shaped (9, 9)

There are 24 blocks shaped (12, 12)

There are 8 blocks shaped (13, 13)

There are 54 blocks shaped (20, 20)

There are 12 blocks shaped (25, 25)

There are 48 blocks shaped (36, 36)

There are 6 blocks shaped (45, 45)

There are 8 blocks shaped (52, 52)

There are 12 blocks shaped (68, 68)

There are 6 blocks shaped (72, 72)

There is 1 block shaped (113, 113)

Time taken to run entire program --- 1.184 --- seconds.

The SCKY-IMSRG is descriptive. For example, certain class instances are named. This is because the code does runtime checks, and alerts the user to information unique to each instance. Care is taken to ensure that runtime checks do not affect the program’s performance. These runtime alerts provide generic information, warnings, and errors. Alerts with named class instances are incorporated to help developers pinpoint sources of runtime errors, or worse yet, unusual behaviour. Although mundane, a logging system is important to give developers runtime debugging tools, in addition to confidence that the program is working as intended.

3.2 Big Data Management: Parsing IMSRG Outputs

Each IMSRG output contains a trove of interesting data. Moreover, a large amount of IMSRG output files are created when generating the EOS. It is thus paramount that data are properly labeled, sorted, and accessible to everyone with access to the project. To achieve these goals, the SCKY-IMSRG is equipped with scripts that label and parse all program outputs, aggregate parsed data, and plot quantities of interest such as the EOS, performance statistics, and IMSRG flow data.

3.3 Nuclear Forces

The SCKY-IMSRG contains momentum space representations of the One Pion Exchange (OPE) [24], N2LO_{opt} [23, 25],⁴ and Minnesota [17, 19] potentials—implemented directly within a finite box. Moreover, the SCKY-IMSRG has wrappers to convert free space two-

⁴The SCKY-IMSRG uses wrappers to a Fortran implementation of N2LO_{opt} in a finite box, proudly stolen from Ekström *et al.* [23, 25].

and three-body interactions from Drischler *et al.* [1], into their respective box representations (see Eq. (E.14)). Free space interactions from Drischler *et al.* [1] are obtained using the partial wave expansion (PWE). And the machinery of Drischler *et al.* [1] has been validated by comparing matrix elements of the One Pion Exchange interaction (OPE) summed into a finite box using the PWE (see Eq. (E.12)) from Drischler *et al.* [1], to matrix elements of OPE implemented directly in a finite box—seen in Eq. (D.21). See Appendices D and E for additional details. Although the partial wave expansion is not directly utilized by the SCKY-IMSRG, we include its derivation for two-body interactions in Appendix E. We hope that Appendix E clarifies the derivation of the partial wave expansion given by Jensen *et al.* [19]. In Appendix B, we derive momentum space representations—within a finite box—of local interactions, originally given in coordinate space. Subsequently, we derive the momentum space representation of the Minnesota potential [17] in Appendix C. Although the Minnesota potential is not used in this work, it is included due its historical significance in nuclear matter calculations [16, 19, 23]. And, we add a correction to its momentum space representation within a finite box, given by Jensen *et al.* [19], by including the appropriate error functions in Eq. (C.22).

3.4 SCKY-IMSRG Program Hierarchy

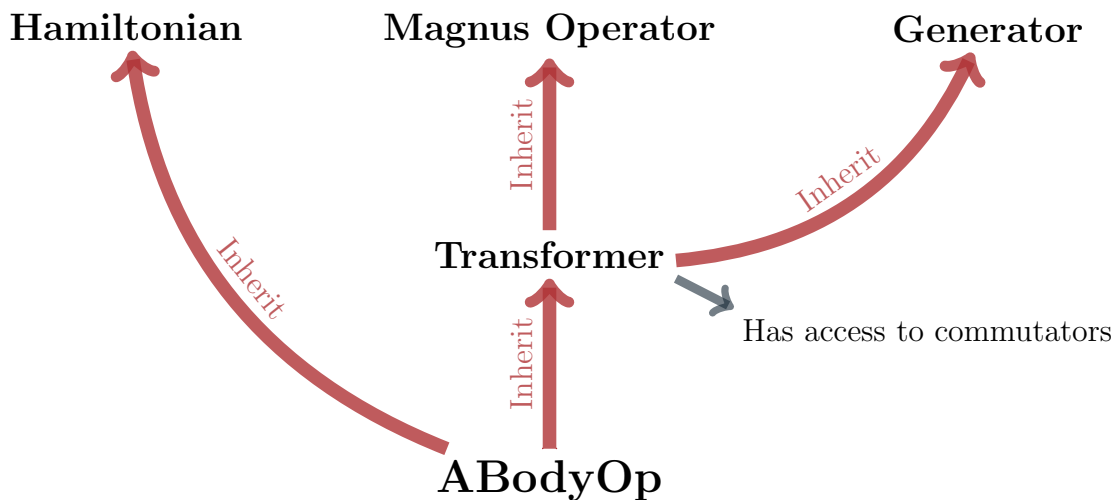
The SCKY-IMSRG creates an A-particle basis—which currently stores zero-, one-, two-, and up to three-particle bases.⁵ The zero-particle basis contratrivially contains only one block with one state (for scalars). The one-particle basis stores the physical single-particle states, in addition to metadata such as the number of occupied (hole) and unoccupied (particle) states

⁵The three-particle basis is omitted if three-body operators are not present.

in the system, with locations of hole and particle states. Data from the one-particle basis are propagated to higher rank bases to form two- and three-particle states, and organize them into blocks according to symmetries of the Hamiltonian—i.e. center-of-mass momentum and charge conservation. Data stored in the A-particle basis are then propagated to the programs’ many-body functions such as normal orderings, commutators, generators, and norms for ground state decoupling. See Jensen *et al.* [19] and Hergert *et al.* [10] for more details regarding these many-body functions.

ABodyOps (meaning *A*-body operators) are the foundational data structure of the SCKY-IMSRG. Representing a linear combination of body-operators, each ABodyOp stores an array of BodyOps. BodyOps (meaning body-operators) store blocks of complex-double Eigen matrices of varying sizes. BodyOps contain block matrices to store only the symmetry preserving parts of our operators—conserving memory. ABodyOps and BodyOps are imbued with arithmetic operations for series expansions. And commutators are defined between ABodyOps. ABodyOps are designed to abstract away administration of the individual body components of the IMSRG (and UCC). For example, we solve the flow implementation of the IMSRG directly in Eq. (2.2e)’s form, and the Magnus expansion in Eq. (2.7b)’s form. By doing so, we let the commutators handle the individual components of ABodyOps—so long the input ABodyOps are normal-ordered (see Listing 3.1). Thus, extensions to four- and higher-body forces can be implemented without rewriting the SCKY-IMSRG’s administration. Users can specify the individual BodyOp components of an ABodyOp to be constructed. Therefore, if an ABodyOp is guaranteed to only have one nonzero BodyOp, users can only store that nonzero rank of the ABodyOp—conserving memory. Moreover, all ABodyOps provide access to their individual BodyOps for users that need to work directly with BodyOps.

Operators in the SCKY-IMSRG are built with the following hierarchy:⁶

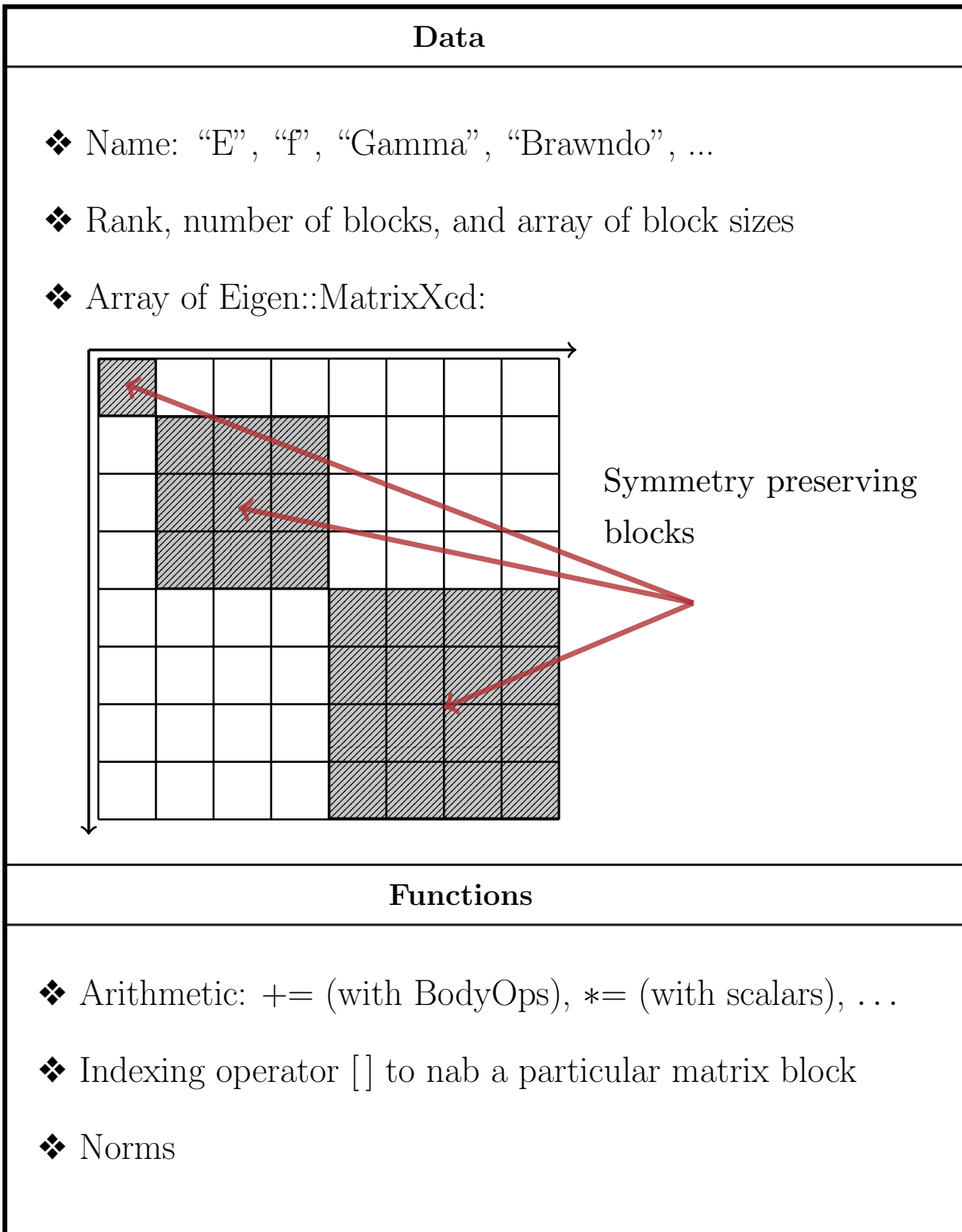


Data
<ul style="list-style-type: none"> ❖ Name: “H”, “Omega”, “Eta”, “Richard”, ... ❖ A-particle basis ❖ Array of rank 0, 1, 2, ... -BodyOps ❖ Hermitized, normal-ordered and anti-symmetrized status
Functions
<ul style="list-style-type: none"> ❖ Normal-ordering ❖ Commutators defined between ABodyOps ❖ Arithmetic: += (with ABodyOps), *= (with scalars), ... ❖ Indexing operator [] to grab a particular BodyOp ❖ Norms, anti-symmetrization

⁶Commutators are actually defined outside of ABodyOps, but they could be placed inside the class!

All BodyOps have the following design pattern:

BodyOp



Listing 3.1: Commutators handle the individual operator components of ABodyOps.

```

void Commutator::Commute(const ABodyOp &op1, const ABodyOp &op2, ABodyOp &buffer){
    VerifyInputs(op1, op2, buffer);
    PrepareBuffer(op1, op2, buffer);
    const unsigned maxRank = pBasis->maxRank;
    const std::vector<unsigned> rankStatus1 = op1.GetRankStatus();
    const std::vector<unsigned> rankStatus2 = op2.GetRankStatus();
    for(unsigned i = 0U; i <= maxRank; i++){
        for(unsigned j = 0U; j <= maxRank; j++){
            if(rankStatus1[i] == 1U and rankStatus2[j] == 1U){
                Commute(op1[i], op2[j], buffer);
            }
        }
    }
}

```

Transformers are ABodyOps with access to commutators. And commutators are defined in Listing 3.1. Using the ABodyOp data structure, series expansions involving nested commutators of A -body operators (e.g. BCH and Magnus) become easily abstracted. We include the transformation function used to compute the BCH and Magnus expansions in Listing 3.2.

Listing 3.2: Transform used by Transformers for expansions involving nested commutators

```

void Transformer::Transform(const ABodyOp &operand, ABodyOp &buffer,
                           const std::vector<double> &seriesCoeffs,
                           const std::vector<double> &coeffsForConvergenceCheck,
                           const unsigned rankForConvergenceCheck,
                           const double tolerance, const double seriesCoeffTolerance){
    if(temps->GetNumTemps() < 2U){
        Error(std::string("Failure in Transformer::Transform(): temps only contains ")
              + std::to_string(temps->GetNumTemps())
              + std::string(" ABodyOps. A minimum of 2 is needed to store results "
                             "from the nested commutators."));
    }
}

```

```

if(seriesCoeffs.empty()){
    Error("Failure in Transformer::Transform(): Input series has no coefficients.");
}
if(seriesCoeffs.size() != coeffsForConvergenceCheck.size()){
    Error("Failure in Transformer::Transform(): "
        "seriesCoeffs.size != coeffsForConvergenceCheck.size().");
}
if(&operand == &buffer and seriesCoeffs[0U] != 1.0){
    Error("Failure in Transformer::Transform(): &operand == &buffer,"
        " yet seriesCoeffs[0U] != 1.0.");
}
CollectionOfTemps &arrayOfTemps = *temps; // We'll treat temps like an array!
const std::vector<double> &cvgCoeff = coeffsForConvergenceCheck;
const unsigned maxOrder = seriesCoeffs.size()-1U;
const unsigned rank = rankForConvergenceCheck;

// Set C = c_0 * B
buffer = operand;
buffer *= seriesCoeffs[0U];

// Run checks to see if we need to go past 0th order
if(maxOrder == 0U) {return;}
if(maxOrder == 1U and abs(seriesCoeffs[1U]) <= seriesCoeffTolerance) {return;}

// Now, compute 1st order adjoint = [A,B]
ABodyOp &adjoint = arrayOfTemps[0U];
commutator->Commute(*this, operand, adjoint);
if(maxOrder == 1U){
    adjoint *= seriesCoeffs[1U];
    buffer += adjoint;
    return;
}

// Now, sum remaining terms into C
for(unsigned n = 2U; n <= maxOrder; n++){
    ABodyOp &previousAdjoint = arrayOfTemps[n % 2U]; // Stores [A, B]^(n-1)

```

```

ABodyOp &currentAdjoint = arrayOfTemps[(n + 1U) % 2U]; // Ready to store [A, B]^(n)

// Compute [A, [A, B]^(n-1)] if [A, B]^(n-1) != "0"
const auto prevNorm = abs(cvgCoeff[n-1U] * previousAdjoint[rank].FrobeniusNorm());
if(prevNorm > tolerance){
    commutator->Commute(*this, previousAdjoint, currentAdjoint);
}
// Sum: C += c_{n-1} * [A, B]^(n-1) if c_{n-1} != "0"
if(abs(seriesCoeffs[n-1U]) > seriesCoeffTolerance){
    previousAdjoint *= seriesCoeffs[n-1U];
    buffer += previousAdjoint;
}
// If [A, B]^(n-1) = "0", then the series has converged
if(prevNorm <= tolerance) {
    break;
}

// If the series hasn't yet converged, but we're at n = maxOrder,
// sum: C += c_{maxOrder} * [A, B]^(maxOrder)
if(n == maxOrder){
    if(abs(seriesCoeffs[maxOrder]) > seriesCoeffTolerance){
        currentAdjoint *= seriesCoeffs[maxOrder];
        buffer += currentAdjoint;
    }
}
}
}
}

```

With these developments, the BCH and Magnus series are easily given by Listing 3.3 and Listing 3.4, respectively.

Listing 3.3: Implementation of BCH expansion

```

void Transformer::BCHOptimized(const ABodyOp &operand, ABodyOp &buffer) {
    const unsigned maxOrder = 12U;
    const double tolerance = 1.0e-4;
    const unsigned rankForConvergenceCheck = 0U;
    const double seriesCoeffTolerance = 1.0e-10;
    const std::vector<double> expCoeffs = ExpXPowerSeriesCoeffs(maxOrder);
    const std::vector<double> invFactorial = this->ExpXPowerSeriesCoeffs(maxOrder);
    this->Transform(operand, buffer, expCoeffs, invFactorial,
                   rankForConvergenceCheck, tolerance, seriesCoeffTolerance);
}

```

Listing 3.4: Implementation of Magnus series

```

void MagnusOp::MagnusSeriesOptimized(const Generator &Eta, ABodyOp &dOmegas){
    const unsigned maxOrder = 12U;
    double tolerance = 1e-6;
    const unsigned rankForConvergenceCheck = 2U;
    const double seriesCoeffTolerance = 1.0e-10;
    const std::vector<double> bernoulliCoeffs1stKind = BernoulliCoeffs1stKind(maxOrder);
    const std::vector<double> invFactorial = this->ExpXPowerSeriesCoeffs(maxOrder);
    std::vector<double> coeffsForConvergenceCheck = invFactorial;
    if(useMorrisBognerTruncation){
        tolerance = 1e-4;
        double normOmega = abs((*this)[rankForConvergenceCheck].FrobeniusNorm());
        if(normOmega == 0.0){ normOmega = 1.0;}
        for(unsigned k = 0U; k <= maxOrder; k++) {
            double bernoulliWeight = abs(bernoulliCoeffs1stKind[k]);
            if(bernoulliWeight == 0.0){ bernoulliWeight = 1.0;}
            coeffsForConvergenceCheck[k] *= bernoulliWeight / normOmega;
        }
    }
    this->Transform(Eta, dOmegas, bernoulliCoeffs1stKind, coeffsForConvergenceCheck,
                   rankForConvergenceCheck, tolerance, seriesCoeffTolerance);
}

```

We denote the variable “tolerance” as $\epsilon_{\text{BCH}} = 1e-4$ and $\epsilon_{\text{Magnus}} = 1e-4$ in the BCH and Magnus series, respectively. We truncate the BCH and Magnus expansions according to Morris *et al.* [20]. The Magnus-IMSRG evolution is likewise, easily implemented in Listing 3.5.

Listing 3.5: Implementation of Magnus-IMSRG Evolution

```

for (int i = 0; i < maxiterations; i++){
    // Evolve
    Omega->MagnusSeriesOptimized(*Eta, *dOmegads); // Eta initialized outside
    *dOmegads *= ds;
    *Omega += *dOmegads;
    Omega->BCHOptimized(H0, *Hs); // H0 is the original Hamiltonian being diagonalized
    Eta->Update(*Hs);

    // Extract energies
    E = (*Hs)[0U][0U](0,0);
    mbptResultBuffer = Eta->DEFromMBPT(*Hs, useGeneralizedMBPT);
    DE2 = mbptResultBuffer[2U];
    DE3 = mbptResultBuffer[3U];
    CheckForImagEnergies(E, DE2 + DE3);

    // Print data
    PrintFlowResults(i+1, ds, A);

    // Convergence check
    if (abs(DE2)/abs(E) < epsilon){ // MBPT(3) unused since it is generally bad for UCC generators
        break;
    }
}

```

3.5 High-Performance Optimizations

It is essential to be efficient with memory and compute utilization to perform large-scale IMSRG calculations. The SCKY-IMSRG is optimized to that effect. Although we forgo including the internals of commutators between BodyOps in Listing 3.1 (for brevity), we describe the many optimizations made to such commutators in this section.

Since we only work with anti-symmetrized two-body operators, we only store one quadrant of each operator. Consider a two-body operator O . We partition O into $O_{\text{stored}} = O_{p<q, r<s}$ and $O_{\text{omitted}} \in \{O_{p>q, r<s}, O_{p<q, r>s}, O_{p>q, r>s}\}$. This cuts memory costs of the two-body operators by a factor of 4X. Moreover, we can recover O_{omitted} using O_{stored} with the appropriate sign—if needs be. Better yet, if we know the operation (such as a matrix product) that utilizes O_{omitted} , we can likely determine the result of the operation from O_{stored} with the appropriate sign. This saves an additional 4X in compute, modulo administrative costs.

Commutators between two-body operators are the most expensive computations in the IMSRG, if no three- or higher-body forces are present. Such commutators can be decomposed between so-called “ladder” and “particle-hole” terms. Ladder terms given by [10]

$$\left[A, B \right]_{pqrs} += \sum_{t<u} (1 - n_t - n_u) \times (A_{pqtu} B_{turs} - B_{pqtu} A_{turs}) \quad (3.1)$$

are already in matrix multiplication form, and are easily evaluated using Eigen’s optimized BLAS/MKL interface. Particle-hole terms are not given in matrix multiplication form, and are thus much harder to optimize. We detail the many optimizations on the particle-hole terms used in the SCKY-IMSRG in Appendix F, in addition to this thesis’ supporting graphic

presentation.

Commutators are further optimized using multiple strategies. We strategically reuse data as much as possible while minimizing function calls. We exploit hermiticity and anti-symmetry to avoid matrix products that can be deduced through symmetries. We avoid unnecessary copying of large objects through aliasing; and we write expressions in ways favorable to Eigen’s lazy evaluator. Moreover, OpenMP multi-threading directives are strategically placed to avoid threads writing to the same cache line—thus invalidating it. We assume that all rank 1 BodyOps are diagonal to eliminate summations in commutators involving one-body operators, while casting those expressions into more cache friendly forms. Lastly, we store all two-body occupation operators as diagonal matrices to save memory, and further minimize cache misses.

3.5.1 Performance Results

We perform multiple SCKY-IMSRG calculations while increasing the single-particle basis size to see general trends of the SCKY-IMSRG’s computational scaling. Results are obtained using high-performance compute resources provided by the Institute for Cyber-Enabled Research (ICER) at Michigan State University. The IMSRG outputs for these results are included in the project’s repository; and the resulting figures are plotted by our automated data managers.

Figure 3.1 displays the growing memory cost needed to create nine ABodyOps, in addition to all diagonal occupation matrices, and temporaries for particle-hole terms. Three ABodyOps are internally used to evaluate one commutator.⁷ Two temporaries are needed to

⁷Of the three ABodyOps stored in a commutator, one ABodyOp is used to store a one-body occupation operator. Only the one-body rank of said ABodyOp is allocated to save memory.

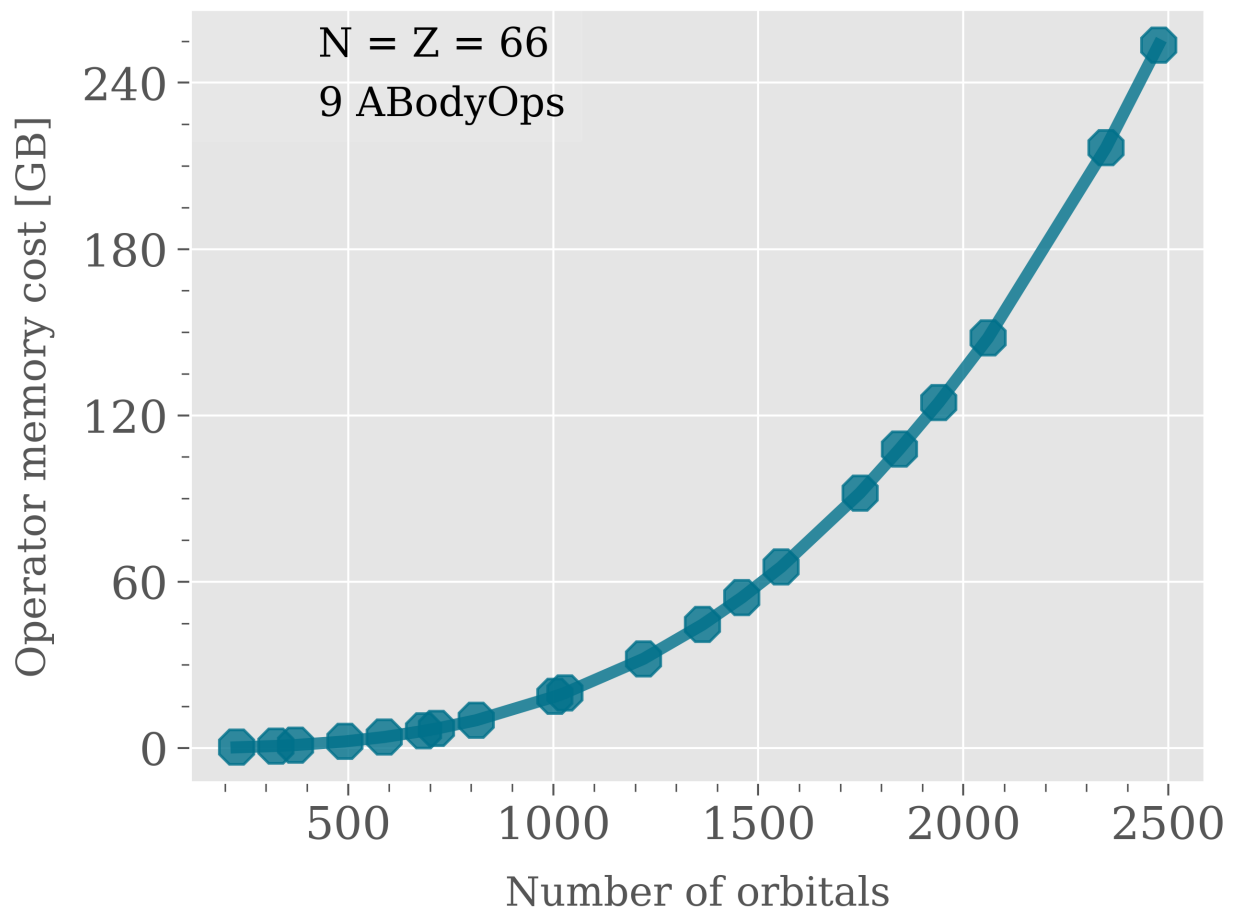


Figure 3.1: Memory cost of all operators in the SCKY-IMSRG as we increase the basis size. The majority of the SCKY-IMSRG’s memory requirements come from ABodyOps.

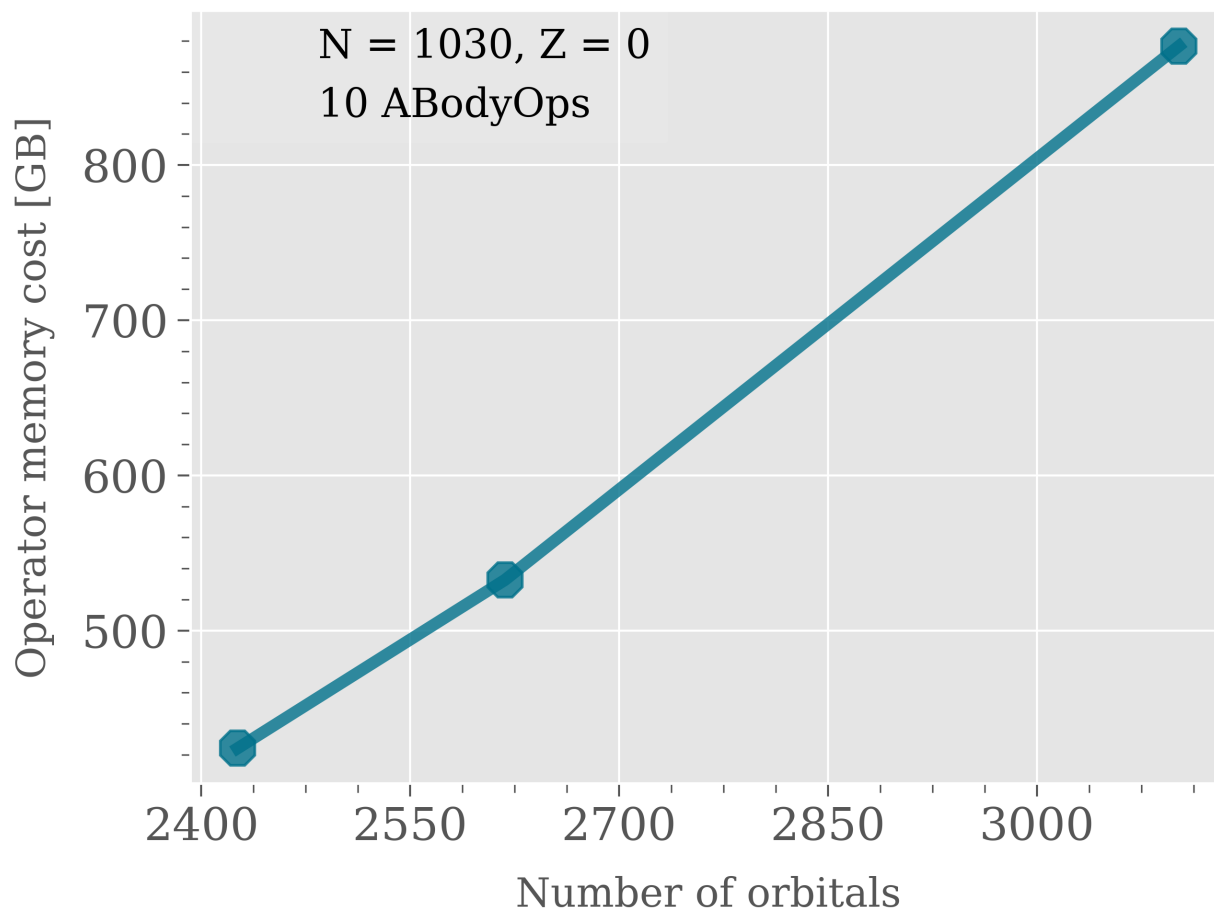


Figure 3.2: Growing memory cost needed to do SCKY-IMSRG calculations in model spaces composed of 1030 particles. We can easily need up to 1 terabyte of memory, depending on the basis size. These calculations use Born’s generator seen in Chapter 5. Born’s generator creates an additional ABodyOp to store energy denominators used in the generalized Born expansion. Therefore, 10 ABodyOps are created. Here is a fun fact: the IMSRG calculation with $N_{\text{orbitals}} = 3102$ stores and evolves $\sim 5e10$ complex-double matrix elements.

cache intermediate commutator evaluations when doing nested commutators. The remaining four ABodyOps are H , $H(s)$, $\eta(s)$ and $\Omega(s)$.⁸ Additional temporaries are needed to calculate particle-hole terms. Those temporaries are not written as ABodyOps (or BodyOps) to avoid storing zeros in sectors that can be eliminated within the particle-hole transformation. The memory cost of particle-hole temporaries are also included in Figure 3.1. We prefer to store all SCKY-IMSRG objects in random access memory (RAM) to reduce latency in our calculations. In Figures 3.1 and 3.2, notice that we utilize hundreds of gigabytes of RAM to do IMSRG calculations in large model spaces.

Figure 3.3 shows that we can obtain SNM calculations in large model spaces within hours, so long density-dependent three-body nuclear forces (DD3NF) are omitted. However, it is apparent in Figure 3.4 that the use of DD3NF noticeably worsens the performance of the SCKY-IMSRG. This is partly due to the many invocations of computationally expensive three-body force functions when normal-ordering. Despite the many optimizations in the SCKY-IMSRG, large-scale NM-EOS computations using DD3NF still require several days to complete.

Without DD3NF, commutator evaluations account for the majority of IMSRG runtimes. This is desired, since our commutator implementation is highly optimized. Figure 3.5 exhibits total commutator runtimes, in addition to runtimes needed to evaluate ladder and particle-hole terms. Runtimes for ladder terms dominate particle-hole terms. This is preferred since particle-hole terms require significantly more administration (and potential overhead) to implement compared to ladder terms. Figure 3.5 shows the payoff of the optimizations made in the particle-hole terms.

Given the many optimizations made in the commutators, we can do novel IMSRG(2)

⁸We store $\frac{d\Omega(s)}{ds}$ in $\eta(s)$.

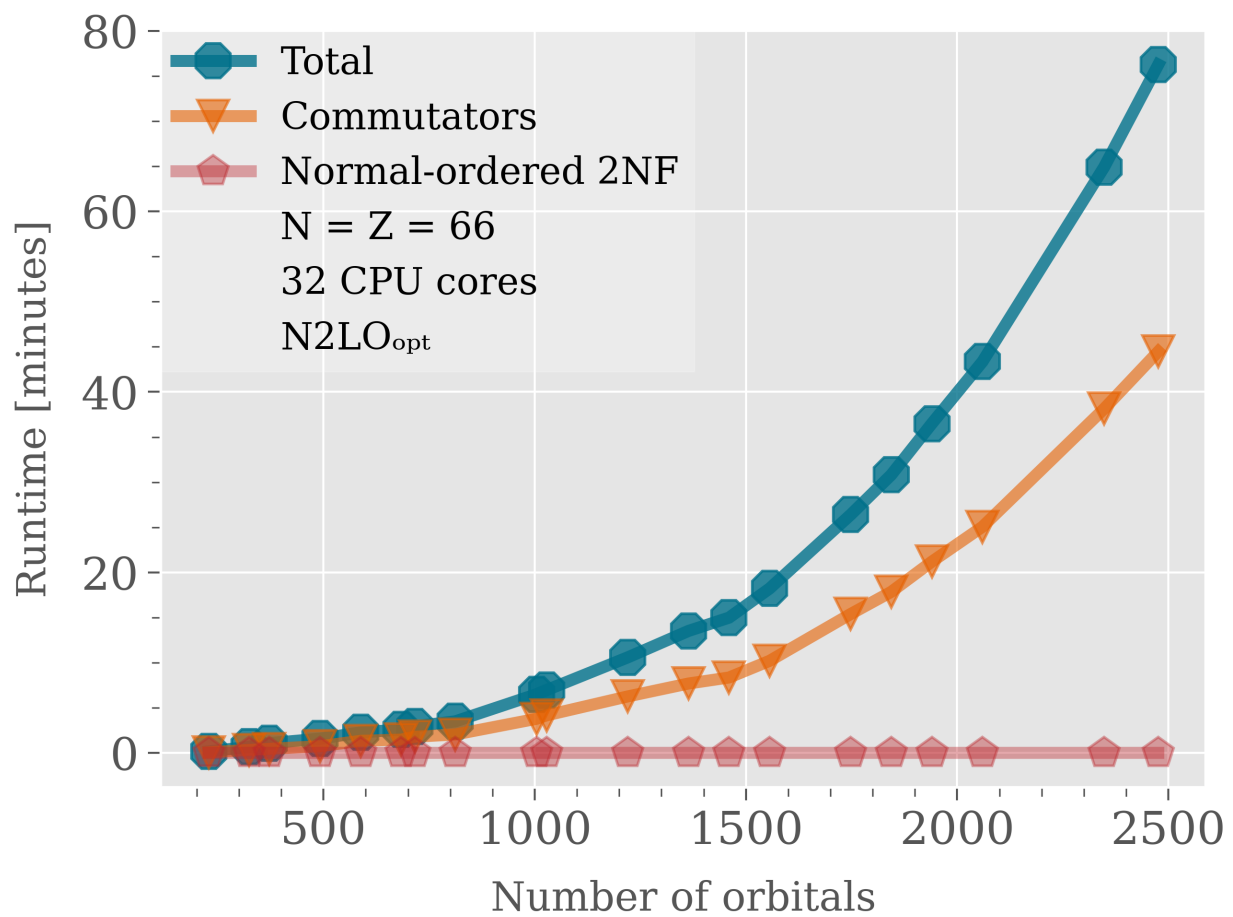


Figure 3.3: Runtime of the SCKY-IMSRG as we increase the basis size. We include the total time needed to evaluate all commutators in each program, as well as the time needed to normal-order without three-body forces. We can obtain converged calculations (in terms of the basis size) within hours when omitting density-dependent three-body forces.

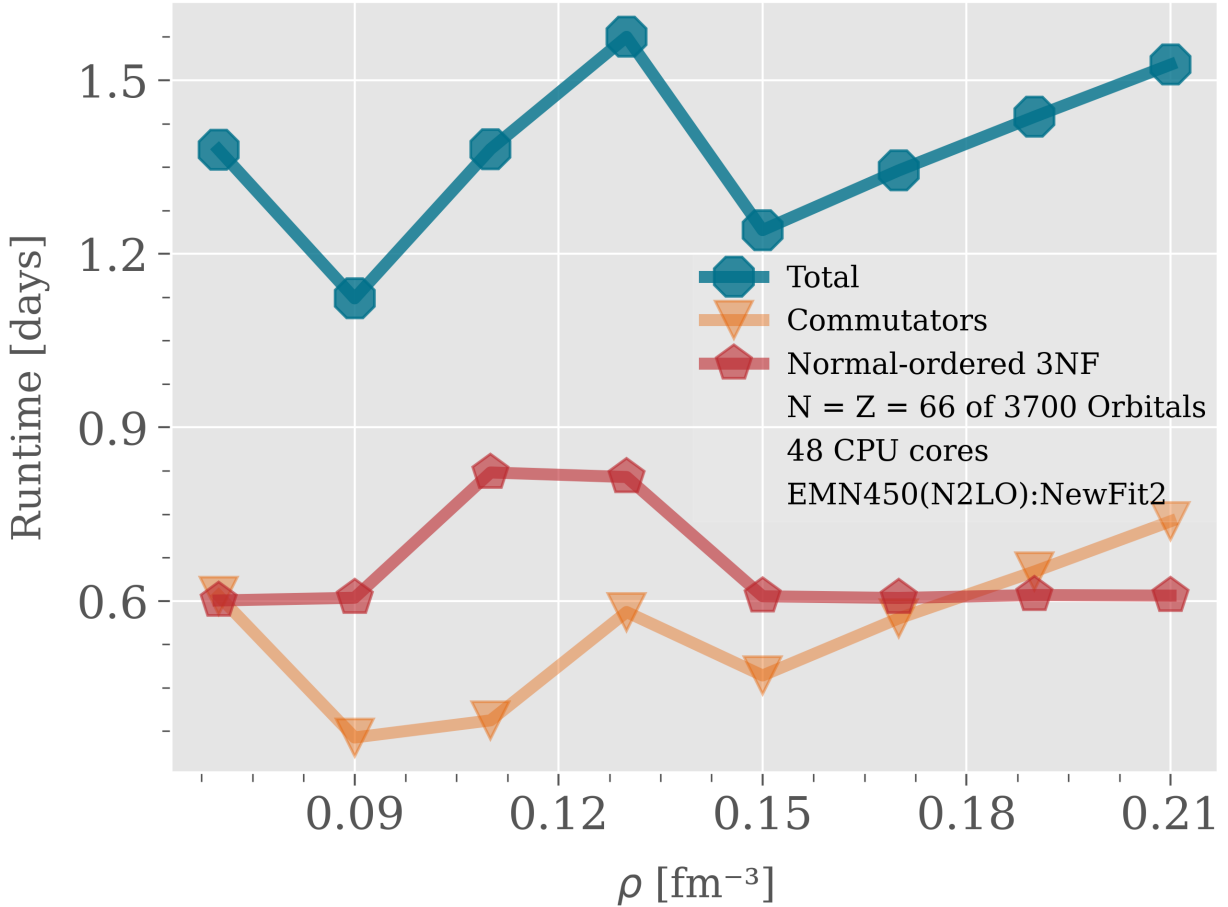


Figure 3.4: Runtime of the SCKY-IMSRG, varying the particle density ρ . We include the total time needed to evaluate all commutators in each program, as well as the time needed to normal-order with three-body forces included. Normal-ordering accounts for nearly half of each program’s total runtime. In theory, the normal-order runtime should remain unaffected by changes in ρ . This is largely seen here—barring runtime variability from the operating machines. Likewise, the time needed to evaluate *one* commutator should be insensitive to changes in ρ . However, the number of iterations (and likewise, commutator evaluations) needed for the IMSRG to converge, can vary depending on ρ . Barring variability from the operating machines, variations in total commutator runtimes are due to the varying amount of IMSRG iterations.

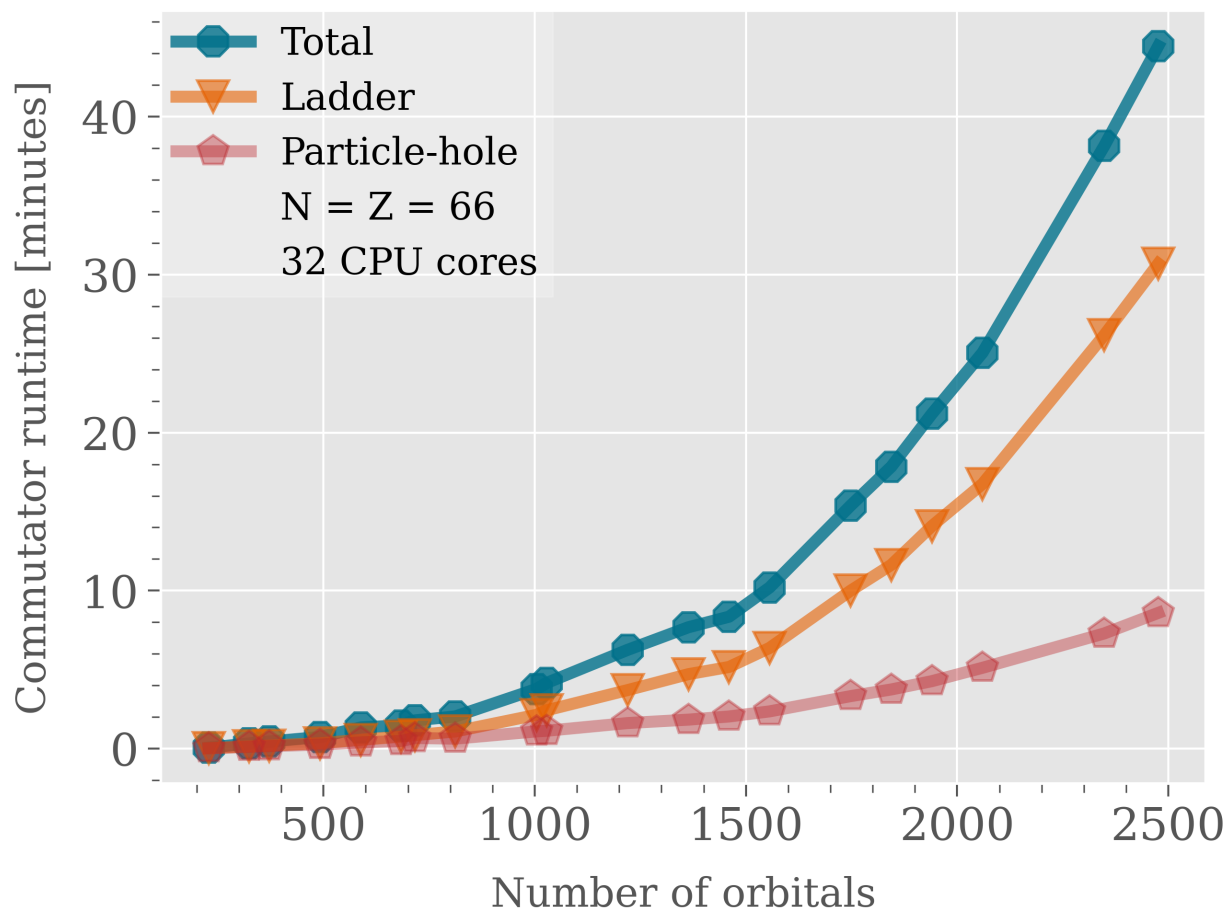


Figure 3.5: Breakdown of the time taken to evaluate all commutators throughout the lifetime of each IMSRG program seen in Figure 3.3. Ladder commutators account for the majority of commutator runtimes, while particle-hole commutators account for a minority of runtimes. This is desired since ladder commutators primarily involve matrix products optimized by Eigen’s BLAS/MKL interface, while particle-hole commutators require administration to be evaluated as matrix products.

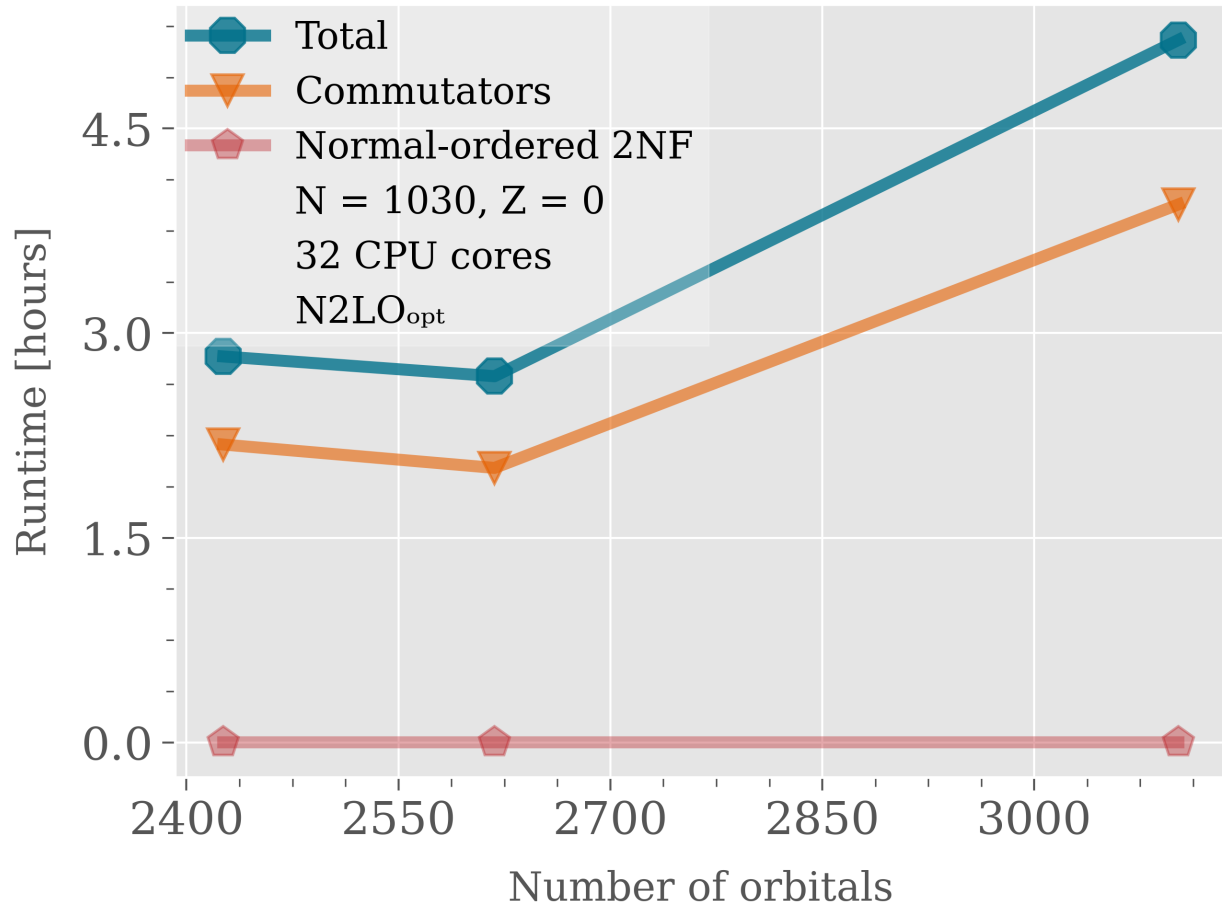


Figure 3.6: Runtime of the SCKY-IMSRG in model spaces composed of 1030 particles. We can do these calculations within hours, without the presence of density-dependent three-body forces.

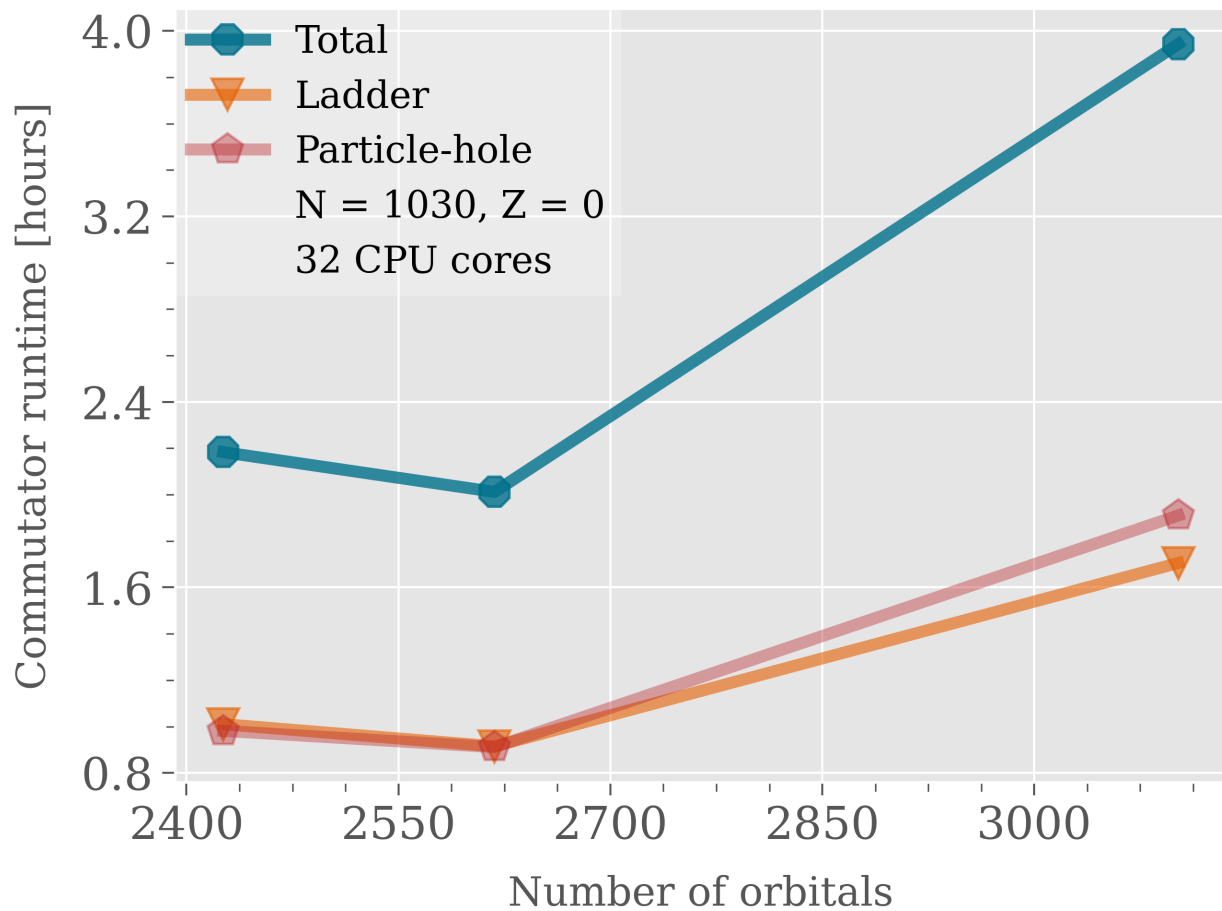


Figure 3.7: Breakdown of the time taken to evaluate all commutators throughout the lifetime of each IMSRG program seen in Figure 3.6. The gains from the optimizations made in the particle-hole commutators seen in Eq. (F.9d), are lessened in these systems since the number of particles is comparable to the number of orbitals. Consequently, runtimes of the ladder and particle-hole commutators are also comparable.

calculations simulating 1030 neutrons in large model spaces.⁹ Figure 3.2 and Figure 3.6 respectively show that these calculations require hundreds of gigabytes of RAM, and can be completed within a few hours. Figure 3.7 shows that runtime costs of the ladder and particle-hole commutators are comparable when using 1030 neutrons. This is expected since we optimize particle-hole commutators by exploiting the fact that the number of orbitals in the basis is typically much larger than the number of particles.

The largest calculations performed with 1030 neutrons utilize 3102 basis orbitals, requiring 876 gigabytes of RAM (seen in Figure 3.2). By using 1030 particles, we reduce errors in the IMSRG incurred by the use of a finite number of particles. However, we also reduce the maximum momentum in the basis—worsening errors in the IMSRG related to the use of a truncated single-particle basis.¹⁰ Subsequently, we suspect that we need significantly more orbitals than 3102 to sufficiently reduce artifacts from the incomplete basis. However, such calculations would exceed 1 terabyte of RAM consumption—complicating our ability to obtain the needed resources on ICER. We expect this barrier to be obviated when clusters with > 1 terabyte of RAM are easily accessible. We include IMSRG(2) calculations with 1030 particles in this work as a *proof-of-principle*. There are ongoing questions regarding the existence of super heavy elements (and isotopes) beyond the periodic table. The IMSRG may shed light on such questions. Since IMSRG calculations simulating 1030 particles in infinite nuclear matter are possible, the same may also be possible in finite nuclear matter!

⁹ $A = 1030$ calculations need not be restricted to pure neutron matter alone!

¹⁰The box-size is given by $\mathcal{L} = (A/\rho)^{1/3}$. By increasing the number of particles at a fixed particle density, we subsequently increase the box-size—lowering all momenta in the basis.

3.6 Concluding Remarks with Perspectives

We have developed a state-of-the-art, high-performant nuclear matter IMSRG(2) program (dubbed “SCKY-IMSRG”) with a multitude of two-body and density-dependent three-body forces from Drischler *et al.* [1]. The program is verbose, unit-tested, and sufficiently general for future needs. Moreover, the SCKY-IMSRG is equipped with automated data managers (to ensure that data is preserved and easily accessible), novel IMSRG generators from Chapter 5, and novel IMSRG extrapolators seen in Chapter 6. Commutators in the program are highly optimized for large-scale computations. And such calculations can be executed in within hours to days—depending on the inclusion of density-dependent three-body forces. The SCKY-IMSRG exploits operator symmetries to be efficient with memory. Despite memory optimizations, the program consumes hundreds of gigabytes of computer memory in large systems.

Given the program’s many features, we hope that the SCKY-IMSRG becomes a foundation for future IMSRG and many-body developments. Operators in the SCKY-IMSRG are versatile, and can be used to compute quantities beyond energies—e.g. momentum distributions, static structure factors, etc. Furthermore, the SCKY-IMSRG is written at zero temperature. Future developers can add finite temperature extensions using insights from Smith *et al.* [26].¹¹ The SCKY-IMSRG can also be extended to finite nuclei via a change of basis. Optimizations made in the program’s commutators enable novel $A = 1030$ IMSRG(2) calculations. Such calculations in finite nuclear systems may shed light on the existence of heavy nuclei beyond the periodic table. Lastly, the SCKY-IMSRG implements 3rd-order

¹¹Beware, the distinction between particles and holes, exploited in Appendix F, is lost if occupation operators become continuously valued.

Many-Body Perturbation Theory (MBPT) using nested commutators seen in Appendix H. This enables intermediaries within MBPT(3) diagrams to be cached and reused—significantly improving the compute performance of MBPT(3). If higher-order MBPT expressions can be similarly written in terms of commutators, then they can be implemented without explicit handling of the exploding number of MBPT diagrams [27]. We exhibit equations-of-state that are calculated from the SCKY-IMSRG program in the next chapter.

Chapter 4. Nuclear Matter Equation-of-State

“Only when it is dark enough

can you see the stars”

—Carl & MLK, Jr.

We utilize the SCKY-IMSRG to calculate the zero temperature nuclear matter equation-of-state (NM-EOS) using the $N2LO_{\text{opt}}$, Hebeler, and the N2LO Entem-Machleidt-Nosyk (EMN) inter-nucleon interactions derived from chiral EFT [4, 25, 28]. We compare results from the IMSRG(2) to those of Many-Body Perturbation Theory (MBPT). And when necessary, we also make comparisons to IMSRG’s nonperturbative relative—Coupled-Cluster (CC) theory. We do so to establish similarities and differences between the perturbative and nonperturbative many-body methods using multiple inter-nucleon forces. These interactions are chosen due to their wide use in the literature [1, 23], and because they run the gamut from the very soft and perturbative Hebeler and $N2LO_{\text{opt}}$ interactions, to the significantly harder and less perturbative EMN potentials.

As will be seen, the disagreement between IMSRG(2) and 3rd-order MBPT (denoted “MBPT(3)”) is noticeably larger in symmetric nuclear matter (SNM), as correlations play a much greater role than they do for pure neutron matter (PNM), even for soft interactions.¹ To better investigate these differences, we include data from CC, whenever available. Particularly, we include CC results containing doubles excitations “CCD,” and approximate triples excitations “CCD(T)”—obtained in collaboration with Gaute Hagen.² This serves as a useful consistency check, as it is empirically known that IMSRG(2) ground state en-

¹This is primarily because the iterated tensor force in the ${}^3S_1 - {}^3D_1$ channel, which is active in SNM but inactive in PNM, is known to produce significant correlations. Additionally, certain short-range terms vanish in pure neutron matter due to the Pauli Principle that are non-vanishing in symmetric matter.

²As a consequence of momentum conservation, singles excitations should be zero in infinite nuclear matter.

ergies almost always fall between the CCSD and CCSD(T) results in finite nuclei that are of single-reference (i.e., closed-shell) character [10]. We therefore expect a similar pattern for our nuclear matter calculations, which are carried out for “magic” particle numbers corresponding to closed-shell configurations in the periodic box.

We also include MBPT(4) results to compare against the IMSRG(2) results. MBPT(4) is the lowest order of perturbation theory that contains triples excitations [27]. If correlations from triples excitations are large, MBPT might not be well-converged. Lastly, we include results from a reduced version of MBPT(4)—which subtracts from MBPT(4), diagrams that are excluded or undercounted by IMSRG(2). This is based on the earlier work of Titus Morris, who carried out a diagrammatic analysis of the perturbative content of IMSRG(2) [10]. This analysis showed that the IMSRG(2) is “3rd-order exact”, which means that the IMSRG(2) energy contains all MBPT diagrams up to 3rd-order.³ At 4th-order, the IMSRG(2) starts to miss some diagrams. For instance, MBPT(4) diagrams that correspond to triple excitations (i.e., $3p3h$ intermediate states) are missed completely, see diagrams T_1 thru T_{16} in Fig. 4.1. Additionally, the so-called asymmetric quadruple-excitation diagrams, Q_6 and Q_7 in Fig. 4.1, are under-counted by a factor of 1/2 [10].

Like the IMSRG(2), CCD can be shown to contain all MBPT(3) contributions, while missing the MBPT(4) triples-excitation diagrams completely. However, unlike the IMSRG(2), CCD correctly counts the asymmetric quadruples diagrams Q_6 and Q_7 with their full weight. Similarly, CCD(T) can be shown to be “4th-order exact”, as it includes the 4th-order triples-excitation diagrams. Lastly, we stress that while CCD and CCD(T) are 3rd- and 4th-order exact from the perspective of MBPT, both also include infinite partial summations of higher-

³It is important to stress that the IMSRG(2) is an intrinsically non-perturbative method. While it correctly includes MBPT contributions up to 3rd-order, it also includes bits and pieces of all higher-orders of perturbation theory. For example, it can be shown that particle-particle and hole-hole ladder diagrams, as well as particle-hole ring diagrams, are summed to all orders in the IMSRG(2).

order MBPT diagrams [27]. For instance, CCD (like the IMSRG(2)) sums up all two-particle ladder and ring diagrams, while CCD(T) sums up analogous diagrams involving three particles.

We note that the IMSRG(2)'s undercounting of the asymmetric quadruple-excitation diagrams explains the empirical observation that IMSRG(2) results tend to fall between CCD and CCD(T). This is because diagrams Q_6 and Q_7 are positive-definite, while the dominant 4th-order triples diagrams,⁴ T_{15} and T_{16} , can be shown to be negative-definite. Note also that the asymmetric quadruples diagrams and the two dominant triples diagrams have a similar structure—i.e., they look like a MBPT(2) diagram where one of the internal lines has a self-energy insertion. Therefore, undercounting diagrams Q_6 and Q_7 roughly mimics some of the attraction that would be gained if the triple-excitation contributions were included.

The reduced version of MBPT(4) is obtained by subtracting from MBPT(4): all diagrams associated with triples excitations $\Delta E_{\text{triples}}^{(4)}$ (diagrams T_1 - T_{16} in Fig. 4.1), as well as half the asymmetric quadruples contributions (diagrams Q_6 and Q_7 in Fig. 4.1) $\Delta E_{\text{asymmQ}}^{(4)}$.

$$\Delta E_{\text{reduced}}^{(4)} \equiv \Delta E^{(4)} - \Delta E_{\text{triples}}^{(4)} - \frac{1}{2} \Delta E_{\text{asymmQ}}^{(4)}. \quad (4.1)$$

We therefore expect the reduced MBPT(4) to yield energies that are closer to that of IMSRG(2) than the unmodified MBPT(4), since they are now equivalent thru 4th-order. Any discrepancy between the reduced MBPT(4) and the IMSRG(2) results are therefore due to the higher-order contributions that are summed by the IMSRG.

The *true* NM-EOS is only obtained with a full accounting of the uncertainties in the

⁴For the interactions studied here, these two diagrams accounted for more than 95% of the total triples-excitation energy contribution.

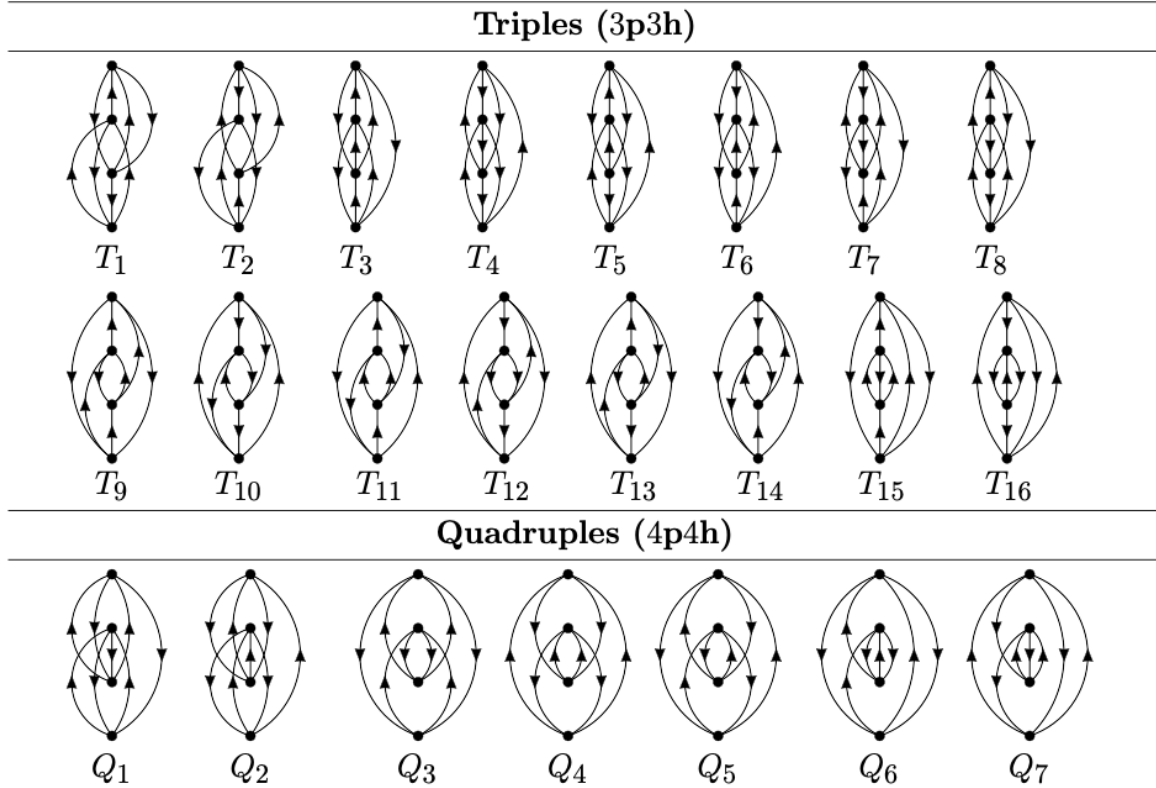


Figure 4.1: A subset of the MBPT(4) Hugenholtz diagrams corresponding to irreducible triples ($3p3h$) and quadruples ($4p4h$) excitations. The IMSRG(2) misses the triples diagrams T_1 - T_{16} completely, and undercounts the asymmetric quadruples diagrams Q_6 and Q_7 by a factor of $1/2$. This figure is obtained courtesy of Hergert *et al.* [10].

nuclear forces arising from the EFT truncation errors and the uncertainties in the fitted low-energy constants, as well as the truncation errors in the many-body methods used to calculate the NM-EOS. While we get a qualitative feeling for the many-body uncertainties by comparing the energies obtained from different orders and truncations of MBPT, IMSRG, and CC, we do not assess the uncertainties arising from EFT truncation errors and/or the uncertainties in the low-energy constants that appear in the chiral interactions. We view calculations provided in this work as the first step towards obtaining an uncertainty-quantified NM-EOS using the IMSRG. Eventually, we are hopeful that the uncertainty-quantified NM-EOS using the IMSRG can be obtained by generating sample NM-EOS calculations for a multitude of forces. Such equations-of-state can then be utilized by the Bayesian approach

of Drischler *et al.* to determine EFT truncation errors [29]. Moreover, emulation of the low energy constants of the nuclear force using techniques such as Eigenvector Continuation, will likely be useful in obtaining an uncertainty-quantified IMSRG-calculated EOS [30, 31].

All results presented below are obtained using high-performance compute resources provided by the Institute for Cyber-Enabled Research at Michigan State University. And, all figures stylized in Matplotlib’s “ggplot” are plotted by our automated data handlers.⁵

4.1 Results

We start by discussing our calculations of pure neutron matter, which as mentioned above has much weaker correlations to contend with compared to symmetric nuclear matter. Figure 4.2 shows that IMSRG(2) and MBPT(3) with the N2LO_{opt} two-nucleon potential, produce similar NM-EOS in pure $N = 66$ neutron matter. This is expected since many-body methods in PNM are considered to be highly convergent when using most typical chiral EFT interactions⁶. Likewise, Figure 4.3 shows the near identical NM-EOS produced by IMSRG(2) and MBPT(3) in pure $N = 1030$ neutron matter. Consequent to using such a large number of particles, we note that the 3102 orbitals used are insufficient to eliminate errors due to the truncated single-particle basis. Despite concerns regarding the sufficiency of the number of orbitals, we include Figure 4.3 to highlight the payoff of the SCKY-IMSRG optimizations made in Chapter 3.

⁵The ggplot style is used as a throwback to my early days learning how to program using R!

⁶Possible exceptions are for chiral interactions at higher resolution scales that are constructed to be local in coordinate space. Such interactions are generally difficult to handle in CC or IMSRG calculations as they require an excessively large single-particle basis to reach convergence.

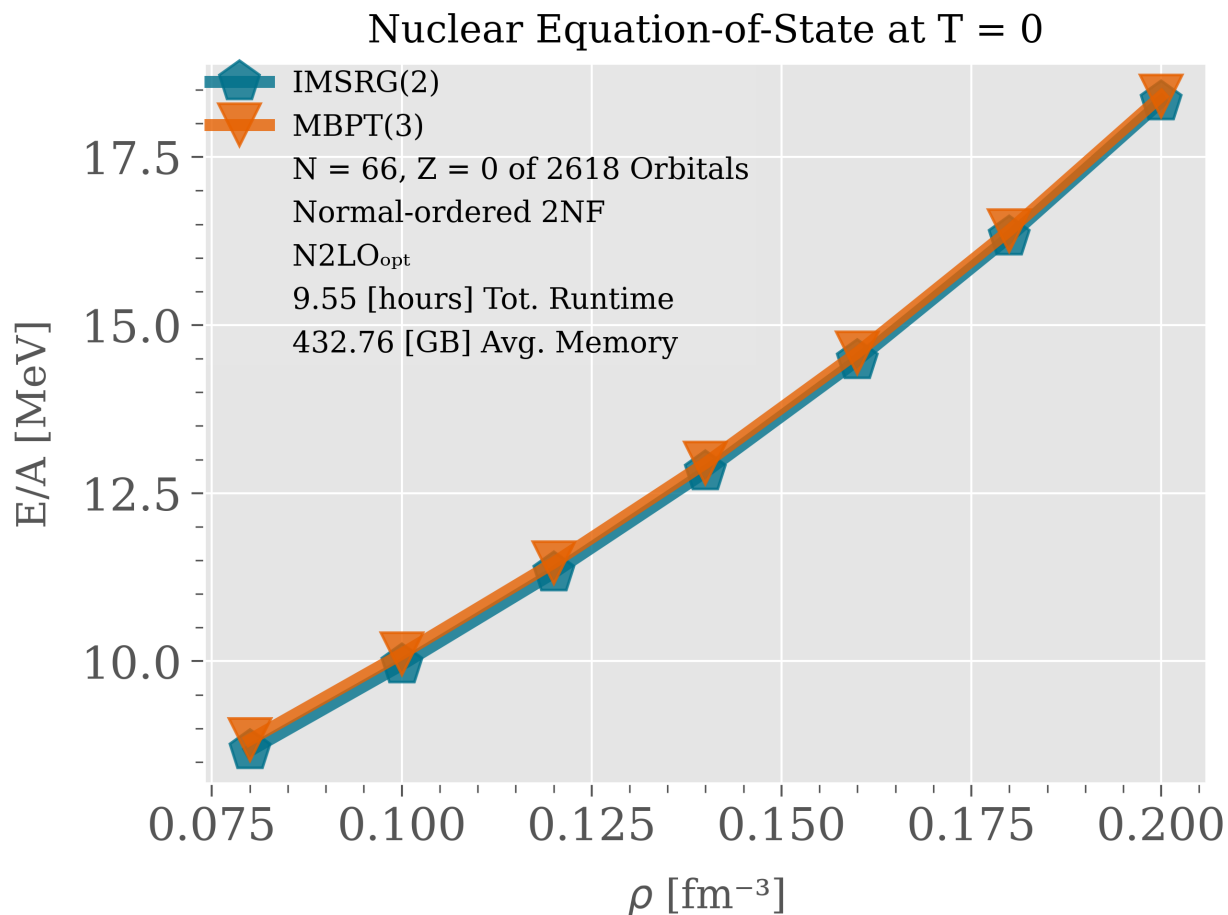


Figure 4.2: Pure $N = 66$ neutron matter sample EOS obtained using IMSRG(2) and MBPT(3) with the N2LO_{opt} two-nucleon potential [25]. In this system, we consider 2618 orbitals to be sufficiently large to reduce errors due to the truncated single-particle basis. A total of 9.55 hours is taken to do all seven SCKY-IMSRG calculations over the various density points. And, each calculation requires the same 432.76 gigabytes amount of memory. MBPT(3), acquired using Algorithm 9, tracks IMSRG(2) quite well, with slight discrepancies at low densities.

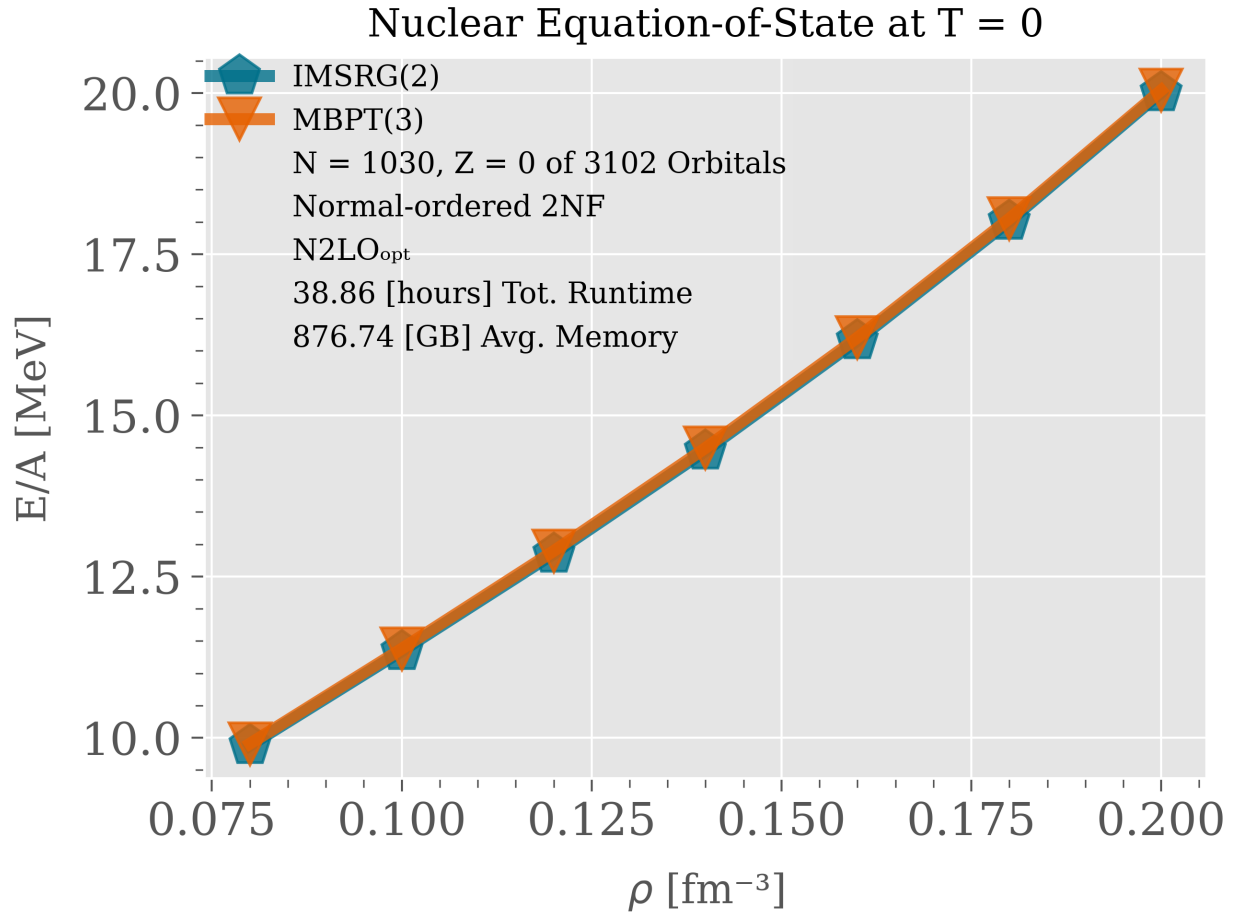


Figure 4.3: Pure $N = 1030$ neutron matter sample EOS obtained using IMSRG(2) and MBPT(3) with the $N2LO_{opt}$ two-nucleon potential [25]. A total of 38.86 hours is taken to do all seven SCKY-IMSRG calculations over the various density points. And, each calculation requires the same 876.74 gigabytes amount of memory. MBPT(3), acquired using Algorithm 9, tracks IMSRG(2) exceedingly well in this system.

The MBPT calculated ground state energy per particle in the thermodynamic limit $E_{\text{MBPT}}^{\text{Thermo}}/A$, and in the finite box $E_{\text{MBPT}}^{\text{Box}}/A$, are defined in Eqs. (4.2a) and (4.2b), respectively.

$$E_{\text{MBPT}}^{\text{Thermo}}/A \equiv E_{\text{HF}}^{\text{Thermo}}/A + \Delta E^{\text{Thermo}}/A \quad (4.2a)$$

$$E_{\text{MBPT}}^{\text{Box}}/A \equiv E_{\text{HF}}^{\text{Box}}/A + \Delta E^{\text{Box}}/A \quad (4.2b)$$

$$E_{\text{MBPT}}^{\text{Box}}/A \approx E_{\text{HF}}^{\text{Box}}/A + \Delta E^{\text{Thermo}}/A. \quad (4.2c)$$

The thermodynamic limit and box-acquired Hartree-Fock energies per particle are denoted by $E_{\text{HF}}^{\text{Thermo}}/A$ and $E_{\text{HF}}^{\text{Box}}/A$, respectively. And the thermodynamic limit and box-acquired MBPT correlation energies per particle are denoted by $\Delta E^{\text{Thermo}}/A$ and $\Delta E^{\text{Box}}/A$, respectively. MBPT(3) was not implemented in the finite box at the time of data collection for this work. However, $E_{\text{MBPT}}^{\text{Thermo}}/A$ is available through collaboration with Christian Drischler. We can thus approximate $E_{\text{MBPT}}^{\text{Box}}/A$ by assuming $\Delta E^{\text{Box}}/A \approx \Delta E^{\text{Thermo}}/A$ in Eq. (4.2c). All MBPT results in Figures 4.4–4.12 are procured in the finite box using Eq. (4.2c). After implementing MBPT(3) in the finite box, we observe differences between the box acquired MBPT(3) correlation energy per particle and its thermodynamic limit counterpart to be at most 0.1 MeV per particle using $N = 66$ and/or $Z = 66$ nucleons. Thus, we consider thermodynamic limit MBPT(3) correlation energies per particle to be sufficiently representative of their box-acquired counterparts.

The IMSRG(2) and MBPT(3) agreement in pure $N = 66$ neutron matter is further seen in Figures 4.4 and 4.5—which feature NM-EOS from the $\lambda = 1.8 \text{ fm}^{-1}$ and $\lambda = 2.8 \text{ fm}^{-1}$ SRG evolved Hebeler force, respectively. The $\lambda = 2.8 \text{ fm}^{-1}$ Hebeler force is *less* SRG softened than its $\lambda = 1.8 \text{ fm}^{-1}$ counterpart, and is thus a harder force. Hence, Figures 4.4

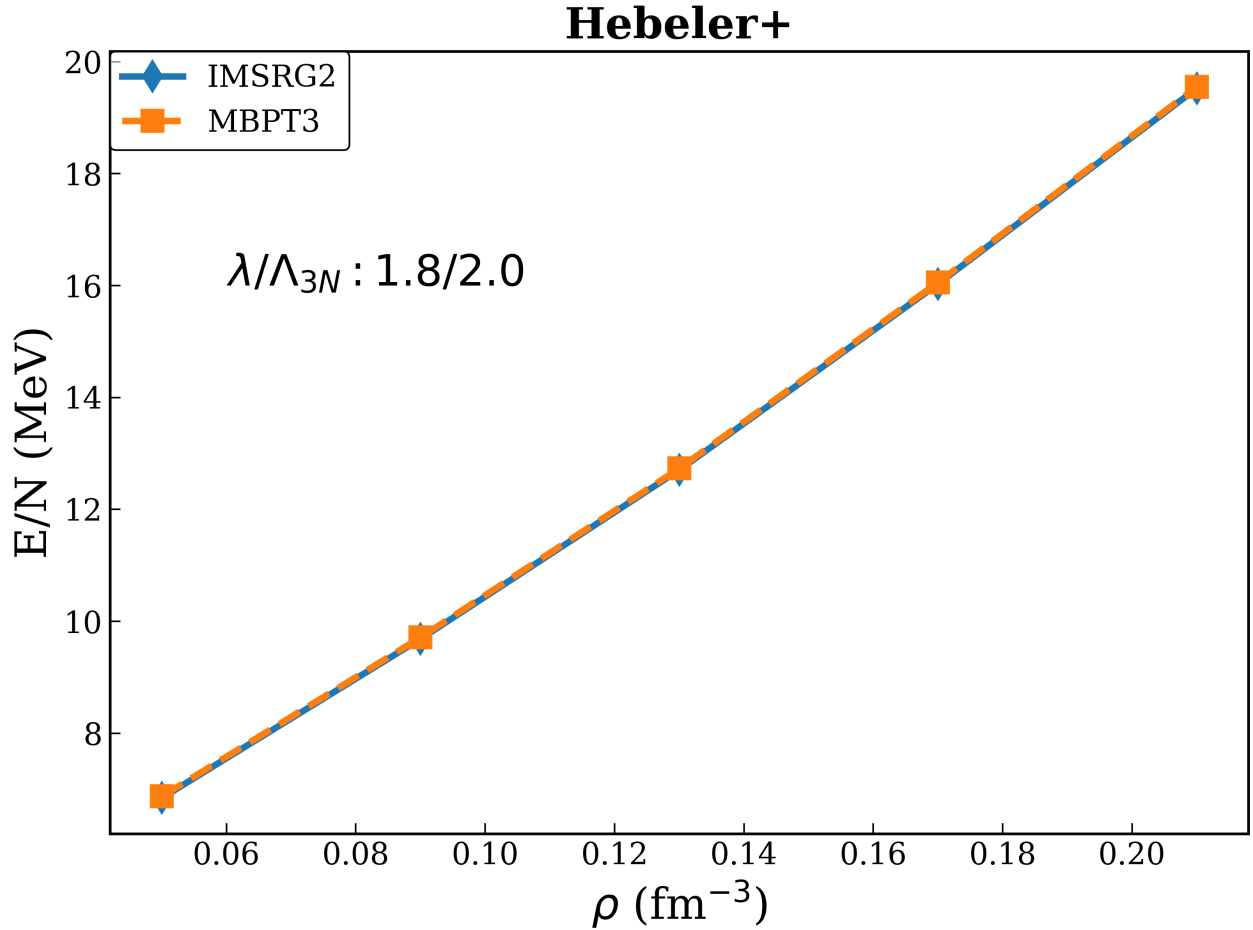


Figure 4.4: Pure $N = 66$ neutron matter sample EOS for the $\lambda = 1.8 \text{ fm}^{-1}$ SRG evolved Hebeler force with $\Lambda_{3N} = 2.0 \text{ fm}^{-1}$ regulator cutoff [4]. The three-body force is used when normal-ordering, but is subsequently truncated after normal-ordering. In other words, the Hamiltonian is treated at the normal-ordered two-body (NO2B) approximation. We see excellent agreement between energies obtained from IMSRG(2) and MBPT(3).

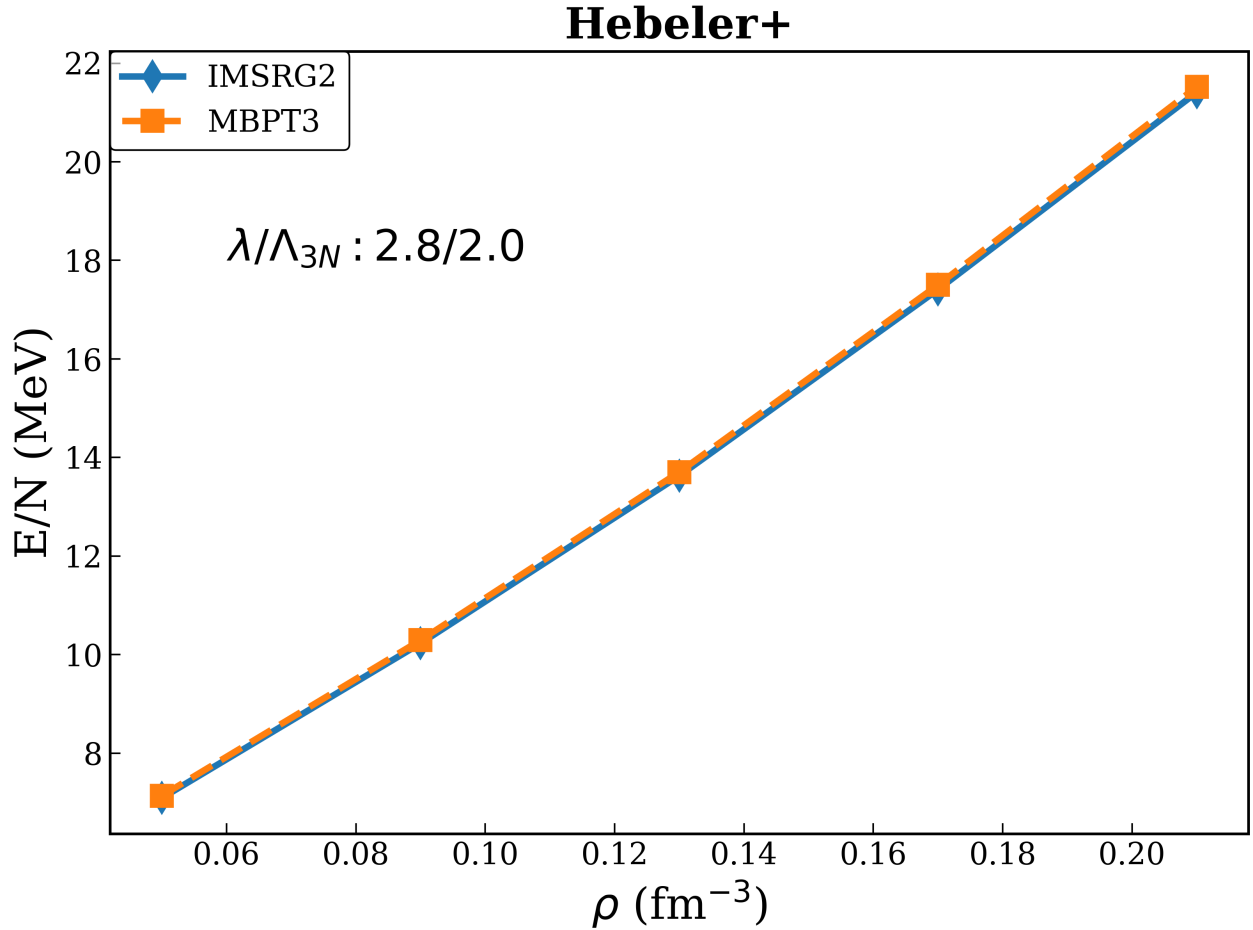


Figure 4.5: Pure $N = 66$ neutron matter sample EOS for the $\lambda = 2.8 \text{ fm}^{-1}$ SRG evolved Hebeler force with $\Lambda_{3N} = 2.0 \text{ fm}^{-1}$ regulator cutoff [4]. This figure compliments Figure 4.4, with the primary difference being in the utilized Hebeler force with increased SRG resolution scale λ . Thus, see Figure 4.4 for additional details. We see excellent agreement between energies obtained from IMSRG(2) and MBPT(3).

and 4.5 show that IMSRG(2) and MBPT(3) are in excellent agreement in PNM, regardless of the hardness of the Hebeler force.

Figures 4.6 and 4.7 also feature the same IMSRG(2) and MBPT(3) NM-EOS agreement in pure $N = 66$ neutron matter. Figure 4.6 is obtained using the N2LO EMN potential with low energy constant $c_D = 2.5$, and a 450 MeV regulator cutoff. Likewise, Figure 4.7 is obtained using the N2LO EMN potential with $c_D = -1.5$, and a 500 MeV regulator cutoff [28]. The regulator cutoff is the interaction resolution scale. Thus, the EMN potential is harder using a 500 MeV regulator cutoff versus a 450 MeV cutoff. Furthermore, given that the EMN potential is not SRG softened, it is considered to have a harder core than the Hebeler force. Again, consistent with our expectations, Figures 4.4–4.7 confirm that IMSRG(2) and MBPT(3) coincide in PNM— regardless of the hardness of the employed inter-nucleon force. We include Figure 4.8 to demonstrate that the SCKY-IMSRG can compute NM-EOS for nuclear matter beyond PNM and SNM alone.⁷ We again see excellent agreement between IMSRG(2) and MBPT(3) in nuclear matter with a 0.05 proton fraction.

The disagreement between IMSRG(2) and MBPT(3) is however, substantially larger in SNM. This is prominently seen in Figures 4.10–4.12, which employ the Hebeler and harder N2LO EMN forces. To better investigate these differences, we also make comparisons to CC in Figures 4.9, 4.10, and 4.12.⁸ Lastly, we include Figure 4.13 to convey the large computational expenses needed to generate the NM-EOS seen in Figure 4.11. All NM-EOS calculations (particularly for SNM) in this chapter are *highly* computationally demanding. Note, for IMSRG(2), and all CC and MBPT variants, the three-body force is used when

⁷By working in a closed shell system, the SCKY-IMSRG is restricted to only use particle numbers that are magic. However, by using large particle numbers, we can obtain NM-EOS for a variety of proton fractions. Going forward, we might be able to interpolate IMSRG-acquired NM-EOS between proton fractions using the insights of Drischler *et al.* [29].

⁸CC results are excluded in Figure 4.11, since they are currently unavailable.

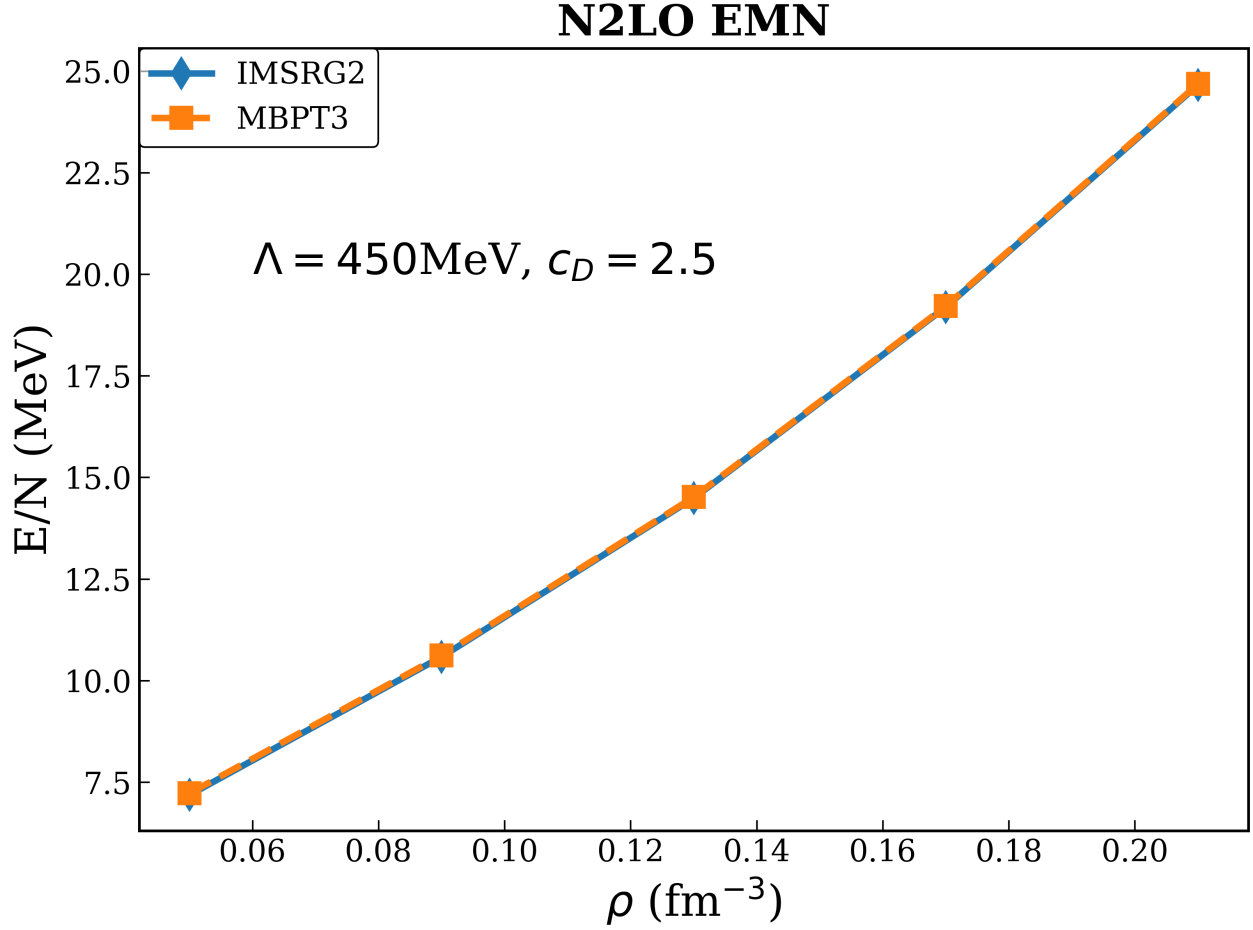


Figure 4.6: Pure $N = 66$ neutron matter sample EOS for the N2LO EMN two- and three-nucleon potential with low energy constant $c_D = 2.5$, and 450 MeV regulator cutoff [28]. The Hamiltonian is treated at the normal-ordered two-body (NO2B) approximation. This figure compliments Figure 4.4, with the primary difference being in the harder EMN force in use. Thus, see Figure 4.4 for additional details. Despite using a harder force than the Hebeler force, we still see excellent agreement between energies obtained from IMSRG(2) and MBPT(3).

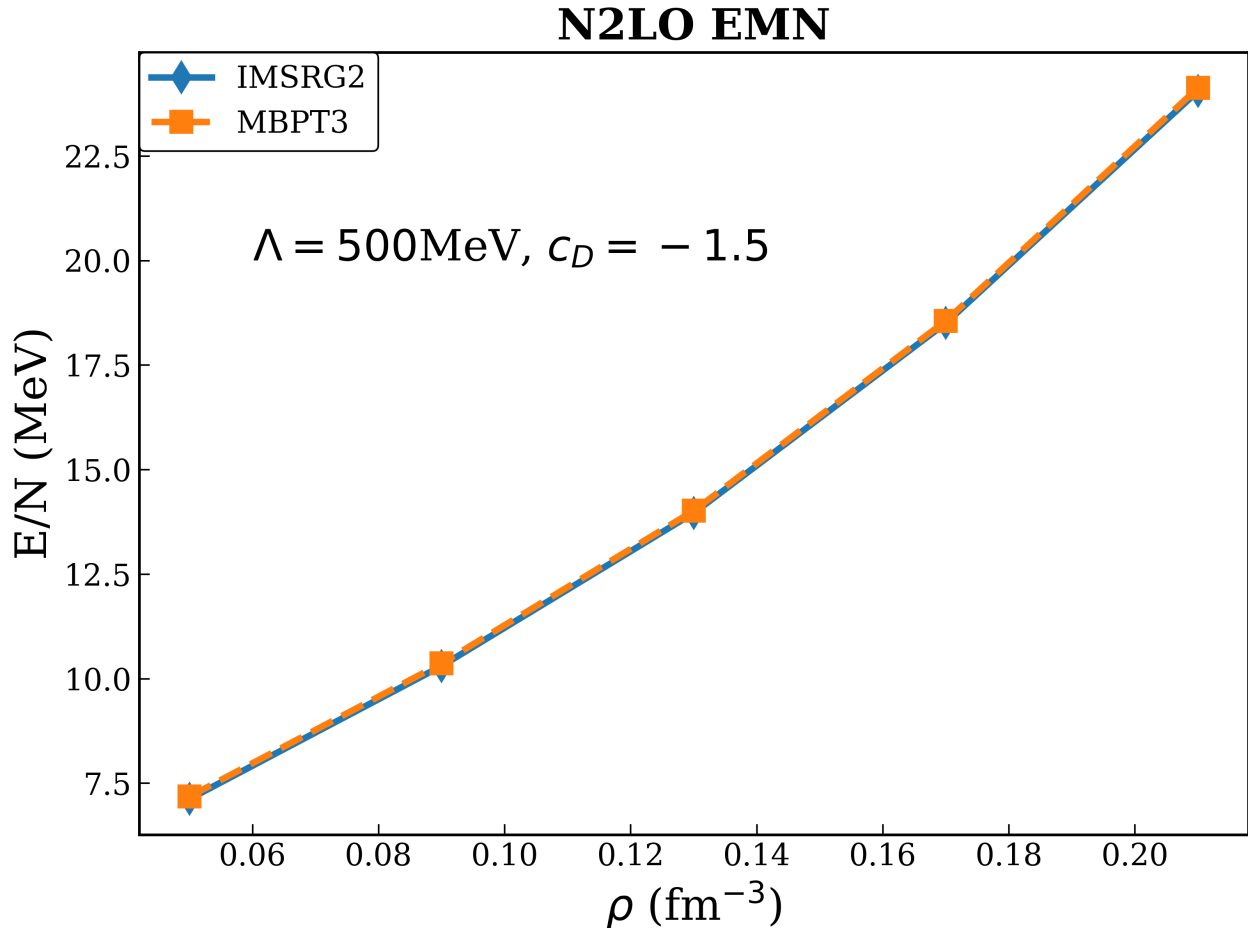


Figure 4.7: Pure $N = 66$ neutron matter sample EOS for the N2LO EMN two- and three-nucleon potential with low energy constant $c_D = -1.5$, and 500 MeV regulator cutoff [28]. The Hamiltonian is treated at the normal-ordered two-body (NO2B) approximation. This figure compliments Figure 4.6, with two main differences: the lowered value of c_D , and the increased resolution scale Λ . Thus, see Figure 4.6 for additional details. Despite increasing Λ , we still see excellent agreement between energies obtained from IMSRG(2) and MBPT(3).

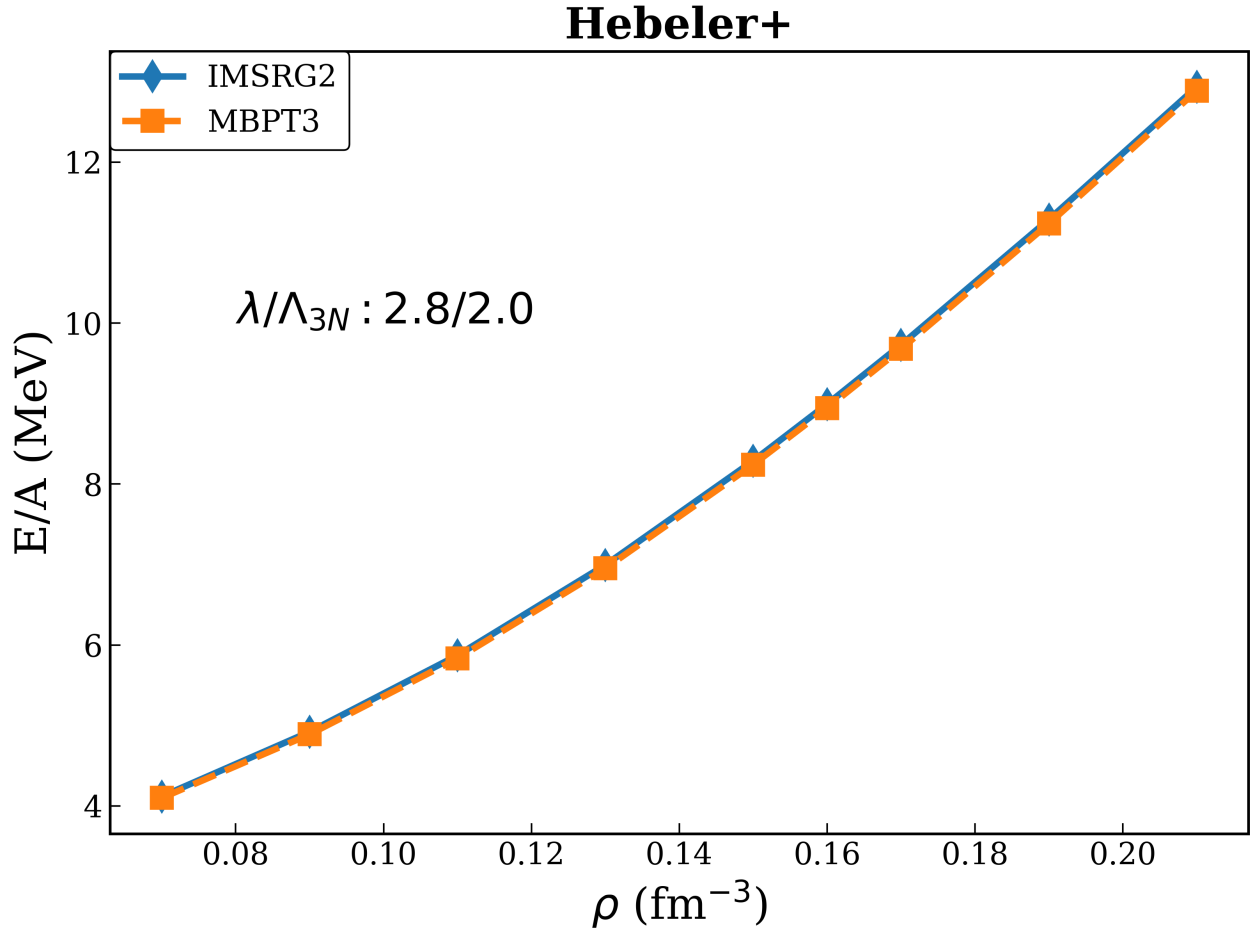


Figure 4.8: $N = 38$, $Z = 2$ nuclear matter sample EOS for the $\lambda = 2.8 \text{ fm}^{-1}$ SRG evolved Hebeler force with $\Lambda_{3N} = 2.0 \text{ fm}^{-1}$ regulator cutoff [4]. The three-body force is used when normal-ordering, but is subsequently truncated after normal-ordering. And we see excellent agreement between energies obtained from IMSRG(2) and MBPT(3).

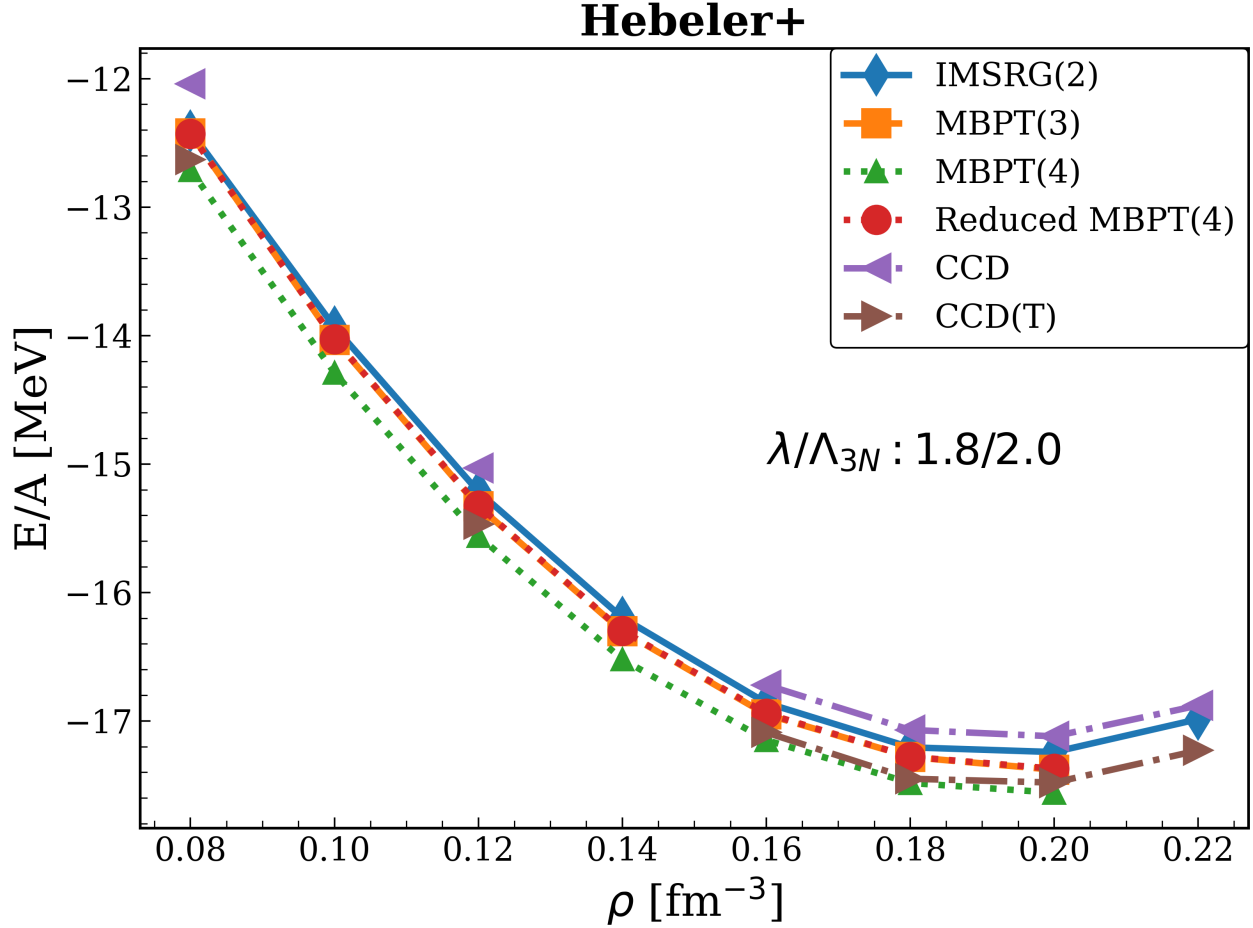


Figure 4.9: Symmetric $N = Z = 66$ nuclear matter sample EOS for the $\lambda = 1.8 \text{ fm}^{-1}$ SRG evolved Hebeler force with $\Lambda_{3N} = 2.0 \text{ fm}^{-1}$ regulator cutoff [4]. These results are obtained in the same system as Figure 4.4, with the difference being in the utilized $Z = 66$ protons and the sampled density range. As expected, Reduced MBPT(4) is closer to IMSRG(2) than MBPT(4). And, IMSRG(2) energies fall between CCD and CCD(T) energies. All methods predict energies that saturate near $\rho = 0.19 \text{ fm}^{-3}$, but not at the empirical saturation point $\rho_{\text{sat}} = 0.16 \text{ fm}^{-3}$. The largest difference in E/A between the methods is 0.67 MeV per particle—seen between CCD and MBPT(4) at $\rho = 0.08 \text{ fm}^{-3}$. IMSRG(2) and CCD energies differ from MBPT(3) energies by 0.02–0.14 MeV per particle and 0.21–0.38 MeV per particle, respectively. CCD(T) and MBPT(4) energies differ by 0.03–0.09 MeV per particle. And CCD(T) and CCD energies differ by 0.35–0.59 MeV per particle.

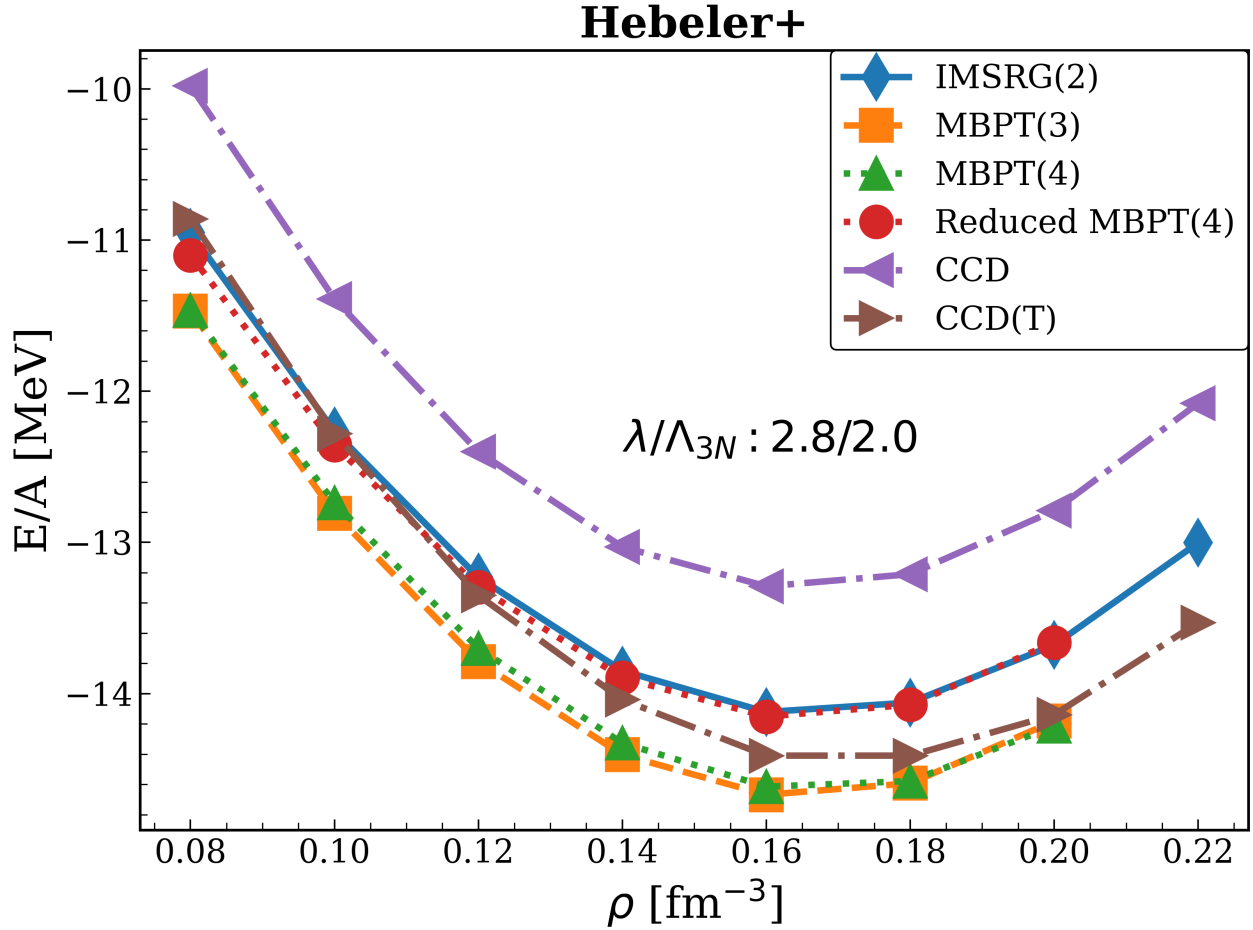


Figure 4.10: Symmetric $N = Z = 66$ nuclear matter sample EOS for the $\lambda = 2.8 \text{ fm}^{-1}$ SRG evolved Hebeler force with $\Lambda_{3N} = 2.0 \text{ fm}^{-1}$ regulator cutoff [4]. These results are obtained in the same system as Figure 4.5, with the difference being in the utilized $Z = 66$ protons and the sampled density range. All methods predict nuclear saturation around the empirical saturation point $\rho_{\text{sat}} = 0.16 \text{ fm}^{-3}$. The largest difference in E/A between the methods is 1.48 MeV per particle—seen between CCD and MBPT(4) at $\rho = 0.08 \text{ fm}^{-3}$. This disparity between CCD and MBPT(4) is more than twice that of the disparity seen in Figure 4.9. Moreover, IMSRG(2) energies differ from both MBPT(4) and CCD(T) energies by at most 0.54 MeV per particle. Notably, reduced MBPT(4) energies effectively coincide with IMSRG(2) energies, but differ from both MBPT(3) and MBPT(4) energies by 0.36–0.55 MeV per particle, while MBPT(3) and MBPT(4) effectively coincide. IMSRG(2) and CCD energies differ from MBPT(3) energies by 0.5–0.56 MeV per particle and 1.37–1.49 MeV per particle, respectively. CCD(T) and MBPT(4) energies differ by 0.07–0.6 MeV per particle. CCD(T) and CCD energies differ by 0.88–1.45 MeV per particle. And IMSRG(2) energies fall between CCD and CCD(T) energies. Notably, energy differences between CCD and CCD(T) grow in increasing ρ and are largest at $\rho = 0.22 \text{ fm}^{-3}$.

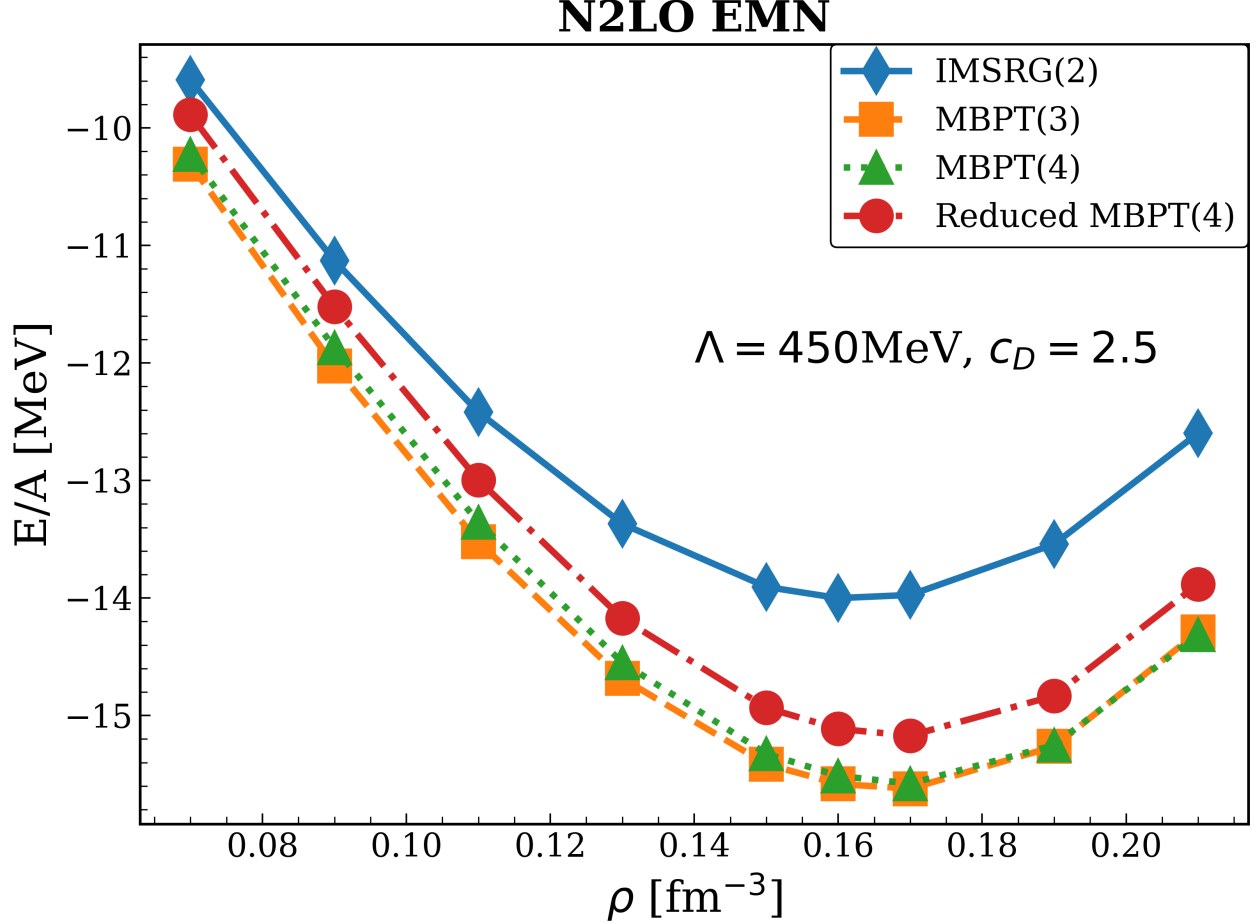


Figure 4.11: Symmetric $N = Z = 66$ nuclear matter sample EOS for the N2LO EMN potential with low energy constant $c_D = 2.5$, and 450 MeV regulator cutoff [28]. These results are obtained in the same system as Figure 4.6, with the difference being in the utilized $Z = 66$ protons, and the sampled density range. CCD and CCD(T) results are currently unavailable in this system. Note, this system’s MBPT(2) energies calculated within a finite box, can also be seen in Figure 4.13. All methods predict nuclear saturation near the empirical saturation point $\rho_{\text{sat}} = 0.16 \text{ fm}^{-3}$. MBPT(3) and MBPT(4) are nearly converged. And notably, MBPT(3) and MBPT(4) energies are 0.72–1.72 MeV per particle and 0.63–1.71 MeV per particle more bound than IMSRG(2), respectively. Using the reduced MBPT(4), we still see 0.3–1.29 MeV per particle more attraction than IMSRG(2).

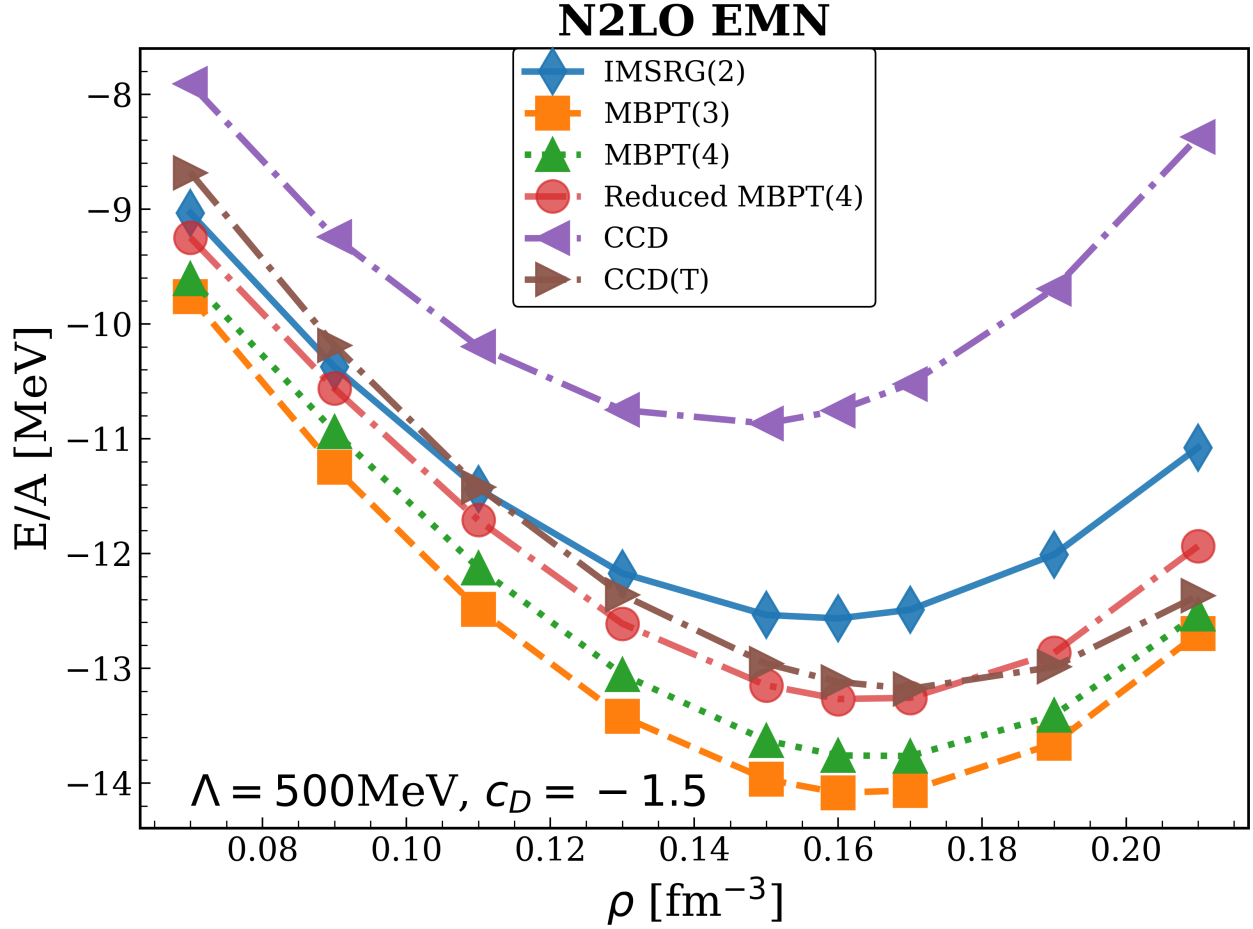


Figure 4.12: Symmetric $N = Z = 66$ nuclear matter sample EOS for the N2LO EMN potential with low energy constant $c_D = -1.5$, and 500 MeV regulator cutoff [28]. These results are obtained in the same system as Figure 4.7, with the difference being in the utilized $Z = 66$ protons, and the sampled density range. This figure also compliments Figure 4.11, with two main differences: the lowered value of c_D , and the increased resolution scale Λ . Most methods predict nuclear saturation near the empirical saturation point $\rho_{\text{sat}} = 0.16 \text{ fm}^{-3}$, with CCD being the main exception. MBPT(4) energies are 0.59–1.47 MeV per particle more bound than IMSRG(2). Using the reduced MBPT(4), we still see 0.23–0.88 MeV per particle more attraction than IMSRG(2). IMSRG(2) and CCD energies differ from MBPT(3) energies by 0.73–1.64 MeV per particle and 1.85–4.32 MeV per particle, respectively. CCD(T) and MBPT(4) energies differ by 0.16–0.92 MeV per particle. CCD(T) and CCD energies differ by 0.77–3.99 MeV per particle. And IMSRG(2) energies often fall between CCD and CCD(T) energies. Notably, energy differences between CCD and CCD(T) grow in increasing ρ , and are largest at $\rho = 0.21 \text{ fm}^{-3}$.

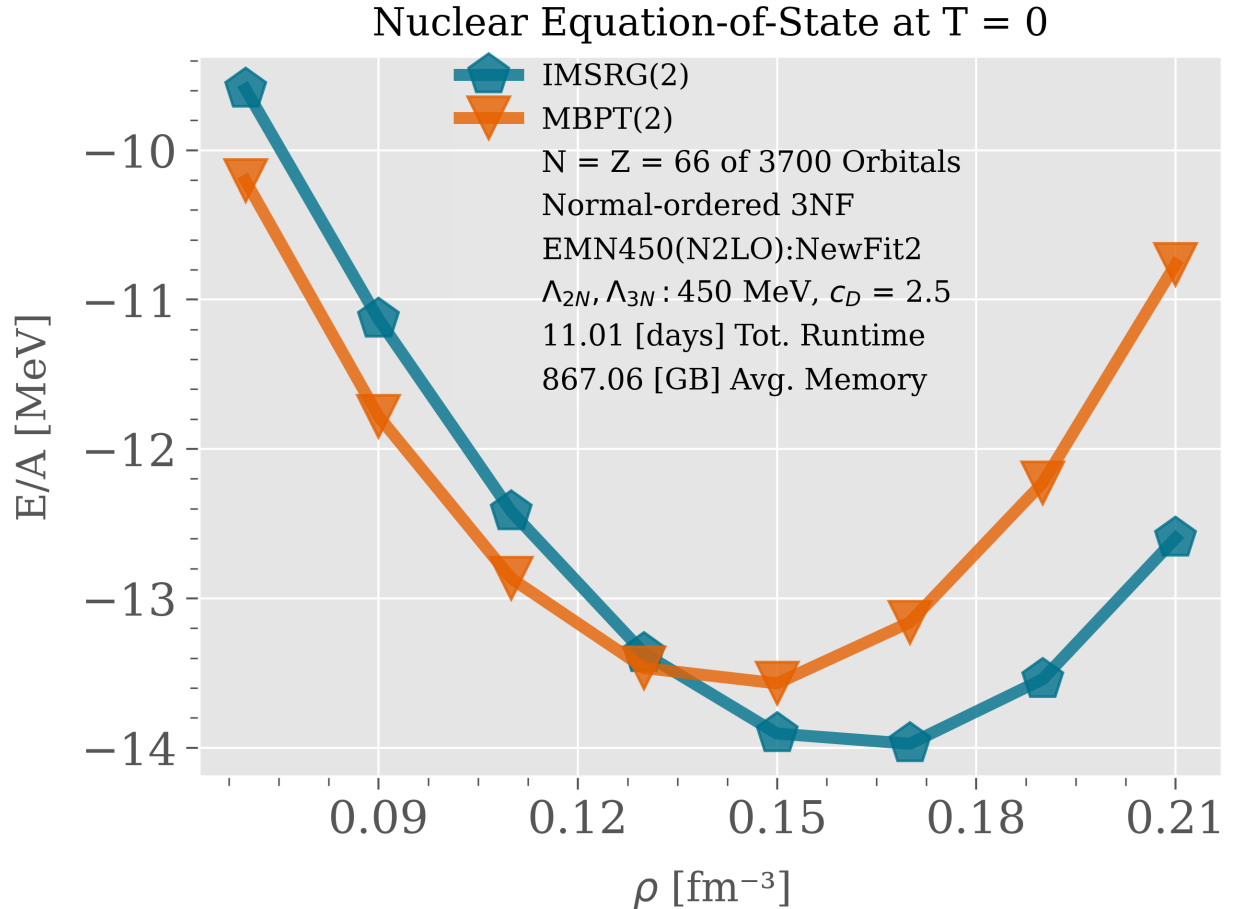


Figure 4.13: Symmetric $N = Z = 66$ nuclear matter sample EOS obtained using IMSRG(2) and MBPT(2), with the N2LO EMN potential with low energy constant $c_D = 2.5$, and 450 MeV regulator cutoff [28]. This figure is made in the same system as Figure 4.11. The three-body force is used when normal-ordering, but is subsequently truncated after normal-ordering. In this system, we consider 3700 orbitals to be sufficiently large to reduce errors due to the truncated single-particle basis. A total of 11.01 days is taken to do all eight SCKY-IMSRG calculations over the various density points. And the breakdown of the runtime is seen in Figure 3.4. Each SCKY-IMSRG calculation requires the same 867.06 gigabytes amount of memory. MBPT(2), acquired using Algorithm 8, predicts saturation near IMSRG(2), but yields energies that significantly disagree with energies from IMSRG(2). MBPT(3) is not included since these results were obtained before its implementation.

normal-ordering, but is subsequently truncated after normal-ordering. In other words, the Hamiltonian is treated at the NO2B approximation for all reported calculations.

We summarize some notable differences in NM-EOS calculated from IMSRG(2), CC and MBPT below. We see at most a 1.72 MeV per particle difference between IMSRG and MBPT(3) computed energies (found in Figure 4.11). Likewise, we see at most a 4.32 MeV per particle difference between CCD and MBPT(3) computed energies (seen in Figure 4.12). Comparing CCD(T) and MBPT(4), we observe at most a 0.92 MeV per particle difference in computed energies (seen in Figure 4.12). Lastly, we observe at most a 3.99 MeV per particle difference between CCD and CCD(T) computed energies (found in Figure 4.12). These discrepancies between the many-body methods are significant, and must be understood. Although, we observe discrepancies in energies computed from the methods, we however, see that all methods share similar predictions of nuclear saturation. This is noticeably seen in Figures 4.10–4.12, where most many-body methods predict saturation near the empirical saturation point $\rho_{\text{sat}} = 0.16 \text{ fm}^{-3}$. Curiously, all methods predict saturation near $\rho = 0.19 \text{ fm}^{-3}$ with the softened $\lambda = 1.8 \text{ fm}^{-1}$ Hebeler force in Figure 4.9.

Figures 4.9–4.12 confirm that energies from reduced MBPT(4) are indeed closer to those of IMSRG(2), than energies from MBPT(4). Notably, energies from the reduced MBPT(4) effectively coincide with IMSRG(2) energies in Figure 4.10. This means that the missing triples and undercounted asymmetric quadruples in IMSRG(2), primarily account for the IMSRG(2)–MBPT(4) disparity in that system. However, energies from the reduced MBPT(4) do not always coincide with those of IMSRG(2). This is notably seen in Figure 4.11 where the reduced MBPT(4) yields energies that are 0.3–1.29 MeV per particle more bound than IMSRG(2) energies. Interestingly, the disparity between energies from the reduced MBPT(4) and IMSRG(2) is slightly lower when using the harder N2LO EMN force with an increased

resolution scale $\Lambda = 500$ MeV, in Figure 4.12. However, it should be stressed that the two EMN potentials have different two- and three-nucleon contact interactions associated with them, so simply comparing the two resolution scales to infer that one should be more non-perturbative than the other is likely misguided. For instance, the low-energy 3N constant c_D is somewhat stronger for the $\Lambda = 450$ MeV interaction.

As expected, IMSRG(2) energies generally fall between CCD and CCD(T) energies in Figures 4.9, 4.10, and 4.12. In Figures 4.10 and 4.12, we see that the disagreement between the many-body methods—with the exception of MBPT(3) and MBPT(4)—tends to widen as the SNM nucleon density ρ , is increased. This behavior is prominently seen between CCD and CCD(T) in Figure 4.12, where energies from both methods differ by at most 3.99 MeV per particle (at $\rho = 0.21 \text{ fm}^{-3}$). This suggests that correlations from triples excitations are increasingly dominant in CC (and perhaps IMSRG) as ρ is increased. As seen in Figures 4.9, 4.10, and 4.12, the energies of IMSRG(2) are close to those of CCD(T) when $\rho < 0.13 \text{ fm}^{-3}$, but with larger deviations at higher densities—albeit to a smaller extent than CCD. We suspect that triples also account for the overbinding of IMSRG(2) relative to CCD(T) at higher density. Conversely, energies from MBPT are farthest from those of CCD(T) at the low-end of the density range $\rho \sim 0.08 \text{ fm}^{-3}$, but become notably closer as ρ is increased. Recall that CCD(T) contains all MBPT diagrams up to 4th-order and includes infinite partial summations of higher-order diagrams [27]. Therefore, the 0.07–0.6 MeV per particle and 0.16–0.92 MeV per particle disparities between MBPT(4) and CCD(T) in Figures 4.10 and 4.12, respectively, are due to correlations in CCD(T) beyond 4th-order. Interestingly, these higher-order correlations in CCD(T) are most dominant when $\rho < 0.13 \text{ fm}^{-3}$, but become less prominent at higher densities $\rho \sim 0.2 \text{ fm}^{-3}$. Turning our attention to IMSRG(2) and CCD, recall that both methods contain all MBPT diagrams up to 3rd-order

and include infinite partial summations of higher-order diagrams [10, 27]. Therefore, the IMSRG(2)–MBPT(3) and CCD–MBPT(3) disparities seen in Figures 4.9–4.12, are due to correlations in IMSRG(2) and CCD beyond 3rd-order. Converse to the CCD(T)–MBPT(4) relationship, these higher-order correlations in IMSRG(2) and CCD are most dominant at the high-end of our sampled density range $\rho \sim 0.2 \text{ fm}^{-3}$, but become less prominent when $\rho < 0.13 \text{ fm}^{-3}$.

Unlike CC (and perhaps IMSRG), the net effect of triples correlations in MBPT is generally small. This is reflected in the decent MBPT convergence from 3rd to 4th-order—seen in Figures 4.9–4.12. For example, MBPT(3) and MBPT(4) are effectively converged in Figure 4.10. However, energies from the reduced MBPT(4) differ from those of MBPT(3) and MBPT(4) by 0.36–0.55 MeV per particle. This implies that in Eq. (4.1), there are substantial 0.36–0.55 MeV per particle cancellations within MBPT(4) between $\Delta E_{\text{reduced}}^{(4)}$ and $\Delta E_{\text{triples}}^{(4)} + \frac{1}{2}\Delta E_{\text{asymmQ}}^{(4)}$.

4.2 Discussion

Given the excellent agreement seen between IMSRG(2) and MBPT(3) in PNM, we expect to see the same agreement when also considering MBPT(4) and CC. Therefore, we turn our attention towards the more interesting SNM results. Consistent with observations in finite nuclei [10], IMSRG(2) generally falls between CCD and CCD(T) energies in Figures 4.9, 4.10, and 4.12. We consider this a validation of our IMSRG(2) implementation. As is the case in finite nuclei, the correlations from 4th-order triples and asymmetric quadruples are attractive and repulsive, respectively [10]. While both IMSRG(2) and CCD miss attractive correlations from 4th-order triples, the IMSRG(2) undercounts repulsive asymmetric

quadruples—yielding to more attraction than CCD. Therefore, IMSRG(2) mimics the attraction of triples by undercounting the repulsive asymmetric quadruples. CCD(T) is exact at 4th-order MBPT and thus includes all attractive 4th-order correlations due to triples [10]. Consequently, CCD(T) tends to yield more attraction than both CCD and IMSRG(2).

Figures 4.9, 4.10, and 4.12 imply that correlations from attractive triples become larger in CC and IMSRG as the density of SNM is increased. This observation can be interpreted using the old hole-line expansion arguments of Brueckner theory for nuclear matter [32]. Methods like CC and IMSRG have superseded Brueckner theory in recent years, though intuition from the latter is still useful since the dominant contributions to CC and IMSRG correlation energies are of the Brueckner type. Brueckner’s hole-line expansion is an expansion in the “diluteness” of the many-body system, where the small parameter is the ratio of the range of the repulsive core of the NN potential divided by the average interparticle spacing. The leading term in the hole-line expansion sums the particle-particle ladders between pairs of particles to all orders, while the next term in the expansion treats the particle-particle ladders between interacting triplets of particles to all orders, and so on. In CC theory, for example, CCD and CCDT reduces to leading-order and next-to-leading order Brueckner theory if one drops the terms with particle-hole intermediate states. Therefore, it is quite reasonable that we find the attractive triples contributions are becoming rather large as the density increases, since the expansion parameter of the hole-line expansion is becoming large.

It is important to mention that we are inclined to most trust CCD(T) results since from the perspective of MBPT, it completely sums all 4th-order correlations, it partially sums higher-order correlations, and it incorporates triples excitations. However, the non-iterative implementation of triples in CCD(T) assumes that the effect of triples in the CC correlation energy is small [23]. This is clearly not the case in Figures 4.10 and 4.12, which show

that triples introduce substantial 1.45–3.99 MeV per particle attraction in CCD(T) over CCD. Therefore, a full treatment of triples in CCDT (or perhaps IMSRG(3)) is needed to properly account for triples correlations using a nonperturbative method. Unfortunately, it is currently intractable to store and evolve three-body operators at scale.

Figures 4.9, 4.10, and 4.12 show that energies from CCD(T) and MBPT(4) are closest (around $\rho = 0.2 \text{ fm}^{-3}$) when triples correlations are highest in CC. We are unsure of how to interpret this observation. Given that MBPT seems relatively converged from 3rd- to 4th-order, perhaps both methods are converging to the true NM-EOS (for the Hebeler and EMN forces) around $\rho = 0.2 \text{ fm}^{-3}$. Or perhaps both methods happen to cross around $\rho = 0.2 \text{ fm}^{-3}$, but may diverge at further densities. It is important to note that the observed trends between the many-body methods are not guaranteed to hold outside of our sampled density range. Going forward, it will be interesting to compare the many-body methods at densities going up to $2\rho_{\text{sat}}$. It will also be very interesting to implement the approximate (and hence computationally viable) IMSRG(3) scheme outlined in Ref. [22].

4.3 Conclusion

We find that NM-EOS computed using IMSRG(2) and MBPT(3) coincide in PNM, irrespective of the hardness of the employed inter-nucleon force. And we expect similar agreement in NM-EOS obtained using CC in PNM. However, within SNM, we find substantial disagreements in energies computed from IMSRG(2), MBPT, and CC using the Hebeler and harder N2LO EMN forces [4, 28]. At most, we observe energy differences of 1.72, 4.32, 0.92, and 3.99 MeV per particle between the following methods, respectively: IMSRG(2)–MBPT(3), CCD–MBPT(3), CCD(T)–MBPT(4), and CCD(T)–CCD. Despite the significant energy dis-

agreements between the methods, we find that the methods often predict energies that saturate near the empirical saturation point $\rho_{\text{sat}} = 0.16 \text{ fm}^{-3}$.

Consistent with findings in finite nuclei [10], we observe that IMSRG(2) energies generally fall between those of CCD and CCD(T). We consider this a validation of our nuclear matter IMSRG(2) implementation. Therefore, as is the case in finite nuclei, we conclude that the correlations from 4th-order triples and asymmetric quadruples are also attractive and repulsive, respectively, in nuclear matter. IMSRG(2) and CCD are not only 3rd-order exact from the perspective of MBPT but also include infinite partial summations of higher-order MBPT diagrams [10,27]. Also, CCD(T) is 4th-order exact from the perspective of MBPT and includes infinite partial summations of higher-order MBPT diagrams [27]. Hence, we conclude that observed IMSRG(2)–MBPT(3) and CCD–MBPT(3) energy disparities are due to correlations in IMSRG(2) and CCD beyond 3rd-order. Likewise, we also conclude that observed CCD(T)–MBPT(4) energy disparities are due to correlations in CCD(T) beyond 4th-order. Though, given that triples account for at most 3.99 MeV per particle more attraction in CCD(T) over CCD, we worry that CCD(T) may not be fully converged, and a full treatment of triples in CCDT may be needed.

Comparing CCD to CCD(T), we see that correlations from attractive triples become larger in CC and IMSRG as the density of SNM is increased. And we realize that this observation can be qualitatively understood using Brueckner’s hole-line expansion [32]. We find that MBPT is decently converged from 3rd to 4th-order. Though, we see substantial 0.36–0.55 MeV per particle cancellations between diagrammatic terms of MBPT(4). We also observe that energies from CCD(T) and MBPT(4) are closest (at the higher-end of our density range) when triples correlations are highest in CC. And we are unsure of how to interpret this observation. Given that MBPT seems relatively converged from 3rd- to

4th-order, perhaps both methods are converging to the true NM-EOS at the higher-end of our density range. This needs further investigation.

4.4 Outlook

The disparity between energies obtained from IMSRG, CC and MBPT in SNM need to be further investigated by extending the sampled density range, going up to perhaps $2\rho_{\text{sat}}$. Moreover, all IMSRG calculations in this work are done using normal-ordered 2NF and 3NF IMSRG(2) schemes. Given the large discrepancy observed between CCD and CCD(T) calculated NM-EOS in Figures 4.9, 4.10, and 4.12, we look towards a future nuclear matter IMSRG implementation with approximate triples. And developments from Stroberg *et al.* [22] will likely be needed in this endeavor. We suspect that the inclusion of approximate triples in the IMSRG should yield more attractive energies at higher densities.

NM-EOS are acquired using only three chiral forces at next-to-next-to leading-order (N2LO) of χ -EFT in this work. The *true* NM-EOS is only obtained with a full accounting of the uncertainties in the nuclear force. We do no such accounting in this work. Therefore, going forward, IMSRG computed NM-EOS will be acquired using a much larger number of forces—perhaps ten, with some at next-to-next-to-next-to leading-order (N3LO) of χ -EFT—in the immediate continuation of this project. Subsequent acquired NM-EOS can then be fed into the Bayesian machine-learning approach of Drischler *et al.*, to determine EFT truncation errors [29].

As seen in Figure 4.13, the computational cost needed to obtain NM-EOS using the IMSRG for one force alone is massive. Therefore, there is great interest in using emulation techniques including Eigenvector Continuation (EC) [30], Dynamical Mode Decomposition

(DMD) [33], and Parametric Matrix Models (PMM) [34] to emulate results from the IMSRG, while varying the low energy constants of the nuclear force. This interest follows the work of Ekström *et al.* [31]—which saw great success emulating binding energies in finite nuclei, obtained from Coupled-Cluster theory using EC. Perhaps these methods could be applied to obtain an uncertainty-quantified NM-EOS that is calculated with the IMSRG—while using less computational resources. While doing preliminary explorations of a potential EC application in the IMSRG, we realized that a generalized form of the Baker-Campbell-Hausdorff expansion (BCH) might be a useful tool in such an endeavor. Subsequently, we derive the generalized BCH in Appendix A. Given the large computational costs needed to obtain NM-EOS using the IMSRG, we look towards novel ideas to accelerate IMSRG calculations using Unitary Coupled-Cluster (UCC)-inspired IMSRG generators in Chapter 5, and Shanks and Padé IMSRG extrapolators in Chapter 6.

Chapter 5. UCC-Inspired IMSRG Generators

“I call it Coupled-Cluster

-Fock theory”

—Robert Branson

We view IMSRG generators $\eta(H(s))$ as approximate diagonalizers of $H(s)$ within the Magnus-IMSRG formulation. Therefore, the IMSRG’s convergence can be accelerated by improving the diagonalizing power of $\eta(H(s))$. Given the striking similarities between the Magnus-IMSRG and Unitary Coupled-Cluster theory (UCC), we improve on existing IMSRG generators by constructing approximate UCC diagonalizers. We view UCC as a nonlinear inverse problem; and we realize that UCC amplitudes at any order of UCC, are given by a generalization of the Born series—so long the series converges. We introduce three UCC-inspired IMSRG generators named the Born, UCC-Born, and Carinae generators, which use regulated Born expansions to approximately solve UCC. Born’s generator targets 1st-order UCC, while UCC-Born and Carinae target high-order UCC. UCC-Born is iteratively constructed using a gradient descent based UCC ansatz seen in Appendix I. Carinae is constructed by iteratively solving UCC with a strict convergence criterion. UCC-Born and Carinae are obtained using preconditioners to improve the convergence of the Born series. Using all novel generators with the Magnus-IMSRG, we often observe noticeable reductions in commutator evaluations needed for IMSRG’s convergence compared to using the existing White generator—translating to observed IMSRG speedups. We sometimes observe 2–4X IMSRG speedup using the novel generators, particularly when the IMSRG with White’s generator is slowly convergent. In all, we connect two historically separate theories—IMSRG and UCC by using approximate UCC solutions as generators of the IMSRG. We introduce the Born

expansion as a tool to solve UCC. And we use preconditioners to aid the convergence of the Born series. Moreover, we provide an ansatz for a renormalized Hamiltonian in UCC. We hope this work leads to further developments of these methods within many-body physics.

5.1 Motivation

The IMSRG is a powerful, yet computationally expensive method—especially in large systems. We dub the “realistic limit” as the combination of the thermodynamic and the complete basis set limit in infinite nuclear matter calculations. Approaching the realistic limit is essential to obtain results that are free from finite size and incomplete basis set artifacts, in nuclear matter. Approaching the realistic limit, we must increase the number of orbitals N_{orbitals} in the infinite matter basis and increase the number of particles—which are computationally costly.

Commutator evaluations are the most computationally limiting operations of the IMSRG and UCC methods. The computational cost to evaluate a commutator at the two-body level in the IMSRG and UCC scales as $\mathcal{O}(N_{\text{orbitals}}^6)$ [19]. Moreover, the IMSRG can sometimes require hundreds of commutator evaluations to converge, especially in strongly correlated systems. This can significantly hamper IMSRG runtimes in large systems. Therefore, there is growing interest in efficiently accelerating the convergence of the IMSRG—obtaining more converged results with fewer commutator evaluations.

Recent ideas have centered around utilizing data driven methods including the Shanks and Padé transformation (seen in Chapter 6 of this work), and machine learning to extrapolate on the IMSRG flow. Yoshida notably used neural networks to accurately extrapolate IMSRG operators with great success [35]. We aim to expand on this emerging research

area by taking a different approach. Particularly, we combine the IMSRG with UCC in the form of novel UCC-inspired IMSRG generators. We then introduce physics-motivated techniques in UCC to accelerate the generator calculations—translating to an efficient IMSRG convergence acceleration.¹

5.2 Assumptions

All generator calculations in this chapter make the following assumptions:

All Hamiltonians $H = E + f + \Gamma$ satisfy Assumption 1, and Assumption 2.

Assumption 0 All A -body operators are truncated at the two-body level.

Assumption 1 $f_{pq} = \delta_{pq} \times f_{pq} \quad \forall pq \quad \longrightarrow \quad H_{od} = \cancel{f_{ai}} + \Gamma_{abij} \quad \forall abij$.²

Assumption 2 $\Delta_{abij} \equiv f_{aa} + f_{bb} - f_{ii} - f_{jj} \neq 0 \quad \forall abij$.³

Assumption 3 We denote approximate diagonalizers of H by

$$\eta(H) \equiv \sum_{ai} \eta_{ai}(H) : a_a^\dagger a_i : + \frac{1}{4} \sum_{abij} \eta_{abij}(H) : a_a^\dagger a_b^\dagger a_j a_i : - \text{H.c.} \quad (5.1)$$

where “H.c.” denotes the Hermitian conjugate of the first two terms in Eq. (5.1). $\eta(H)$ is assumed to be zero in its diagonal sectors. We also assume $\eta_{ai}(H) \propto f_{ai}$, and $f_{ai} = 0$ under Assumption 1.

¹The computational performance of the IMSRG and UCC at similar truncation levels are generally considered to be similar. The exact performance difference between both methods is however, not investigated in this work due to the lack of a computer program using existing state-of-the-art UCC techniques in infinite nuclear matter. The success of this work is measured by efficient convergence acceleration *seen in the IMSRG*. We however, suspect that the introduced UCC techniques should also confer improvements in standard UCC.

²Assumption 1 is partly justified in infinite matter due to momentum conservation, and the spin-diagonal nature of the nuclear force at NNLO. Though, we observe that Assumption 1 is weakly broken during the Magnus-IMSRG evolution. As a consequence of Assumption 1 holding exceedingly well in nuclear matter, the one-body components of all diagonalizers η and Ω are negligible.

³Assumption 2 holds well in our existing single-reference nuclear matter IMSRG. We suspect this is due to the spin unpolarized nature of the infinite matter basis.

5.3 Magnus-IMSRG Convergence Acceleration

Consider a given Hamiltonian $H(0)$. In the Magnus-IMSRG formulation, we iteratively diagonalize $H(0)$ with unitary transformation $H(s) = U(s)H(0)U(s)^\dagger$ by solving⁴

$$\frac{dU(s)}{ds} = \eta(H(s))U(s) \quad (5.2)$$

$$U(s) \equiv e^{\Omega(s)}. \quad (5.3)$$

$\Omega(s)$ is obtained by integrating Eq. (2.7). $\eta(H(s))$ could be considered a driving force in the diagonalization, and is chosen as an approximate diagonalizer⁵ of $H(s)$. Some existing generators include the White, Imaginary-time, and Wegner generators. Using perturbative analysis of the flow equations with the aforementioned generators [19],

$$H_{od}(s) = \Gamma_{abij}(s) \approx \Gamma_{abij}(0) \times e^{-s \times \Delta_{abij} \times G_{abij}} \quad (5.4a)$$

$$\Delta_{abij} \times G_{abij} \geq 0 \longrightarrow \lim_{s \rightarrow \infty} H_{od}(s) = 0. \quad (5.4b)$$

⁴ $U(0) \equiv \mathbb{1}$. Also note, $\eta(s)$ is ultimately dependent on $H(s)$.

⁵Ideally, one could construct $U(ds)$ (ds is some step-size) where $H_{od}(ds) = 0$. However, as we will see, this is a highly nonlinear problem from the perspective of UCC. Thus, we construct approximate diagonalizers (generators) of $H(s)$, and integrate them via the Magnus expansion to construct a full diagonalizer of $H(0)$. Note, we view diagonalizers as operators that eliminate $H_{od}(s)$ when exponentiated.

G_{abij} depends on the chosen generator. White's generator is notable due its observed numerical stability so long Assumption 2 holds [20, 36]. White's generator is given by⁶

$$\eta^{WhiteMP}(H(s)) = \sum_{ai} \eta_{ai}^{WhiteMP}(H(s)) : a_a^\dagger a_i : \quad (5.5a)$$

$$+ \frac{1}{4} \sum_{abij} \eta_{abij}^{WhiteMP}(H(s)) : a_a^\dagger a_b^\dagger a_j a_i : - \text{H.c.}$$

$$\eta_{ai}^{WhiteMP}(H(s)) \equiv \frac{\cancel{f_{ai}(s)}}{f_{aa}(s) - f_{ii}(s)} = \frac{\cancel{f_{ai}(s)}}{\Delta_{ai}(s)} \quad (5.5b)$$

$$\eta_{abij}^{WhiteMP}(H(s)) \equiv \frac{\Gamma_{abij}(s)}{f_{aa}(s) + f_{bb}(s) - f_{ii}(s) - f_{jj}(s)} = \frac{\Gamma_{abij}(s)}{\Delta_{abij}(s)}. \quad (5.5c)$$

Viewing $\eta(H(s))$ as an approximate diagonalizer of $H(s)$, we hypothesize that the IMSRG's convergence can be accelerated by improving the diagonalizing power of $\eta(H(s))$. Given the similarity of Magnus-IMSRG and UCC theory, we look towards UCC for candidate IMSRG generators.

⁶This chapter uses White's generator with energy denominators from Møller–Plesset perturbation theory denoted by $\eta^{WhiteMP}$.

5.4 Unitary Coupled-Cluster Theory

Consider a given Hamiltonian H .⁷ Single-reference UCC theory diagonalizes H via the exponential ansatz $U = e^\eta$. Thus, we construct η such that $[e^\eta H e^{-\eta}]_{od} = 0$.⁸ At the two-body level, η is given by Eq. (5.1). Therefore, $\eta = -\eta^\dagger$ and $UU^\dagger = U^\dagger U = \mathbb{1}$. Using the Baker-Campbell-Hausdorff (BCH) formula,

$$[e^\eta H e^{-\eta}]_{od} = \left[\sum_{m=0}^{\infty} \frac{[\eta, H]^{(m)}}{m!} \right]_{od} = 0 \quad (5.6a)$$

$$[\eta, H]^{(m)} \equiv [\eta, [\eta, H]^{(m-1)}], \quad \forall m > 0 \quad (5.6b)$$

$$[\eta, H]^{(0)} \equiv H. \quad (5.6c)$$

Expanding Eq. (5.6a), then utilizing the linearity of commutators,⁹

$$[e^\eta H e^{-\eta}]_{od} = H_{od} + \left[\sum_{m=1}^{\infty} \frac{[\eta, H]^{(m)}}{m!} \right]_{od} = 0 \quad (5.7)$$

$$-H_{od} = [\eta, H]_{od} + \frac{[\eta, H]_{od}^{(2)}}{2!} + \frac{[\eta, H]_{od}^{(3)}}{3!} + \dots$$

$$-H_{od} = \left[\eta, \underbrace{\sum_{m=0}^{\infty} \frac{[\eta, H]^{(m)}}{(m+1)!}}_{H^{RG}(\eta)} \right]_{od}. \quad (5.8)$$

⁷For the remainder of this chapter, we drop the flow parameter s for brevity. We also drop η 's dependence on H since that is implied.

⁸We use od as a subscript to denote the off-diagonal sectors of the transformed Hamiltonian.

⁹All commutators are truncated at the two-body level.

Eq. (5.8) is nonterminating due to the excitation ($: a_a^\dagger a_b^\dagger a_j a_i :$) and de-excitation ($: a_i^\dagger a_j^\dagger a_b a_a :$) structure of η , enforced by its anti-hermiticity.¹⁰ This is unlike standard Coupled-Cluster (CC), where η has a pure excitation structure that guarantees a fixed termination order of Eq. (5.8) [27]. Although Eq. (5.8) is nonterminating, we truncate the expansion for $H^{RG}(\eta)$ at some m^* such that¹¹

$$\left| \left\{ \frac{[\eta, H]^{(m^*)}}{(m^* + 1)!} \right\}_{0\text{-body}} \right| \leq \epsilon'_{\text{BCH}}. \quad (5.9)$$

The operator $\{\}_{0\text{-body}}$ projects out the zero-body component of $\frac{1}{(m^*+1)!}[\eta, H]^{(m^*)}$. The truncation parameter $\epsilon'_{\text{BCH}} = 1\text{e-}4$ is used for this work.¹² So long Eq. (5.8) is invertible, the main task of UCC is to approximate $H^{RG}(\eta)$. In this light, UCC can be viewed as a nonlinear commutator inversion problem.

5.5 Linearized UCC

It is important to note that η is the solution of Eq. (5.8). η is however, unknown since H^{RG} is dependent on η . Moreover, Eq. (5.8) is highly nonlinear in η . We can however, linearize Eq. (5.8) using successive approximations to η . Let k denote an iteration count. Letting $\eta = \eta^{\{k\}} + \delta\eta$, we can approximate $H^{RG}(\eta) \approx H^{RG}(\eta^{\{k\}})$ if $\delta\eta$ is sufficiently small. The choice of $\eta^{\{k\}}$ is thus of paramount importance. If $\delta\eta$ is sufficiently small, and η is an

¹⁰A closed expression of Eq. (5.8) with a maximum power of $[\eta, H]$ may be possible if the rank of η is known [37].

¹¹The diagonal sectors of the 1 and two-body ranks of $\frac{1}{(m^*+1)!}[\eta, H]^{(m^*)}$ are observed to converge at the rate as its zero-body rank.

¹²Eq. (5.9) and $\epsilon'_{\text{BCH}} = 1\text{e-}4$ is chosen to be consistent with the BCH truncation scheme in the vanilla IMSRG.

attractive solution of Eq. (5.8), then solving

$$-H_{abij} = \left[\eta^{\{k+1\}}, H^{RG}(\eta^{\{k\}}) \right]_{abij}, \quad (5.10)$$

for $\eta^{\{k+1\}}$, we can expect

$$\eta^{\{k\}}, \eta^{\{k+1\}}, \eta^{\{k+2\}}, \dots \rightarrow \eta. \quad (5.11)$$

The Born, UCC-Born, and Carinae generators all solve linearized UCC in some form. Notice, $\eta^{\{k\}}$ and subsequently, $H^{RG}(\eta^{\{k\}}) = \sum_{m=0}^{\infty} \frac{1}{(m+1)!} [\eta^{\{k\}}, H]^{(m)}$ are presumed to be known in Eq. (5.10). Thus, Eq. (5.10) is solvable if there exists a way to invert the commutator for $\eta^{\{k+1\}}$.

5.6 Commutator Inversion via Born Series

Suppose we are tasked with inverting the following commutator¹³

$$-H_{abij} = \left[\eta, H^{RG} \right]_{abij}. \quad (5.12)$$

¹³The view of UCC as a nonlinear commutator inversion problem was partly inspired by Kutzelnigg [38]. Note, H^{RG} 's dependence on η is dropped in Eq. (5.12) for brevity. The following derivation of the Born series assumes H^{RG} is known, if not estimated.

H is known, and H^{RG} assumed to be known or approximated. Both operators are of the form

$$H = E + f + \Gamma \longrightarrow H_{abij} = \Gamma_{abij} \quad (5.13a)$$

$$H^{RG} = E^{RG} + f^{RG} + \Gamma^{RG}. \quad (5.13b)$$

η is to be calculated, and has an operator structure given by Eq. (5.1). Eq. (5.12) can be expanded

$$-\Gamma_{abij} = \left[\eta, \cancel{E^{RG}} \right]_{abij} + \left[\eta, f^{RG} \right]_{abij} + \left[\eta, \Gamma^{RG} \right]_{abij}. \quad (5.14)$$

Assumption 1 implies

$$\left[\eta, f^{RG} \right]_{abij} = \left(f_{ii}^{RG} + f_{jj}^{RG} - f_{aa}^{RG} - f_{bb}^{RG} \right) \times \eta_{abij} = -\Delta_{abij}^{RG} \times \eta_{abij}, \quad (5.15)$$

which together with Eq. (5.14) gives

$$-\Gamma_{abij} = -\Delta_{abij}^{RG} \times \eta_{abij} + \left[\eta, \Gamma^{RG} \right]_{abij}, \quad (5.16)$$

$$\Delta_{abij}^{RG} \times \eta_{abij} = \Gamma_{abij} + \left[\eta, \Gamma^{RG} \right]_{abij}.$$

So long Assumption 2 holds,

$$\eta_{abij} = \frac{\Gamma_{abij}}{\Delta_{abij}^{RG}} + \frac{\left[\eta, \Gamma^{RG} \right]_{abij}}{\Delta_{abij}^{RG}}. \quad (5.17)$$

Adopting the following notation for any A -body operator O ¹⁴

$$(O_*)_{abij} \equiv \frac{O_{abij}}{\Delta_{abij}^{RG}}, \quad (5.18)$$

we can cleanly cast Eq. (5.17) into an operator form

$$\eta = \Gamma_* + \left[\eta, \Gamma^{RG} \right]_* . \quad (5.19)$$

Eq. (5.19) is the master equation that generates the generalized Born series. It is a Lippmann-Schwinger type of equation in operator form, and is a fixed point equation for η . Iterating Eq. (5.19) yields

$$\begin{aligned} \eta &= \Gamma_* + \left[\Gamma_* + \left[\eta, \Gamma^{RG} \right]_* , \Gamma^{RG} \right]_* \\ &= \Gamma_* + \left[\Gamma_* , \Gamma^{RG} \right]_* + \left[\left[\eta, \Gamma^{RG} \right]_* , \Gamma^{RG} \right]_* . \end{aligned} \quad (5.20)$$

Let us define the following adjoint for A -body operators A and B :

$$[A, B]_*^{(m)} \equiv \left[[A, B]_*^{(m-1)}, B \right]_* , \quad \forall m \geq 1 \quad (5.21a)$$

$$[A, B]_*^{(0)} \equiv A . \quad (5.21b)$$

Iterating to n th order, we assume η is given by

$$\eta \stackrel{?}{=} \sum_{m=0}^n \left[\Gamma_* , \Gamma^{RG} \right]_*^{(m)} + \left[\eta , \Gamma^{RG} \right]_*^{(n+1)} , \quad n \geq 0. \quad (5.22)$$

¹⁴Note, all sectors of O_* other than $(O_*)_{abij}$ are defined to be zero. For example, $(O_*)_{abcd} \equiv 0 \quad \forall abcd$.

We seek to prove Eq. (5.22). First, notice Eq. (5.22) cotrivially recovers Eq. (5.19) with $n = 0$:

$$\left[\Gamma_*, \Gamma^{RG} \right]_*^{(0)} + \left[\eta, \Gamma^{RG} \right]_*^{(1)} = \Gamma_* + \left[\underbrace{\left[\eta, \Gamma^{RG} \right]_*^{(0)}}_{\eta}, \Gamma^{RG} \right]_* = \eta. \quad (5.23)$$

Likewise, Eq. (5.22) recovers Eq. (5.20) with $n = 1$:

$$\begin{aligned} & \left[\Gamma_*, \Gamma^{RG} \right]_*^{(0)} + \left[\Gamma_*, \Gamma^{RG} \right]_*^{(1)} + \left[\eta, \Gamma^{RG} \right]_*^{(2)} \\ &= \Gamma_* + \left[\Gamma_*, \Gamma^{RG} \right]_* + \left[\left[\eta, \Gamma^{RG} \right]_*^{(1)}, \Gamma^{RG} \right]_* = \eta. \end{aligned} \quad (5.24)$$

Inserting Eq. (5.19) into the RHS of Eq. (5.22) yields

$$\eta = \sum_{m=0}^n \left[\Gamma_*, \Gamma^{RG} \right]_*^{(m)} + \left[\Gamma_* + \left[\eta, \Gamma^{RG} \right]_* , \Gamma^{RG} \right]_*^{(n+1)}. \quad (5.25)$$

In Appendix G, we show adjoints of the form $\left[\Gamma_* + \left[\eta, \Gamma^{RG} \right]_* , \Gamma^{RG} \right]_*^{(n+1)}$ can be cleanly separated using linearity. Utilizing Eq. (G.1),

$$\begin{aligned} \eta &= \sum_{m=0}^n \left[\Gamma_*, \Gamma^{RG} \right]_*^{(m)} + \left[\Gamma_*, \Gamma^{RG} \right]_*^{(n+1)} + \left[\left[\eta, \Gamma^{RG} \right]_* , \Gamma^{RG} \right]_*^{(n+1)} \\ &= \sum_{m=0}^{n+1} \left[\Gamma_*, \Gamma^{RG} \right]_*^{(m)} + \left[\left[\eta, \Gamma^{RG} \right]_* , \Gamma^{RG} \right]_*^{(n+1)}. \end{aligned} \quad (5.26)$$

Utilizing Eq. (G.3),

$$\left[\left[\eta, \Gamma^{RG} \right]_* , \Gamma^{RG} \right]_*^{(n+1)} = \left[\eta, \Gamma^{RG} \right]_*^{(n+2)} \quad (5.27)$$

$$\eta = \sum_{m=0}^{n+1} \left[\Gamma_* , \Gamma^{RG} \right]_*^{(m)} + \left[\eta, \Gamma^{RG} \right]_*^{(n+2)}. \quad (5.28)$$

Therefore, we have demonstrated if Eq. (5.22) holds for some $n \geq 0$, it also holds for $n + 1$.

Since Eq. (5.22) holds for $n = 0$ (and $n = 1$), then it indeed holds for all $n \geq 0$.

Exact computation of Eq. (5.22) is nontrivial due to its RHS's dependence on η . Practically, we approximate η by summing only the convergent terms of Eq. (5.22) at a potentially high order¹⁵

$$\eta \approx \sum_{m=0}^n \left[\Gamma_* , \Gamma^{RG} \right]_*^{(m)} \quad (5.29a)$$

$$: \quad \left\| \left[\Gamma_* , \Gamma^{RG} \right]_*^{(n+1)} \right\| > \left\| \left[\Gamma_* , \Gamma^{RG} \right]_*^{(n)} \right\| \quad (5.29b)$$

$$\vee \quad : \quad \left\| \left[\Gamma_* , \Gamma^{RG} \right]_*^{(n)} \right\| \leq \epsilon_{\text{Born}} \quad (5.29c)$$

$$\vee \quad : \quad n = n_{\text{MaxBornOrder}} \cdot \quad (5.29d)$$

To clarify, we sum Eq. (5.29a) to some order n , such that either Eqs. (5.29b), (5.29c), or (5.29d) are true. Truncation parameter $\epsilon_{\text{Born}} = 1\text{e-}3$ is used for this work. $n_{\text{MaxBornOrder}}$ is a chosen maximum order of the Born series. Eq. (5.29) is called the generalized Born series honoring Dr. Max Born for his perturbative solution to the Lippmann–Schwinger

¹⁵“ $\|\cdot\|$ ” denotes a Frobenius operator norm. “:” is notation for “such that.” And “ \vee ” is the logical “or.” Only a few terms of the Born series are typically needed to approximate 1st-order UCC well. Born’s generator will be obtained with $n_{\text{MaxBornOrder}} = 5$, while the UCC-Born and Carinae generator will be obtained with $n_{\text{MaxBornOrder}} = 100$.

equation [39]. If

$$\|\Gamma_*\| \gg \left\| \left[\eta, \Gamma^{RG} \right]_* \right\|, \quad (5.30)$$

the leading term Γ_* will likely be a sufficient commutator inverter, and the Born series is considered highly perturbative.¹⁶ If Eq. (5.30) does not hold, Γ_* will likely be an insufficient commutator inverter, and the Born series is considered nonperturbative. Hence, the Born series likely improves on Γ_* when Eq. (5.30) does not hold. Following van der Sijs *et al.* [40], we introduce the parameter γ to quantify the nonperturbativity of the Born series

$$\gamma \equiv \frac{\left\| \left[\Gamma_*, \Gamma^{RG} \right]_*^{(2)} \right\|}{\left\| \left[\Gamma_*, \Gamma^{RG} \right]_*^{(1)} \right\|}. \quad (5.31)$$

Similar to the geometric series, the Born series converges or diverges if $\gamma < 1$ or $\gamma > 1$, respectively [40].

5.7 Regulating the Born Series

We ultimately aim to exponentiate η given by Eq. (5.29) when performing unitary transformations in the Magnus-IMSRG or UCC. Although BCH transformations with η are unitary, we still need those transformations to eliminate off-diagonal components of the target Hamiltonian. Given the immense nonlinearity of UCC seen in Eq. (5.8), all methods that are described in this work to obtain diagonalizers are *ultimately approximate*. Hence, η is only approximately known. And we run the risk of introducing large and uncontrollable errors

¹⁶If $\Gamma^{RG} = \Gamma$, then Γ_* is *exactly* White's generator with Møller–Plesset energy denominators. Moreover, if Eq. (5.30) holds, then $\eta \approx \eta^{WhiteMP}$.

that hamper our diagonalization with large η .¹⁷ Therefore, to obtain the Born, UCC-Born, and Carinae generators, we regulate Eq. (5.29) as follows:

$$\eta \approx \sum_{m=0}^n \left[\Gamma_*, \Gamma^{RG} \right]_*^{(m)} \quad (5.32a)$$

$$: \quad \left\| \sum_{m=0}^{n+1} \left[\Gamma_*, \Gamma^{RG} \right]_*^{(m)} \right\| > \Lambda_{\text{UCC}} \quad (5.32b)$$

$$\vee : \quad \left\| \left[\Gamma_*, \Gamma^{RG} \right]_*^{(n+1)} \right\| > \left\| \left[\Gamma_*, \Gamma^{RG} \right]_*^{(n)} \right\| \quad (5.32c)$$

$$\vee : \quad \left\| \left[\Gamma_*, \Gamma^{RG} \right]_*^{(n)} \right\| \leq \epsilon_{\text{Born}} \quad (5.32d)$$

$$\vee : \quad n = n_{\text{MaxBornOrder}} \cdot \quad (5.32e)$$

To clarify, we sum Eq. (5.32a) to some order n , such that one or more conditions in Eqs. (5.32b)–(5.32e) are satisfied. Eq. (5.32b) ensures $\|\eta\| \leq \Lambda_{\text{UCC}}$, so long $\|\Gamma_*\| \leq \Lambda_{\text{UCC}}$.¹⁸ Regulator cutoff $\Lambda_{\text{UCC}} = 8$ is used for this work. By using Eq. (5.32) instead of Eq. (5.29), we potentially worsen our inversion of Eq. (5.12) to avoid large errors in the Magnus-IMSRG and UCC—which utilize η dependent transformations (such as the BCH expansion). We detail the regulated Born series in Algorithm 1.

¹⁷The regulation of the Born series is due to inspiration from White—who cautioned against the use of large rotation angles when performing Jacobi canonical diagonalization [36].

¹⁸A better regularization scheme might instead enforce $\|\eta\|/\mathcal{V}_\eta \leq \Lambda_{\text{UCC}}$, where \mathcal{V}_η is the number of nonzero matrix elements of η . This regularization scheme would account for changes in the size of the basis—of which η is built upon.

Algorithm 1 Regulated Born Series

Input: $H = E + f + \Gamma$, $H^{RG} = E^{RG} + f^{RG} + \Gamma^{RG}$, $n_{\text{MaxBornOrder}}$

Output: η ▷ Approximate solution to $-H_{abij} = [\eta, H^{RG}]_{abij}$

```
1: function GENERATOR::BORN SERIES( $H$ ,  $H^{RG}$ ,  $n_{\text{MaxBornOrder}}$ )
2:   initialization
3:      $\Delta_{abij}^{RG} = f_{aa}^{RG} + f_{bb}^{RG} - f_{ii}^{RG} - f_{jj}^{RG} \quad \forall abij$ 
4:      $\eta = \Gamma_*$  ▷  $\eta_{abij} = \Gamma_{abij} / \Delta_{abij}^{RG} \quad \forall abij$ 
5:      $\text{ad} = \eta$  ▷ Stores Born series adjoints
6:      $\Lambda_{\text{UCC}} = 8$  ▷ Regulator cutoff so  $\eta$  stays small
7:      $\epsilon_{\text{Born}} = 1\text{e-}3$  ▷ Truncation parameter for residuals in the Born series
8:   end initialization
9:   for  $m \leftarrow 1$  to  $n_{\text{MaxBornOrder}}$  do
10:     $\text{ad}_{\text{previous}} = \text{ad}$ 
11:     $\text{ad} = [\text{ad}_{\text{previous}}, \Gamma^{RG}]_*$ 
12:    if  $\|\text{ad}\| > \|\text{ad}_{\text{previous}}\|$  then
13:      break ▷ Terminate if subsequent adjoints are increasing in norm
14:    end if
15:     $\eta += \text{ad}$ 
16:    if  $\|\eta\| > \Lambda_{\text{UCC}}$  then
17:       $\eta -= \text{ad}$  ▷ “Error” correction :)
18:      break
19:    end if
20:    if  $\|\text{ad}\| \leq \epsilon_{\text{Born}}$  then
21:      break
22:    end if
23:  end for
24:  return  $\eta$ 
25: end function
```

5.8 Preconditioning the Born Series

All UCC-inspired generators in this work strongly rely on the Born series; therefore, its convergence behaviour is of paramount importance. We seek to aid its convergence using preconditioning.¹⁹ Suppose we are again tasked with inverting the commutator given by Eq. (5.12). Suppose we have a *reasonable* guess η^{Guess} as a solution to Eq. (5.12). We can then let $\eta = \eta^{Guess} + \delta\eta$,

$$-H_{abij} = \left[\underbrace{\eta}_{\eta^{Guess} + \delta\eta}, H^{RG} \right]_{abij} \quad (5.33)$$

$$- \left(H_{abij} + \left[\eta^{Guess}, H^{RG} \right]_{abij} \right) = \left[\delta\eta, H^{RG} \right]_{abij}. \quad (5.34)$$

Eq. (5.34) is then another commutator inversion problem that can be solved for $\delta\eta$ via the regulated Born series. Once $\delta\eta$ is obtained, we reconstruct $\eta = \eta^{Guess} + \delta\eta$.²⁰ If η^{Guess} is reasonable, then the norm of Eq. (5.34)'s LHS will be reduced—improving the rate of convergence of the Born expansion for $\delta\eta$. η^{Guess} is given by any existing approximation to η when computing the UCC-Born and Carinae generators. We detail the preconditioned Born series in Algorithm 2.

¹⁹We find it prudent to mention that the preconditioned Born series introduced in this work is somewhat reminiscent of the Newton-Krylov method in CC, detailed by Yang *et al.* [41]. Yang *et al.* also use preconditioning and regularization in differing contexts from this work [41]. This realization was made after the completion of this work. All insights contained in this work were independently made.

²⁰We reconstruct $\eta = \eta^{Guess} + \delta\eta$ without ensuring $\|\eta\| \leq \Lambda_{UCC}$. This is observed to be OK.

Algorithm 2 Preconditioned Born Series

Input: η^{Guess} , H , H^{RG} , $n_{MaxBornOrder}$ **Output:** η \triangleright Approximate solution to $-H_{abij} = [\eta, H^{RG}]_{abij}$

```
1: function GENERATOR::BORNSERIES( $\eta^{Guess}$ ,  $H$ ,  $H^{RG}$ ,  $n_{MaxBornOrder}$ )
2:   initialization
3:      $H^{LHS} = H + [\eta^{Guess}, H^{RG}]$ 
4:   end initialization
5:    $\delta\eta = \text{GENERATOR::BORNSERIES}(H^{LHS}, H^{RG}, n_{MaxBornOrder})$ 
6:   return  $\eta^{Guess} + \delta\eta$ 
7: end function
```

5.9 Born Generator

Detailed in Algorithm 3, Born's generator η^{Born} is obtained by approximating $H^{RG}(\eta) \approx H$, then inverting $-H_{abij} = [\eta^{Born}, H]_{abij}$ with the regulated Born expansion. Therefore, Born's generator is an approximate 1st-order UCC solution. We observe that only a few terms of the Born series are typically needed to approximate 1st-order UCC well. Thus, we set $n_{MaxBornOrder} = 5$. Notice, the leading term of the Born series is exactly White's generator when $\Gamma^{RG} = \Gamma$. Hence, White's generator is an approximate solution to 1st-order UCC. We view Born's generator as an extension of White's generator.

Algorithm 3 Born generator

Input: H ▷ Hamiltonian to be diagonalized—this is IMSRG’s $H(s)$
Output: η^{Born} ▷ Approximation to a 1st-order UCC diagonalizer of H

```
1: function GENERATOR::BORN( $H$ )
2:   initialization
3:      $n_{MaxBornOrder} = 5$ 
4:   end initialization
5:    $\eta^{Born} = \text{GENERATOR}::\text{BORNSERIES}(H, H, n_{MaxBornOrder})$ 
6:   return  $\eta^{Born}$ 
7: end function
```

5.10 UCC-Born Generator

The UCC-Born generator $\eta^{UCC-Born}$ is designed to be a cheap, yet effective high-order UCC diagonalizer. Initially coinciding with Born’s generator η^{Born} , it determines if η^{Born} is a sufficient UCC diagonalizer of H using a generalized form of MBPT(2) seen in Algorithm 11. If η^{Born} is deemed insufficient, $H^{RG}(\eta)$ is approximated $H^{RG}(\eta) \approx \sum_{m=0}^{\infty} a_m(1) [\eta^{Born}, H]^{(m)}$ using the ansatz seen in Eq. (I.16). The UCC-Born generator is then updated by inverting $-H_{abij} = [\eta^{UCC-Born}, H^{RG}(\eta)]_{abij}$ using η^{Born} as a preconditioner in the Born expansion. We detail the construction of the UCC-Born generator in Algorithm 4.

Algorithm 4 UCC-Born generator

Input: H \triangleright Hamiltonian to be diagonalized—this is IMSRG’s $H(s)$
Output: $\eta^{UCC-Born}$ \triangleright Approximation to a UCC diagonalizer of H

```
1: function GENERATOR::UCCBORN( $H$ )
2:   initialization
3:      $\eta^{Born} = \text{GENERATOR}::\text{BORN}(H)$ 
4:      $\epsilon_{RG} = 1e-4$   $\triangleright$  Cutoff for series in Eq. (I.16)
5:      $\epsilon_{\text{GMBPT}} = 1e-3$   $\triangleright$  MBPT cutoff in case 1st-order UCC is sufficient
6:      $n_{\text{MaxBornOrder}} = 100$   $\triangleright$  We want a high fidelity inversion for  $\eta^{UCC-Born}$ 
7:   end initialization
8:    $\triangleright$  MBPT truncation scheme is detailed in Appendix-Section H.1.
9:   if  $\left| \text{MBPT2TRUNCATION}(\eta^{Born}, H) \right| < \epsilon_{\text{GMBPT}}$  then
10:     return  $\eta^{Born}$ 
11:   end if
12:    $H^{RG} = \sum_{m=0}^{m^*} a_m(1)[\eta^{Born}, H]^{(m)} : \left| \left\{ a_{m^*}(1)[\eta^{Born}, H]^{(m^*)} \right\}_{0\text{-body}} \right| \leq \epsilon_{RG}$ 
13:    $\eta^{UCC-Born} = \text{GENERATOR}::\text{BORNSERIES}(\eta^{Born}, H, H^{RG}, n_{\text{MaxBornOrder}})$ 
14:   return  $\eta^{UCC-Born}$ 
15: end function
```

5.11 Carinae Generator

The Carinae generator $\eta^{Carinae}$ is designed to be a potentially expensive and effective UCC diagonalizer.²¹ Initially coinciding with Born’s generator η^{Born} , the Carinae generator determines if η^{Born} is a sufficient UCC diagonalizer of H using a generalized form of MBPT(2) seen in Algorithm 11. If η^{Born} is deemed insufficient, it iterates Eq. (5.10) starting with $\eta^{\{0\}} = \eta^{Born}$. The iteration of Eq. (5.10) is terminated at $k^* + 1$ using a standard MBPT(2) convergence criterion seen in Algorithm 10. To better understand the termination scheme

²¹ $\eta^{Carinae}$ is potentially expensive since it is designed to yield convergent IMSRG results within one flow step.

for the Carinae generator, notice we obtain $\eta^{Carinae} = \eta^{\{k^*+1\}}$ by solving

$$\begin{aligned}
-H_{abij} &= \left[\underbrace{\eta^{\{k^*+1\}}}_{\eta^{\{k^*\}} + \delta\eta}, H^{RG}(\eta^{\{k^*\}}) \right]_{abij} \\
&- \left(\underbrace{H + [\eta^{\{k^*\}}, H^{RG}(\eta^{\{k^*\}})]}_{H^{Unitary}(\eta^{\{k^*\}})} \right)_{abij} = [\delta\eta, H^{RG}(\eta^{\{k^*\}})]_{abij} .
\end{aligned} \tag{5.35}$$

$$\begin{aligned}
H^{Unitary}(\eta^{\{k^*\}}) &= H + \left[\eta^{\{k^*\}}, \sum_{m=0}^{\infty} \frac{[\eta^{\{k^*\}}, H]^{(m)}}{(m+1)!} \right] \\
&= \sum_{m=0}^{\infty} \frac{1}{m!} [\eta^{\{k^*\}}, H]^{(m)} = e^{\eta^{\{k^*\}}} H e^{-\eta^{\{k^*\}}} .
\end{aligned} \tag{5.36}$$

Therefore, $H^{Unitary}(\eta^{\{k^*\}})$ approximates the unitary transformed Hamiltonian from a converged UCC calculation! If $\left| \text{MBPT2TRUNCATION}\left(H^{Unitary}(\eta^{\{k^*\}})\right) \right|$ is sufficiently small, we expect $H^{Unitary}(\eta^{\{k^*+1\}})$ to be sufficiently diagonal.

Of the three novel generators, the Carinae generator is most traditional because it iteratively approximates η with a strict convergence criterion. So long the Carinae generator is convergent, we can expect convergence of the IMSRG with this generator within one flow step. We detail the construction of the Carinae generator in Algorithm 5.

Algorithm 5 Carinae generator

Input: H ▷ Hamiltonian to be diagonalized—this is IMSRG’s $H(s)$
Output: $\eta^{Carinae}$ ▷ Approximation to a UCC diagonalizer of H

```
1: function GENERATOR::CARINAE( $H$ )
2:   initialization
3:      $\eta^{\{0\}} = \eta^{Born} = \text{GENERATOR::BORN}(H)$ 
4:      $\max_k = 100$  ▷ Max UCC iterations
5:      $\epsilon'_{\text{BCH}} = 1\text{e-}4$  ▷ Cutoff for  $H^{RG}$  series from the BCH expansion
6:      $\epsilon_{\text{GMBPT}} = 1\text{e-}3$  ▷ MBPT cutoff in case 1st-order UCC is sufficient
7:      $\epsilon_{\text{MBPT}} = 1\text{e-}6$  ▷ MBPT cutoff for UCC transformed Hamiltonian
8:      $n_{\text{MaxBornOrder}} = 100$  ▷ We want high fidelity inversions for  $\eta^{\{k\}}$ 
9:   end initialization
10:  ▷ MBPT truncation schemes are detailed in Appendix-Section H.1.
11:  if  $\left| \text{MBPT2TRUNCATION}(\eta^{\{0\}}, H) \right| < \epsilon_{\text{GMBPT}}$  then
12:    return  $\eta^{\{0\}}$ 
13:  end if
14:  for  $k \leftarrow 0$  to  $\max_k - 1$  do
15:     $H^{RG} = \sum_{m=0}^{m^*} \frac{[\eta^{\{k\}}, H]^{(m)}}{(m+1)!} : \left\{ \frac{[\eta^{\{k\}}, H]^{(m^*)}}{(m^*+1)!} \right\}_{0\text{-body}} \leq \epsilon'_{\text{BCH}}$ 
16:     $H^{Unitary} = H + [\eta^{\{k\}}, H^{RG}]$ 
17:     $\eta^{\{k+1\}} = \text{GENERATOR::BORNSERIES}(\eta^{\{k\}}, H, H^{RG}, n_{\text{MaxBornOrder}})$ 
18:     $\eta^{Carinae} = \eta^{\{k+1\}}$ 
19:    if  $\left| \text{MBPT2TRUNCATION}(H^{Unitary}) \right| < \epsilon_{\text{MBPT}}$  then
20:      break
21:    end if
22:  end for
23:  return  $\eta^{Carinae}$ 
24: end function
```

5.12 Results

The success of the Born, UCC-Born, and Carinae generators is measured by their speedup of the IMSRG relative to the existing White generator while maintaining small discrepan-

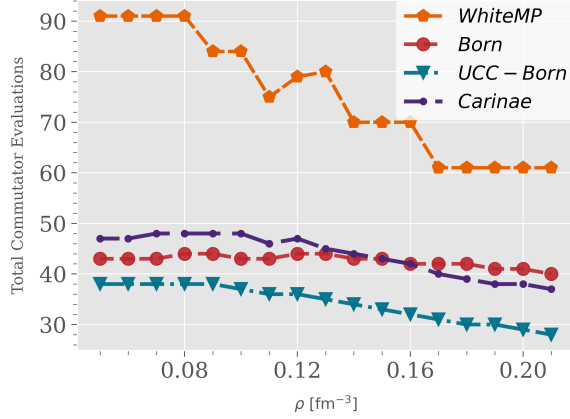
cies in final predicted IMSRG energies. The evaluation of commutators with $\mathcal{O}(N_{\text{orbitals}}^6)$ time complexity (in the realistic limit) in both the BCH and Magnus expansions comprises the most computationally expensive operation of the Magnus-IMSRG in an ideal computer program. In addition, White’s generator has time complexity $\mathcal{O}(N_{\text{orbitals}}^4)$ in the realistic limit. Therefore, the cost of constructing White’s generator is computationally cheap compared to the rest of the IMSRG. Additionally, the computational cost of constructing White’s generator is cheap compared to that of the construction of all three UCC-inspired generators—which require the same $\mathcal{O}(N_{\text{orbitals}}^6)$ commutators evaluations as the IMSRG. Therefore, computational speedup with all novel generators can only be achieved by reducing the total number of $\mathcal{O}(N_{\text{orbitals}}^6)$ commutator evaluations throughout the lifetime of the IMSRG program, while incurring little additional overhead.

We evaluate the success of this work by comparing Magnus-IMSRG calculations using UCC-inspired generators versus the current standard in closed shell systems—White’s generator. IMSRG calculations are performed in infinite nuclear matter over a range of particle numbers $A = N + Z$ and densities ρ . All calculations are done within the normal-ordered 2NF IMSRG(2) scheme using the same Magnus-IMSRG parameters: $\epsilon_{\text{BCH}} = 1\text{e-}4$, $\epsilon_{\text{Magnus}} = 1\text{e-}4$, $\epsilon_{\text{MBPT}} = 1\text{e-}6$, and step-size $ds = 1$. Results are obtained using high-performance compute resources provided by the Institute for Cyber-Enabled Research at Michigan State University. We measure the runtime of IMSRG calculations using all generators—since that is a key quantity of interest in this work. To its detriment, runtime data has intrinsic variability dependent on the machine performing the IMSRG calculation. Therefore, we also measure the total number of commutator evaluations throughout the lifetime of each IMSRG program to explain trends in runtime data. We measure differences in converged IMSRG ground state energies using the UCC-inspired generators versus White’s

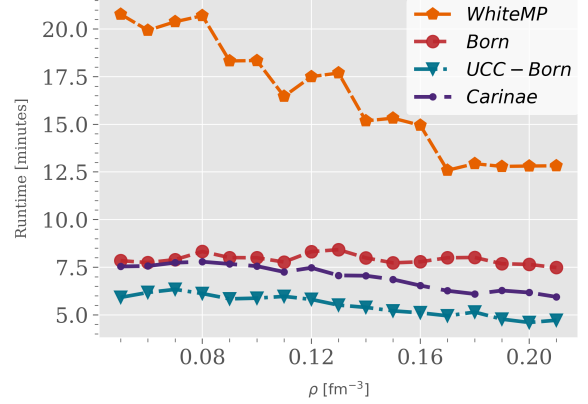
generator to establish the extent of agreement in energies between all generators. Lastly, we measure the convergence profile of IMSRG calculations to establish the extent of convergence acceleration conferred by the novel generators.

Figures 5.1–5.7 show that using all novel generators, we often observe a reduction in the total number of commutator evaluations in the IMSRG compared to using White’s generator. This commutator reduction translates to observed computational speedups of the IMSRG in various nuclear matter systems. We sometimes observe speedups of 2–4X in some systems—notably seen in Figures 5.1, 5.5, and 5.6. Figures 5.1–5.7 show that IMSRG speedup is attained using the UCC-inspired generators by reducing the total number of commutator evaluations in the IMSRG. The UCC-inspired generators reduce commutator evaluations by accelerating the convergence of the IMSRG—thereby reducing the number of IMSRG iterations needed for convergence. Notably, the UCC-Born generator often yields the best speedup of the IMSRG, as seen in Figure 5.1.

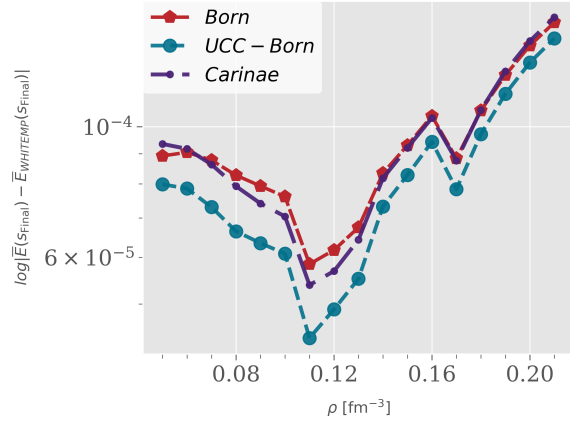
Moreover, we see little discrepancies in converged energies per particle $\bar{E}(s_{final}) \equiv E(s_{final})/A$ between IMSRG calculations using all UCC-inspired generators versus White’s generator. We at most observe a $\sim 1\text{e-}2$ MeV discrepancy in $\bar{E}(s_{final})$ within $N = Z = 14$ symmetric nuclear matter at $\rho = 0.1 \text{ fm}^{-3}$ (see Figure 5.6). Curiously, we see the greatest IMSRG speedups of $\sim 3\text{X} - 4\text{X}$ using the UCC-inspired generators in this system. Lastly, we generally observe that the IMSRG converges using the novel generators, so long $\gamma < 0.8$. We suspect that this criterion is related to the convergence criteria of the Magnus expansion. Given these results, we conclude the Born, UCC-Born, and Carinae generators improve the quality of the IMSRG integration by accelerating the convergence of the IMSRG, while introducing little deviations in the converged IMSRG energy.



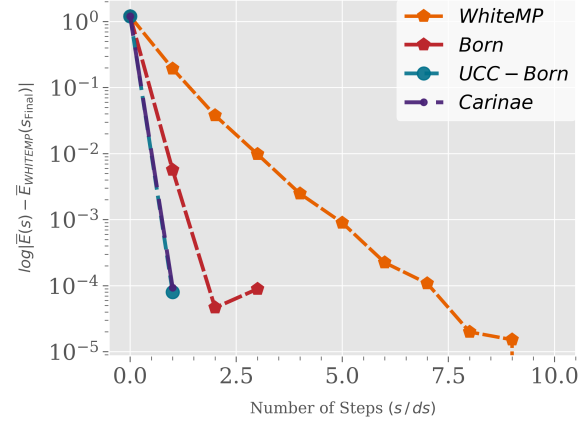
(a) Total number of commutator evaluations throughout the lifetime of IMSRG programs varying particle density, and using all generators.



(b) IMSRG runtimes varying particle density, and using all generators.

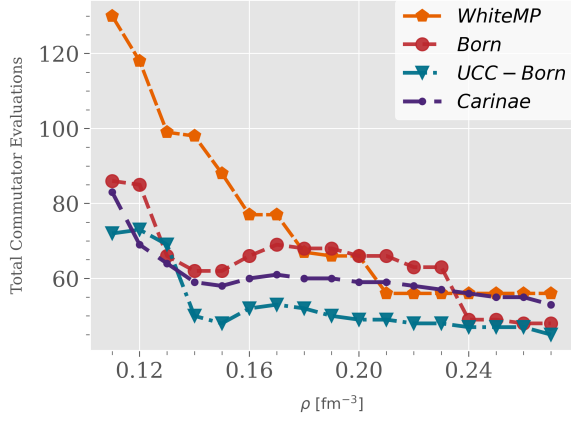


(c) Differences in $\bar{E}(s_{final})$ using all novel generators relative to White's generator.

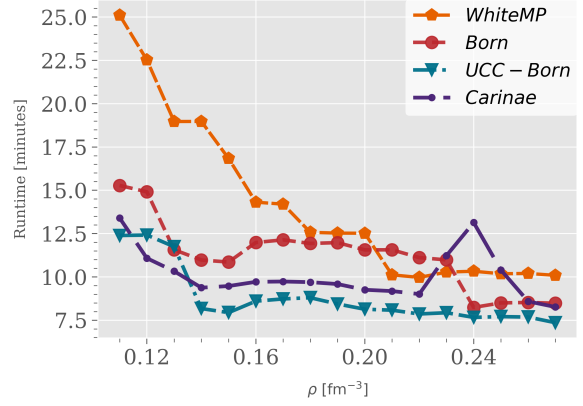


(d) Convergence profile of $\bar{E}(s)$ using all generators at $\rho = 0.05 \text{ fm}^{-3}$.

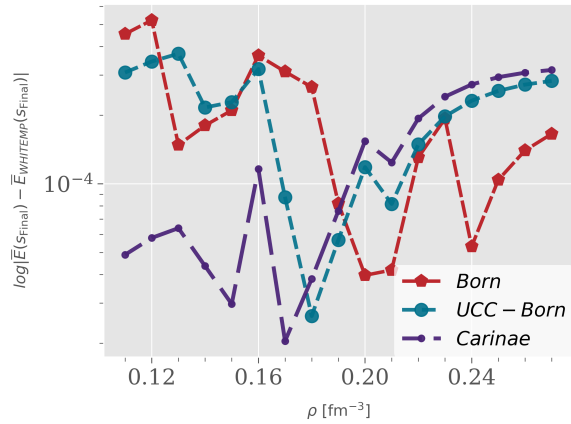
Figure 5.1: Comparison of Magnus-IMSRG nuclear matter calculations with the NNLO_{opt} interaction, $N = 66$, $Z = 0$, and $N_{\text{orbitals}} = 1478$ using UCC-inspired generators and White's generator.



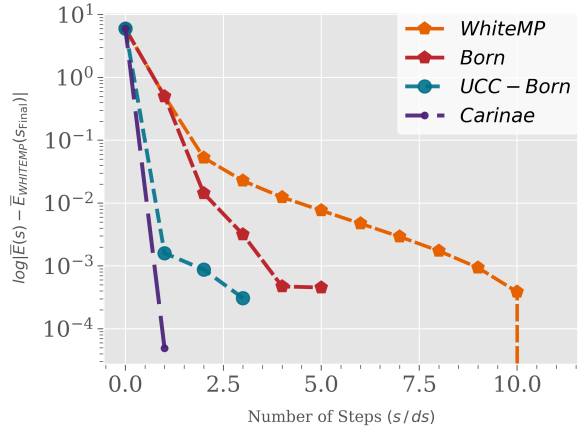
(a) Total number of commutator evaluations throughout the lifetime of IMSRG programs varying particle density, and using all generators.



(b) IMSRG runtimes varying particle density, and using all generators.

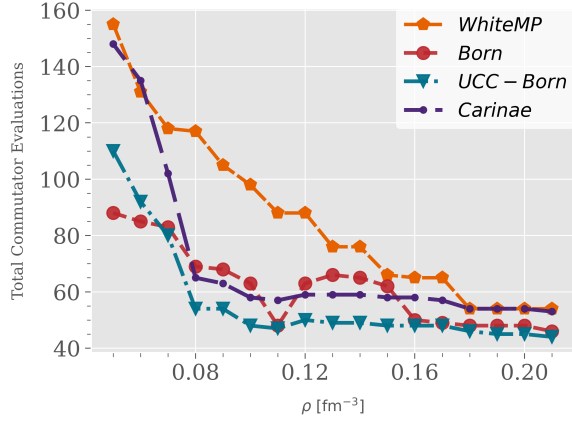


(c) Differences in $\bar{E}(s_{final})$ using all novel generators relative to White's generator.

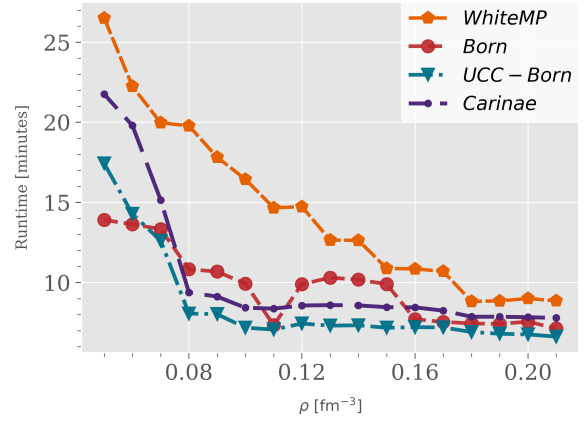


(d) Convergence profile of $\bar{E}(s)$ using all generators at $\rho = 0.11 \text{ fm}^{-3}$.

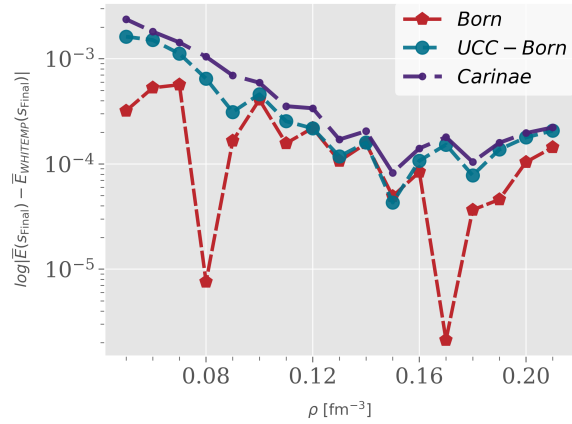
Figure 5.2: Comparison of Magnus-IMSRG nuclear matter calculations with the NNLO_{opt} interaction, $N = Z = 66$, and $N_{\text{orbitals}} = 1460$ using UCC-inspired generators and White's generator. Calculations with $\rho < 0.11 \text{ fm}^{-3}$ are not included due to the divergence of the Magnus-IMSRG regardless of generator choice.



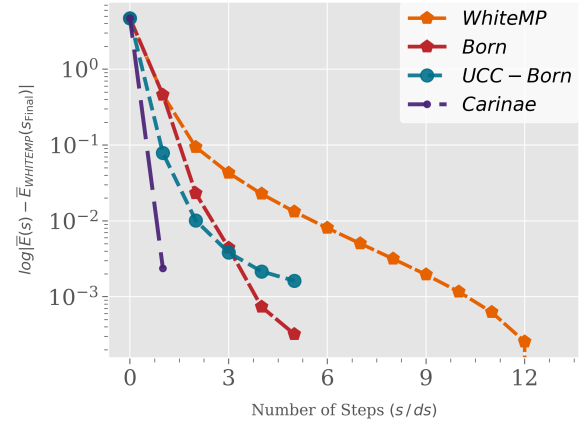
(a) Total number of commutator evaluations throughout the lifetime of IMSRG programs varying particle density, and using all generators.



(b) IMSRG runtimes varying particle density, and using all generators.

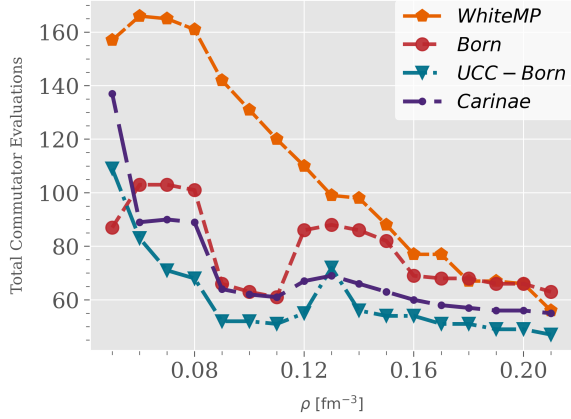


(c) Differences in $\bar{E}(s_{final})$ using all novel generators relative to White's generator.

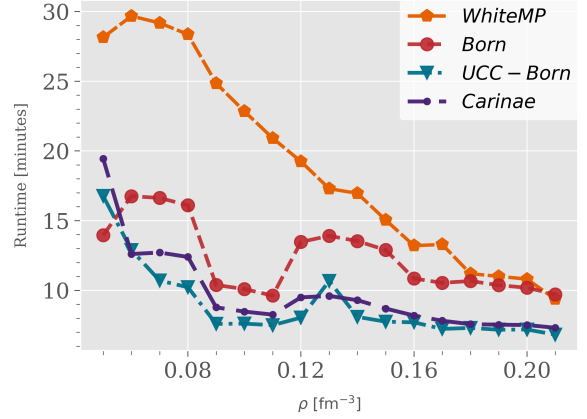


(d) Convergence profile of $\bar{E}(s)$ using all generators at $\rho = 0.05 \text{ fm}^{-3}$.

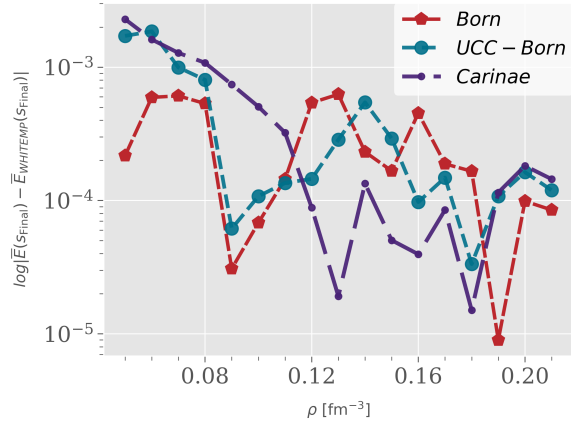
Figure 5.3: Comparison of Magnus-IMSRG nuclear matter calculations with the NNLO_{opt} interaction, $N = 66$, $Z = 54$, and $N_{\text{orbitals}} = 1460$ using UCC-inspired generators and White's generator.



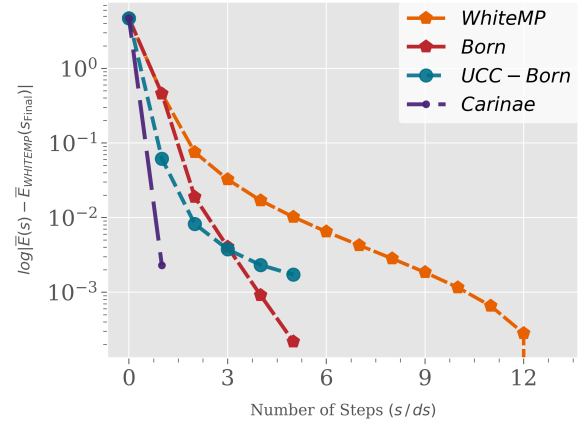
(a) Total number of commutator evaluations throughout the lifetime of IMSRG programs varying particle density, and using all generators.



(b) IMSRG runtimes varying particle density, and using all generators.

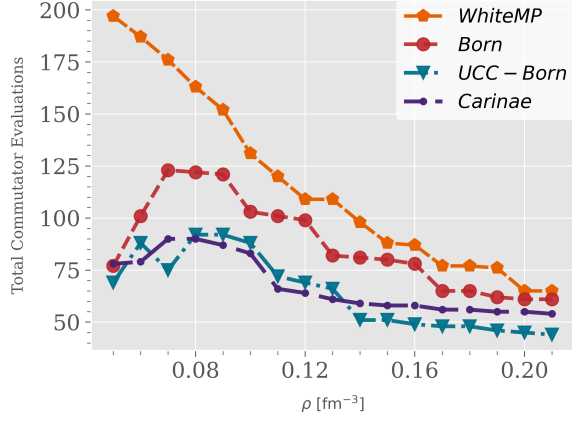


(c) Differences in $\bar{E}(s_{final})$ using all novel generators relative to White's generator.

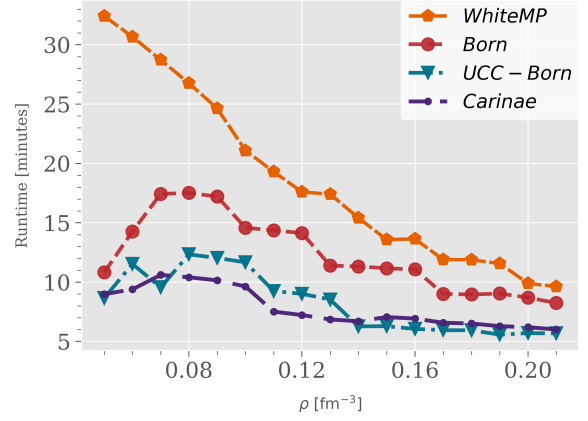


(d) Convergence profile of $\bar{E}(s)$ using all generators at $\rho = 0.05 \text{ fm}^{-3}$.

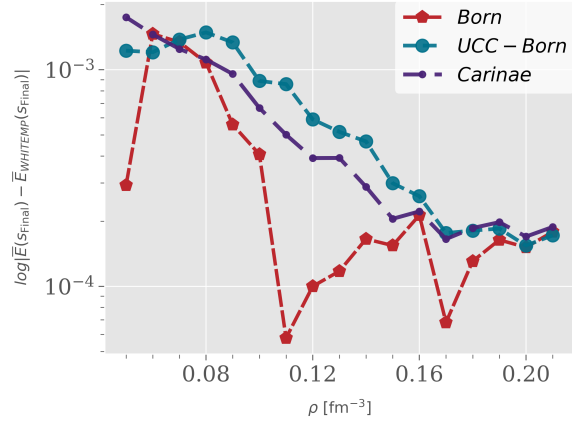
Figure 5.4: Comparison of Magnus-IMSRG nuclear matter calculations with the NNLO_{opt} interaction, $N = 66$, $Z = 38$, and $N_{\text{orbitals}} = 1460$ using UCC-inspired generators and White's generator.



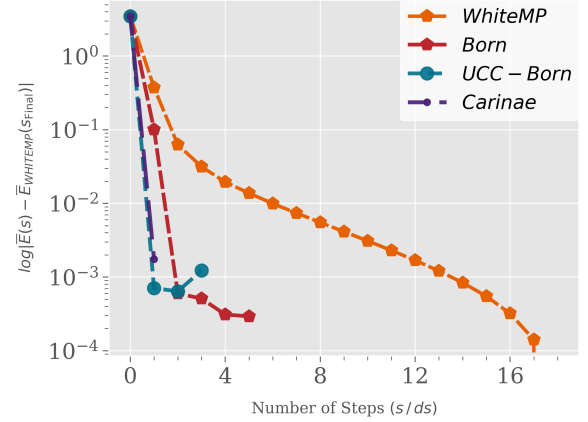
(a) Total number of commutator evaluations throughout the lifetime of IMSRG programs varying particle density, and using all generators.



(b) IMSRG runtimes varying particle density, and using all generators.

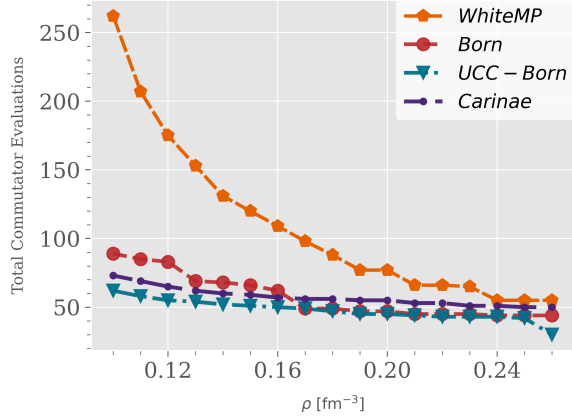


(c) Differences in $\bar{E}(s_{final})$ using all novel generators relative to White's generator.

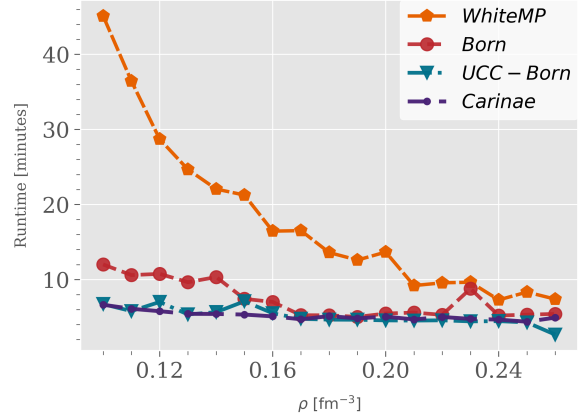


(d) Convergence profile of $\bar{E}(s)$ using all generators at $\rho = 0.05 \text{ fm}^{-3}$.

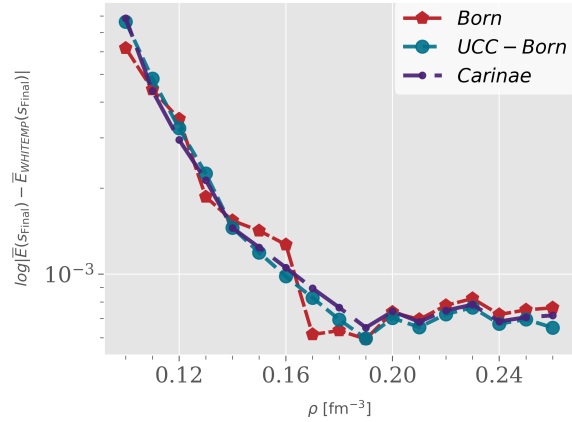
Figure 5.5: Comparison of Magnus-IMSRG nuclear matter calculations with the NNLO_{opt} interaction, $N = 66$, $Z = 14$, and $N_{\text{orbitals}} = 1460$ using UCC-inspired generators and White's generator.



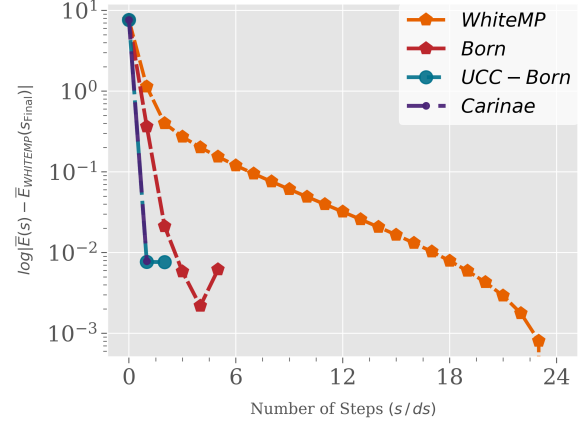
(a) Total number of commutator evaluations throughout the lifetime of IMSRG programs varying particle density, and using all generators.



(b) IMSRG runtimes varying particle density, and using all generators.

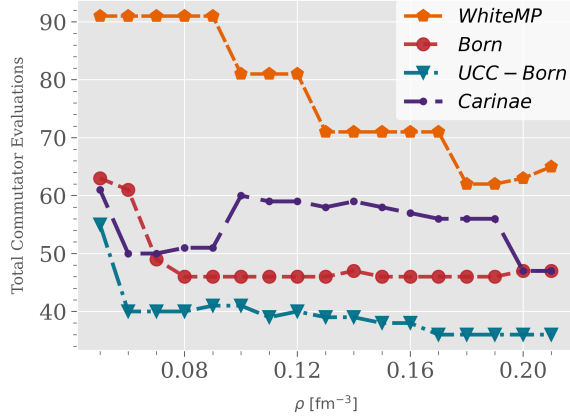


(c) Differences in $\bar{E}(s_{final})$ using all novel generators relative to White's generator.

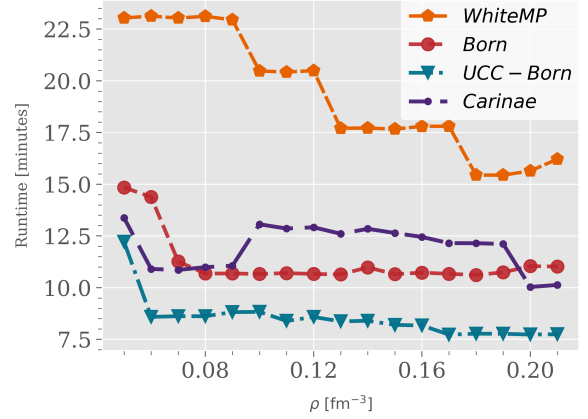


(d) Convergence profile of $\bar{E}(s)$ using all generators at $\rho = 0.1 \text{ fm}^{-3}$.

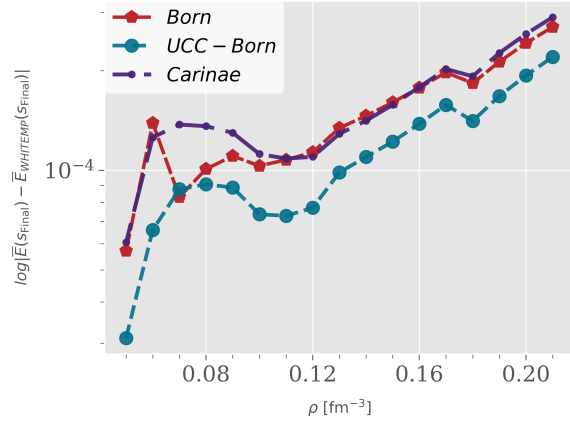
Figure 5.6: Money-plot comparison of Magnus-IMSRG nuclear matter calculations with the NNLO_{opt} interaction, $N = 14$, $Z = 14$, and $N_{\text{orbitals}} = 1556$ using UCC-inspired generators and White's generator.



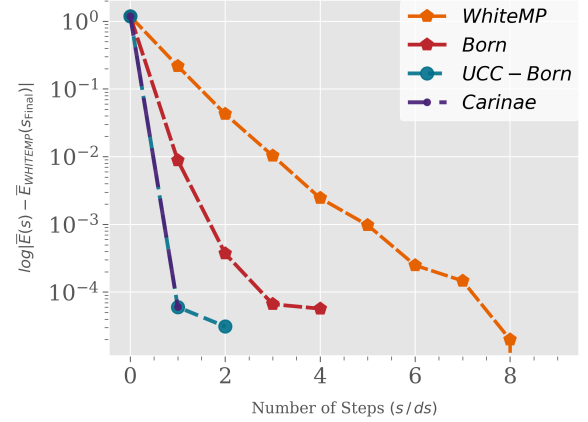
(a) Total number of commutator evaluations throughout the lifetime of IMSRG programs varying particle density, and using all generators.



(b) IMSRG runtimes varying particle density, and using all generators.



(c) Differences in $\bar{E}(s_{final})$ using all novel generators relative to White's generator.



(d) Convergence profile of $\bar{E}(s)$ using all generators at $\rho = 0.05 \text{ fm}^{-3}$.

Figure 5.7: Comparison of Magnus-IMSRG nuclear matter calculations with the NNLO_{opt} interaction, $N = 114$, $Z = 0$, and $N_{\text{orbitals}} = 1502$ using UCC-inspired generators and White's generator.

5.13 A Few Remarks

Observed IMSRG speedup with all novel generators is strongly system dependent. We suspect this system dependence is rooted at the regulation and convergence of the Born series. More work is currently needed to understand this. The regulation of the Born series in Algorithm 1 is rather crude. While solving linearized UCC, we could perhaps use a more sophisticated regulator by replacing Eq. (5.10) with $-H_{abij} \times e^{-(\|\Gamma_*\|/\Lambda_{\text{UCC}})^\alpha} = \left[\eta^{\{k+1\}}, H^{RG}(\eta^{\{k\}}) \right]_{abij}$ —solved by an *unregulated* Born series. $\alpha \geq 0$ can be viewed as a measure of how well $H^{RG}(\eta^{\{k\}})$ approximates $H^{RG}(\eta)$. If $H^{RG}(\eta^{\{k\}}) = H^{RG}(\eta)$, we can likely choose $\alpha = 0$ without issue. Lastly, although three-body forces are not considered in this chapter, we find that the UCC-inspired generators are still effective when using the IMSRG(2) + normal-ordered 3NF scheme detailed in Chapter 2.

5.14 Summary

Viewing IMSRG generators as diagonalizers of IMSRG flowing Hamiltonians $H(s)$, we looked towards UCC to efficiently construct approximate diagonalizers of $H(s)$. We therefore introduced physics-motivated techniques to accelerate our UCC calculations. With inspiration from Kutzelnigg [38], we introduced the Born expansion as a tool to invert commutators in UCC—so long a renormalized Hamiltonian $H^{RG}(\eta)$ is approximated. And we posed an ansatz for $H^{RG}(\eta)$ utilizing gradient descent in Appendix I. With inspiration from White [36], we regulated the Born series to improve the convergence of η dependent transformations in UCC and IMSRG. Lastly, we preconditioned the Born expansion to accelerate its rate of convergence when solving high-order UCC.

Utilizing these developments, we subsequently introduced three UCC-inspired IMSRG generators—Born, UCC-Born, and Carinae. Approximately solving 1st-order UCC, Born’s generator is an extension to the existing White’s generator. The UCC-Born generator, designed to be a cheap high-order UCC solver, uses Born’s generator in conjunction with the aforementioned $H^{RG}(\eta)$ ansatz to approximate high-order UCC solutions. The Carinae generator conventionally iterates linearized UCC until a strict convergence criterion is met. Using these UCC-inspired generators, we often see noticeable speedups in the IMSRG with little differences in converged energies—sometimes amounting to 2–4X in nuclear matter systems.

5.15 Perspectives

Looking forward, we expect the Born, UCC-Born, and Carinae generators to be beneficial in existing IMSRG(2) implementations—so long Section 5.2’s assumptions are met, if not weakly broken. Although, not rigorously tested, we observed noticeable speedups in our calculations for the UCC-Born and Carinae generators by using preconditioners in the Born series. Therefore, we suspect that the use of preconditioned and regulated Born series may confer computational speedup in existing UCC implementations—so long Section 5.2’s assumptions are met, if not weakly broken.

Future work is needed to construct better regulation schemes of the Born series. Moreover, all calculations in this chapter were restricted to the two-body level. Going forward, it may be lucrative to extend the Born series to invert commutators acting on three-body operators. Perhaps, one could solve the commutator inversion at the two-body level (as is described in this work), then use that solution to better obtain the three-body commutator

inverter. Excitingly, we wonder if the Born series could be used to implement approximate triples in the IMSRG. In the following chapter, we apply known data driven methods to accelerate the IMSRG by extrapolating converged IMSRG energies.

Chapter 6. IMSRG Post-Processors

*“If you don’t know
something, pretend you do.
Then ask, what would be
consequent to you knowing
that? Sometimes guessing is
enough!”*

—Hoon Hong

Moving along the IMSRG flow in s , we calculate and store approximations to the converged IMSRG energy. We store these energies in

$$C = \left\{ E(0) + \Delta E^{(2)}(0), E(ds) + \Delta E^{(2)}(ds), \dots, E(s) + \Delta E^{(2)}(s) \right\}.$$

The number of elements in C is denoted by $N_{\text{samples}} = 1 + s/ds$. We include MBPT(2) corrections on the IMSRG energies to obtain better approximations to the converged IMSRG energy. And the converged IMSRG energy is given by $E(\infty) + \Delta E^{(2)}(\infty)$.¹

We introduce the use of the Shanks and Padé methods in the IMSRG, which use elements of C to extrapolate the converged IMSRG energy. As described in this work, these methods are post-processors which sit on top of the IMSRG to extrapolate the final IMSRG energy.

¹As seen in Figure 2.2, $\Delta E^{(2)}(\infty)$ is actually zero.

6.1 Shanks Transformation

We store the last three energies of C in²

$$\tilde{C} = \left\{ C_{N_{\text{samples}}-3}, C_{N_{\text{samples}}-2}, C_{N_{\text{samples}}-1} \right\}. \quad (6.1)$$

\tilde{C} holds our best three approximations to the final IMSRG energy as we move along the flow. The 1st-order Shanks transformation on C is given by [42]

$$S(C) \equiv \tilde{C}_2 - \frac{(\tilde{C}_2 - \tilde{C}_1)^2}{\tilde{C}_2 - 2\tilde{C}_1 + \tilde{C}_0}, \quad (6.2)$$

and is taken as the extrapolated final IMSRG energy $E(\infty) + \Delta E^{(2)}(\infty)$. A minimum of three samples are needed for the 1st-order Shanks transform. If $N_{\text{samples}} < 3$, no extrapolation is made and $S(C)$ is programmed to return $C_{N_{\text{samples}}-1}$. The Shanks transform is derived by assuming that the elements of \tilde{C} are exponentially related [42, 43]. By using the Shanks transform in the IMSRG, we assume that IMSRG energies converge exponentially.

6.2 Padé Approximant

We store energy differences of C along the flow in

$$\delta = \left\{ \frac{C_0}{g^0}, \frac{C_1 - C_0}{g^1}, \frac{C_2 - C_1}{g^2}, \dots, \frac{C_{N_{\text{samples}}-1} - C_{N_{\text{samples}}-2}}{g^{N_{\text{samples}}-1}} \right\},$$

²We index all arrays starting from 0.

where g is some dimensionless parameter—for power counting. Notice, $C_{N_{\text{samples}}-1} = \sum_{n=0}^{N_{\text{samples}}-1} \delta_n g^n$. Defining $M \equiv \left\lfloor \frac{N_{\text{samples}}}{2} \right\rfloor$ and $L \equiv N_{\text{samples}} - M - 1$, the polynomial coefficients a_n and b_m of the Padé approximant are obtained by solving³

$$\sum_{n=0}^L a_n g^n = \left(1 + \sum_{m=1}^M b_m g^m\right) \times \sum_{n=0}^{N_{\text{samples}}-1} \delta_n g^n, \quad (6.3)$$

and discarding any induced terms with degrees greater than L in Eq. (6.3)’s RHS [44]. And the extrapolated final IMSRG energy is then given by

$$P(C) \equiv \frac{\sum_{n=0}^L a_n g^n}{1 + \sum_{m=1}^M b_m g^m}, \quad (6.4)$$

with $g = 1$. A minimum of 2 samples are needed to use the Padé approximant. Whenever $N_{\text{samples}} < 2$, no extrapolation is made and $P(C)$ is programmed to return $C_{N_{\text{samples}}-1}$.

6.3 Results

We perform multiple Magnus-IMSRG calculations testing the efficacy of the Shanks and Padé extrapolators. All calculations are made with step-size $ds = 1$ using White’s generator with Epstein–Nesbet energy denominators.⁴ The IMSRG outputs for these results are included in the SCKY-IMSRG repository; and the resulting figures are plotted by our automated data managers. At each step of the flow, we have three methods which give approximations to the converged IMSRG energy: $C_{N_{\text{samples}}-1}$, $S(C)$, and $P(C)$. We measure differences

³The polynomial coefficients a_n and b_m , are implicit functions of C .

⁴Unless otherwise stated, we employ a generalized form of MBPT(2) seen in Algorithm 6. Our MBPT expressions are consequently, generator dependent. Using White’s generator with Epstein–Nesbet denominators, we suspect that MBPT results in this chapter are with the Epstein–Nesbet partitioning.

of $C_{N_{\text{samples}}-1}$ relative to $E(\infty) + \Delta E^{(2)}(\infty)$ to establish the baseline convergence of the IMSRG with MBPT(2) contributions. We also measure differences of $S(C)$, and $P(C)$ relative to $E(\infty) + \Delta E^{(2)}(\infty)$ to measure the extrapolators' efficacy.

In Figures 6.1, 6.2, and 6.3, we see that both the Shanks and Padé methods can extrapolate $E(\infty) + \Delta E^{(2)}(\infty)$ with impressive accuracy. Notably, we sometimes observe 1-2 orders of magnitude improvement over $C_{N_{\text{samples}}-1}$, using the extrapolators. And both extrapolators tend to track each other quite well. Unfortunately, both methods have numerical instabilities, notably seen in Figures 6.3 and 6.4. These instabilities are suspected to occur when these methods become ill-conditioned—diminishing their reliability.

The accuracy of the Shanks and Padé extrapolators is generally highest halfway through the flow. Terminating the IMSRG flow when extrapolation accuracies are sufficiently high, and quoting the extrapolated energies, we could obtain $\sim 2X$ IMSRG speedup. However, it is unclear *a priori* when the IMSRG is halfway through the flow, let alone when the Shanks and Padé extrapolation accuracy is high. Alternatively, we could terminate the IMSRG when the Shanks and Padé extrapolations are converged. This would yield a more reliable extrapolated energy. But, we would obtain less than $2X$ IMSRG speedup, since both extrapolators tend to converge much later in the flow.

The extrapolators can yield poor results, particularly seen in IMSRG calculations with the hard Entem-Machleidt-Nosyk potential [28] (see Figure 6.5). Notably, the IMSRG's convergence behaviour is not smooth for the Entem-Machleidt-Nosyk potential with $ds = 1$, compared to the softer N2LO_{opt} potential [25]. Perhaps, the lack of smoothness of $C_{N_{\text{samples}}-1}$ is the source of failure for the Shanks and Padé extrapolators. This hypothesis is consistent with preliminary explorations—which saw that the Shanks and Padé extrapolators work best when taking small IMSRG step-sizes.

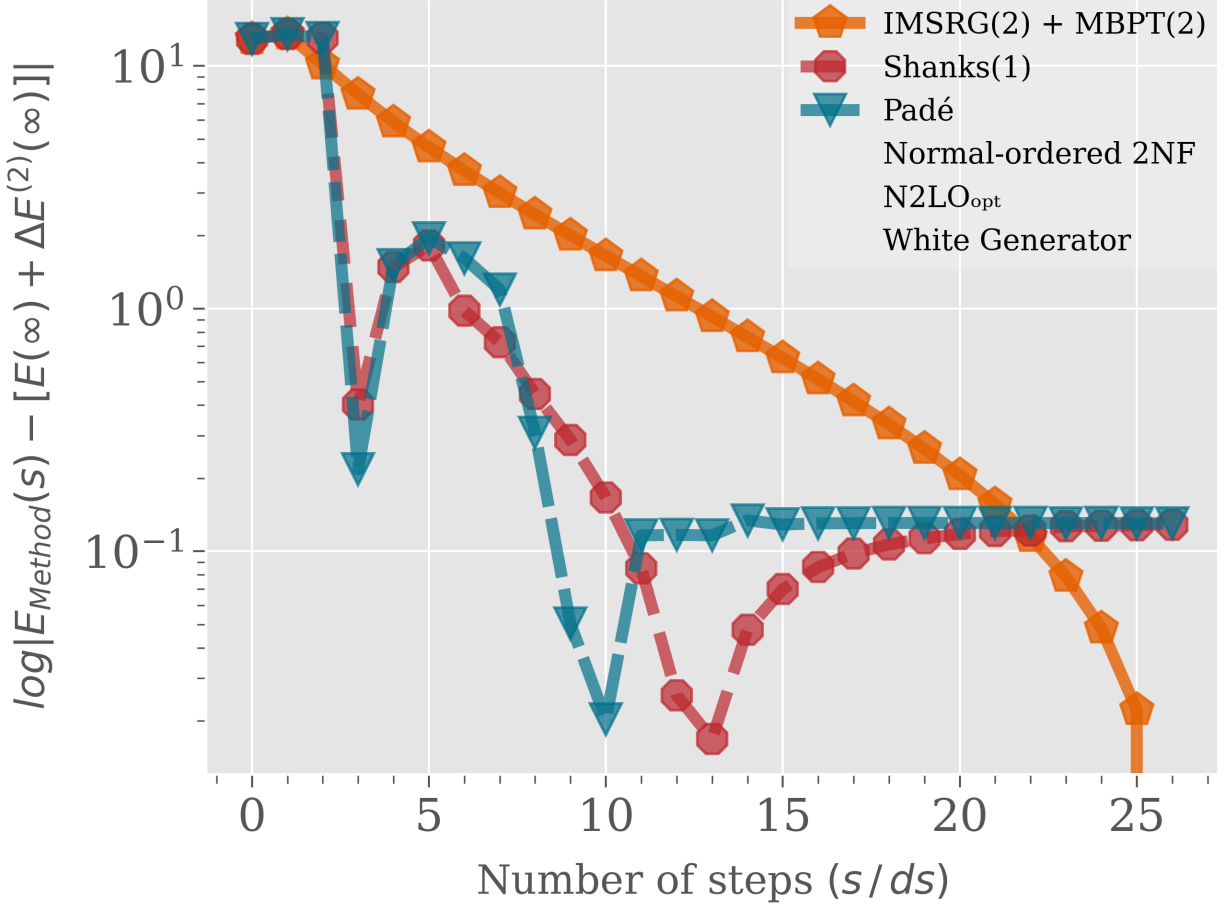


Figure 6.1: Magnus-IMSRG’s convergence profile using the 1st-order Shanks and Padé extrapolators with $N = Z = 14$, $\rho = 0.11 \text{ fm}^{-3}$, and $N_{\text{orbitals}} = 228$. The Magnus-IMSRG is slowly convergent in this system—and is divergent with $\rho = 0.1 \text{ fm}^{-3}$. The sharp turning points in the Padé and Shanks curves at $s/ds = 10$ and $s/ds = 13$ respectively, are due to the extrapolators predicting converged energies that narrowly cross $E(26) + \Delta E^{(2)}(26)$ from above. At these turning points, we see 2 orders of magnitude improvement over the IMSRG with MBPT(2). And terminating the IMSRG at these turning points would confer 2 – 2.6X speedup, with little loss in accuracy.

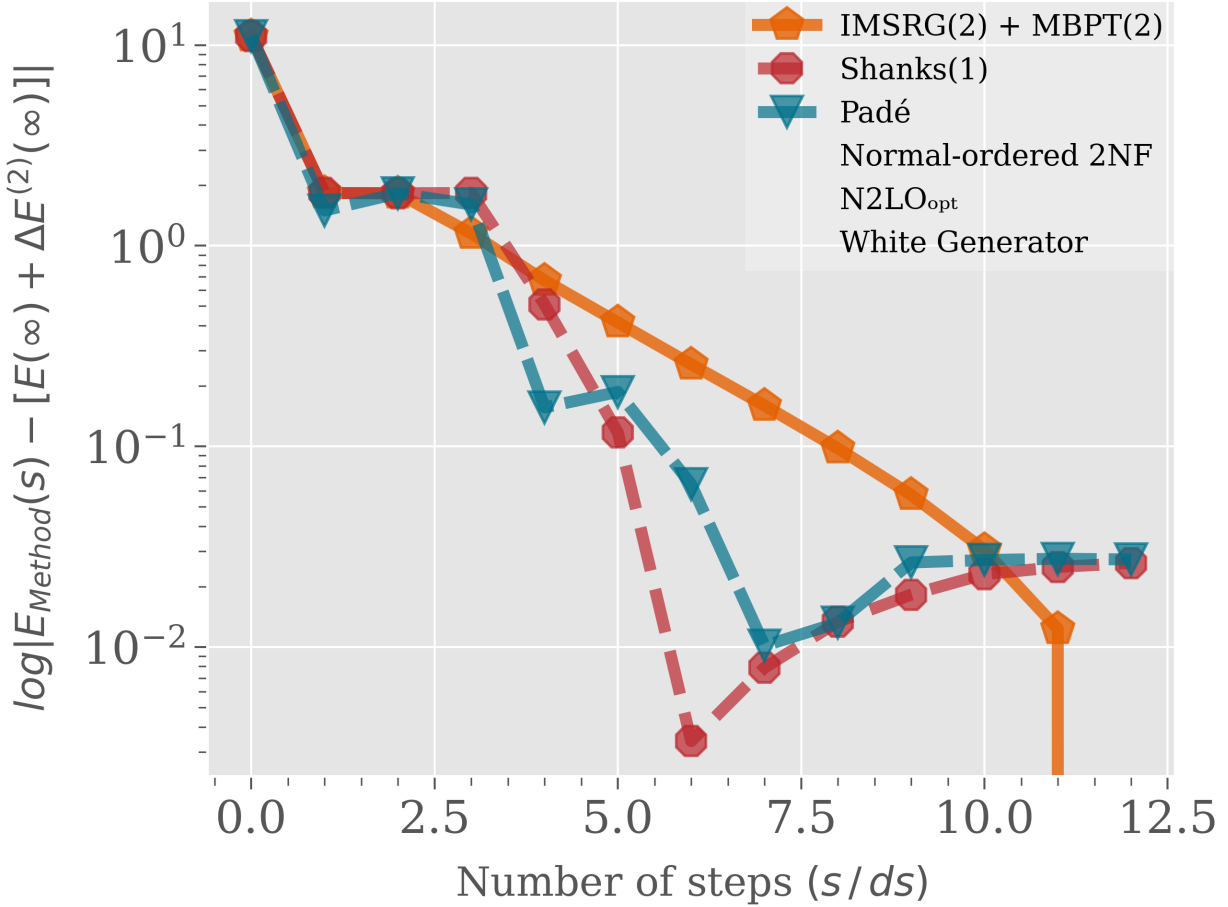


Figure 6.2: Magnus-IMSRG’s convergence profile using the 1st-order Shanks and Padé extrapolators with $N = Z = 14$, $\rho = 0.14 \text{ fm}^{-3}$, and $N_{\text{orbitals}} = 324$. The turning points in the Shanks and Padé curves at $s/ds = 6$ and $s/ds = 7$ respectively, are due to the extrapolators predicting converged energies that narrowly cross $E(12) + \Delta E^{(2)}(12)$ from above. At these turning points, we see at least 1 order of magnitude improvement over the IMSRG with MBPT(2). And terminating the IMSRG at these turning points would confer 1.7 – 2X speedup, with little loss in accuracy.

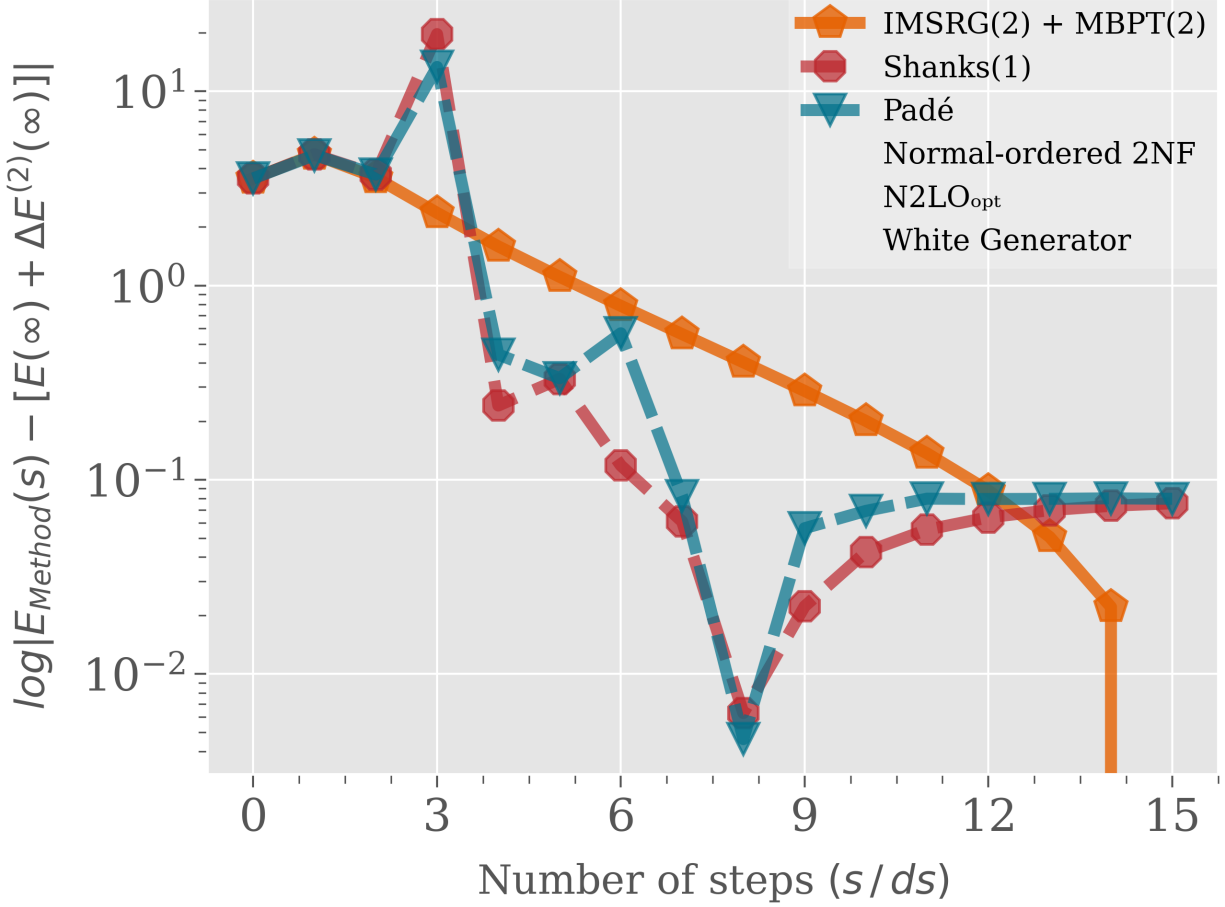


Figure 6.3: Magnus-IMSRG’s convergence profile using the 1st-order Shanks and Padé extrapolators with $N = Z = 66$, $\rho = 0.16 \text{ fm}^{-3}$, and $N_{\text{orbitals}} = 324$. We see numerical instabilities in both extrapolators at $s/ds = 3$ yielding extrapolations that are roughly 1 order of magnitude further away from the converged energy than $E(3) + \Delta E^{(2)}(3)$. The sharp turning points in the Shanks and Padé curves at $s/ds = 8$ are due to the extrapolators predicting converged energies that narrowly cross $E(15) + \Delta E^{(2)}(15)$ from above. At these $s/ds = 8$ turning points, we see nearly 2 orders of magnitude improvement over $E(8) + \Delta E^{(2)}(8)$. And terminating the IMSRG at these turning points would confer 1.9X speedup, with little loss in accuracy.

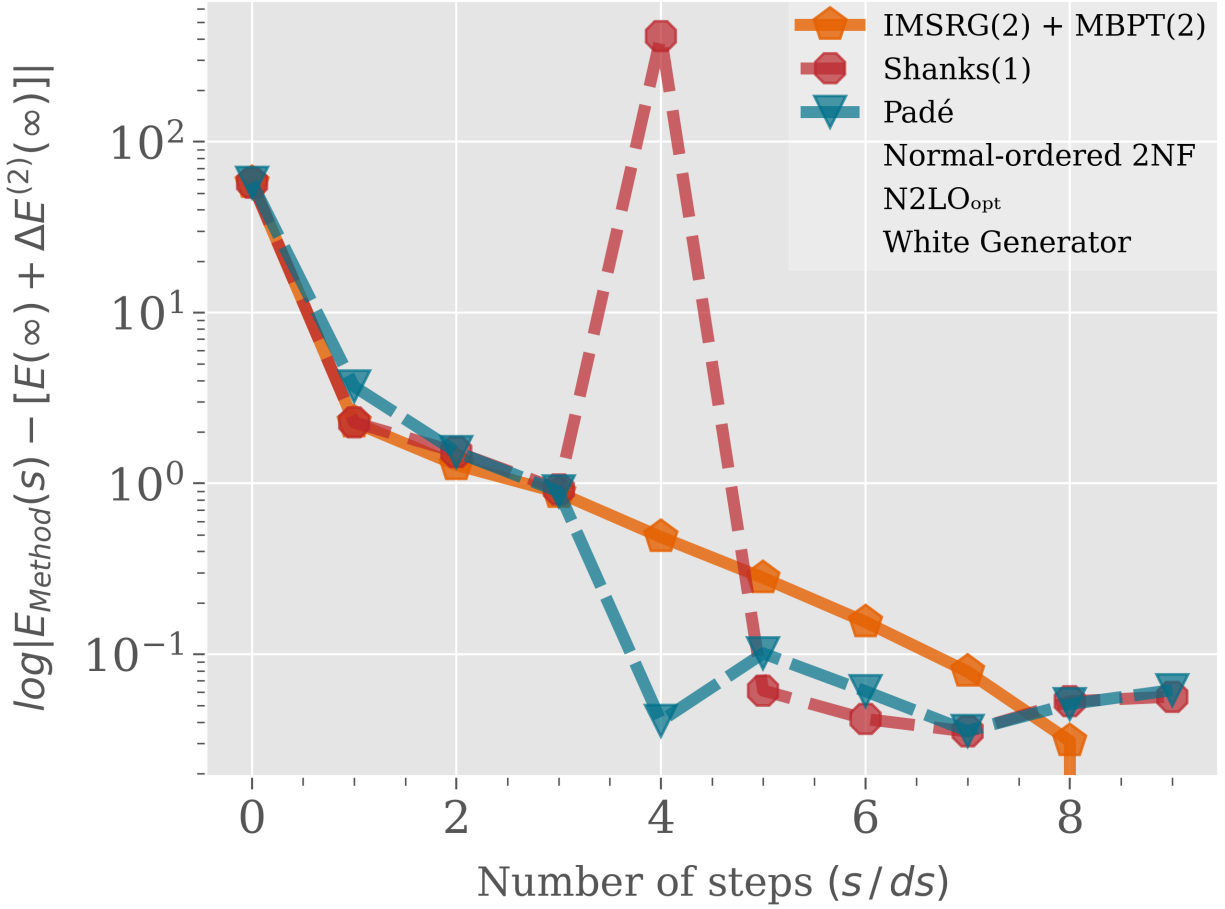


Figure 6.4: Magnus-IMSRG’s convergence profile using the 1st-order Shanks and Padé extrapolators with $N = Z = 66$, $\rho = 0.16 \text{ fm}^{-3}$, and $N_{\text{orbitals}} = 684$. We see a numerical instability in the Shanks extrapolator at $s/ds = 4$ yielding an extrapolation that is 2 orders of magnitude further away from the converged energy than $E(4) + \Delta E^{(2)}(4)$. Both extrapolators generally yield small improvements over the IMSRG with MBPT(2) in this system. However, terminating the IMSRG at $s/ds = 4$, and taking the Padé extrapolated energy would confer 2.2X speedup, with little loss in accuracy.

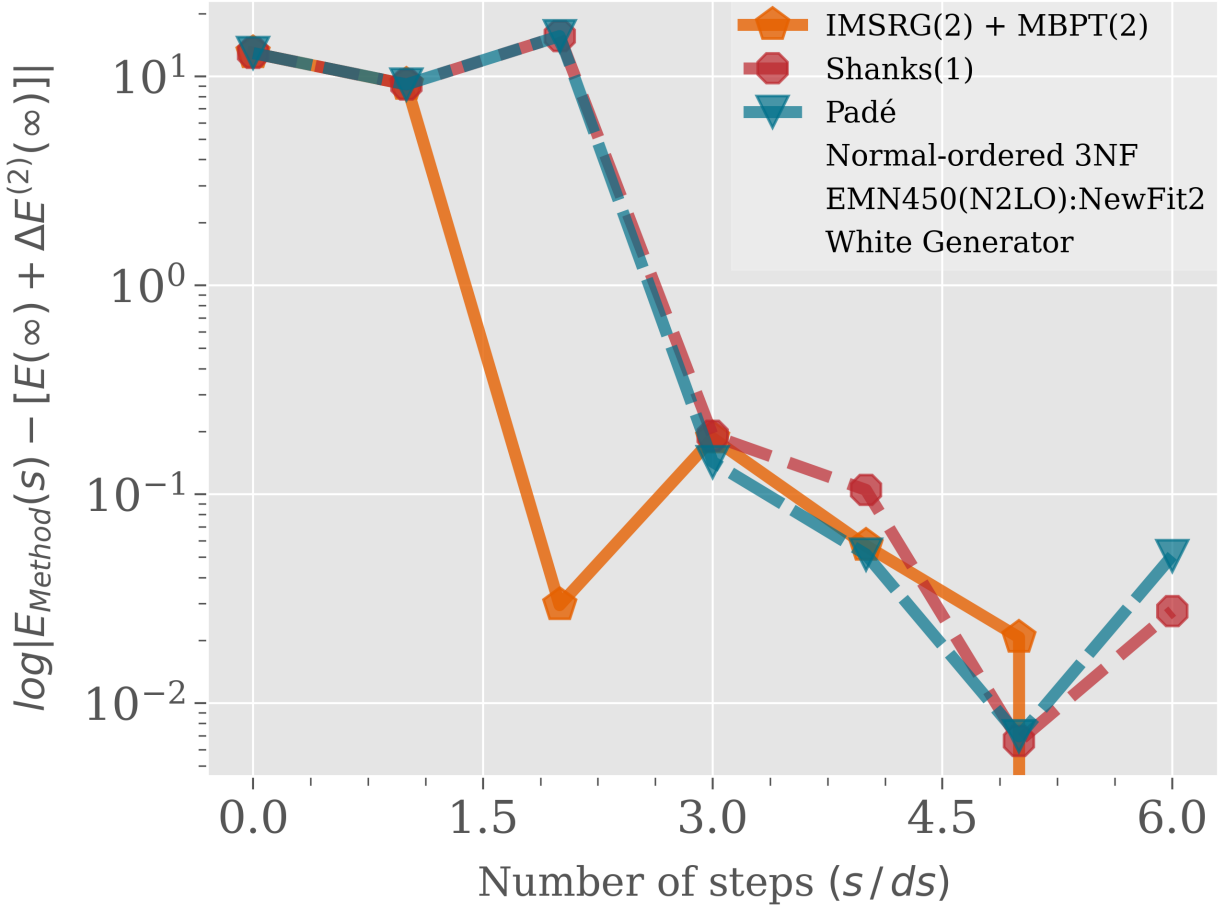


Figure 6.5: Magnus-IMSRG’s convergence profile using the 1st-order Shanks and Padé extrapolators with $N = Z = 66$, $\rho = 0.13 \text{ fm}^{-3}$, and $N_{\text{orbitals}} = 3700$. This result is obtained with the Entem-Machleidt-Nosyk potential at the normal-ordered three-body level [28]. Generalized MBPT is *not* employed in this system, and MBPT is thus implemented with Møller–Plesset partitioning. Both the Shanks and Padé methods are poor extrapolators in this system.

6.4 Discussion

Given the extrapolation power of the Shanks and Padé methods, we view them as noninvasive extrapolators that can obtain converged IMSRG energies when the IMSRG’s convergence behavior is smooth. These extrapolators could be used to invasively accelerate the IMSRG’s convergence by terminating the flow early. However, one would need a better handle on when these methods fail in the IMSRG. Moreover, preliminary explorations suggest that the Shanks and Padé methods can be applied directly on the matrix elements of the Magnus operator $\Omega(s)$ to successfully extrapolate $\Omega(\infty)$.⁵ This would enable the extrapolation of observables beyond energies at the cost of storing multiple temporaries of $\Omega(s)$. A future SCKY-IMSRG implementation of the Shanks and Padé extrapolations on $\Omega(s)$ might be lucrative. Future work is needed to understand when these methods fail in the IMSRG, and when they can be used to terminate the IMSRG early.

6.5 Conclusion and Perspectives

We generally observe that Shanks and Padé transforms can extrapolate converged IMSRG energies with impressive accuracy. When these methods work, they can extrapolate converged IMSRG energies within $1e-2$ MeV accuracy. Terminating the IMSRG flow once when the Shanks and Padé extrapolation accuracies are sufficiently high, and quoting the extrapolated energies, we *could* obtain $\sim 2X$ IMSRG speedup. However, we have yet to devise a scheme to reliably do so. Moreover, these methods are prone to numerical instabilities; and their extrapolation power can markedly vary, depending on the interaction in use.

⁵Care must be taken to avoid extrapolating over matrix elements of $\Omega(s)$ that are purely zeros. This would produce zeros in the denominator of Eq. (6.2).

Thus, more work is needed to understand when these methods fail in the IMSRG.

Currently, these methods are best seen as noninvasive IMSRG extrapolators which guide users to potential converged IMSRG energies. Going forward, one could explore ways to reliably terminate the IMSRG early using the extrapolators. Additionally, preliminary explorations suggest that the Shanks and Padé transforms can also extrapolate on the Magnus operator $\Omega(s)$. One could explore using these methods to invasively accelerate the convergence of the Magnus-IMSRG evolution.

Chapter 7. Closing Remarks

“I got cash”

—Chief Keef, *I got cash*

7.1 Summary

The nuclear matter equation-of-state (NM-EOS) is of great interest to the nuclear and astrophysics community. Recent advances in *ab initio* theory have led to an explosion of nuclear forces from Chiral Effective Field Theory (χ -EFT) that are amenable to many-body methods [1, 4]. Some of such methods include Many-Body Perturbation Theory (MBPT), and nonperturbative approaches: In-Medium Similarity Renormalization Group (IMSRG) and Coupled-Cluster theory (CC). The IMSRG is a powerful diagonalization method that, until now, has not been applied to study NM-EOS with χ -EFT forces. We have now computed various NM-EOS using the IMSRG with the N2LO_{opt}, Hebeler, and the harder N2LO Entem-Machleidt-Nosyk (EMN) interactions [4, 25, 28].¹ To achieve this goal, we developed a state-of-the-art, high-performant nuclear matter IMSRG program with access to a multitude of two-body and density-dependent three-body forces from Drischler *et al.* [1]. And we made comparisons to MBPT and CC results, obtained in collaboration with Christian Drischler and Gaute Hagen, respectively. We qualitatively validated our IMSRG obtained results with CC, by comparing trends in our data to observed trends seen in finite nuclei—within

¹For clarity, we have access to significantly more forces than N2LO_{opt}, Hebeler, and EMN alone. The N2LO_{opt} and Hebeler forces were chosen to obtain the first batch of IMSRG calculated NM-EOS, due to their existing use with MBPT and CC [1, 23]. The N2LO_{opt} and Hebeler forces were chosen to obtain the first batch of IMSRG calculated NM-EOS, due to their existing use with many-body methods [1, 23]. The harder EMN potential was identified as a good candidate to probe for nonperturbative physics in nuclear matter.

the literature. And, we observed the presence of nonperturbative physics when using hard interactions in symmetric nuclear matter (SNM).

Most IMSRG NM-EOS computations were done at scale, and required days to be completed. This is due to the high computational demands of the IMSRG in large systems. Therefore, we developed novel ideas to accelerate IMSRG computations using Unitary Coupled-Cluster (UCC) inspired IMSRG generators. In doing so, we made novel insights into the IMSRG and UCC. Particularly, we realized that approximate solutions of UCC can be used as IMSRG generators. Viewing UCC as a nonlinear commutator inversion problem, we realized that UCC amplitudes at any order of UCC are given by a generalization of the Born series—so long the series converges. And we used preconditioners to accelerate the convergence of the Born series. Moreover, we provided a gradient descent based ansatz for a renormalized Hamiltonian in UCC, seen in Appendix I. Using these developments, we subsequently introduced three IMSRG generators named “Born,” “UCC-Born,” and “Carinae.” Notably, we sometimes observed 2–4X IMSRG speedup when using the novel generators, particularly when the IMSRG was slowly convergent.

We also applied to the IMSRG, known nonlinear methods—i.e. Shanks and Padé transforms—which can remarkably accelerate slowly converging series [42, 44]. We saw that both methods can extrapolate on converged IMSRG energies with impressive $1e-2$ MeV accuracy. However, we also observed numerical instabilities in the methods. And, we were unable to use the extrapolators to reliably terminate the IMSRG early, and obtain noticeable speedup. Consequently, these methods are currently viewed as noninvasive IMSRG extrapolators, which guide users to potential converged IMSRG energies.

7.2 Outlook

Given the few chiral interactions used in this work, we look forward to IMSRG calculated NM-EOS with a wider range of interactions. Such calculations using uncertainty quantification tools from Drischler *et al.* [29], will provide nonperturbative benchmarks to the existing literature [29]. Furthermore, we observed the growing importance of triples excitations in CC, at higher densities of SNM. We suspect that triples may likewise be important in the IMSRG at higher SNM densities—but perhaps to a lesser extent than CC. Thus, we also look forward to incorporating triples excitations into our nuclear matter IMSRG program. Developments from Stroberg *et al.* [22] will likely be needed in this endeavor.

We have developed an IMSRG program that is versatile, and can be used to study a variety of interesting physics using an emerging nonperturbative method in nuclear matter. For example, there are exciting developments on the horizon being made by Kang Yu for IMSRG computed momentum distributions, static structure factors, and pair correlation functions in nuclear matter. A finite temperature extension to our IMSRG program can also be implemented using insights from Smith *et al.* [26]. Such an implementation would produce an interesting nonperturbative benchmark to existing finite temperature MBPT results [1].

We connected two historically separate theories—IMSRG and UCC by using approximate UCC solutions as generators of the IMSRG. We are curious to see the potential performance gains of the UCC-inspired IMSRG generators in other systems beyond nuclear matter. And, we hope that insights from this work lead to further developments of UCC and IMSRG within many-body physics. Moreover, we are interested to see the potential value of the Shanks and Padé IMSRG extrapolators in other systems beyond nuclear matter. Lastly, our nuclear matter IMSRG program can also be extended to finite nuclei via a change of basis.

Optimizations made in the program's commutators enabled novel preliminary $A = 1030$ IMSRG(2) calculations. Such calculations for finite nuclei may shed light on the existence of heavy nuclei beyond the periodic table!

BIBLIOGRAPHY

- [1] C. Drischler, J. Holt, and C. Wellenhofer, “Chiral effective field theory and the high-density nuclear equation of state,” *Annual Review of Nuclear and Particle Science*, vol. 71, p. 403432, Sept. 2021.
- [2] S. Huth, C. Wellenhofer, and A. Schwenk, “New equations of state constrained by nuclear physics, observations, and qcd calculations of high-density nuclear matter,” *Phys. Rev. C*, vol. 103, p. 025803, Feb 2021.
- [3] Bombaci, Ignazio and Logoteta, Domenico, “Equation of state of dense nuclear matter and neutron star structure from nuclear chiral interactions,” *A&A*, vol. 609, p. A128, 2018.
- [4] K. Hebeler, S. K. Bogner, R. J. Furnstahl, A. Nogga, and A. Schwenk, “Improved nuclear matter calculations from chiral low-momentum interactions,” *Phys. Rev. C*, vol. 83, p. 031301, Mar 2011.
- [5] W. G. Jiang, A. Ekström, C. Forssén, G. Hagen, G. R. Jansen, and T. Papenbrock, “Accurate bulk properties of nuclei from $a = 2$ to ∞ from potentials with Δ isobars,” *Phys. Rev. C*, vol. 102, p. 054301, Nov 2020.
- [6] A. Ekström, G. R. Jansen, K. A. Wendt, G. Hagen, T. Papenbrock, B. D. Carlsson, C. Forssn, M. Hjorth-Jensen, P. Navrtil, and W. Nazarewicz, “Accurate nuclear radii and binding energies from a chiral interaction,” *Physical Review C*, vol. 91, May 2015.
- [7] A. Ekström, C. Forssén, G. Hagen, G. R. Jansen, W. Jiang, and T. Papenbrock, “What is ab initio in nuclear theory?,” *Frontiers in Physics*, vol. 11, Feb. 2023.
- [8] E. Epelbaum, H.-W. Hammer, and U.-G. Meiner, “Modern theory of nuclear forces,” *Reviews of Modern Physics*, vol. 81, p. 17731825, Dec. 2009.
- [9] H.-W. Hammer, S. Knig, and U. van Kolck, “Nuclear effective field theory: Status and perspectives,” *Reviews of Modern Physics*, vol. 92, June 2020.
- [10] H. Hergert, S. Bogner, T. Morris, A. Schwenk, and K. Tsukiyama, “The in-medium similarity renormalization group: A novel ab initio method for nuclei,” *Physics Reports*, vol. 621, p. 165222, Mar. 2016.
- [11] H. Hergert, “A guided tour of ab initio nuclear many-body theory,” *Frontiers in Physics*, vol. 8, 2020.
- [12] C. Drischler and S. K. Bogner, “A brief account of steven weinbergs legacy in ab initio many-body theory: Special issue in few-body systems: Celebrating 30 years of steven

- weinbergs papers on nuclear forces from chiral lagrangians,” *Few-Body Systems*, vol. 62, Oct. 2021.
- [13] K. Tsukiyama, S. K. Bogner, and A. Schwenk, “In-medium similarity renormalization group for nuclei,” *Phys. Rev. Lett.*, vol. 106, p. 222502, Jun 2011.
- [14] N. M. Parzuchowski, T. D. Morris, and S. K. Bogner, “Ab initio excited states from the in-medium similarity renormalization group,” *Phys. Rev. C*, vol. 95, p. 044304, Apr 2017.
- [15] M. Heinz, A. Tichai, J. Hoppe, K. Hebeler, and A. Schwenk, “In-medium similarity renormalization group with three-body operators,” *Physical Review C*, vol. 103, Apr. 2021.
- [16] H. Hergert, S. K. Bogner, J. G. Lietz, T. D. Morris, S. Novario, N. M. Parzuchowski, and F. Yuan, “In-Medium Similarity Renormalization Group Approach to the Nuclear Many-Body Problem,” *Lect. Notes Phys.*, vol. 936, pp. 477–570, 2017.
- [17] Y. Tang, M. LeMere, and D. Thompson, “Resonating-group method for nuclear many-body problems,” *Physics Reports*, vol. 47, no. 3, pp. 167–223, 1978.
- [18] R. Machleidt and F. Sammarruca, “Chiral eft based nuclear forces: achievements and challenges,” *Physica Scripta*, vol. 91, p. 083007, July 2016.
- [19] M. Hjorth-Jensen, M. Lombardo, and U. van Kolck, *An Advanced Course in Computational Nuclear Physics: Bridging the Scales from Quarks to Neutron Stars*, pp. 521–529. Springer Nature, 01 2017.
- [20] T. D. Morris, N. M. Parzuchowski, and S. K. Bogner, “Magnus expansion and in-medium similarity renormalization group,” *Physical Review C*, vol. 92, Sept. 2015.
- [21] G. C. Wick, “The evaluation of the collision matrix,” *Phys. Rev.*, vol. 80, pp. 268–272, Oct 1950.
- [22] S. R. Stroberg, T. D. Morris, and B. C. He, “Imsrg with flowing 3 body operators, and approximations thereof,” 2024.
- [23] G. Hagen, T. Papenbrock, A. Ekström, K. A. Wendt, G. Baardsen, S. Gandolfi, M. Hjorth-Jensen, and C. J. Horowitz, “Coupled-cluster calculations of nucleonic matter,” *Physical Review C*, vol. 89, Jan. 2014.
- [24] E. Epelbaum, H. Krebs, and P. Reinert, “Semi-local nuclear forces from chiral eft: State-of-the-art & challenges,” 2022.

- [25] A. Ekström, G. Baardsen, C. Forssén, G. Hagen, M. Hjorth-Jensen, G. R. Jansen, R. Machleidt, W. Nazarewicz, T. Papenbrock, J. Sarich, and S. M. Wild, “Optimized chiral nucleon-nucleon interaction at next-to-next-to-leading order,” *Phys. Rev. Lett.*, vol. 110, p. 192502, May 2013.
- [26] I. G. Smith, H. Hergert, and S. K. Bogner, “The in-medium similarity renormalization group at finite temperature,” 2024.
- [27] I. Shavitt and R. J. Bartlett, *Many-Body Methods in Chemistry and Physics: MBPT and Coupled-Cluster Theory*. Cambridge Molecular Science, Cambridge University Press, 2009.
- [28] D. R. Entem, R. Machleidt, and Y. Nosyk, “High-quality two-nucleon potentials up to fifth order of the chiral expansion,” *Physical Review C*, vol. 96, Aug. 2017.
- [29] C. Drischler, J. A. Melendez, R. J. Furnstahl, and D. R. Phillips, “Quantifying uncertainties and correlations in the nuclear-matter equation of state,” *Physical Review C*, vol. 102, Nov. 2020.
- [30] S. Knig, A. Ekström, K. Hebeler, D. Lee, and A. Schwenk, “Eigenvector continuation as an efficient and accurate emulator for uncertainty quantification,” *Physics Letters B*, vol. 810, p. 135814, 2020.
- [31] A. Ekström and G. Hagen, “Global sensitivity analysis of bulk properties of an atomic nucleus,” *Phys. Rev. Lett.*, vol. 123, p. 252501, Dec 2019.
- [32] H. Q. Song, M. Baldo, G. Giansiracusa, and U. Lombardo, “Bethe-brueckner-goldstone expansion in nuclear matter,” *Phys. Rev. Lett.*, vol. 81, pp. 1584–1587, Aug 1998.
- [33] J. Davison, *Theoretical and Computational Improvements to the In-Medium Similarity Renormalization Group*. PhD dissertation, Michigan State University, 2023.
- [34] P. Cook, D. Jammooa, M. Hjorth-Jensen, D. D. Lee, and D. Lee, “Parametric matrix models,” 2024.
- [35] S. Yoshida, “Imsrg-net: A machine-learning-based solver for the in-medium similarity renormalization group method,” *Physical Review C*, vol. 108, Oct. 2023.
- [36] S. R. White, “Numerical canonical transformation approach to quantum many-body problems,” *The Journal of Chemical Physics*, vol. 117, p. 74727482, Oct. 2002.
- [37] T. S. Untidt and N. C. Nielsen, “Closed solution to the baker-campbell-hausdorff problem: Exact effective hamiltonian theory for analysis of nuclear-magnetic-resonance experiments,” *Phys. Rev. E*, vol. 65, p. 021108, Jan 2002.

- [38] W. Kutzelnigg, *Unconventional Aspects of Coupled-Cluster Theory*, pp. 299–356. Dordrecht: Springer Netherlands, 2010.
- [39] M. Born, “Quantenmechanik der Stoßvorgänge,” *Zeitschrift für Physik*, vol. 38, pp. 803–827, Nov. 1926.
- [40] T. A. van der Sijs, O. El Gawhary, and H. P. Urbach, “Electromagnetic scattering beyond the weak regime: Solving the problem of divergent born perturbation series by padé approximants,” *Phys. Rev. Res.*, vol. 2, p. 013308, Mar 2020.
- [41] C. Yang, J. Brabec, L. Veis, D. B. Williams-Young, and K. Kowalski, “Solving coupled cluster equations by the newton krylov method,” *Frontiers in Chemistry*, vol. 8, 2020.
- [42] D. Shanks, “Non-linear transformations of divergent and slowly convergent sequences,” *Journal of Mathematics and Physics*, vol. 34, no. 1-4, pp. 1–42, 1955.
- [43] C. Bender, “Mathematical physics 03 - carl bender,” Apr 2012.
- [44] G. A. Baker and P. Graves-Morris, *Padé Approximants*. Encyclopedia of Mathematics and its Applications, Cambridge University Press, 2 ed., 1996.
- [45] J. W. Holt and N. Kaiser, “Equation of state of nuclear and neutron matter at third-order in perturbation theory from chiral effective field theory,” *Phys. Rev. C*, vol. 95, no. 3, p. 034326, 2017.

APPENDIX A. Generalized Baker-Campbell-Hausdorff Formula

Given recent interests in emulation for the IMSRG, the following quantity is of interest

$$\langle \Psi_A | H | \Psi_B \rangle = \langle \Phi | e^A H e^{-B} | \Phi \rangle . \quad (\text{A.1})$$

A and B are generic A -body operators. $|\Psi_A\rangle$ and $|\Psi_B\rangle$ are correlated wavefunctions associated with A and B , respectively. And $|\Phi\rangle$ is the usual Fermi vacuum. Let x be a continuous variable. Consider

$$F(x) = e^{Ax} H e^{-Bx} \quad (\text{A.2})$$

$$\begin{aligned} \frac{d}{dx} F(x) &= \frac{d e^{Ax}}{dx} H e^{-Bx} + e^{Ax} H \frac{d e^{-Bx}}{dx} \\ &= A e^{Ax} H e^{-Bx} - e^{Ax} H B e^{-Bx} . \end{aligned} \quad (\text{A.3})$$

Since $[A, e^{Ax}] = \sum_{n=0}^{\infty} \frac{x^n}{n!} [A, A^n] = 0$,

$$\frac{d}{dx} F(x) = e^{Ax} (AH - HB) e^{-Bx} . \quad (\text{A.4})$$

We define the three-argument commutator

$$[A, H, B] \equiv [A, H, B]^{(1)} \equiv AH - HB . \quad (\text{A.5})$$

Then,

$$\begin{aligned} \frac{d^2}{dx^2} F(x) &= e^{Ax} (A[A, H, B] - [A, H, B]B) e^{-Bx} \\ &= e^{Ax} [A, [A, H, B], B] e^{-Bx} . \end{aligned} \quad (\text{A.6})$$

Likewise, we define the two-fold nested three-argument commutator

$$[A, H, B]^{(2)} \equiv [A, [A, H, B], B] . \quad (\text{A.7})$$

In general, the n -fold nested three-argument commutator is given by

$$[A, H, B]^{(n)} \equiv [A, [A, H, B]^{(n-1)}, B] , \quad n > 0 \quad (\text{A.8a})$$

$$[A, H, B]^{(0)} \equiv H . \quad (\text{A.8b})$$

Assume that for some $n \geq 0$,

$$\frac{d^n}{dx^n} F(x) = e^{Ax} [A, H, B]^{(n)} e^{-Bx} . \quad (\text{A.9})$$

Therefore,

$$\begin{aligned} \frac{d}{dx} \frac{d^n}{dx^n} F(x) &= e^{Ax} \left(A [A, H, B]^{(n)} - [A, H, B]^{(n)} B \right) e^{-Bx} \\ &= e^{Ax} [A, [A, H, B]^{(n)}, B] e^{-Bx} \\ &= e^{Ax} [A, H, B]^{(n+1)} e^{-Bx} . \end{aligned} \quad (\text{A.10})$$

Thus, we have demonstrated that if Eq. (A.9) is valid for a given value of n , then the successive $n + 1$ derivative of $F(x)$ is also guaranteed by Eq. (A.9). Since we have shown that Eq. (A.9) is valid for $n = 1$ (and cotrivially valid for $n = 0$), then Eq. (A.9) must be valid for *all* values of n .

Taylor expanding $F(x)$ about $x = 0$ using Eq. (A.9), yields a modified variant to a famous

expression

$$\begin{aligned} F(x) &= \sum_{n=0}^{\infty} \frac{d^n}{dx^n} F(x) \Big|_{x=0} \frac{x^n}{n!} = \sum_{n=0}^{\infty} \frac{x^n [A, H, B]^{(n)}}{n!} \\ \implies F(1) &= e^A H e^{-B} = \sum_{n=0}^{\infty} \frac{[A, H, B]^{(n)}}{n!}. \end{aligned} \tag{A.11}$$

APPENDIX B. Fourier Transform of Local Two-Body Force in a Box

In this work, the IMSRG is performed in a finite box, manipulating interactions written in momentum space. Input interactions (e.g. the Minnesota potential) may be given in coordinate space representation. Therefore, it is essential that we know how to convert interaction matrix elements between coordinate and momentum space representations. Consider some momentum space interaction matrix element $\langle \vec{k}_1 \vec{k}_2 | \hat{V} | \vec{k}_3 \vec{k}_4 \rangle_{Direct}$, obtained in a box (of volume $\mathcal{V} = \mathcal{L}^3 [\text{fm}^3]$) containing normalized single-particle plane wave states given in Eq. (2.12). The subscript ‘‘Direct’’ is used to denote a matrix element that is *not* anti-symmetrized. We aim to write the aforementioned matrix element in a position space representation. For this derivation, we ignore spin and isospin quantum numbers—as they are irrelevant for understanding how the Fourier transform is performed in a box.

Inserting four complete sets into $\langle \vec{k}_1 \vec{k}_2 | \hat{V} | \vec{k}_3 \vec{k}_4 \rangle_{Direct}$ with basis states specifying the independent location of all incoming and outgoing particles yields

$$\begin{aligned} \langle \vec{k}_1 \vec{k}_2 | \hat{V} | \vec{k}_3 \vec{k}_4 \rangle_{Direct} &= \int_{\mathcal{V}} d^3 r_3 \int_{\mathcal{V}} d^3 r_4 \int_{\mathcal{V}} d^3 r_1 \int_{\mathcal{V}} d^3 r_2 \langle \vec{k}_1 \vec{k}_2 | \vec{r}_3 \vec{r}_4 \rangle \langle \vec{r}_1 \vec{r}_2 | \vec{k}_3 \vec{k}_4 \rangle \\ &\quad \times \langle \vec{r}_3 \vec{r}_4 | \hat{V} | \vec{r}_1 \vec{r}_2 \rangle . \end{aligned} \quad (\text{B.1})$$

Notice our chosen boundary of integration: we assume that all relevant single-particle wavefunctions exist within our box. We assume that the interaction is local, i.e.

$$\hat{V} | \vec{r}_1 \vec{r}_2 \rangle = V(\vec{r}_1 - \vec{r}_2) | \vec{r}_1 \vec{r}_2 \rangle \quad (\text{B.2a})$$

\Downarrow

$$\langle \vec{r}_3 \vec{r}_4 | \hat{V} | \vec{r}_1 \vec{r}_2 \rangle = V(\vec{r}_1 - \vec{r}_2) \delta(\vec{r}_1 - \vec{r}_3) \delta(\vec{r}_2 - \vec{r}_4) . \quad (\text{B.2b})$$

It is important to emphasize that the potential $V(\vec{r}_1 - \vec{r}_2)$ is a nuclear interaction, and is thus generated by the interacting particles. Consequently, $V(\vec{r}_1 - \vec{r}_2)$ depends *only* on the relative distance between particles. This means that we can confine our particles in *any* region of space, and the observables related to $V(\vec{r}_1 - \vec{r}_2)$ should be unchanged—so long there are no external forces. For convenience in this calculation, we place our box with one of its vertices located at the origin

$$\begin{aligned} 0 &\leq r_{1x} \leq \mathcal{L} \\ 0 &\leq r_{2x} \leq \mathcal{L} . \end{aligned}$$

Using Eq. (B.2b), we can simplify the integration:

$$\langle \vec{k}_1 \vec{k}_2 | \hat{V} | \vec{k}_3 \vec{k}_4 \rangle_{Direct} = \int_{\mathcal{V}} d^3 r_1 \int_{\mathcal{V}} d^3 r_2 \langle \vec{k}_1 \vec{k}_2 | \vec{r}_1 \vec{r}_2 \rangle \langle \vec{r}_1 \vec{r}_2 | \vec{k}_3 \vec{k}_4 \rangle V(\vec{r}_1 - \vec{r}_2) . \quad (\text{B.3})$$

Since,

$$\langle \vec{k}_1 \vec{k}_2 | \vec{r}_1 \vec{r}_2 \rangle = \frac{1}{\sqrt{\mathcal{V}}} e^{-i\vec{k}_1 \cdot \vec{r}_1} \frac{1}{\sqrt{\mathcal{V}}} e^{-i\vec{k}_2 \cdot \vec{r}_2} \quad (\text{B.4a})$$

$$\langle \vec{r}_1 \vec{r}_2 | \vec{k}_3 \vec{k}_4 \rangle = \frac{1}{\sqrt{\mathcal{V}}} e^{i\vec{k}_3 \cdot \vec{r}_1} \frac{1}{\sqrt{\mathcal{V}}} e^{i\vec{k}_4 \cdot \vec{r}_2} , \quad (\text{B.4b})$$

we can expand Eq. (B.3)

$$\langle \vec{k}_1 \vec{k}_2 | \hat{V} | \vec{k}_3 \vec{k}_4 \rangle_{Direct} = \frac{1}{\mathcal{V}^2} \int_{\mathcal{V}} d^3 r_1 \int_{\mathcal{V}} d^3 r_2 e^{-i(\vec{k}_1 \cdot \vec{r}_1 + \vec{k}_2 \cdot \vec{r}_2)} e^{i(\vec{k}_3 \cdot \vec{r}_1 + \vec{k}_4 \cdot \vec{r}_2)} V(\vec{r}_1 - \vec{r}_2) . \quad (\text{B.5})$$

Since the potential is assumed to only depend on the relative distance between incident particles, it is convenient to transform from lab coordinates into relative coordinates $\vec{r} \equiv$

$\vec{r}_1 - \vec{r}_2$ and center-of-mass coordinates $\vec{R} \equiv \frac{\vec{r}_1 + \vec{r}_2}{2}$. Then, $\vec{r}_1 = \vec{R} + \frac{\vec{r}}{2}$ and $\vec{r}_2 = \vec{R} - \frac{\vec{r}}{2}$. And the new volume element is given by

$$d^3r_1 d^3r_2 = d^3R d^3r |\det(J)|. \quad (\text{B.6})$$

The Jacobian is given by

$$J = \begin{bmatrix} \frac{\partial r_{1x}}{\partial R_x} & \frac{\partial r_{1x}}{\partial r_x} & \frac{\partial r_{1x}}{\partial R_y} & \frac{\partial r_{1x}}{\partial r_y} & \frac{\partial r_{1x}}{\partial R_z} & \frac{\partial r_{1x}}{\partial r_z} \\ \frac{\partial r_{1y}}{\partial R_x} & \frac{\partial r_{1y}}{\partial r_x} & \frac{\partial r_{1y}}{\partial R_y} & \frac{\partial r_{1y}}{\partial r_y} & \frac{\partial r_{1y}}{\partial R_z} & \frac{\partial r_{1y}}{\partial r_z} \\ \frac{\partial r_{1z}}{\partial R_x} & \frac{\partial r_{1z}}{\partial r_x} & \frac{\partial r_{1z}}{\partial R_y} & \frac{\partial r_{1z}}{\partial r_y} & \frac{\partial r_{1z}}{\partial R_z} & \frac{\partial r_{1z}}{\partial r_z} \\ \frac{\partial r_{2x}}{\partial R_x} & \frac{\partial r_{2x}}{\partial r_x} & \frac{\partial r_{2x}}{\partial R_y} & \frac{\partial r_{2x}}{\partial r_y} & \frac{\partial r_{2x}}{\partial R_z} & \frac{\partial r_{2x}}{\partial r_z} \\ \frac{\partial r_{2y}}{\partial R_x} & \frac{\partial r_{2y}}{\partial r_x} & \frac{\partial r_{2y}}{\partial R_y} & \frac{\partial r_{2y}}{\partial r_y} & \frac{\partial r_{2y}}{\partial R_z} & \frac{\partial r_{2y}}{\partial r_z} \\ \frac{\partial r_{2z}}{\partial R_x} & \frac{\partial r_{2z}}{\partial r_x} & \frac{\partial r_{2z}}{\partial R_y} & \frac{\partial r_{2z}}{\partial r_y} & \frac{\partial r_{2z}}{\partial R_z} & \frac{\partial r_{2z}}{\partial r_z} \end{bmatrix} = \begin{bmatrix} 1 & \frac{1}{2} & 0 & 0 & 0 & 0 \\ 0 & 0 & 1 & \frac{1}{2} & 0 & 0 \\ 0 & 0 & 0 & 0 & 1 & \frac{1}{2} \\ 1 & -\frac{1}{2} & 0 & 0 & 0 & 0 \\ 0 & 0 & 1 & -\frac{1}{2} & 0 & 0 \\ 0 & 0 & 0 & 0 & 1 & -\frac{1}{2} \end{bmatrix}, \quad (\text{B.7})$$

with $\det(J) = 1$. Therefore,

$$\begin{aligned} \langle \vec{k}_1 \vec{k}_2 | \hat{V} | \vec{k}_3 \vec{k}_4 \rangle_{Direct} &= \frac{1}{\mathcal{V}^2} \int_{\mathcal{V}'} d^3R \int_{\mathcal{V}''} d^3r e^{i(\vec{k}_3 \cdot [\vec{R} + \frac{\vec{r}}{2}] + \vec{k}_4 \cdot [\vec{R} - \frac{\vec{r}}{2}] - \vec{k}_1 \cdot [\vec{R} + \frac{\vec{r}}{2}] - \vec{k}_2 \cdot [\vec{R} - \frac{\vec{r}}{2}])} V(\vec{r}) \\ &= \frac{1}{\mathcal{V}^2} \int_{\mathcal{V}'} d^3R e^{i(\vec{k}_3 + \vec{k}_4 - \vec{k}_1 - \vec{k}_2) \cdot \vec{R}} \int_{\mathcal{V}''} d^3r e^{\frac{i(\vec{k}_3 - \vec{k}_4 - \vec{k}_1 + \vec{k}_2) \cdot \vec{r}}{2}} V(\vec{r}), \end{aligned} \quad (\text{B.8})$$

where \mathcal{V} and \mathcal{V}' are new boundaries of integration. The integration region over R is still restricted to be within the box, while the integration region over r will lie outside of the box.

To see this, observe that

$$\max R_x = \max \left(\frac{r_{1x} + r_{2x}}{2} \right) = \frac{\mathcal{L} + \mathcal{L}}{2} = \mathcal{L} \quad (\text{B.9a})$$

$$\min R_x = \frac{0 + 0}{2} = 0 \quad (\text{B.9b})$$

$$\max r_x = \max (r_{1x} - r_{2x}) = \mathcal{L} - 0 \quad (\text{B.9c})$$

$$\min r_x = 0 - \mathcal{L} = -\mathcal{L} . \quad (\text{B.9d})$$

Likewise can also be concluded for the y and z Cartesian coordinates. Thus, $\mathcal{V}' = \mathcal{V}$ and $\mathcal{V}'' = 2^3\mathcal{V}$. For convenience, let us define the incoming and outgoing relative momenta

$$\vec{k} \equiv \frac{\vec{k}_3 - \vec{k}_4}{2} \quad (\text{B.10a})$$

$$\vec{k}' \equiv \frac{\vec{k}_1 - \vec{k}_2}{2} . \quad (\text{B.10b})$$

The momentum transfer is given by

$$\vec{q} \equiv \vec{k}' - \vec{k} = \frac{\vec{k}_1 - \vec{k}_2}{2} - \frac{\vec{k}_3 - \vec{k}_4}{2} . \quad (\text{B.11})$$

And center-of-mass momenta are given by

$$\vec{K}' \equiv \vec{k}_1 + \vec{k}_2 \quad (\text{B.12a})$$

$$\vec{K} \equiv \vec{k}_3 + \vec{k}_4 . \quad (\text{B.12b})$$

Thus,

$$\langle \vec{k}_1 \vec{k}_2 | \hat{V} | \vec{k}_3 \vec{k}_4 \rangle_{Direct} = \frac{1}{\mathcal{V}^2} \int_{\mathcal{V}} d^3 R e^{i(\vec{K}-\vec{K}') \cdot \vec{R}} \int_{2^3 \mathcal{V}} d^3 r e^{-i\vec{q} \cdot \vec{r}} V(\vec{r}) . \quad (\text{B.13})$$

Note, the integration boundary $2^3 \mathcal{V}$, means that Eq. (B.13)'s integration over r is done within the boundary of a cube (with sides of length $2\mathcal{L}$) that is centered at the origin. Eq. (B.13)'s integration over R can be easily done in Cartesian coordinates

$$\int_{\mathcal{V}} d^3 R e^{i(\vec{K}-\vec{K}') \cdot \vec{R}} = \int_0^{\mathcal{L}} dR_x e^{i(K_x - K'_x) R_x} \int_0^{\mathcal{L}} dR_y e^{i(K_y - K'_y) R_y} \int_0^{\mathcal{L}} dR_z e^{i(K_z - K'_z) R_z} . \quad (\text{B.14})$$

$$\begin{aligned} \int_0^{\mathcal{L}} dR_x e^{i(K_x - K'_x) R_x} &= \left. \frac{-ie^{i(K_x - K'_x) R_x}}{K_x - K'_x} \right|_{R_x=0}^{R_x=\mathcal{L}} \\ &= \frac{-i}{K_x - K'_x} \left(e^{i(K_x - K'_x) \mathcal{L}} - 1 \right) . \end{aligned} \quad (\text{B.15})$$

Since

$$K_x - K'_x = k_{3x} + k_{4x} - k_{1x} - k_{2x} = \frac{2\pi}{\mathcal{L}} (n_{3x} + n_{4x} - n_{1x} - n_{2x}) , \quad (\text{B.16})$$

we can conveniently define

$$\bar{n}_x \equiv n_{3x} + n_{4x} - n_{1x} - n_{2x} \in \mathbb{Z} . \quad (\text{B.17})$$

Hence,

$$\int_0^{\mathcal{L}} dR_x e^{i(K_x - K'_x) R_x} = \frac{-i\mathcal{L}}{2\pi} \frac{(e^{2\pi i \bar{n}_x} - 1)}{\bar{n}_x} . \quad (\text{B.18})$$

Note that Eq. (B.18) is only non-zero when $\bar{n}_x = 0$. Therefore,

$$\begin{aligned} \int_0^{\mathcal{L}} dR_x e^{i(K_x - K'_x)R_x} &= \lim_{\bar{n}_x \rightarrow 0} \frac{-i\mathcal{L} \frac{d}{d\bar{n}_x} (e^{2\pi i \bar{n}_x} - 1)}{\frac{d}{d\bar{n}_x} \bar{n}_x} \\ &= \delta_{\bar{n}_x, 0} \frac{-i\mathcal{L} 2\pi i}{2\pi \cdot 1} = \mathcal{L} \delta_{\bar{n}_x, 0} = \mathcal{L} \delta_{K_x, K'_x}. \end{aligned} \quad (\text{B.19})$$

Similarly,

$$\int_0^{\mathcal{L}} dR_y e^{i(K_y - K'_y)R_y} = \mathcal{L} \delta_{K_y, K'_y} \quad (\text{B.20a})$$

$$\int_0^{\mathcal{L}} dR_z e^{i(K_z - K'_z)R_z} = \mathcal{L} \delta_{K_z, K'_z}. \quad (\text{B.20b})$$

Combining Eqs. (B.19) and (B.20) with Eq. (B.14),

$$\int_{\mathcal{V}} d^3 R e^{i(\vec{K} - \vec{K}') \cdot \vec{R}} = \mathcal{L}^3 \delta_{\vec{K}, \vec{K}'} = \mathcal{V} \delta_{\vec{K}, \vec{K}'}. \quad (\text{B.21})$$

Finally, combining Eq. (B.21) with Eq. (B.13),

$$\begin{aligned} \langle \vec{k}_1 \vec{k}_2 | \hat{V} | \vec{k}_3 \vec{k}_4 \rangle_{Direct} &= \frac{\delta_{\vec{k}_1 + \vec{k}_2, \vec{k}_3 + \vec{k}_4}}{\mathcal{V}} \times \int_{2^3 \mathcal{V}} d^3 r e^{-\frac{i}{2}(\vec{k}_1 - \vec{k}_2 - \vec{k}_3 + \vec{k}_4) \cdot \vec{r}} V(\vec{r}) \\ &= \frac{\delta_{\vec{K}, \vec{K}'}}{\mathcal{V}} \int_{2^3 \mathcal{V}} d^3 r e^{-i\vec{q} \cdot \vec{r}} V(\vec{r}). \end{aligned} \quad (\text{B.22})$$

Since Eq. (B.22) is derived independent of spin and isospin considerations, we can simply

extend it

$$\begin{aligned}
\left\langle \vec{k}_1 \sigma_{z_1} \tau_{z_1} \vec{k}_2 \sigma_{z_2} \tau_{z_2} \left| \hat{V} \right| \vec{k}_3 \sigma_{z_3} \tau_{z_3} \vec{k}_4 \sigma_{z_4} \tau_{z_4} \right\rangle_{Direct} &= \underbrace{\frac{\delta_{\vec{K}, \vec{K}'}}{\mathcal{V}}}_{\text{Box normalization}} \quad (B.23) \\
&\times \int_{2^3 \mathcal{V}} d^3 r e^{-i\vec{q} \cdot \vec{r}} \underbrace{\left\langle \sigma_{z_1} \tau_{z_1} \sigma_{z_2} \tau_{z_2} \left| \hat{V} \left(\vec{r}, \hat{\vec{\sigma}}, \hat{\vec{\tau}} \right) \right| \sigma_{z_3} \tau_{z_3} \sigma_{z_4} \tau_{z_4} \right\rangle}_{\text{Free position space representation}} \\
&= \frac{\delta_{\vec{K}, \vec{K}'}}{\mathcal{V}} \underbrace{\left\langle \vec{k}' \sigma_{z_1} \tau_{z_1} \sigma_{z_2} \tau_{z_2} \left| \hat{V} \left(\hat{k}', \hat{k}, \hat{\vec{\sigma}}, \hat{\vec{\tau}}, \mathcal{V} \right) \right| \vec{k} \sigma_{z_3} \tau_{z_3} \sigma_{z_4} \tau_{z_4} \right\rangle}_{\text{Momentum space representation}}.
\end{aligned}$$

For generality, Eq. (B.23) is written in a form where \hat{V} depends on the operators \hat{k}' and \hat{k} , and acts on two-particle states $|\vec{k}'\rangle$ and $|\vec{k}\rangle$. If the momentum space representation of the interaction is *not* obtained using the partial wave expansion (seen in Appendix E), then we can easily write $\langle \vec{k}' | \hat{V} \left(\hat{k}', \hat{k}, \hat{\vec{\sigma}}, \hat{\vec{\tau}}, \mathcal{V} \right) | \vec{k} \rangle = \hat{V} \left(\vec{k}', \vec{k}, \hat{\vec{\sigma}}, \hat{\vec{\tau}}, \mathcal{V} \right)$. Most interactions used in this work are given in a momentum space representation. Such interactions including the One Pion Exchange (OPE), and chiral forces from Drischler *et al.* [1], assume that the box-size is infinitely large. We still convert those interactions into the finite box using Eq. (B.23), and dropping the \mathcal{V} dependence in $\langle \vec{k}' \sigma_{z_1} \tau_{z_1} \sigma_{z_2} \tau_{z_2} \left| \hat{V} \left(\hat{k}', \hat{k}, \hat{\vec{\sigma}}, \hat{\vec{\tau}}, \mathcal{V} \right) \right| \vec{k} \sigma_{z_3} \tau_{z_3} \sigma_{z_4} \tau_{z_4} \rangle$.¹

Finally, the anti-symmetrized variant of Eq. (B.23) is given by

$$\begin{aligned}
&\left\langle \vec{k}_1 \sigma_{z_1} \tau_{z_1} \vec{k}_2 \sigma_{z_2} \tau_{z_2} \left| \hat{V} \right| \vec{k}_3 \sigma_{z_3} \tau_{z_3} \vec{k}_4 \sigma_{z_4} \tau_{z_4} \right\rangle_{AS} \quad (B.24) \\
&\equiv \left\langle \vec{k}_1 \sigma_{z_1} \tau_{z_1} \vec{k}_2 \sigma_{z_2} \tau_{z_2} \left| \hat{V} \right| \vec{k}_3 \sigma_{z_3} \tau_{z_3} \vec{k}_4 \sigma_{z_4} \tau_{z_4} \right\rangle_{Direct} \\
&- \left\langle \vec{k}_1 \sigma_{z_1} \tau_{z_1} \vec{k}_2 \sigma_{z_2} \tau_{z_2} \left| \hat{V} \right| \vec{k}_4 \sigma_{z_4} \tau_{z_4} \vec{k}_3 \sigma_{z_3} \tau_{z_3} \right\rangle_{Direct}.
\end{aligned}$$

¹See Eqs. (D.21) and (E.12).

APPENDIX C. Minnesota Potential in a Finite Box

The Minnesota potential is of the form [17, 19]

$$\begin{aligned} \hat{V}_{\text{Minn}}(\vec{r}, \hat{\sigma}, \hat{\tau}) = & \frac{1}{2} \left(V_{0R} e^{-k_R |\vec{r}|^2} + \frac{V_{0T}}{2} e^{-k_T |\vec{r}|^2} (1 + \hat{P}_{12}^\sigma) \right. \\ & \left. + \frac{V_{0S}}{2} e^{-k_S |\vec{r}|^2} (1 - \hat{P}_{12}^\sigma) \right) \times \left(1 - \hat{P}_{12}^\sigma \hat{P}_{12}^\tau \right). \end{aligned} \quad (\text{C.1})$$

$V_{0R} = 200.0 \text{ MeV}$, $V_{0T} = -178.0 \text{ MeV}$, $V_{0S} = -91.85 \text{ MeV}$, $k_R = 1.487 \text{ fm}^{-2}$, $k_T = 0.639 \text{ fm}^{-2}$, and $k_S = 0.465 \text{ fm}^{-2}$. \hat{P}_{12}^σ and \hat{P}_{12}^τ are spin and isospin exchange operators, respectively

$$\hat{P}_{12}^\sigma = \frac{1}{2} (1 + \hat{\sigma}_1 \cdot \hat{\sigma}_2) \quad (\text{C.2a})$$

$$\hat{P}_{12}^\tau = \frac{1}{2} (1 + \hat{\tau}_1 \cdot \hat{\tau}_2). \quad (\text{C.2b})$$

\hat{P}_{12}^σ and \hat{P}_{12}^τ act on orthonormal two-particle spin and isospin projection states on the z axis, respectively in the following manner:

$$\hat{P}_{12}^\sigma |\sigma_{z_1} = \uparrow, \sigma_{z_2} = \uparrow\rangle = |\uparrow\uparrow\rangle, \quad \hat{P}_{12}^\sigma |\downarrow\downarrow\rangle = |\downarrow\downarrow\rangle, \quad \hat{P}_{12}^\sigma |\uparrow\downarrow\rangle = |\downarrow\uparrow\rangle, \quad \hat{P}_{12}^\sigma |\downarrow\uparrow\rangle = |\uparrow\downarrow\rangle, \quad (\text{C.3})$$

$$\hat{P}_{12}^\tau |\tau_{z_1} = \uparrow, \tau_{z_2} = \uparrow\rangle = |\uparrow\uparrow\rangle, \quad \hat{P}_{12}^\tau |\downarrow\downarrow\rangle = |\downarrow\downarrow\rangle, \quad \hat{P}_{12}^\tau |\uparrow\downarrow\rangle = |\downarrow\uparrow\rangle, \quad \hat{P}_{12}^\tau |\downarrow\uparrow\rangle = |\uparrow\downarrow\rangle.$$

And going forward, the following identity will be useful

$$\hat{P}_{12}^\sigma \hat{P}_{12}^\sigma = \hat{P}_{12}^\tau \hat{P}_{12}^\tau = 1. \quad (\text{C.4})$$

We seek to compute the matrix elements of the Minnesota potential using Eq. (B.23):

$$\begin{aligned} & \left\langle \vec{k}_1 \sigma_{z_1} \tau_{z_1} \vec{k}_2 \sigma_{z_2} \tau_{z_2} \left| \hat{V}_{\text{Minn}} \right| \vec{k}_3 \sigma_{z_3} \tau_{z_3} \vec{k}_4 \sigma_{z_4} \tau_{z_4} \right\rangle_{\text{Direct}} = \frac{\delta_{\vec{K}, \vec{K}'}}{\mathcal{V}} \\ & \times \int_{2^3 \mathcal{V}} d^3 r e^{-i\vec{q} \cdot \vec{r}} \langle \sigma_{z_1} \tau_{z_1} \sigma_{z_2} \tau_{z_2} | \hat{V}_{\text{Minn}}(\vec{r}, \hat{\sigma}, \hat{\tau}) | \sigma_{z_3} \tau_{z_3} \sigma_{z_4} \tau_{z_4} \rangle. \end{aligned} \quad (\text{C.5})$$

Since spin and isospin are two independent operator spaces, we can easily factor our analysis.

$$\begin{aligned} & \langle \sigma_{z_1} \tau_{z_1} \sigma_{z_2} \tau_{z_2} | \hat{V}_{\text{Minn}}(\vec{r}, \hat{\sigma}, \hat{\tau}) | \sigma_{z_3} \tau_{z_3} \sigma_{z_4} \tau_{z_4} \rangle \\ & = \langle \sigma_{z_1} \sigma_{z_2} | \langle \tau_{z_1} \tau_{z_2} | \hat{V}_{\text{Minn}}(\vec{r}, \hat{\sigma}, \hat{\tau}) | \tau_{z_3} \tau_{z_4} \rangle | \sigma_{z_3} \sigma_{z_4} \rangle. \end{aligned} \quad (\text{C.6})$$

First, consider matrix elements between orthonormal isospin states.

$$\begin{aligned} \langle \tau_{z_1} \tau_{z_2} | \hat{V}_{\text{Minn}}(\vec{r}, \hat{\sigma}, \hat{\tau}) | \tau_{z_3} \tau_{z_4} \rangle & = \frac{1}{2} \left(V_{0R} e^{-k_R |\vec{r}|^2} + \frac{V_{0T}}{2} e^{-k_T |\vec{r}|^2} (1 + \hat{P}_{12}^\sigma) \right. \\ & \left. + \frac{V_{0S}}{2} e^{-k_S |\vec{r}|^2} (1 - \hat{P}_{12}^\sigma) \right) \times \langle \tau_{z_1} \tau_{z_2} | 1 - \hat{P}_{12}^\sigma \hat{P}_{12}^\tau | \tau_{z_3} \tau_{z_4} \rangle. \end{aligned} \quad (\text{C.7})$$

For convenience, let us define

$$C_R \equiv V_{0R} e^{-k_R |\vec{r}|^2} \quad (\text{C.8a})$$

$$C_T \equiv \frac{V_{0T}}{2} e^{-k_T |\vec{r}|^2} (1 + \hat{P}_{12}^\sigma) \quad (\text{C.8b})$$

$$C_S \equiv \frac{V_{0S}}{2} e^{-k_S |\vec{r}|^2} (1 - \hat{P}_{12}^\sigma). \quad (\text{C.8c})$$

Combining Eqs. (C.8) and (C.7), we obtain

$$\langle \tau_{z_1} \tau_{z_2} | \hat{V}_{\text{Minn}}(\vec{r}, \hat{\sigma}, \hat{\tau}) | \tau_{z_3} \tau_{z_4} \rangle = \frac{1}{2} (C_R + C_T + C_S) \langle \tau_{z_1} \tau_{z_2} | 1 - \hat{P}_{12}^\sigma \hat{P}_{12}^\tau | \tau_{z_3} \tau_{z_4} \rangle. \quad (\text{C.9})$$

Using Eqs. (C.3) and (C.4) in Eq. (C.9),

$$\begin{aligned} \langle \tau_{z_1} \tau_{z_2} | 1 - \hat{P}_{12}^\sigma \hat{P}_{12}^\tau | \tau_{z_3} \tau_{z_4} \rangle &= \delta_{\tau_{z_1}, \tau_{z_3}} \delta_{\tau_{z_2}, \tau_{z_4}} - \hat{P}_{12}^\sigma \langle \tau_{z_1} \tau_{z_2} | \hat{P}_{12}^\tau | \tau_{z_3} \tau_{z_4} \rangle \\ &= \delta_{\tau_{z_1}, \tau_{z_3}} \delta_{\tau_{z_2}, \tau_{z_4}} - \hat{P}_{12}^\sigma \delta_{\tau_{z_1}, \tau_{z_4}} \delta_{\tau_{z_2}, \tau_{z_3}} . \end{aligned} \quad (\text{C.10})$$

Now, consider matrix elements of $\langle \tau_{z_1} \tau_{z_2} | 1 - \hat{P}_{12}^\sigma \hat{P}_{12}^\tau | \tau_{z_3} \tau_{z_4} \rangle$ between orthonormal spin states. Combining Eqs. (C.6) and (C.9),

$$\begin{aligned} \langle \sigma_{z_1} \tau_{z_1} \sigma_{z_2} \tau_{z_2} | \hat{V}_{\text{Minn}}(\vec{r}, \hat{\sigma}, \hat{\tau}) | \sigma_{z_3} \tau_{z_3} \sigma_{z_4} \tau_{z_4} \rangle &= \frac{1}{2} \langle \sigma_{z_1} \sigma_{z_2} | (C_R + C_T + C_S) \\ &\times \left(\delta_{\tau_{z_1}, \tau_{z_3}} \delta_{\tau_{z_2}, \tau_{z_4}} - \hat{P}_{12}^\sigma \delta_{\tau_{z_1}, \tau_{z_4}} \delta_{\tau_{z_2}, \tau_{z_3}} \right) | \sigma_{z_3} \sigma_{z_4} \rangle . \end{aligned} \quad (\text{C.11})$$

Using Eqs. (C.3) and (C.4), we can evaluate the individual terms of Eq. (C.11):

$$\begin{aligned} &\langle \sigma_{z_1} \sigma_{z_2} | C_R \left(\delta_{\tau_{z_1}, \tau_{z_3}} \delta_{\tau_{z_2}, \tau_{z_4}} - \hat{P}_{12}^\sigma \delta_{\tau_{z_1}, \tau_{z_4}} \delta_{\tau_{z_2}, \tau_{z_3}} \right) | \sigma_{z_3} \sigma_{z_4} \rangle \\ &= V_{0R} e^{-kR |\vec{r}|^2} \times \langle \sigma_{z_1} \sigma_{z_2} | \left(\delta_{\tau_{z_1}, \tau_{z_3}} \delta_{\tau_{z_2}, \tau_{z_4}} - \hat{P}_{12}^\sigma \delta_{\tau_{z_1}, \tau_{z_4}} \delta_{\tau_{z_2}, \tau_{z_3}} \right) | \sigma_{z_3} \sigma_{z_4} \rangle \\ &= V_{0R} e^{-kR |\vec{r}|^2} \times \left(\delta_{\tau_{z_1}, \tau_{z_3}} \delta_{\tau_{z_2}, \tau_{z_4}} \delta_{\sigma_{z_1}, \sigma_{z_3}} \delta_{\sigma_{z_2}, \sigma_{z_4}} - \delta_{\tau_{z_1}, \tau_{z_4}} \delta_{\tau_{z_2}, \tau_{z_3}} \delta_{\sigma_{z_1}, \sigma_{z_4}} \delta_{\sigma_{z_2}, \sigma_{z_3}} \right) . \end{aligned} \quad (\text{C.12})$$

Likewise, the C_T terms are given by

$$\begin{aligned}
& \langle \sigma_{z_1} \sigma_{z_2} | C_T \left(\delta_{\tau_{z_1}, \tau_{z_3}} \delta_{\tau_{z_2}, \tau_{z_4}} - \hat{P}_{12}^\sigma \delta_{\tau_{z_1}, \tau_{z_4}} \delta_{\tau_{z_2}, \tau_{z_3}} \right) | \sigma_{z_3} \sigma_{z_4} \rangle \quad (\text{C.13}) \\
&= \frac{V_{0T}}{2} e^{-k_T |\vec{r}|^2} \times \langle \sigma_{z_1} \sigma_{z_2} | \left(1 + \hat{P}_{12}^\sigma \right) \left(\delta_{\tau_{z_1}, \tau_{z_3}} \delta_{\tau_{z_2}, \tau_{z_4}} - \hat{P}_{12}^\sigma \delta_{\tau_{z_1}, \tau_{z_4}} \delta_{\tau_{z_2}, \tau_{z_3}} \right) | \sigma_{z_3} \sigma_{z_4} \rangle \\
&= \frac{V_{0T}}{2} e^{-k_T |\vec{r}|^2} \times \langle \sigma_{z_1} \sigma_{z_2} | \left(\delta_{\tau_{z_1}, \tau_{z_3}} \delta_{\tau_{z_2}, \tau_{z_4}} - \underbrace{\hat{P}_{12}^\sigma \hat{P}_{12}^\sigma}_1 \delta_{\tau_{z_1}, \tau_{z_4}} \delta_{\tau_{z_2}, \tau_{z_3}} \right) \\
&\quad + \left(\delta_{\tau_{z_1}, \tau_{z_3}} \delta_{\tau_{z_2}, \tau_{z_4}} - \delta_{\tau_{z_1}, \tau_{z_4}} \delta_{\tau_{z_2}, \tau_{z_3}} \right) \hat{P}_{12}^\sigma | \sigma_{z_3} \sigma_{z_4} \rangle \\
&= \frac{V_{0T}}{2} e^{-k_T |\vec{r}|^2} \times \langle \sigma_{z_1} \sigma_{z_2} | \left(\delta_{\tau_{z_1}, \tau_{z_3}} \delta_{\tau_{z_2}, \tau_{z_4}} - \delta_{\tau_{z_1}, \tau_{z_4}} \delta_{\tau_{z_2}, \tau_{z_3}} \right) \left(1 + \hat{P}_{12}^\sigma \right) | \sigma_{z_3} \sigma_{z_4} \rangle \\
&= \frac{V_{0T}}{2} e^{-k_T |\vec{r}|^2} \left(\delta_{\tau_{z_1}, \tau_{z_3}} \delta_{\tau_{z_2}, \tau_{z_4}} - \delta_{\tau_{z_1}, \tau_{z_4}} \delta_{\tau_{z_2}, \tau_{z_3}} \right) \left(\delta_{\sigma_{z_1}, \sigma_{z_3}} \delta_{\sigma_{z_2}, \sigma_{z_4}} + \delta_{\sigma_{z_1}, \sigma_{z_4}} \delta_{\sigma_{z_2}, \sigma_{z_3}} \right).
\end{aligned}$$

Lastly, the C_S terms are given by

$$\begin{aligned}
& \langle \sigma_{z_1} \sigma_{z_2} | C_S \left(\delta_{\tau_{z_1}, \tau_{z_3}} \delta_{\tau_{z_2}, \tau_{z_4}} - \hat{P}_{12}^\sigma \delta_{\tau_{z_1}, \tau_{z_4}} \delta_{\tau_{z_2}, \tau_{z_3}} \right) | \sigma_{z_3} \sigma_{z_4} \rangle \quad (\text{C.14}) \\
&= \frac{V_{0S}}{2} e^{-k_S |\vec{r}|^2} \times \langle \sigma_{z_1} \sigma_{z_2} | \left(1 - \hat{P}_{12}^\sigma \right) \left(\delta_{\tau_{z_1}, \tau_{z_3}} \delta_{\tau_{z_2}, \tau_{z_4}} - \hat{P}_{12}^\sigma \delta_{\tau_{z_1}, \tau_{z_4}} \delta_{\tau_{z_2}, \tau_{z_3}} \right) | \sigma_{z_3} \sigma_{z_4} \rangle \\
&= \frac{V_{0S}}{2} e^{-k_S |\vec{r}|^2} \times \langle \sigma_{z_1} \sigma_{z_2} | \left(\delta_{\tau_{z_1}, \tau_{z_3}} \delta_{\tau_{z_2}, \tau_{z_4}} + \underbrace{\hat{P}_{12}^\sigma \hat{P}_{12}^\sigma}_1 \delta_{\tau_{z_1}, \tau_{z_4}} \delta_{\tau_{z_2}, \tau_{z_3}} \right) \\
&\quad - \left(\delta_{\tau_{z_1}, \tau_{z_3}} \delta_{\tau_{z_2}, \tau_{z_4}} + \delta_{\tau_{z_1}, \tau_{z_4}} \delta_{\tau_{z_2}, \tau_{z_3}} \right) \hat{P}_{12}^\sigma | \sigma_{z_3} \sigma_{z_4} \rangle \\
&= \frac{V_{0S}}{2} e^{-k_S |\vec{r}|^2} \times \langle \sigma_{z_1} \sigma_{z_2} | \left(\delta_{\tau_{z_1}, \tau_{z_3}} \delta_{\tau_{z_2}, \tau_{z_4}} + \delta_{\tau_{z_1}, \tau_{z_4}} \delta_{\tau_{z_2}, \tau_{z_3}} \right) \left(1 - \hat{P}_{12}^\sigma \right) | \sigma_{z_3} \sigma_{z_4} \rangle \\
&= \frac{V_{0S}}{2} e^{-k_S |\vec{r}|^2} \left(\delta_{\tau_{z_1}, \tau_{z_3}} \delta_{\tau_{z_2}, \tau_{z_4}} + \delta_{\tau_{z_1}, \tau_{z_4}} \delta_{\tau_{z_2}, \tau_{z_3}} \right) \left(\delta_{\sigma_{z_1}, \sigma_{z_3}} \delta_{\sigma_{z_2}, \sigma_{z_4}} - \delta_{\sigma_{z_1}, \sigma_{z_4}} \delta_{\sigma_{z_2}, \sigma_{z_3}} \right).
\end{aligned}$$

In conclusion, combining Eqs. (C.12)–(C.14) into Eq. (C.11), we obtain the spin and isospin

matrix elements of the Minnesota potential:

$$\begin{aligned}
& \langle \sigma_{z_1} \tau_{z_1} \sigma_{z_2} \tau_{z_2} | \hat{V}_{\text{Minn}}(\vec{r}, \hat{\sigma}, \hat{\tau}) | \sigma_{z_3} \tau_{z_3} \sigma_{z_4} \tau_{z_4} \rangle \quad (\text{C.15}) \\
&= \frac{V_{0R}}{2} e^{-k_R |\vec{r}|^2} \left(\delta_{\tau_{z_1}, \tau_{z_3}} \delta_{\tau_{z_2}, \tau_{z_4}} \delta_{\sigma_{z_1}, \sigma_{z_3}} \delta_{\sigma_{z_2}, \sigma_{z_4}} - \delta_{\tau_{z_1}, \tau_{z_4}} \delta_{\tau_{z_2}, \tau_{z_3}} \delta_{\sigma_{z_1}, \sigma_{z_4}} \delta_{\sigma_{z_2}, \sigma_{z_3}} \right) \\
&+ \frac{V_{0T}}{4} e^{-k_T |\vec{r}|^2} \left(\delta_{\tau_{z_1}, \tau_{z_3}} \delta_{\tau_{z_2}, \tau_{z_4}} - \delta_{\tau_{z_1}, \tau_{z_4}} \delta_{\tau_{z_2}, \tau_{z_3}} \right) \left(\delta_{\sigma_{z_1}, \sigma_{z_3}} \delta_{\sigma_{z_2}, \sigma_{z_4}} + \delta_{\sigma_{z_1}, \sigma_{z_4}} \delta_{\sigma_{z_2}, \sigma_{z_3}} \right) \\
&+ \frac{V_{0S}}{4} e^{-k_S |\vec{r}|^2} \left(\delta_{\tau_{z_1}, \tau_{z_3}} \delta_{\tau_{z_2}, \tau_{z_4}} + \delta_{\tau_{z_1}, \tau_{z_4}} \delta_{\tau_{z_2}, \tau_{z_3}} \right) \left(\delta_{\sigma_{z_1}, \sigma_{z_3}} \delta_{\sigma_{z_2}, \sigma_{z_4}} - \delta_{\sigma_{z_1}, \sigma_{z_4}} \delta_{\sigma_{z_2}, \sigma_{z_3}} \right).
\end{aligned}$$

Going forward, we consider only pure neutron matter (PNM) calculations. This greatly simplifies Eq. (C.15).

$$\begin{aligned}
\langle \sigma_{z_1} \downarrow \sigma_{z_2} \downarrow | \hat{V}_{\text{Minn}}(\vec{r}, \hat{\sigma}, \hat{\tau}) | \sigma_{z_3} \downarrow \sigma_{z_4} \downarrow \rangle &= \left(\frac{V_{0R}}{2} e^{-k_R |\vec{r}|^2} + \frac{V_{0S}}{2} e^{-k_S |\vec{r}|^2} \right) \quad (\text{C.16}) \\
&\times \left(\delta_{\sigma_{z_1}, \sigma_{z_3}} \delta_{\sigma_{z_2}, \sigma_{z_4}} - \delta_{\sigma_{z_1}, \sigma_{z_4}} \delta_{\sigma_{z_2}, \sigma_{z_3}} \right).
\end{aligned}$$

The Minnesota potential in a finite box is then obtained using Eqs. (C.5) and (C.16).

$$\begin{aligned}
& \langle \vec{k}_1 \sigma_{z_1} \downarrow \vec{k}_2 \sigma_{z_2} \downarrow | \hat{V}_{\text{Minn}} | \vec{k}_3 \sigma_{z_3} \downarrow \vec{k}_4 \sigma_{z_4} \downarrow \rangle_{\text{Direct}} \quad (\text{C.17}) \\
&= \frac{\delta_{\vec{K}, \vec{K}'}}{2\mathcal{V}} \left(\delta_{\sigma_{z_1}, \sigma_{z_3}} \delta_{\sigma_{z_2}, \sigma_{z_4}} - \delta_{\sigma_{z_1}, \sigma_{z_4}} \delta_{\sigma_{z_2}, \sigma_{z_3}} \right) \\
&\times \int_{2^3\mathcal{V}} d^3r e^{-i\vec{q}\cdot\vec{r}} \left(V_{0R} e^{-k_R |\vec{r}|^2} + V_{0S} e^{-k_S |\vec{r}|^2} \right).
\end{aligned}$$

Let us consider just the first term of Eq. (C.17)'s integral.

$$\begin{aligned}
\int_{2^3\mathcal{V}} d^3r e^{-i\vec{q}\cdot\vec{r}} V_{0R} e^{-k_R |\vec{r}|^2} &= V_{0R} \int_{-\mathcal{L}}^{\mathcal{L}} dr_x e^{-iq_x r_x - k_R r_x^2} \quad (\text{C.18}) \\
&\times \int_{-\mathcal{L}}^{\mathcal{L}} dr_y e^{-iq_y r_y - k_R r_y^2} \int_{-\mathcal{L}}^{\mathcal{L}} dr_z e^{-iq_z r_z - k_R r_z^2}.
\end{aligned}$$

Eq. (C.18)'s integral over r_x is given by

$$\int_{-\mathcal{L}}^{\mathcal{L}} dr_x e^{-iq_x r_x - k_R r_x^2} = \sqrt{\frac{\pi}{k_R}} e^{-\frac{q_x^2}{4k_R}} \frac{1}{2} \left(\operatorname{erf} \left(\frac{2\mathcal{L}k_R - iq_x}{2\sqrt{k_R}} \right) + \operatorname{erf} \left(\frac{2\mathcal{L}k_R + iq_x}{2\sqrt{k_R}} \right) \right). \quad (\text{C.19})$$

And solutions to Eq. (C.18)'s integral over r_y and r_z , share the same structure as Eq. (C.19).

Therefore, Eq. (C.18) is given by

$$\begin{aligned} \int_{2^3\mathcal{V}} d^3r e^{-i\vec{q}\cdot\vec{r}} V_{0R} e^{-k_R |\vec{r}|^2} &= V_{0R} \sqrt{\frac{\pi^3}{k_R^3}} e^{-\frac{q_x^2 + q_y^2 + q_z^2}{4k_R}} \frac{1}{2^3} \\ &\times \left(\operatorname{erf} \left(\frac{2\mathcal{L}k_R - iq_x}{2\sqrt{k_R}} \right) + \operatorname{erf} \left(\frac{2\mathcal{L}k_R + iq_x}{2\sqrt{k_R}} \right) \right) \left(\operatorname{erf} \left(\frac{2\mathcal{L}k_R - iq_y}{2\sqrt{k_R}} \right) + \operatorname{erf} \left(\frac{2\mathcal{L}k_R + iq_y}{2\sqrt{k_R}} \right) \right) \\ &\times \left(\operatorname{erf} \left(\frac{2\mathcal{L}k_R - iq_z}{2\sqrt{k_R}} \right) + \operatorname{erf} \left(\frac{2\mathcal{L}k_R + iq_z}{2\sqrt{k_R}} \right) \right). \end{aligned} \quad (\text{C.20})$$

Likewise, the second term of Eq. (C.17)'s integral is given by

$$\begin{aligned} \int_{2^3\mathcal{V}} d^3r e^{-i\vec{q}\cdot\vec{r}} V_{0S} e^{-k_S |\vec{r}|^2} &= V_{0S} \sqrt{\frac{\pi^3}{k_S^3}} e^{-\frac{q_x^2 + q_y^2 + q_z^2}{4k_S}} \frac{1}{2^3} \\ &\times \left(\operatorname{erf} \left(\frac{2\mathcal{L}k_S - iq_x}{2\sqrt{k_S}} \right) + \operatorname{erf} \left(\frac{2\mathcal{L}k_S + iq_x}{2\sqrt{k_S}} \right) \right) \left(\operatorname{erf} \left(\frac{2\mathcal{L}k_S - iq_y}{2\sqrt{k_S}} \right) + \operatorname{erf} \left(\frac{2\mathcal{L}k_S + iq_y}{2\sqrt{k_S}} \right) \right) \\ &\times \left(\operatorname{erf} \left(\frac{2\mathcal{L}k_S - iq_z}{2\sqrt{k_S}} \right) + \operatorname{erf} \left(\frac{2\mathcal{L}k_S + iq_z}{2\sqrt{k_S}} \right) \right). \end{aligned} \quad (\text{C.21})$$

In total, combining Eqs. (C.20)–(C.21) into Eq. (C.17), the direct matrix element of the

Minnesota potential for PNM is obtained

$$\begin{aligned}
& \left\langle \vec{k}_1\sigma_{z_1} \downarrow \vec{k}_2\sigma_{z_2} \downarrow \left| \hat{V}_{\text{Minn}} \right| \vec{k}_3\sigma_{z_3} \downarrow \vec{k}_4\sigma_{z_4} \downarrow \right\rangle_{\text{Direct}} \quad (\text{C.22}) \\
&= \frac{\delta_{\vec{k}_1+\vec{k}_2, \vec{k}_3+\vec{k}_4}}{2\mathcal{L}^3} \left(\delta_{\sigma_{z_1}, \sigma_{z_3}} \delta_{\sigma_{z_2}, \sigma_{z_4}} - \delta_{\sigma_{z_1}, \sigma_{z_4}} \delta_{\sigma_{z_2}, \sigma_{z_3}} \right) \\
&\times \left[V_{0R} \sqrt{\frac{\pi^3}{k_R^3}} e^{-\frac{|q|^2}{4k_R}} \frac{1}{2^3} \left(\text{erf} \left(\frac{2\mathcal{L}k_R - iq_x}{2\sqrt{k_R}} \right) + \text{erf} \left(\frac{2\mathcal{L}k_R + iq_x}{2\sqrt{k_R}} \right) \right) \right. \\
&\times \left(\text{erf} \left(\frac{2\mathcal{L}k_R - iq_y}{2\sqrt{k_R}} \right) + \text{erf} \left(\frac{2\mathcal{L}k_R + iq_y}{2\sqrt{k_R}} \right) \right) \left(\text{erf} \left(\frac{2\mathcal{L}k_R - iq_z}{2\sqrt{k_R}} \right) + \text{erf} \left(\frac{2\mathcal{L}k_R + iq_z}{2\sqrt{k_R}} \right) \right) \\
&\quad + V_{0S} \sqrt{\frac{\pi^3}{k_S^3}} e^{-\frac{|q|^2}{4k_S}} \frac{1}{2^3} \left(\text{erf} \left(\frac{2\mathcal{L}k_S - iq_x}{2\sqrt{k_S}} \right) + \text{erf} \left(\frac{2\mathcal{L}k_S + iq_x}{2\sqrt{k_S}} \right) \right) \\
&\times \left. \left(\text{erf} \left(\frac{2\mathcal{L}k_S - iq_y}{2\sqrt{k_S}} \right) + \text{erf} \left(\frac{2\mathcal{L}k_S + iq_y}{2\sqrt{k_S}} \right) \right) \left(\text{erf} \left(\frac{2\mathcal{L}k_S - iq_z}{2\sqrt{k_S}} \right) + \text{erf} \left(\frac{2\mathcal{L}k_S + iq_z}{2\sqrt{k_S}} \right) \right) \right]
\end{aligned}$$

. Error functions are present in Eq. (C.22), because Eq. (C.17) is integrated within a finite box. Consequently, Eq. (C.22) differs from the expression given by Jensen *et al.* [19]—which perform the Eq. (C.17) integration within an *infinite* box. Given that we only work in a finite box, we suspect that Eq. (C.17) should indeed be integrated with finite \mathcal{L} . In practice, this is likely a minor issue since we generally work in large boxes. Note, $q \propto \frac{1}{\mathcal{L}}$ in Eq. (C.22). Hence, in the limit of large \mathcal{L} , all error functions converge to 1 in Eq. (C.22).

We can then anti-symmetrize Eq. (C.22) via subtracting the exchange matrix element from the direct matrix element

$$\begin{aligned}
& \left\langle \vec{k}_1\sigma_{z_1} \downarrow \vec{k}_2\sigma_{z_2} \downarrow \left| \hat{V}_{\text{Minn}} \right| \vec{k}_3\sigma_{z_3} \downarrow \vec{k}_4\sigma_{z_4} \downarrow \right\rangle_{AS} \quad (\text{C.23}) \\
&\equiv \left\langle \vec{k}_1\sigma_{z_1} \downarrow \vec{k}_2\sigma_{z_2} \downarrow \left| \hat{V}_{\text{Minn}} \right| \vec{k}_3\sigma_{z_3} \downarrow \vec{k}_4\sigma_{z_4} \downarrow \right\rangle_{\text{Direct}} \\
&\quad - \left\langle \vec{k}_1\sigma_{z_1} \downarrow \vec{k}_2\sigma_{z_2} \downarrow \left| \hat{V}_{\text{Minn}} \right| \vec{k}_4\sigma_{z_4} \downarrow \vec{k}_3\sigma_{z_3} \downarrow \right\rangle_{\text{Direct}} .
\end{aligned}$$

APPENDIX D. One Pion Exchange Interaction in a Finite Box

Within a finite box, we aim to calculate matrix elements of the leading order contact interaction, denoted ‘‘One Pion Exchange’’ (OPE).

$$\begin{aligned}
& \left\langle \vec{k}_1 \sigma_{z_1} \tau_{z_1} \vec{k}_2 \sigma_{z_2} \tau_{z_2} \left| \hat{V}_\Lambda^{1\pi} \right| \vec{k}_3 \sigma_{z_3} \tau_{z_3} \vec{k}_4 \sigma_{z_4} \tau_{z_4} \right\rangle_{Direct} \\
&= \frac{\delta_{\vec{K}', \vec{K}}}{\mathcal{V}} \left\langle \vec{k}' \sigma_{z_1} \tau_{z_1} \sigma_{z_2} \tau_{z_2} \left| \hat{V}_\Lambda^{1\pi} \left(\hat{k}', \hat{k}, \hat{\sigma}, \hat{\tau}, \mathcal{V} \right) \right| \vec{k} \sigma_{z_3} \tau_{z_3} \sigma_{z_4} \tau_{z_4} \right\rangle \\
&= \frac{\delta_{\vec{K}', \vec{K}}}{\mathcal{V}} \left\langle \sigma_{z_1} \tau_{z_1} \sigma_{z_2} \tau_{z_2} \left| \hat{V}_\Lambda^{1\pi} \left(\vec{k}', \vec{k}, \hat{\sigma}, \hat{\tau}, \mathcal{V} \right) \right| \sigma_{z_3} \tau_{z_3} \sigma_{z_4} \tau_{z_4} \right\rangle,
\end{aligned} \tag{D.1}$$

In this work, all chiral interactions will not depend on the box volume—implying that $\mathcal{V} \rightarrow \infty$. Thus, the box volume is dropped: $\hat{V}_\Lambda^{1\pi} \left(\vec{k}', \vec{k}, \hat{\sigma}, \hat{\tau}, \mathcal{V} \right) = \hat{V}_\Lambda^{1\pi} \left(\vec{k}', \vec{k}, \hat{\sigma}, \hat{\tau} \right)$. Moreover, the OPE only depends on the momentum transfer¹

$$\vec{q} \equiv \frac{\vec{k}_1 - \vec{k}_2 - \vec{k}_3 + \vec{k}_4}{2} = \vec{k}_1 - \vec{k}_3. \tag{D.2}$$

Thus, $\hat{V}_\Lambda^{1\pi} \left(\vec{k}', \vec{k}, \hat{\sigma}, \hat{\tau} \right) = \hat{V}_\Lambda^{1\pi} \left(\vec{q}, \hat{\sigma}, \hat{\tau} \right)$. And the OPE is given by [24]

$$\hat{V}_\Lambda^{1\pi} \left(\vec{q}, \hat{\sigma}, \hat{\tau} \right) = -\frac{(\hbar c)^3 g_A^2}{4F_\pi^2} (\hat{\tau}_1 \cdot \hat{\tau}_2) \left[\frac{(\hat{\sigma}_1 \cdot \vec{q})(\hat{\sigma}_2 \cdot \vec{q})}{q^2 + \left(\frac{M_\pi}{\hbar c}\right)^2} + C(\hat{\sigma}_1 \cdot \hat{\sigma}_2) \right] e^{-\frac{(\hbar c q)^2 + M_\pi^2}{\Lambda^2}} \tag{D.3a}$$

$$C = -\frac{\Lambda(\Lambda^2 - 2M_\pi^2) + 2\sqrt{\pi}M_\pi^3 e^{\frac{M_\pi^2}{\Lambda^2}} \operatorname{erfc}\left(\frac{M_\pi}{\Lambda}\right)}{3\Lambda^3}. \tag{D.3b}$$

$g_A = 1.267$ is the nucleon axial-vector coupling constant. $M_\pi = 139.57$ MeV is the pion mass. $F_\pi = 92.4$ MeV is the pion decay constant, and $\hbar c = 197.33$ MeV \times fm. The momentum transfer \vec{q} , is in units of fm⁻¹; the box volume \mathcal{V} , is in units of fm³; and C is unitless.² And

¹Momentum conservation $\vec{k}_1 + \vec{k}_2 = \vec{k}_3 + \vec{k}_4$, is used to simplify Eq. (D.2).

²We manually set $C = 0$ in this work.

the regulator cutoff Λ , is in units of MeV. All spin/isospin Pauli operators are unitless; and $|\hat{\vec{\tau}}| = |\hat{\vec{\sigma}}| = 1$. Lastly, $\text{erfc}(\frac{M\pi}{\Lambda})$ is the complimentary error function.

Since spin and isospin operators act on two independent spaces, we can easily factor our analysis.

$$\begin{aligned} & \langle \sigma_{z_1} \tau_{z_1} \sigma_{z_2} \tau_{z_2} | \hat{V}_\Lambda^{1\pi}(\vec{q}, \hat{\vec{\sigma}}, \hat{\vec{\tau}}) | \sigma_{z_3} \tau_{z_3} \sigma_{z_4} \tau_{z_4} \rangle \\ &= \langle \sigma_{z_1} \sigma_{z_2} | \langle \tau_{z_1} \tau_{z_2} | \hat{V}_\Lambda^{1\pi}(\vec{q}, \hat{\vec{\sigma}}, \hat{\vec{\tau}}) | \tau_{z_3} \tau_{z_4} \rangle | \sigma_{z_3} \sigma_{z_4} \rangle \end{aligned} \quad (\text{D.4})$$

We first consider matrix elements between orthonormal isospin states.

$$\begin{aligned} \langle \tau_{z_1} \tau_{z_2} | \hat{V}_\Lambda^{1\pi}(\vec{q}, \hat{\vec{\sigma}}, \hat{\vec{\tau}}) | \tau_{z_3} \tau_{z_4} \rangle &= -\frac{(\hbar c)^3 g_A^2}{4F_\pi^2} \langle \tau_{z_1} \tau_{z_2} | \hat{\vec{\tau}}_1 \cdot \hat{\vec{\tau}}_2 | \tau_{z_3} \tau_{z_4} \rangle \\ &\times \left[\frac{(\hat{\vec{\sigma}}_1 \cdot \vec{q})(\hat{\vec{\sigma}}_2 \cdot \vec{q})}{q^2 + (\frac{M\pi}{\hbar c})^2} + C(\hat{\vec{\sigma}}_1 \cdot \hat{\vec{\sigma}}_2) \right] e^{-\frac{(\hbar c q)^2 + M_\pi^2}{\Lambda^2}}. \end{aligned} \quad (\text{D.5})$$

Note, the Pauli operators can be written in terms of permutation operators

$$\hat{\vec{\sigma}}_1 \cdot \hat{\vec{\sigma}}_2 = 2\hat{P}_{12}^\sigma - 1 \quad (\text{D.6a})$$

$$\hat{\vec{\tau}}_1 \cdot \hat{\vec{\tau}}_2 = 2\hat{P}_{12}^\tau - 1. \quad (\text{D.6b})$$

\hat{P}_{12}^σ and \hat{P}_{12}^τ act on orthonormal two-particle spin and isospin projection states on the z axis, respectively in the following manner:

$$\hat{P}_{12}^\sigma | \sigma_{z_1} = \uparrow, \sigma_{z_2} = \uparrow \rangle = |\uparrow\uparrow\rangle, \quad \hat{P}_{12}^\sigma |\downarrow\downarrow\rangle = |\downarrow\downarrow\rangle, \quad \hat{P}_{12}^\sigma |\uparrow\downarrow\rangle = |\downarrow\uparrow\rangle, \quad \hat{P}_{12}^\sigma |\downarrow\uparrow\rangle = |\uparrow\downarrow\rangle, \quad (\text{D.7})$$

$$\hat{P}_{12}^\tau | \tau_{z_1} = \uparrow, \tau_{z_2} = \uparrow \rangle = |\uparrow\uparrow\rangle, \quad \hat{P}_{12}^\tau |\downarrow\downarrow\rangle = |\downarrow\downarrow\rangle, \quad \hat{P}_{12}^\tau |\uparrow\downarrow\rangle = |\downarrow\uparrow\rangle, \quad \hat{P}_{12}^\tau |\downarrow\uparrow\rangle = |\uparrow\downarrow\rangle.$$

Thus, we can rewrite Eq. (D.5)

$$\begin{aligned} \langle \tau_{z_1} \tau_{z_2} | \hat{V}_\Lambda^{1\pi} (\vec{q}, \hat{\vec{\sigma}}, \hat{\vec{\tau}}) | \tau_{z_3} \tau_{z_4} \rangle &= -\frac{(\hbar c)^3 g_A^2}{4F_\pi^2} \langle \tau_{z_1} \tau_{z_2} | 2\hat{P}_{12}^\tau - 1 | \tau_{z_3} \tau_{z_4} \rangle \\ &\times \left[\frac{(\hat{\vec{\sigma}}_1 \cdot \vec{q})(\hat{\vec{\sigma}}_2 \cdot \vec{q})}{q^2 + (\frac{M_\pi}{\hbar c})^2} + C(2\hat{P}_{12}^\sigma - 1) \right] e^{-\frac{(\hbar c q)^2 + M_\pi^2}{\Lambda^2}}, \end{aligned} \quad (\text{D.8})$$

where

$$\langle \tau_{z_1} \tau_{z_2} | 2\hat{P}_{12}^\tau - 1 | \tau_{z_3} \tau_{z_4} \rangle = 2 \delta_{\tau_{z_1}, \tau_{z_4}} \delta_{\tau_{z_2}, \tau_{z_3}} - \delta_{\tau_{z_1}, \tau_{z_3}} \delta_{\tau_{z_2}, \tau_{z_4}}. \quad (\text{D.9})$$

For brevity, we choose to define the overlap

$$O(\tau_z) \equiv \langle \tau_{z_1} \tau_{z_2} | 2\hat{P}_{12}^\tau - 1 | \tau_{z_3} \tau_{z_4} \rangle = 2 \delta_{\tau_{z_1}, \tau_{z_4}} \delta_{\tau_{z_2}, \tau_{z_3}} - \delta_{\tau_{z_1}, \tau_{z_3}} \delta_{\tau_{z_2}, \tau_{z_4}}. \quad (\text{D.10})$$

Therefore,

$$\begin{aligned} \langle \tau_{z_1} \tau_{z_2} | \hat{V}_\Lambda^{1\pi} (\vec{q}, \hat{\vec{\sigma}}, \hat{\vec{\tau}}) | \tau_{z_3} \tau_{z_4} \rangle &= -\frac{(\hbar c)^3 g_A^2}{4F_\pi^2} O(\tau_z) \\ &\times \left[\frac{(\hat{\vec{\sigma}}_1 \cdot \vec{q})(\hat{\vec{\sigma}}_2 \cdot \vec{q})}{q^2 + (\frac{M_\pi}{\hbar c})^2} + C(2\hat{P}_{12}^\sigma - 1) \right] e^{-\frac{(\hbar c q)^2 + M_\pi^2}{\Lambda^2}}. \end{aligned} \quad (\text{D.11})$$

Revisiting Eq. (D.4), we now consider overlaps between orthonormal spin states.

$$\begin{aligned} &\langle \sigma_{z_1} \tau_{z_1} \sigma_{z_2} \tau_{z_2} | \hat{V}_\Lambda^{1\pi} (\vec{q}, \hat{\vec{\sigma}}, \hat{\vec{\tau}}) | \sigma_{z_3} \tau_{z_3} \sigma_{z_4} \tau_{z_4} \rangle \\ &= \langle \sigma_{z_1} \sigma_{z_2} | -\frac{(\hbar c)^3 g_A^2}{4F_\pi^2} O(\tau_z) \left[\frac{(\hat{\vec{\sigma}}_1 \cdot \vec{q})(\hat{\vec{\sigma}}_2 \cdot \vec{q})}{q^2 + (\frac{M_\pi}{\hbar c})^2} + C(2\hat{P}_{12}^\sigma - 1) \right] e^{-\frac{(\hbar c q)^2 + M_\pi^2}{\Lambda^2}} | \sigma_{z_3} \sigma_{z_4} \rangle \\ &= -\frac{(\hbar c)^3 g_A^2}{4F_\pi^2} O(\tau_z) e^{-\frac{(\hbar c q)^2 + M_\pi^2}{\Lambda^2}} \langle \sigma_{z_1} \sigma_{z_2} | \left[\frac{(\hat{\vec{\sigma}}_1 \cdot \vec{q})(\hat{\vec{\sigma}}_2 \cdot \vec{q})}{q^2 + (\frac{M_\pi}{\hbar c})^2} + C(2\hat{P}_{12}^\sigma - 1) \right] | \sigma_{z_3} \sigma_{z_4} \rangle. \end{aligned} \quad (\text{D.12})$$

$$\begin{aligned}
& \langle \sigma_{z_1} \sigma_{z_2} | \left[\frac{(\hat{\vec{\sigma}}_1 \cdot \vec{q})(\hat{\vec{\sigma}}_2 \cdot \vec{q})}{q^2 + (\frac{M\pi}{\hbar c})^2} + C(2\hat{P}_{12}^\sigma - 1) \right] | \sigma_{z_3} \sigma_{z_4} \rangle \\
&= \langle \sigma_{z_1} \sigma_{z_2} | \frac{(\hat{\vec{\sigma}}_1 \cdot \vec{q})(\hat{\vec{\sigma}}_2 \cdot \vec{q})}{q^2 + (\frac{M\pi}{\hbar c})^2} | \sigma_{z_3} \sigma_{z_4} \rangle + C \langle \sigma_{z_1} \sigma_{z_2} | 2\hat{P}_{12}^\sigma - 1 | \sigma_{z_3} \sigma_{z_4} \rangle .
\end{aligned} \tag{D.13}$$

Reminiscent of Eq. (D.9), the second term of Eq. (D.13) is easily given by

$$\langle \sigma_{z_1} \sigma_{z_2} | 2\hat{P}_{12}^\sigma - 1 | \sigma_{z_3} \sigma_{z_4} \rangle = 2 \delta_{\sigma_{z_1}, \sigma_{z_4}} \delta_{\sigma_{z_2}, \sigma_{z_3}} - \delta_{\sigma_{z_1}, \sigma_{z_3}} \delta_{\sigma_{z_2}, \sigma_{z_4}} . \tag{D.14}$$

Therefore,

$$\begin{aligned}
& \langle \sigma_{z_1} \sigma_{z_2} | \left[\frac{(\hat{\vec{\sigma}}_1 \cdot \vec{q})(\hat{\vec{\sigma}}_2 \cdot \vec{q})}{q^2 + (\frac{M\pi}{\hbar c})^2} + C(2\hat{P}_{12}^\sigma - 1) \right] | \sigma_{z_3} \sigma_{z_4} \rangle \\
&= \frac{1}{q^2 + (\frac{M\pi}{\hbar c})^2} \langle \sigma_{z_1} \sigma_{z_2} | (\hat{\vec{\sigma}}_1 \cdot \vec{q})(\hat{\vec{\sigma}}_2 \cdot \vec{q}) | \sigma_{z_3} \sigma_{z_4} \rangle \\
&+ C \times \left(2 \delta_{\sigma_{z_1}, \sigma_{z_4}} \delta_{\sigma_{z_2}, \sigma_{z_3}} - \delta_{\sigma_{z_1}, \sigma_{z_3}} \delta_{\sigma_{z_2}, \sigma_{z_4}} \right) .
\end{aligned} \tag{D.15}$$

Since both interacting particles are described by independent single-particle wavefunctions, we can easily factor our analysis.

$$\begin{aligned}
& \langle \sigma_{z_1} \sigma_{z_2} | (\hat{\vec{\sigma}}_1 \cdot \vec{q})(\hat{\vec{\sigma}}_2 \cdot \vec{q}) | \sigma_{z_3} \sigma_{z_4} \rangle = \langle \sigma_{z_1} | (\hat{\vec{\sigma}}_1 \cdot \vec{q}) | \sigma_{z_3} \rangle \langle \sigma_{z_2} | (\hat{\vec{\sigma}}_2 \cdot \vec{q}) | \sigma_{z_4} \rangle \\
&= [\langle \sigma_{z_1} | \hat{\sigma}_{x_1} | \sigma_{z_3} \rangle q_x + \langle \sigma_{z_1} | \hat{\sigma}_{y_1} | \sigma_{z_3} \rangle q_y + \langle \sigma_{z_1} | \hat{\sigma}_{z_1} | \sigma_{z_3} \rangle q_z] \\
&\times [\langle \sigma_{z_2} | \hat{\sigma}_{x_2} | \sigma_{z_4} \rangle q_x + \langle \sigma_{z_2} | \hat{\sigma}_{y_2} | \sigma_{z_4} \rangle q_y + \langle \sigma_{z_2} | \hat{\sigma}_{z_2} | \sigma_{z_4} \rangle q_z]
\end{aligned} \tag{D.16}$$

$|\sigma_x\rangle$, and $|\sigma_y\rangle$ are spin projection states along the x -axis and y -axis, respectively. Due to the uncertainty principle, $|\sigma_x\rangle$, and $|\sigma_y\rangle$ are unknown if $|\sigma_z\rangle$ is known. Thus, we must write

$\hat{\sigma}_x$ and $\hat{\sigma}_y$ in terms of raising and lowering operators that act upon $|\sigma_z\rangle$.

$$\hat{\sigma}_x = \frac{1}{2}(\hat{\sigma}_+ + \hat{\sigma}_-) \quad (\text{D.17a})$$

$$\hat{\sigma}_y = \frac{1}{2i}(\hat{\sigma}_+ - \hat{\sigma}_-) , \quad (\text{D.17b})$$

where³

$$\hat{\sigma}_\pm |\sigma, \sigma_z\rangle = \sqrt{\sigma(\sigma+2) - \sigma_z(\sigma_z \pm 2)} |\sigma, \sigma_z \pm 2\rangle . \quad (\text{D.18})$$

Therefore,

$$\langle \sigma, \sigma_{z_1} | \hat{\sigma}_\pm | \sigma, \sigma_{z_3} \rangle = \delta_{\sigma_{z_1}, \sigma_{z_3} \pm 2} \times \sqrt{\sigma(\sigma+2) - \sigma_{z_3} \sigma_{z_1}} \quad (\text{D.19a})$$

$$\langle \sigma, \sigma_{z_1} | \hat{\sigma}_x | \sigma, \sigma_{z_3} \rangle = \frac{1}{2}(\delta_{\sigma_{z_1}, \sigma_{z_3}+2} + \delta_{\sigma_{z_1}, \sigma_{z_3}-2}) \times \sqrt{\sigma(\sigma+2) - \sigma_{z_3} \sigma_{z_1}} \quad (\text{D.19b})$$

$$\langle \sigma, \sigma_{z_1} | \hat{\sigma}_y | \sigma, \sigma_{z_3} \rangle = \frac{1}{2i}(\delta_{\sigma_{z_1}, \sigma_{z_3}+2} - \delta_{\sigma_{z_1}, \sigma_{z_3}-2}) \times \sqrt{\sigma(\sigma+2) - \sigma_{z_3} \sigma_{z_1}} \quad (\text{D.19c})$$

$$\langle \sigma, \sigma_{z_1} | \hat{\sigma}_z | \sigma, \sigma_{z_3} \rangle = \delta_{\sigma_{z_1}, \sigma_{z_3}} \times \sigma_{z_3} . \quad (\text{D.19d})$$

³In this appendix, $\sigma_z = \pm 1$ and likewise, $\tau_z = \pm 1$. Therefore, spin up and spin down states are separated by 2 units of spin. The same can also be said for isospin states.

Using Eqs. (D.16) and (D.19),

$$\begin{aligned}
& \langle \sigma_{z_1} \sigma_{z_2} | (\hat{\vec{\sigma}}_1 \cdot \vec{q})(\hat{\vec{\sigma}}_2 \cdot \vec{q}) | \sigma_{z_3} \sigma_{z_4} \rangle \quad (D.20) \\
&= \left[q_z \sigma_{z_3} \delta_{\sigma_{z_1}, \sigma_{z_3}} + \sqrt{\sigma(\sigma+2) - \sigma_{z_3} \sigma_{z_1}} \right. \\
&\times \left[\frac{q_x}{2} (\delta_{\sigma_{z_1}, \sigma_{z_3}+2} + \delta_{\sigma_{z_1}, \sigma_{z_3}-2}) + \frac{q_y}{2i} (\delta_{\sigma_{z_1}, \sigma_{z_3}+2} - \delta_{\sigma_{z_1}, \sigma_{z_3}-2}) \right] \\
&\times \left[q_z \sigma_{z_4} \delta_{\sigma_{z_2}, \sigma_{z_4}} + \sqrt{\sigma(\sigma+2) - \sigma_{z_4} \sigma_{z_2}} \right. \\
&\times \left. \left. \left[\frac{q_x}{2} (\delta_{\sigma_{z_2}, \sigma_{z_4}+2} + \delta_{\sigma_{z_2}, \sigma_{z_4}-2}) + \frac{q_y}{2i} (\delta_{\sigma_{z_2}, \sigma_{z_4}+2} - \delta_{\sigma_{z_2}, \sigma_{z_4}-2}) \right] \right] \right].
\end{aligned}$$

In conclusion,

$$\begin{aligned}
& \langle \vec{k}_1 \sigma_{z_1} \tau_{z_1} \vec{k}_2 \sigma_{z_2} \tau_{z_2} | \hat{V}_\Lambda^{1\pi} | \vec{k}_3 \sigma_{z_3} \tau_{z_3} \vec{k}_4 \sigma_{z_4} \tau_{z_4} \rangle_{Direct} \quad (D.21) \\
&= -\frac{(\hbar c)^3 g_A^2}{4\mathcal{V}F_\pi^2} \times \delta_{\vec{K}', \vec{K}} \times \left(2 \delta_{\tau_{z_1}, \tau_{z_4}} \delta_{\tau_{z_2}, \tau_{z_3}} - \delta_{\tau_{z_1}, \tau_{z_3}} \delta_{\tau_{z_2}, \tau_{z_4}} \right) \times e^{-\frac{(\hbar c q)^2 + M_\pi^2}{\Lambda^2}} \\
&\times \left[\frac{\langle \sigma_{z_1} \sigma_{z_2} | (\hat{\vec{\sigma}}_1 \cdot \vec{q})(\hat{\vec{\sigma}}_2 \cdot \vec{q}) | \sigma_{z_3} \sigma_{z_4} \rangle}{q^2 + \left(\frac{M_\pi}{\hbar c}\right)^2} + C \times \left(2 \delta_{\sigma_{z_1}, \sigma_{z_4}} \delta_{\sigma_{z_2}, \sigma_{z_3}} - \delta_{\sigma_{z_1}, \sigma_{z_3}} \delta_{\sigma_{z_2}, \sigma_{z_4}} \right) \right],
\end{aligned}$$

where $\langle \sigma_{z_1} \sigma_{z_2} | (\hat{\vec{\sigma}}_1 \cdot \vec{q})(\hat{\vec{\sigma}}_2 \cdot \vec{q}) | \sigma_{z_3} \sigma_{z_4} \rangle$ is given in Eq. (D.20). And the anti-symmetrized

OPE is then given by

$$\begin{aligned}
& \langle \vec{k}_1 \sigma_{z_1} \tau_{z_1} \vec{k}_2 \sigma_{z_2} \tau_{z_2} | \hat{V}_\Lambda^{1\pi} | \vec{k}_3 \sigma_{z_3} \tau_{z_3} \vec{k}_4 \sigma_{z_4} \tau_{z_4} \rangle_{AS} \quad (D.22) \\
&\equiv \langle \vec{k}_1 \sigma_{z_1} \tau_{z_1} \vec{k}_2 \sigma_{z_2} \tau_{z_2} | \hat{V}_\Lambda^{1\pi} | \vec{k}_3 \sigma_{z_3} \tau_{z_3} \vec{k}_4 \sigma_{z_4} \tau_{z_4} \rangle_{Direct} \\
&- \langle \vec{k}_1 \sigma_{z_1} \tau_{z_1} \vec{k}_2 \sigma_{z_2} \tau_{z_2} | \hat{V}_\Lambda^{1\pi} | \vec{k}_4 \sigma_{z_4} \tau_{z_4} \vec{k}_3 \sigma_{z_3} \tau_{z_3} \rangle_{Direct}.
\end{aligned}$$

APPENDIX E. Partial Wave Expansion for Two-Body Forces

Chiral two-body forces are typically given in terms of partial waves where the following quantum numbers are specified: two-particle total orbital angular momentum L & L' , total spin S & S' , total isospin T & T' and isospin projection M_T & M'_T , total momentum $J = \|\vec{L} + \vec{S}\|$ & $J' = \|\vec{L}' + \vec{S}'\|$ and respective projections M_J & M'_J , and norms of relative momenta $k = \|\vec{k}\|$ & $k' = \|\vec{k}'\|$ for both incoming and outgoing particles, respectively. Given that we primarily work in a basis where the quantum numbers of single-particle states are decoupled (called “m-scheme”), it is essential to know how to convert matrix elements of an interaction given in a coupled representation (called “J-scheme”) into a decoupled representation. We will do such conversions in this appendix. Moreover, we will exploit convenient symmetries of the nuclear force such as: charge conservation $M_T = M'_T$, total spin and isospin conservation $S = S'$ and $T = T'$, total momentum conservation $J = J'$, and degeneracy in M_J .

We aim to compute $\langle \vec{k}' \sigma_{z_1} \tau_{z_1} \sigma_{z_2} \tau_{z_2} | \hat{V}(\hat{k}', \hat{k}, \hat{\sigma}, \hat{\tau}, \mathcal{V}) | \vec{k} \sigma_{z_3} \tau_{z_3} \sigma_{z_4} \tau_{z_4} \rangle$ —seen in Eq. (B.23), using the partial wave expansion. In this work, all chiral interactions will not depend on the box volume—implying that $\mathcal{V} \rightarrow \infty$. Thus, the box volume is dropped: $\hat{V}(\hat{k}', \hat{k}, \hat{\sigma}, \hat{\tau}, \mathcal{V}) = \hat{V}(\hat{k}', \hat{k}, \hat{\sigma}, \hat{\tau})$. Going forward, for brevity, we omit the operator dependence of \hat{k}' , \hat{k} , $\hat{\sigma}$, and $\hat{\tau}$ in \hat{V} , since the states $|\vec{k}' \sigma_{z_1} \tau_{z_1} \sigma_{z_2} \tau_{z_2}\rangle$ imply as such. Hence, $\hat{V} \equiv \hat{V}(\vec{k}', \vec{k}, \hat{\sigma}, \hat{\tau})$. Notice,¹

$$\begin{aligned} & \langle \vec{k}' \sigma_{z_1} \tau_{z_1} \sigma_{z_2} \tau_{z_2} | \hat{V} | \vec{k} \sigma_{z_3} \tau_{z_3} \sigma_{z_4} \tau_{z_4} \rangle \\ &= \langle \vec{k}' | \langle \sigma_{z_1} \tau_{z_1} \sigma_{z_2} \tau_{z_2} | \hat{V} | \sigma_{z_3} \tau_{z_3} \sigma_{z_4} \tau_{z_4} \rangle | \vec{k} \rangle \end{aligned} \quad (\text{E.1})$$

We first will calculate the spin and isospin matrix elements of \hat{V} . The spin and isospin

¹Although σ_{z_3} , τ_{z_3} , σ_{z_4} , τ_{z_4} are typically integers, we use them as half-integers in this appendix.

wavefunctions are given by

$$\begin{aligned}
|\sigma_{z_3}\tau_{z_3}\sigma_{z_4}\tau_{z_4}\rangle &= \sum_{T \in \{0,1\}} \mathcal{C}_{\frac{1}{2}\tau_{z_3}\frac{1}{2}\tau_{z_4}}^{TM_T} |T, M_T = \tau_{z_3} + \tau_{z_4}\rangle \\
&\otimes \sum_{S \in \{0,1\}} \mathcal{C}_{\frac{1}{2}\sigma_{z_3}\frac{1}{2}\sigma_{z_4}}^{SM_S} |S, M_S = \sigma_{z_3} + \sigma_{z_4}\rangle .
\end{aligned} \tag{E.2}$$

Likewise,

$$\begin{aligned}
|\sigma_{z_1}\tau_{z_1}\sigma_{z_2}\tau_{z_2}\rangle^* &= \sum_{T' \in \{0,1\}} \mathcal{C}_{\frac{1}{2}\tau_{z_1}\frac{1}{2}\tau_{z_2}}^{T'M'_T} |T', M'_T = \tau_{z_1} + \tau_{z_2}\rangle^* \\
&\otimes \sum_{S' \in \{0,1\}} \mathcal{C}_{\frac{1}{2}\sigma_{z_1}\frac{1}{2}\sigma_{z_2}}^{S'M'_S} |S', M'_S = \sigma_{z_1} + \sigma_{z_2}\rangle^* .
\end{aligned} \tag{E.3}$$

$\mathcal{C}_{\frac{1}{2}\sigma_{z_3}\frac{1}{2}\sigma_{z_4}}^{SM_S}$ are Clebsch-Gordan coefficients for spin 1/2 particles. Likewise, $\mathcal{C}_{\frac{1}{2}\tau_{z_3}\frac{1}{2}\tau_{z_4}}^{TM_T}$ are Clebsch-Gordan coefficients for isospin 1/2 particles. The nuclear force \hat{V} , conserves total charge $M_T = M'_T$, total spin $S = S'$ and total isospin $T = T'$. Enforcing the symmetries of \hat{V} , we obtain

$$\begin{aligned}
\langle \sigma_{z_1}\tau_{z_1}\sigma_{z_2}\tau_{z_2} | \hat{V} | \sigma_{z_3}\tau_{z_3}\sigma_{z_4}\tau_{z_4} \rangle &= \sum_{\substack{T \in \{0,1\} \\ S \in \{0,1\}}} \mathcal{C}_{\frac{1}{2}\tau_{z_1}\frac{1}{2}\tau_{z_2}}^{TM_T} \mathcal{C}_{\frac{1}{2}\sigma_{z_1}\frac{1}{2}\sigma_{z_2}}^{SM'_S} \mathcal{C}_{\frac{1}{2}\tau_{z_3}\frac{1}{2}\tau_{z_4}}^{TM_T} \mathcal{C}_{\frac{1}{2}\sigma_{z_3}\frac{1}{2}\sigma_{z_4}}^{SM_S} \\
&\times \langle TM_T SM'_S | \hat{V} | TM_T SM_S \rangle .
\end{aligned} \tag{E.4}$$

Combining Eqs. (E.4) and (E.1), we obtain

$$\begin{aligned}
& \left\langle \vec{k}' \sigma_{z_1} \tau_{z_1} \sigma_{z_2} \tau_{z_2} \left| \hat{V} \right| \vec{k} \sigma_{z_3} \tau_{z_3} \sigma_{z_4} \tau_{z_4} \right\rangle \\
&= \sum_{\substack{T \in \{0,1\} \\ S \in \{0,1\}}} \mathcal{C}_{\frac{1}{2}\tau_{z_1} \frac{1}{2}\tau_{z_2}}^{TM_T} \mathcal{C}_{\frac{1}{2}\sigma_{z_1} \frac{1}{2}\sigma_{z_2}}^{SM'_S} \mathcal{C}_{\frac{1}{2}\tau_{z_3} \frac{1}{2}\tau_{z_4}}^{TM_T} \mathcal{C}_{\frac{1}{2}\sigma_{z_3} \frac{1}{2}\sigma_{z_4}}^{SM_S} \times \left\langle \vec{k}' TM_T SM'_S \left| \hat{V} \right| \vec{k} TM_T SM_S \right\rangle.
\end{aligned} \tag{E.5}$$

Ultimately, $\left| \vec{k} TM_T SM_S \right\rangle$ is a vector valued function. We can expand the angular components of this function on a complete basis composed of spherical harmonics. Inserting the identity

$$\mathbb{1} \equiv \sum_{\substack{L \in [0, \infty] \\ -L \leq M_L \leq L}} |LM_L\rangle \langle LM_L| \tag{E.6}$$

into $\langle \vec{k}' TM_T SM'_S | \hat{V} | \vec{k} TM_T SM_S \rangle$ from Eq. (E.5), yields

$$\begin{aligned}
& \langle \vec{k}' TM_T SM'_S | \hat{V} | \vec{k} TM_T SM_S \rangle \tag{E.7} \\
&= \sum_{\substack{L, L' \in [0, \infty] \\ -L' \leq M'_L \leq L' \\ -L \leq M_L \leq L}} \langle \vec{k}' TM_T SM'_S | L' M'_L \rangle \langle L' M'_L | \hat{V} | LM_L \rangle \langle LM_L | \vec{k} TM_T SM_S \rangle \\
&= \sum_{\substack{L, L' \in [0, \infty] \\ -L' \leq M'_L \leq L' \\ -L \leq M_L \leq L}} \langle TM_T SM'_S | \langle \vec{k}' | L' M'_L \rangle \langle L' M'_L | \hat{V} | LM_L \rangle \langle LM_L | \vec{k} \rangle | TM_T SM_S \rangle \\
&= \sum_{\substack{L, L' \in [0, \infty] \\ -L' \leq M'_L \leq L' \\ -L \leq M_L \leq L}} \langle TM_T SM'_S | \left\langle k' \underbrace{\vec{k}'_{\text{unit}}}_{\text{Unit vector}} \middle| L' M'_L \right\rangle \langle L' M'_L | \hat{V} | LM_L \rangle \\
&\quad \times \left\langle LM_L \middle| k \underbrace{\vec{k}_{\text{unit}}}_{\text{Unit vector}} \right\rangle | TM_T SM_S \rangle \\
&= \sum_{\substack{L, L' \in [0, \infty] \\ -L' \leq M'_L \leq L' \\ -L \leq M_L \leq L}} \langle \vec{k}'_{\text{unit}} | L' M'_L \rangle \langle LM_L | \vec{k}_{\text{unit}} \rangle \langle k' TM_T SM'_S L' M'_L | \hat{V} | k TM_T SM_S LM_L \rangle,
\end{aligned}$$

where $\langle \vec{k}'_{\text{unit}} | L' M'_L \rangle$ and $\langle LM_L | \vec{k}_{\text{unit}} \rangle$ are spherical harmonics

$$\langle \vec{k}'_{\text{unit}} | L' M'_L \rangle \equiv 4\pi i^{-L'} Y_{L'}^{M'_L}(\vec{k}'_{\text{unit}}) \tag{E.8a}$$

$$\langle LM_L | \vec{k}_{\text{unit}} \rangle \equiv 4\pi i^L \left(Y_L^{M_L}(\vec{k}_{\text{unit}}) \right)^*. \tag{E.8b}$$

Therefore,

$$\begin{aligned}
& \langle \vec{k}' T M_T S M'_S | \hat{V} | \vec{k} T M_T S M_S \rangle \tag{E.9} \\
&= (4\pi)^2 \sum_{\substack{L, L' \in [0, \infty] \\ -L' \leq M'_L \leq L' \\ -L \leq M_L \leq L}} \left(i^{L-L'} Y_{L'}^{M'_L}(\vec{k}'_{\text{unit}}) Y_L^{M_L^*}(\vec{k}_{\text{unit}}) \right) \\
& \quad \times \langle k' T M_T S M'_S L' M'_L | \hat{V} | k T M_T S M_S L M_L \rangle.
\end{aligned}$$

If \hat{V} contains a nonzero tensor force, then calculating matrix elements of \hat{V} in a basis where orbital angular momentum quantum numbers L & L' are known will be nonoptimal because $\langle \dots L' M'_L | \hat{V} | \dots L M_L \rangle$ may be nondiagonal in L & L' . However, \hat{V} is guaranteed to be not only diagonal in a basis of total angular momentum $\vec{J} = \vec{L} + \vec{S}$, but also independent of projection $M_J = M_L + M_S$. Thus, let us transform into total angular momentum coordinates:

$$|S M_S L M_L\rangle = \sum_{|L-S| \leq J \leq L+S} C_{L M_L S M_S}^{J M_J} |(L S) J M_J\rangle. \tag{E.10}$$

Combining Eqs. (E.10) and (E.9), we obtain

$$\begin{aligned}
& \langle \vec{k}' T M_T S M'_S | \hat{V} | \vec{k} T M_T S M_S \rangle = (4\pi)^2 \sum_{\substack{L, L' \in [0, \infty] \\ -L' \leq M'_L \leq L' \\ -L \leq M_L \leq L}} \left(i^{L-L'} \right) Y_{L'}^{M'_L}(\vec{k}'_{\text{unit}}) Y_L^{M_L*}(\vec{k}_{\text{unit}}) \\
& \times \sum_{\substack{|L-S| \leq J \leq L+S \\ |L'-S| \leq J' \leq L'+S}} C_{L'M'_L S M'_S}^{J' M'_J} C_{L M_L S M_S}^{J M_J} \langle k' T M_T(L'S) J' M'_J | \hat{V} | k T M_T(LS) J M_J \rangle \delta_{J, J'} \\
& = (4\pi)^2 \sum_{\substack{L, L' \in [0, \infty] \\ -L' \leq M'_L \leq L' \\ -L \leq M_L \leq L}} \left(i^{L-L'} \right) Y_{L'}^{M'_L}(\vec{k}'_{\text{unit}}) Y_L^{M_L*}(\vec{k}_{\text{unit}}) \\
& \times \sum_{|L-S| \leq J \leq L+S} C_{L'M'_L S M'_S}^{J M'_J} C_{L M_L S M_S}^{J M_J} \langle k' T M_T(L'S) J | \hat{V} | k T M_T(LS) J \rangle \langle M'_J | M_J \rangle \\
& = (4\pi)^2 \sum_{\substack{L, L' \in [0, \infty] \\ -L' \leq M'_L \leq L' \\ -L \leq M_L \leq L}} \left(i^{L-L'} \right) Y_{L'}^{M'_L}(\vec{k}'_{\text{unit}}) Y_L^{M_L*}(\vec{k}_{\text{unit}}) \\
& \times \sum_{|L-S| \leq J \leq L+S} C_{L'M'_L S M'_S}^{J M_J} C_{L M_L S M_S}^{J M_J} \langle k' T M_T(L'S) J | \hat{V} | k T M_T(LS) J \rangle \delta_{M_{L'}, M_S + M_L - M_{S'}}
\end{aligned} \tag{E.11}$$

Combining Eqs. (B.23), (E.5) and (E.11), we obtain the partial wave decomposition for the

momentum space matrix elements of \hat{V} , in a finite box:

$$\begin{aligned}
& \left\langle \vec{k}_1 \sigma_{z_1} \tau_{z_1} \vec{k}_2 \sigma_{z_2} \tau_{z_2} \left| \hat{V} \right| \vec{k}_3 \sigma_{z_3} \tau_{z_3} \vec{k}_4 \sigma_{z_4} \tau_{z_4} \right\rangle_{Direct} \quad (E.12) \\
&= \mathcal{U} \frac{\delta_{\vec{K}, \vec{K}'}}{\mathcal{V}} (4\pi)^2 \sum_{\substack{L, L' \in [0, \infty] \\ -L \leq M_L \leq L \\ T, S \in \{0, 1\}}} \mathcal{C}_{\frac{1}{2}\tau_{z_1} \frac{1}{2}\tau_{z_2}}^{TM_T} \mathcal{C}_{\frac{1}{2}\sigma_{z_1} \frac{1}{2}\sigma_{z_2}}^{SM'_S} \mathcal{C}_{\frac{1}{2}\tau_{z_3} \frac{1}{2}\tau_{z_4}}^{TM_T} \mathcal{C}_{\frac{1}{2}\sigma_{z_3} \frac{1}{2}\sigma_{z_4}}^{SM_S} \\
&\quad \times \left(i^{L-L'} \right) Y_{L'}^{M'_L}(\vec{k}'_{\text{unit}}) Y_L^{M_L^*}(\vec{k}_{\text{unit}}) \\
&\quad \times \sum_{|L-S| \leq J \leq L+S} \mathcal{C}_{L'M'_L S M'_S}^{JM_J} \mathcal{C}_{LM_L S M_S}^{JM_J} \langle k' T M_T(L'S) J | \hat{V} | k T M_T(LS) J \rangle,
\end{aligned}$$

where $M_{L'} = M_S + M_L - M_{S'}$, and $M_J = M_L + M_S$. The intruder \mathcal{U} , is an appropriate unit conversion factor that ensures that $\left\langle \vec{k}_1 \sigma_{z_1} \tau_{z_1} \vec{k}_2 \sigma_{z_2} \tau_{z_2} \left| \hat{V} \right| \vec{k}_3 \sigma_{z_3} \tau_{z_3} \vec{k}_4 \sigma_{z_4} \tau_{z_4} \right\rangle_{Direct}$ is in units of MeV. For example, $\langle k' T M_T(L'S) J | \hat{V} | k T M_T(LS) J \rangle$ is given in terms of fm² from Drischler *et al.* [1]; therefore, $\mathcal{U} = \hbar c = 197.33 \text{ MeV} \times \text{fm}$. We can then anti-symmetrize Eq. (E.12) via subtracting the exchange matrix element from the direct matrix element

$$\begin{aligned}
& \left\langle \vec{k}_1 \sigma_{z_1} \tau_{z_1} \vec{k}_2 \sigma_{z_2} \tau_{z_2} \left| \hat{V} \right| \vec{k}_3 \sigma_{z_3} \tau_{z_3} \vec{k}_4 \sigma_{z_4} \tau_{z_4} \right\rangle_{AS} \quad (E.13) \\
&\equiv \left\langle \vec{k}_1 \sigma_{z_1} \tau_{z_1} \vec{k}_2 \sigma_{z_2} \tau_{z_2} \left| \hat{V} \right| \vec{k}_3 \sigma_{z_3} \tau_{z_3} \vec{k}_4 \sigma_{z_4} \tau_{z_4} \right\rangle_{Direct} \\
&\quad - \left\langle \vec{k}_1 \sigma_{z_1} \tau_{z_1} \vec{k}_2 \sigma_{z_2} \tau_{z_2} \left| \hat{V} \right| \vec{k}_4 \sigma_{z_4} \tau_{z_4} \vec{k}_3 \sigma_{z_3} \tau_{z_3} \right\rangle_{Direct}.
\end{aligned}$$

Notice the only difference between direct and exchange terms in Eq. (E.12):

$$\begin{aligned}
& \vec{k}_{\text{unit}} \rightarrow -\vec{k}_{\text{unit}} \\
& \mathcal{C}_{\frac{1}{2}\tau_{z_3} \frac{1}{2}\tau_{z_4}}^{TM_T} \mathcal{C}_{\frac{1}{2}\sigma_{z_3} \frac{1}{2}\sigma_{z_4}}^{SM_S} \rightarrow \mathcal{C}_{\frac{1}{2}\tau_{z_4} \frac{1}{2}\tau_{z_3}}^{TM_T} \mathcal{C}_{\frac{1}{2}\sigma_{z_4} \frac{1}{2}\sigma_{z_3}}^{SM_S}.
\end{aligned}$$

And we can exploit the following identities:

$$Y_L^{ML^*}(-\vec{k}_{\text{unit}}) = (-)^L Y_L^{ML^*}(\vec{k}_{\text{unit}})$$

$$\mathcal{C}_{\frac{1}{2}\tau_{z4}\frac{1}{2}\tau_{z3}}^{TM_T} \mathcal{C}_{\frac{1}{2}\sigma_{z4}\frac{1}{2}\sigma_{z3}}^{SM_S} = (-)^{S+T} \mathcal{C}_{\frac{1}{2}\tau_{z3}\frac{1}{2}\tau_{z4}}^{TM_T} \mathcal{C}_{\frac{1}{2}\sigma_{z3}\frac{1}{2}\sigma_{z4}}^{SM_S}.$$

Therefore,

$$\begin{aligned} & \left\langle \vec{k}_1 \sigma_{z1} \tau_{z1} \vec{k}_2 \sigma_{z2} \tau_{z2} \left| \hat{V} \right| \vec{k}_3 \sigma_{z3} \tau_{z3} \vec{k}_4 \sigma_{z4} \tau_{z4} \right\rangle_{AS} = \mathcal{U} \frac{\delta_{\vec{K}, \vec{K}'}}{\mathcal{V}} (4\pi)^2 \quad (\text{E.14}) \\ & \times \sum_{\substack{L, L' \in [0, \infty] \\ -L \leq M_L \leq L \\ T, S \in \{0, 1\}}} \mathcal{C}_{\frac{1}{2}\tau_{z1}\frac{1}{2}\tau_{z2}}^{TM_T} \mathcal{C}_{\frac{1}{2}\sigma_{z1}\frac{1}{2}\sigma_{z2}}^{SM'_S} \mathcal{C}_{\frac{1}{2}\tau_{z3}\frac{1}{2}\tau_{z4}}^{TM_T} \mathcal{C}_{\frac{1}{2}\sigma_{z3}\frac{1}{2}\sigma_{z4}}^{SM_S} \\ & \times \left(i^{L-L'} \right) \left[1 - (-)^{L+S+T} \right] Y_{L'}^{M'_L}(\vec{k}'_{\text{unit}}) Y_L^{M_L^*}(\vec{k}_{\text{unit}}) \\ & \times \sum_{|L-S| \leq J \leq L+S} \mathcal{C}_{L'M'_L SM'_S}^{JM_J} \mathcal{C}_{LM_L SM_S}^{JM_J} V_{L'LSJ}^{TM_T}(k', k), \end{aligned}$$

where

$$M'_S = \sigma_{z1} + \sigma_{z2}$$

$$M_S = \sigma_{z3} + \sigma_{z4}$$

$$M_T = \tau_{z1} + \tau_{z2} = \tau_{z3} + \tau_{z4}$$

$$V_{L'LSJ}^{TM_T}(k', k) \equiv \langle k' TM_T(L'S)J | \hat{V} | k TM_T(LS)J \rangle$$

$$M_{L'} = M_S + M_L - M_{S'}$$

$$M_J = M_L + M_S.$$

APPENDIX F. Optimized Particle-hole Transformation

Commutators between A -body operators A and B generally require the evaluation of so-called “particle-hole” terms [10].¹

$$\left[A, B \right]_{pqrs} += \sum_{tu} (n_t - n_u) \times (1 - P_{pq} - P_{rs} + P_{pq}P_{rs}) \times A_{ptur} B_{uqst} \quad (\text{F.1})$$

We need only focus on the first term of Eq. (F.1).

$$\left[A, B \right]_{pqrs} += \sum_{tu} (n_t - n_u) A_{ptur} B_{uqst} \quad (\text{F.2})$$

The particle-hole term requires careful implementation to be computationally efficient. Ideally, one would implement Eq. (F.2) maximally utilizing a computer’s cache and multi-threading capabilities. If the contraction in Eq. (F.2) is written as a matrix product, computational optimizations in the particle-hole term can be partially offloaded to existing high-performance matrix multiplication algorithms [19]. Eq. (F.2) can be rewritten by defining a diagonal occupation operator O .

$$\begin{aligned} O_{tuwx} &\equiv (n_t - n_u) \times \delta_{tw} \delta_{ux} \quad \forall tuwx \\ \left[A, B \right]_{pqrs} &+= \sum_{tu} O_{tutu} A_{ptur} B_{uqst} \end{aligned} \quad (\text{F.3})$$

¹Eq. (F.1) assumes A and B are anti-symmetrized. P_{pq} and P_{rs} exchange indices on their operand. For example, $P_{pq} \times A_{ptur} B_{uqst} \equiv A_{qtur} B_{upst}$.

Constructing A -body operators \tilde{A}, \tilde{B} such that²

$$\begin{aligned} A_{ptur} &= -\tilde{A}_{prut} \quad \forall tu \\ B_{uqst} &= -\tilde{B}_{utsq} \quad \forall tu, \end{aligned} \tag{F.4}$$

Eq. (F.3) can be almost cast into a matrix product.

$$\left[A, B \right]_{pqrs} \quad += \sum_{tu} O_{tutu} \tilde{A}_{prut} \tilde{B}_{utsq} \tag{F.5}$$

Notice the symmetry $O_{tutu} = -O_{utut}$. Therefore,

$$\left[A, B \right]_{pqrs} \quad += \sum_{tu} -\tilde{A}_{prut} O_{utut} \tilde{B}_{utsq} = -(\tilde{A}O\tilde{B})_{prsq} \tag{F.6}$$

The remaining three terms of Eq. (F.1) are easily obtained.

$$\left[A, B \right]_{pqrs} \quad -= (\tilde{A}O\tilde{B})_{prsq} - (\tilde{A}O\tilde{B})_{qrsp} - (\tilde{A}O\tilde{B})_{psrq} + (\tilde{A}O\tilde{B})_{qsrp} \tag{F.7}$$

The product $\tilde{A}O\tilde{B}$ can be partially precomputed if there is a distinction between particle and hole single-particle states ($n_i = 1$ and $n_a = 0 \quad \forall ai$). If such a distinction exists, \tilde{A} , O , and \tilde{B} can be written in an ordered two-body basis \mathbb{B} where particle-hole states are separated from particle-particle and hole-hole states.

$$\mathbb{B} = \underbrace{\{(p, q) : |n_p - n_q| = 1\}}_{\mathbb{P}} \cup \underbrace{\{(p, q) : |n_p - n_q| = 0\}}_{\mathbb{Q}} \tag{F.8}$$

²A factor of -1 is included in Eq. (F.4) to be consistent with Jensen *et al.* [19]. This does not affect the product $\tilde{A}O\tilde{B}$.

$$O = \begin{bmatrix} O_{\mathbb{P}\mathbb{P}} & O_{\mathbb{P}\mathbb{Q}} = 0 \\ O_{\mathbb{Q}\mathbb{P}} = 0 & O_{\mathbb{Q}\mathbb{Q}} = 0 \end{bmatrix} \quad (\text{F.9a})$$

$$\tilde{A} = \begin{bmatrix} \tilde{A}_{\mathbb{P}\mathbb{P}} & \tilde{A}_{\mathbb{P}\mathbb{Q}} \\ \tilde{A}_{\mathbb{Q}\mathbb{P}} & \tilde{A}_{\mathbb{Q}\mathbb{Q}} \end{bmatrix} \quad (\text{F.9b})$$

$$\tilde{B} = \begin{bmatrix} \tilde{B}_{\mathbb{P}\mathbb{P}} & \tilde{B}_{\mathbb{P}\mathbb{Q}} \\ \tilde{B}_{\mathbb{Q}\mathbb{P}} & \tilde{B}_{\mathbb{Q}\mathbb{Q}} \end{bmatrix} \quad (\text{F.9c})$$

$$\tilde{A}\tilde{O}\tilde{B} = \begin{bmatrix} \tilde{A}_{\mathbb{P}\mathbb{P}} \times O_{\mathbb{P}\mathbb{P}} \times \tilde{B}_{\mathbb{P}\mathbb{P}} & \tilde{A}_{\mathbb{P}\mathbb{P}} \times O_{\mathbb{P}\mathbb{P}} \times \tilde{B}_{\mathbb{P}\mathbb{Q}} \\ \tilde{A}_{\mathbb{Q}\mathbb{P}} \times O_{\mathbb{P}\mathbb{P}} \times \tilde{B}_{\mathbb{P}\mathbb{P}} & \tilde{A}_{\mathbb{Q}\mathbb{P}} \times O_{\mathbb{P}\mathbb{P}} \times \tilde{B}_{\mathbb{P}\mathbb{Q}} \end{bmatrix} \quad (\text{F.9d})$$

$\dim(\mathbb{P}) \sim N_{particles} \times N_{holes}$, and $\dim(\mathbb{Q}) \sim N_{particles}^2 + N_{holes}^2$. Typically, $N_{particles} \gg N_{holes}$, implying $\dim(\mathbb{Q}) > \dim(\mathbb{P})$. Utilizing Eq. (F.9d), the most memory and compute demanding operations involving $\tilde{A}_{\mathbb{Q}\mathbb{Q}}$, and $\tilde{B}_{\mathbb{Q}\mathbb{Q}}$ are averted. If $\|\tilde{A}_{\mathbb{Q}\mathbb{P}}\|$ is sufficiently small, one can forgo computing the second row of Eq. (F.9d) entirely.³ Likewise, if $\|\tilde{B}_{\mathbb{P}\mathbb{Q}}\|$ is sufficiently small, one can forgo computing the second column of Eq. (F.9d) entirely.⁴

Further optimizations can be made by recognizing possible symmetries in the particle-hole transformation. For example, symmetries in A can manifest in \tilde{A} , albeit differently. Suppose A conserves center-of-mass momenta, i.e

$$\vec{k}_p + \vec{k}_t \neq \vec{k}_u + \vec{k}_r \implies A_{ptur} = 0 \quad \forall ptur. \quad (\text{F.10})$$

³For the Magnus operator, $\|\tilde{\Omega}_{\mathbb{Q}\mathbb{P}}\|$ is generally observed to be small. Moreover, $\|\tilde{\eta}_{\mathbb{Q}\mathbb{P}}\| = 0$ for most generators, by construction.

⁴Such situations can arise in the Magnus series where commutators between the Magnus operator and Magnus-like operators are evaluated.

According to Eq. (F.4), \tilde{A} will then conserve *relative* momenta.

$$\vec{k}_p - \vec{k}_r \neq \vec{k}_u - \vec{k}_t \implies \tilde{A}_{prut} = 0 \quad \forall prut \quad (\text{F.11})$$

If both \tilde{A} and \tilde{B} conserve relative momenta, one can conveniently decompose the particle-hole basis

$$\mathbb{B} = \bigcup_m \mathbb{B}_m \quad (\text{F.12})$$

$$\mathbb{B}_m \equiv \{ (p, q) : |n_p - n_q| = 1 \wedge \vec{k}_p - \vec{k}_q = \vec{\kappa}_m \} \quad (\text{F.13})$$

$$\bigcup \{ (p, q) : |n_p - n_q| = 0 \wedge \vec{k}_p - \vec{k}_q = \vec{\kappa}_m \},$$

where $\vec{\kappa}_m$ denotes the conserved relative momenta of the m th block \mathbb{B}_m . $\tilde{A}\tilde{O}\tilde{B}$ can then be evaluated within relative momenta conserving blocks—further reducing memory and compute costs.⁵

If A and B are anti-symmetrized and have definite hermiticity

$$A_{pqrs} = -A_{qprs} = -A_{pqsr} = A_{qpsr} \quad \forall pqrs \quad (\text{F.14})$$

$$B_{pqrs} = -B_{qprs} = -B_{pqsr} = B_{qpsr} \quad \forall pqrs$$

$$A^\dagger = \text{sign}_A \times A$$

$$B^\dagger = \text{sign}_B \times B$$

and $O^* = O$, hermiticity can be easily exploited in Eq. (F.6). Permuting $p \leftrightarrow r$ and $s \leftrightarrow q$,

⁵Notice, if \tilde{A} has the same block structure as \tilde{B} , then (p, r) , (u, t) and (s, q) must all lie in the same block for a nonzero contribution to the RHS of Eq. (F.6).

Eq. (F.6) becomes

$$\left[A, B \right]_{rspq} \quad += \sum_{tu} -\tilde{A}_{rput} O_{tut} \tilde{B}_{utqs} = -(\tilde{A}O\tilde{B})_{rpqs}. \quad (\text{F.15})$$

Using Eq. (F.4) and Eq. (F.14),

$$\begin{aligned} \tilde{A}_{rput} &= -A_{rtup} = -\text{sign}_A \times A_{uprt}^* = -\text{sign}_A \times A_{putr}^* = \text{sign}_A \times \tilde{A}_{prtu}^* \\ \tilde{B}_{utqs} &= -B_{usqt} = -\text{sign}_B \times B_{qtus}^* = -\text{sign}_B \times B_{tqsu}^* = \text{sign}_B \times \tilde{B}_{tusq}^*. \end{aligned} \quad (\text{F.16})$$

Inserting Eq. (F.16) into Eq. (F.15), and exploiting the symmetry $O_{tut} = -O_{tutu}$,

$$\begin{aligned} \left[A, B \right]_{rspq} \quad += \text{sign}_A \times \text{sign}_B \times \sum_{tu} \tilde{A}_{prtu}^* O_{tutu} \tilde{B}_{tusq}^* \\ = \text{sign}_A \times \text{sign}_B \times (\tilde{A}O\tilde{B})_{prsq}^*. \end{aligned} \quad (\text{F.17})$$

If Eq. (F.6) is computed within some block \mathbb{B}_m containing (p, r) and (s, q) , then one can use Eq. (F.17) instead of Eq. (F.15). The importance of this is subtle. Notice (r, p) and (q, s) will lie in a block $\mathbb{B}_{m'}$ where $\vec{\kappa}_{m'} = -\vec{\kappa}_m$. Therefore, one can forgo evaluating $\tilde{A}O\tilde{B}$ in $\mathbb{B}_{m'}$ entirely—further reducing memory and compute costs.⁶

⁶ $\tilde{A}O\tilde{B}=0$ in the block \mathbb{B}_m such that $\vec{\kappa}_m = \vec{0}$. Due to the shelled nature of our basis, for any two-particle state $(p, q) \in \mathbb{B}_m$, the p and q single-particle states must be both on the same momentum shell. Since all shells are closed, hole and particle states are separated in momentum. Therefore, \mathbb{B}_m can only contain hole-hole and/or particle-particle two-particle states. And the occupation operator O , is zero in these sectors. This may however, not hold when applying twist-averaged boundary conditions [23].

APPENDIX G. Properties of Born Series Adjoint

We seek to prove the linearity of nested commutators of A -body operators A , B , and C utilized by Chapter 5.6:

$$[A_* + B_*, C]_*^{(n)} \stackrel{?}{=} [A_*, C]_*^{(n)} + [B_*, C]_*^{(n)}, \quad n \geq 1. \quad (\text{G.1})$$

First note, Eq. (G.1) is automatically guaranteed for $n = 1$ via the linearity of commutators.

This is unaffected by the coefficient-wise division of the energy denominator denoted by “*.”

Assuming Eq. (G.1) holds for some $n \geq 1$, then using Eq. (5.21),

$$\begin{aligned} [A_* + B_*, C]_*^{(n+1)} &\equiv \left[[A_* + B_*, C]_*^{(n)}, C \right]_* \\ &= \left[[A_*, C]_*^{(n)} + [B_*, C]_*^{(n)}, C \right]_* \\ &= \left[[A_*, C]_*^{(n)}, C \right]_* + \left[[B_*, C]_*^{(n)}, C \right]_* \\ &= [A_*, C]_*^{(n+1)} + [B_*, C]_*^{(n+1)}. \end{aligned} \quad (\text{G.2})$$

We have thus demonstrated if Eq. (G.1) holds for some $n \geq 1$, it also holds for $n + 1$. Since

Eq. (G.1) contratrivially holds for $n = 1$, then it indeed holds for all $n \geq 1$. ■

Chapter 5.6 utilizes the following identity:

$$\left[[A, B]_*, B \right]_*^{(n+1)} \stackrel{?}{=} [A, B]_*^{(n+2)}, \quad n \geq 0. \quad (\text{G.3})$$

We seek to prove Eq. (G.3). As a base case, observe Eq. (G.3) is guaranteed for $n = 0$ using

Eq. (5.21)

$$\left[[A, B]_*, B \right]_*^{(1)} = \left[[A, B]_*^{(1)}, B \right]_* \equiv [A, B]_*^{(2)}. \quad (\text{G.4})$$

Assuming Eq. (G.3) holds for some $n \geq 0$, then using Eq. (5.21),

$$\begin{aligned} \left[[A, B]_*, B \right]_*^{(n+2)} &\equiv \left[\left[[A, B]_*, B \right]_*^{(n+1)}, B \right]_* \\ &= \left[[A, B]_*^{(n+2)}, B \right]_* \equiv [A, B]_*^{(n+3)}. \end{aligned} \quad (\text{G.5})$$

Therefore, we have demonstrated if Eq. (G.3) holds for some $n \geq 0$, it also holds for $n + 1$.

Since Eq. (G.3) holds for $n = 0$, then it indeed holds for all $n \geq 0$. ■

APPENDIX H. MBPT Expressed in Terms of IMSRG Commutators

We aim to write MBPT(2) and MBPT(3) evaluated at the two-body level in terms of commutators between a target Hamiltonian and IMSRG's White generator. Consequently, we can offload compute costs—most apparent in MBPT(3)—to an optimized commutator routine. Moreover, we can consequently cache and reuse a commutator in MBPT(3)—significantly improving MBPT(3)'s compute performance.

For a target Hamiltonian $H = E + f + \Gamma$, MBPT's improvement to the ground state energy E is given by

$$E' = E + \Delta E^{(1)} + \Delta E^{(2)} + \Delta E^{(3)}. \quad (\text{H.1})$$

Momentum conservation in infinite nuclear matter implies $\Delta E^{(1)} = 0$. Going forward, note that the s dependence of all operators in this appendix are suppressed for brevity. At the two-body level, 2nd-order MBPT corrections to E are given by [45]

$$\Delta E^{(2)} = \frac{1}{4} \sum_{abij} \frac{|\Gamma_{abij}|^2}{\Delta_{ijab}} \quad (\text{H.2})$$

$$\Delta_{ijab} \equiv f_{ii} + f_{jj} - f_{aa} - f_{bb} \quad \forall abij$$

$$\Delta_{abij} \equiv f_{aa} + f_{bb} - f_{ii} - f_{jj} = -\Delta_{ijab} \quad \forall abij$$

$$\Delta_{ijab} = \Delta_{jiab} = \Delta_{ijba} = \Delta_{jiba} \quad \forall abij$$

$$\Delta_{abij} = \Delta_{baij} = \Delta_{abji} = \Delta_{baji} \quad \forall abij.$$

We aim to demonstrate

$$\Delta E^{(2)} \stackrel{?}{=} \frac{1}{2} \left\{ \left[\eta, \Gamma \right] \right\}_{0\text{-body}}. \quad (\text{H.3})$$

η is White's generator with Møller–Plesset energy denominators in Eq. (5.5).¹ And the operator $\left\{ \right\}_{0\text{-body}}$ projects out the zero-body component of $\left[\eta, \Gamma \right]$. Using Eq. (A.14) of Hergert *et al.* [10],

$$\begin{aligned} \left\{ \left[\eta, \Gamma \right] \right\}_{0\text{-body}} &= \frac{1}{4} \sum_{abij} (\eta_{ijab} \Gamma_{abij} - \Gamma_{ijab} \eta_{abij}) \\ &= \frac{1}{4} \sum_{abij} \left(\frac{\Gamma_{ijab}}{\Delta_{ijab}} \Gamma_{abij} - \Gamma_{ijab} \frac{\Gamma_{abij}}{\Delta_{abij}} \right) \\ &= \frac{1}{4} \sum_{abij} \frac{1}{\Delta_{ijab}} \left(\Gamma_{ijab} \Gamma_{abij} + \Gamma_{ijab} \Gamma_{abij} \right) \\ &= \frac{1}{2} \sum_{abij} \frac{\Gamma_{ijab} \Gamma_{abij}}{\Delta_{ijab}} = \frac{1}{2} \sum_{abij} \frac{\Gamma_{abij}^* \Gamma_{abij}}{\Delta_{ijab}} = \frac{1}{2} \sum_{abij} \frac{|\Gamma_{abij}|^2}{\Delta_{ijab}} = 2 \Delta E^{(2)}. \end{aligned} \quad (\text{H.4})$$

At the two-body level, 3rd order MBPT corrections to E are given by [45]

$$\Delta E^{(3)} = \frac{1}{8} \sum_{abcdij} \frac{\Gamma_{ijab} \Gamma_{abcd} \Gamma_{cdij}}{\Delta_{ijab} \Delta_{ijcd}} + \frac{1}{8} \sum_{abijkl} \frac{\Gamma_{ijab} \Gamma_{abkl} \Gamma_{klij}}{\Delta_{ijab} \Delta_{klab}} - \sum_{abcijk} \frac{\Gamma_{ijab} \Gamma_{ackj} \Gamma_{kbic}}{\Delta_{ijab} \Delta_{kjac}}. \quad (\text{H.5})$$

We aim to demonstrate

$$\Delta E^{(3)} \stackrel{?}{=} \frac{1}{2} \left\{ \left[\eta, \left[\eta, \Gamma \right] \right] \right\}_{0\text{-body}}, \quad (\text{H.6})$$

¹The one-body component of η is assumed to be zero.

assuming $\text{Im}\{\Delta E^{(3)}\} = 0$. η is again White's generator with Møller–Plesset energy denominators. Using Eq. (A.14) and Eq. (A.12) of Hergert *et al.* [10],

$$\begin{aligned}
\left\{ \left[\eta, \left[\eta, \Gamma \right] \right] \right\}_{0\text{-body}} &= \frac{1}{4} \sum_{abij} \left(\eta_{ijab} \left[\eta, \Gamma \right]_{abij} - \left[\eta, \Gamma \right]_{ijab} \eta_{abij} \right) \quad (\text{H.7}) \\
&= \frac{1}{4} \sum_{abij} \left(\eta_{ijab} \left[\eta, \Gamma \right]_{abij} + \left[\eta, \Gamma \right]_{abij}^* \eta_{ijab}^* \right) \\
&= \frac{1}{4} \sum_{abij} \left(\eta_{ijab} \left[\eta, \Gamma \right]_{abij} + \left(\eta_{ijab} \left[\eta, \Gamma \right]_{abij} \right)^* \right) \\
&= \left(\frac{1}{4} \sum_{abij} \eta_{ijab} \left[\eta, \Gamma \right]_{abij} \right) + \left(\frac{1}{4} \sum_{abij} \eta_{ijab} \left[\eta, \Gamma \right]_{abij} \right)^*.
\end{aligned}$$

$$\left[\eta, \Gamma \right]_{abij} = \frac{1}{2} \sum_{pq} (\eta_{abpq} \Gamma_{pqij} - \Gamma_{abpq} \eta_{pqij}) \times (1 - n_p - n_q) \quad (\text{H.8a})$$

$$+ \sum_{pq} (n_p - n_q) \times (\eta_{paqi} \Gamma_{qbpj} - \eta_{pbqi} \Gamma_{qapj} - \eta_{paqj} \Gamma_{qbpj} + \eta_{pbqj} \Gamma_{qapi})$$

$$= -\frac{1}{2} \sum_{kl} \eta_{abkl} \Gamma_{klij} - \frac{1}{2} \sum_{cd} \Gamma_{abcd} \eta_{cdij} \quad (\text{H.8b})$$

$$- \sum_{ck} (\eta_{caki} \Gamma_{kbcj} - \eta_{cbki} \Gamma_{kacj} - \eta_{cakj} \Gamma_{kbcj} + \eta_{cbkj} \Gamma_{kaci})$$

$$= -\frac{1}{2} \sum_{kl} \frac{\Gamma_{abkl}}{\Delta_{abkl}} \Gamma_{klij} - \frac{1}{2} \sum_{cd} \Gamma_{abcd} \frac{\Gamma_{cdij}}{\Delta_{cdij}} \quad (\text{H.8c})$$

$$- \sum_{ck} \left(\frac{\Gamma_{caki}}{\Delta_{caki}} \Gamma_{kbcj} - \frac{\Gamma_{cbki}}{\Delta_{cbki}} \Gamma_{kacj} - \frac{\Gamma_{cakj}}{\Delta_{cakj}} \Gamma_{kbcj} + \frac{\Gamma_{cbkj}}{\Delta_{cbkj}} \Gamma_{kaci} \right)$$

$$= \frac{1}{2} \sum_{kl} \frac{\Gamma_{abkl}}{\Delta_{klab}} \Gamma_{klij} + \frac{1}{2} \sum_{cd} \Gamma_{abcd} \frac{\Gamma_{cdij}}{\Delta_{ijcd}} \quad (\text{H.8d})$$

$$- \sum_{ck} \left(\frac{\Gamma_{caki}}{\Delta_{caki}} \Gamma_{kbcj} - \frac{\Gamma_{cbki}}{\Delta_{cbki}} \Gamma_{kacj} - \frac{\Gamma_{cakj}}{\Delta_{cakj}} \Gamma_{kbcj} + \frac{\Gamma_{cbkj}}{\Delta_{cbkj}} \Gamma_{kaci} \right)$$

$$= \frac{1}{2} \sum_{kl} \frac{\Gamma_{abkl}}{\Delta_{klab}} \Gamma_{klij} + \frac{1}{2} \sum_{cd} \Gamma_{abcd} \frac{\Gamma_{cdij}}{\Delta_{ijcd}} \quad (\text{H.8e})$$

$$- \sum_{ck} \left(\frac{\Gamma_{acki}}{\Delta_{acki}} \Gamma_{kbjc} - \frac{\Gamma_{bcki}}{\Delta_{bcki}} \Gamma_{kajc} - \frac{\Gamma_{ackj}}{\Delta_{ackj}} \Gamma_{kbic} + \frac{\Gamma_{bckj}}{\Delta_{bckj}} \Gamma_{kaic} \right)$$

$$= \frac{1}{2} \sum_{kl} \frac{\Gamma_{abkl}}{\Delta_{klab}} \Gamma_{klij} + \frac{1}{2} \sum_{cd} \Gamma_{abcd} \frac{\Gamma_{cdij}}{\Delta_{ijcd}} \quad (\text{H.8f})$$

$$+ \sum_{ck} \left(\frac{\Gamma_{acki}}{\Delta_{kiac}} \Gamma_{kbjc} - \frac{\Gamma_{bcki}}{\Delta_{kibc}} \Gamma_{kajc} - \frac{\Gamma_{ackj}}{\Delta_{kjac}} \Gamma_{kbic} + \frac{\Gamma_{bckj}}{\Delta_{kjbc}} \Gamma_{kaic} \right).$$

Let us focus on the first term of Eq. (H.7).

$$\begin{aligned}
\frac{1}{4} \sum_{abij} \eta_{ijab} \left[\eta, \Gamma \right]_{abij} &= \frac{1}{8} \sum_{abijkl} \frac{\Gamma_{ijab} \Gamma_{abkl} \Gamma_{klij}}{\Delta_{ijab} \Delta_{klab}} + \frac{1}{8} \sum_{abijcd} \frac{\Gamma_{ijab} \Gamma_{abcd} \Gamma_{cdij}}{\Delta_{ijab} \Delta_{ijcd}} \quad (\text{H.9}) \\
&+ \frac{1}{4} \underbrace{\sum_{abijck} \frac{\Gamma_{ijab} \Gamma_{acki} \Gamma_{kbjc}}{\Delta_{ijab} \Delta_{kiac}}}_{\text{Term 2}} - \frac{1}{4} \underbrace{\sum_{abijck} \frac{\Gamma_{ijab} \Gamma_{bcki} \Gamma_{kajc}}{\Delta_{ijab} \Delta_{kibc}}}_{\text{Term 3}} \\
&- \frac{1}{4} \underbrace{\sum_{abijck} \frac{\Gamma_{ijab} \Gamma_{ackj} \Gamma_{kbic}}{\Delta_{ijab} \Delta_{kjac}}}_{\text{Term 4}} + \frac{1}{4} \underbrace{\sum_{abijck} \frac{\Gamma_{ijab} \Gamma_{bckj} \Gamma_{kaic}}{\Delta_{ijab} \Delta_{kjbc}}}_{\text{Term 5}}.
\end{aligned}$$

Since all indices are summed over in Eq. (H.9), we can freely interchange $a \leftrightarrow b$ and $i \leftrightarrow j$.

$$\text{Term 2} = \sum_{abijck} \frac{\Gamma_{ijab} \Gamma_{acki} \Gamma_{kbjc}}{\Delta_{ijab} \Delta_{kiac}} = \sum_{abijck} \frac{\Gamma_{jiab} \Gamma_{ackj} \Gamma_{kbic}}{\Delta_{jiab} \Delta_{kjac}} = - \sum_{abijck} \frac{\Gamma_{ijab} \Gamma_{ackj} \Gamma_{kbic}}{\Delta_{ijab} \Delta_{kjac}} \quad (\text{H.10a})$$

$$\text{Term 3} = \sum_{abijck} \frac{\Gamma_{ijab} \Gamma_{bcki} \Gamma_{kajc}}{\Delta_{ijab} \Delta_{kibc}} = \sum_{abijck} \frac{\Gamma_{jiba} \Gamma_{ackj} \Gamma_{kbic}}{\Delta_{jiba} \Delta_{kjac}} = \sum_{abijck} \frac{\Gamma_{ijab} \Gamma_{ackj} \Gamma_{kbic}}{\Delta_{ijab} \Delta_{kjac}} \quad (\text{H.10b})$$

$$\text{Term 4} = \sum_{abijck} \frac{\Gamma_{ijab} \Gamma_{ackj} \Gamma_{kbic}}{\Delta_{ijab} \Delta_{kjac}} \longrightarrow \text{Conveniently kept unchanged!} \quad (\text{H.10c})$$

$$\text{Term 5} = \sum_{abijck} \frac{\Gamma_{ijab} \Gamma_{bckj} \Gamma_{kaic}}{\Delta_{ijab} \Delta_{kjbc}} = \sum_{abijck} \frac{\Gamma_{ijba} \Gamma_{ackj} \Gamma_{kbic}}{\Delta_{ijba} \Delta_{kjac}} = - \sum_{abijck} \frac{\Gamma_{ijab} \Gamma_{ackj} \Gamma_{kbic}}{\Delta_{ijab} \Delta_{kjac}} \quad (\text{H.10d})$$

$$\text{Term 2} = -\text{Term 3} = -\text{Term 4} = \text{Term 5}. \quad (\text{H.10e})$$

Therefore, using Eq. (H.9) and Eq. (H.10),

$$\begin{aligned} \Delta E^{(3)} &= \frac{1}{8} \sum_{abijkl} \frac{\Gamma_{ijab} \Gamma_{abkl} \Gamma_{klij}}{\Delta_{ijab} \Delta_{klab}} + \frac{1}{8} \sum_{abijcd} \frac{\Gamma_{ijab} \Gamma_{abcd} \Gamma_{cdij}}{\Delta_{ijab} \Delta_{ijcd}} \\ &\quad - \sum_{abijck} \frac{\Gamma_{ijab} \Gamma_{ackj} \Gamma_{kbic}}{\Delta_{ijab} \Delta_{kjac}} = \frac{1}{4} \sum_{abij} \eta_{ijab} [\eta, \Gamma]_{abij}. \end{aligned} \quad (\text{H.11})$$

Utilizing Eq. (H.7),

$$\left\{ \left[\eta, [\eta, \Gamma] \right] \right\}_{0\text{-body}} = \Delta E^{(3)} + (\Delta E^{(3)})^* = 2 \operatorname{Re} \{ \Delta E^{(3)} \}. \quad (\text{H.12})$$

If $\operatorname{Im} \{ \Delta E^{(3)} \} = 0$,

$$\left\{ \left[\eta, [\eta, \Gamma] \right] \right\}_{0\text{-body}} = 2 \Delta E^{(3)}. \quad (\text{H.13})$$

■

Using Eq. (H.13), we cache and reuse $[\eta, \Gamma]$ —significantly reducing the compute cost of MBPT(3). Given these developments, one wonders if higher-order MBPT expressions can also be written in terms of commutators between IMSRG operators.² Notice that we could relax the requirement that η is White’s generator with Møller–Plesset energy denominators. We could use White’s generator with Epstein–Nesbet energy denominators, perhaps giving canonical MBPT with Epstein–Nesbet partitioning. We could also use the novel IMSRG generators introduced in Chapter 5. To this end, we include generalized MBPT functions detailed in Algorithm 6 and Algorithm 7.

²Perhaps, triples excitations present in MBPT(4) may be accounted for by introducing auxiliary commutators (and potentially departing η from White’s generator), while still truncating η at the two-body level.

Algorithm 6 Generalized MBPT(2)

Input: $\eta, H = E + f + \Gamma$ \triangleright Approximate diagonalizer, and target Hamiltonian

Output: $\left\{ \left[\eta, \Gamma \right] / 2 \right\}_{0\text{-body}}$ \triangleright Generalized $\Delta E^{(2)}$

```
1: function MBPT2( $\eta, H$ )
2:   return  $\left\{ \left[ \eta, \Gamma \right] / 2 \right\}_{0\text{-body}}$ 
3: end function
```

Algorithm 7 Generalized MBPT(3)

Input: $\eta, H = E + f + \Gamma$ \triangleright Approximate diagonalizer, and target Hamiltonian

Output: $\left\{ \left[\eta, \left[\eta, \Gamma \right] \right] / 2 \right\}_{0\text{-body}}$ \triangleright Generalized $\Delta E^{(3)}$

```
1: function MBPT3( $\eta, H$ )
2:   return MBPT2( $\eta, \left[ \eta, \Gamma \right]$ )
3: end function
```

Algorithm 8 Standard MBPT(2)

Input: $H = E + f + \Gamma$ \triangleright Target Hamiltonian

Output: $\left\{ \left[\eta^{WhiteMP}(H), \Gamma \right] / 2 \right\}_{0\text{-body}}$ \triangleright Standard $\Delta E^{(2)}$

```
1: function MBPT2( $H$ )
2:   return MBPT2( $\eta^{WhiteMP}(H), H$ )  $\triangleright$  Using White's generator from Eq. (5.5)
3: end function
```

Algorithm 9 Standard MBPT(3)

Input: $H = E + f + \Gamma$ \triangleright Target Hamiltonian

Output: $\left\{ \left[\eta^{WhiteMP}(H), \left[\eta^{WhiteMP}(H), \Gamma \right] \right] / 2 \right\}_{0\text{-body}}$ \triangleright Standard $\Delta E^{(3)}$

```
1: function MBPT3( $H$ )
2:   return MBPT3( $\eta^{WhiteMP}(H), H$ )  $\triangleright$  Using White's generator from Eq. (5.5)
3: end function
```

H.1 MBPT Truncation for UCC-Inspired Generators

We utilize 2nd-order many body perturbation theory (MBPT) to terminate iterative calculations for the UCC-Born and Carinae generators in Chapter 5. Particularly, we use a generalized form of MBPT(2) seen in Algorithm 6. And, we detail an overloaded truncation function using the standard and generalized MBPT(2) in Algorithm 10 and Algorithm 11, respectively.

Algorithm 10 Standard MBPT(2) Truncation

Input: $H = E + f + \Gamma$ ▷ Target Hamiltonian for MBPT(2)
Output: $\left\{ \left[\eta^{WhiteMP}(H), \Gamma \right] / (2E) \right\}_{0\text{-body}}$ ▷ $\Delta E^{(2)} / E$

- 1: **function** MBPT2TRUNCATION(H)
- 2: **return** MBPT2TRUNCATION($\eta^{WhiteMP}(H), H$) ▷ Using White’s generator from Eq. (5.5)
- 3: **end function**

Algorithm 11 Generalized MBPT(2) Truncation

Input: $\eta, H = E + f + \Gamma$ ▷ Approximate diagonalizer, and target Hamiltonian
Output: $\left\{ \left[\eta, \Gamma \right] / (2E) \right\}_{0\text{-body}}$ ▷ Generalized $\Delta E^{(2)} / E$

- 1: **function** MBPT2TRUNCATION(η, H)
- 2: **return** MBPT2(η, H)/ E
- 3: **end function**

APPENDIX I. UCC Renormalized Hamiltonian Ansatz

We aim to pose an ansatz for $H^{RG}(\eta)$ seen in Eq. (5.8). To do so, we must first tabulate commutator expressions between an approximate diagonalizer η and generic Hamiltonians A that satisfy Assumption 1. Let η be given by Eq. (5.1). Using Eq. (A.8) and Eq. (A.13) of Hergert *et al.* [10],

$$\left[\eta, A\right]_{aa} = - \sum_{rs} \cancel{(n_r - n_s)} \times \underbrace{A_{rs}}_{A_{rr} \times \delta_{rs}} \eta_{sara} \quad (\text{I.1a})$$

$$+ \frac{1}{2} \sum_{pqr} (n_p n_q \bar{n}_r + \bar{n}_p \bar{n}_q n_r) \times (\eta_{rapq} A_{pqra} - A_{rapq} \eta_{pqra})$$

$$\left[\eta, A\right]_{ii} = - \sum_{rs} \cancel{(n_r - n_s)} \times \underbrace{A_{rs}}_{A_{rr} \times \delta_{rs}} \eta_{siri} \quad (\text{I.1b})$$

$$+ \frac{1}{2} \sum_{pqr} (n_p n_q \bar{n}_r + \bar{n}_p \bar{n}_q n_r) \times (\eta_{ripq} A_{pqri} - A_{ripq} \eta_{pqri}) .$$

Enforcing the operator structure of η seen in Eq. (5.1),

$$\left[\eta, A\right]_{aa} = \frac{1}{2} \sum_{klb} (\eta_{bakl} A_{klba} - A_{bakl} \eta_{klba}) \quad (\text{I.2a})$$

$$\left[\eta, A\right]_{ii} = \frac{1}{2} \sum_{abj} (\eta_{jiab} A_{abji} - A_{jiab} \eta_{abji}) . \quad (\text{I.2b})$$

Using Eq. (A.12) of Hergert *et al.* [10],

$$\begin{aligned}
& \left[\eta, A \right]_{abij} = (A_{ii} + A_{jj} - A_{aa} - A_{bb}) \times \eta_{abij} \\
& + \frac{1}{2} \sum_{pq} (\eta_{abpq} A_{pqij} - A_{abpq} \eta_{pqij}) \times (1 - n_p - n_q) \\
& + \sum_{pq} (n_p - n_q) \times (\eta_{paqi} A_{qbpj} - \eta_{pbqi} A_{qapj} - \eta_{paqj} A_{qbpi} + \eta_{pbqj} A_{qapi})
\end{aligned} \tag{I.3a}$$

$$\begin{aligned}
& \left[\eta, A \right]_{akic} = (A_{ii} + A_{cc} - A_{aa} - A_{kk}) \times \eta_{akic} \\
& + \frac{1}{2} \sum_{pq} (\eta_{akpq} A_{pqic} - A_{akpq} \eta_{pqic}) \times (1 - n_p - n_q) \\
& + \sum_{pq} (n_p - n_q) \times (\eta_{paqi} A_{qkpc} - \eta_{pkqi} A_{qapc} - \eta_{paqc} A_{qkpi} + \eta_{pkqc} A_{qapi})
\end{aligned} \tag{I.3b}$$

$$\begin{aligned}
& \left[\eta, A \right]_{abcj} = (A_{cc} + A_{jj} - A_{aa} - A_{bb}) \times \eta_{abcj} \\
& + \frac{1}{2} \sum_{pq} (\eta_{abpq} A_{pqcj} - A_{abpq} \eta_{pqcj}) \times (1 - n_p - n_q) \\
& + \sum_{pq} (n_p - n_q) \times (\eta_{paqc} A_{qbpj} - \eta_{pbqc} A_{qapj} - \eta_{paqj} A_{qbpc} + \eta_{pbqj} A_{qapc})
\end{aligned} \tag{I.3c}$$

$$\begin{aligned}
& \left[\eta, A \right]_{abcd} = (A_{cc} + A_{dd} - A_{aa} - A_{bb}) \times \eta_{abcd} \\
& + \frac{1}{2} \sum_{pq} (\eta_{abpq} A_{pqcd} - A_{abpq} \eta_{pqcd}) \times (1 - n_p - n_q) \\
& + \sum_{pq} (n_p - n_q) \times (\eta_{paqc} A_{qbpd} - \eta_{pbqc} A_{qapd} - \eta_{paqd} A_{qbpc} + \eta_{pbqd} A_{qapc})
\end{aligned} \tag{I.3d}$$

$$\begin{aligned}
& \left[\eta, A \right]_{akij} = (A_{ii} + A_{jj} - A_{aa} - A_{kk}) \times \eta_{akij} \\
& + \frac{1}{2} \sum_{pq} (\eta_{akpq} A_{pqij} - A_{akpq} \eta_{pqij}) \times (1 - n_p - n_q) \\
& + \sum_{pq} (n_p - n_q) \times (\eta_{paqi} A_{qkpj} - \eta_{pkqi} A_{qapj} - \eta_{paqj} A_{qkpi} + \eta_{pkqj} A_{qapi})
\end{aligned} \tag{I.3e}$$

$$\begin{aligned}
& \left[\eta, A \right]_{lkij} = (A_{ii} + A_{jj} - A_{ll} - A_{kk}) \times \eta_{lkij} \\
& + \frac{1}{2} \sum_{pq} (\eta_{lkpq} A_{pqij} - A_{lkpq} \eta_{pqij}) \times (1 - n_p - n_q) \\
& + \sum_{pq} (n_p - n_q) \times (\eta_{plqi} A_{qkpj} - \eta_{pkqi} A_{qlpj} - \eta_{plqj} A_{qkpi} + \eta_{pkqj} A_{qlpi}) .
\end{aligned} \tag{I.3f}$$

Enforcing the operator structure of η seen in Eq. (5.1),

$$\left[\eta, A\right]_{abij} = (A_{ii} + A_{jj} - A_{aa} - A_{bb}) \times \eta_{abij} \quad (\text{I.4a})$$

$$- \frac{1}{2} \sum_{kl} \eta_{abkl} A_{kl ij} - \frac{1}{2} \sum_{cd} A_{abcd} \eta_{cd ij} \\ - \sum_{ck} (\eta_{caki} A_{kbcj} - \eta_{cbki} A_{kacj} - \eta_{cakj} A_{kbc i} + \eta_{cbkj} A_{kaci})$$

$$\left[\eta, A\right]_{akic} = (A_{ii} + A_{cc} - A_{aa} - A_{kk}) \times \eta_{akic} \quad (\text{I.4b})$$

$$+ \frac{1}{2} \sum_{pq} (\eta_{akpq} A_{pq ic} - A_{akpq} \eta_{pq ic}) \times (1 - n_p - n_q) \\ + \sum_{dj} (-\eta_{daji} A_{jkdc} - \eta_{pkqi} A_{qapc} - \eta_{paqc} A_{qkpi} + \eta_{jkdc} A_{daji})$$

$$\left[\eta, A\right]_{abcj} = (A_{cc} + A_{jj} - A_{aa} - A_{bb}) \times \eta_{abcj} \quad (\text{I.4c})$$

$$- \frac{1}{2} \sum_{kl} (\eta_{abkl} A_{klcj} - A_{abpq} \eta_{pq c j}) \\ + \sum_{di} (\eta_{paqc} A_{qbpj} - \eta_{pbqc} A_{qapj} + \eta_{daij} A_{ibdc} - \eta_{dbij} A_{iadc})$$

$$\left[\eta, A\right]_{abcd} = (A_{cc} + A_{dd} - A_{aa} - A_{bb}) \times \eta_{abcd} \quad (\text{I.4d})$$

$$- \frac{1}{2} \sum_{kl} (\eta_{abkl} A_{klcd} - A_{abkl} \eta_{klcd}) \\ + \sum_{pq} (n_p - n_q) \times (\eta_{paqc} A_{qbpd} - \eta_{pbqc} A_{qapd} - \eta_{paqd} A_{qbp c} + \eta_{pbqd} A_{qapc})$$

$$\left[\eta, A\right]_{akij} = (A_{ii} + A_{jj} - A_{aa} - A_{kk}) \times \eta_{akij} \quad (\text{I.4e})$$

$$+ \frac{1}{2} \sum_{cd} (\eta_{akpq} A_{pq ij} - A_{akcd} \eta_{cd ij}) \\ + \sum_{dl} (-\eta_{dali} A_{lkdj} - \eta_{pkqi} A_{qapj} + \eta_{dalj} A_{lkdi} + \eta_{pkqj} A_{qapi})$$

$$\left[\eta, A\right]_{lkij} = (A_{ii} + A_{jj} - A_{ll} - A_{kk}) \times \eta_{lkij} \quad (\text{I.4f})$$

$$+ \frac{1}{2} \sum_{ab} (\eta_{kab} A_{abij} - A_{lkab} \eta_{abij}) \\ + \sum_{pq} (n_p - n_q) \times (\eta_{pkqi} A_{qkpi} - \eta_{pkqi} A_{qkpi} - \eta_{pkqj} A_{qkpi} + \eta_{pkqj} A_{qkpi}) .$$

In conclusion, the tabulated one- and two-body components of $[\eta, A]$ are given by

$$[\eta, A]_{aa} = \frac{1}{2} \sum_{klb} \left(\eta_{bakl} A_{klba} - A_{bakl} \eta_{klba} \right) \quad (\text{I.5a})$$

$$[\eta, A]_{ii} = \frac{1}{2} \sum_{abj} \left(\eta_{jiab} A_{abji} - A_{jiab} \eta_{abji} \right) \quad (\text{I.5b})$$

$$\begin{aligned} [\eta, A]_{abij} &= (A_{ii} + A_{jj} - A_{aa} - A_{bb}) \times \eta_{abij} \\ &\quad - \frac{1}{2} \sum_{kl} \eta_{abkl} A_{kl ij} - \frac{1}{2} \sum_{cd} A_{abcd} \eta_{cd ij} \\ &\quad - \sum_{ck} \left(\eta_{caki} A_{kbcj} - \eta_{cbki} A_{kacj} - \eta_{cakj} A_{kbc i} + \eta_{cbkj} A_{kaci} \right) \end{aligned} \quad (\text{I.5c})$$

$$[\eta, A]_{akic} = \sum_{dj} \left(-\eta_{daji} A_{jkdc} + \eta_{jkdc} A_{daji} \right) \quad (\text{I.5d})$$

$$[\eta, A]_{abcj} = -\frac{1}{2} \sum_{kl} \eta_{abkl} A_{klcj} + \sum_{di} \left(\eta_{daij} A_{ibdc} - \eta_{dbij} A_{iadc} \right) \quad (\text{I.5e})$$

$$[\eta, A]_{abcd} = -\frac{1}{2} \sum_{kl} \left(\eta_{abkl} A_{klcd} - A_{abkl} \eta_{klcd} \right) \quad (\text{I.5f})$$

$$[\eta, A]_{akij} = -\frac{1}{2} \sum_{cd} A_{akcd} \eta_{cdij} + \sum_{dl} \left(-\eta_{dali} A_{lkdj} + \eta_{dalj} A_{lkdi} \right) \quad (\text{I.5g})$$

$$[\eta, A]_{lkij} = \frac{1}{2} \sum_{ab} \left(\eta_{lkab} A_{abij} - A_{lkab} \eta_{abij} \right). \quad (\text{I.5h})$$

Going forward, we use the following notation: O_{od} , O_d and $O_{d'}$ to denote linear combinations of differing sectors of A -body operator O , where¹

$$O_{od} \equiv \cancel{O_{ai}} + O_{abij} \quad (\text{I.6})$$

$$O_d \equiv O_{aa} + O_{ii} + O_{akic} + O_{abcd} + O_{lkij}$$

$$O_{d'} \equiv O_{abcj} + O_{akij}.$$

¹All sectors in Eq. (I.6) include their antisymmetric and/or symmetric counterparts. For example, O_{abij} corresponds to all matrix elements O_{abij} and O_{ijab} .

The UCC constraint in Eq. (5.8) can be rewritten

$$-H_{abij} = \left[\eta, H^{\{0\}} \right]_{abij} \quad (\text{I.7a})$$

$$H^{\{0\}} \equiv \frac{H}{1!} + \left[\eta, H^{\{1\}} \right] \quad (\text{I.7b})$$

$$H^{\{1\}} \equiv \frac{H}{2!} + \left[\eta, H^{\{2\}} \right] \quad (\text{I.7c})$$

$$H^{\{2\}} \equiv \frac{H}{3!} + \left[\eta, H^{\{3\}} \right] \quad (\text{I.7d})$$

↓

⋮

$$H^{\{n\}} \equiv \frac{H}{(n+1)!} + \left[\eta, H^{\{n+1\}} \right] \quad (\text{I.7e})$$

⋮

. Using Eq. (I.5c), notice $H_d^{\{0\}}$ is only relevant in Eq. (I.7a)'s RHS. This implies that $H^{\{0\}}$ is *not* unique. Therefore,

$$-H_{od} = \left[\eta, H^{\{0\}} \right]_{od} = \left[\eta, H_d^{\{0\}} \right]_{od} \quad (\text{I.8})$$

$$H_d^{\{0\}} = \frac{H_d}{1!} + \left[\eta, H^{\{1\}} \right]_d. \quad (\text{I.9})$$

In Eqs. (I.5a), (I.5b), (I.5d), (I.5f), (I.5h), notice $H_{od}^{\{1\}}$ is only relevant in Eq. (I.9)'s RHS.

Therefore,

$$H_d^{\{0\}} = \frac{H_d}{1!} + \left[\eta, H_{od}^{\{1\}} \right]_d \quad (\text{I.10})$$

$$H_{od}^{\{1\}} = \frac{H_{od}}{2!} + \frac{\left[\eta, H \right]_{od}}{3!} + \sum_{m=2}^{\infty} \frac{\left[\eta, H \right]_{od}^{(m)}}{(m+2)!}. \quad (\text{I.11})$$

So long η satisfies Eq. (5.7),

$$\left[\eta, H\right]_{od} = -H_{od} - \sum_{m=2}^{\infty} \frac{\left[\eta, H\right]_{od}^{(m)}}{m!}. \quad (\text{I.12})$$

Let

$$\begin{aligned} \overline{H_{od}^{\{1\}}} &\equiv \frac{H_{od}}{2!} + \frac{1}{3!} \left(-H_{od} - \sum_{m=2}^{\infty} \frac{\left[\eta, H\right]_{od}^{(m)}}{m!} \right) + \sum_{m=2}^{\infty} \frac{\left[\eta, H\right]_{od}^{(m)}}{(m+2)!} \\ &= \left(\frac{1}{2!} - \frac{1}{3!} \right) H_{od} + \sum_{m=2}^{\infty} \left(\frac{1}{(m+2)!} - \frac{1}{3! \times m!} \right) \left[\eta, H\right]_{od}^{(m)}. \end{aligned} \quad (\text{I.13})$$

If η fully satisfies Eq. (5.7), then $H_{od}^{\{1\}}$ and $\overline{H_{od}^{\{1\}}}$ will be *exactly* equal. In practice however, η is our best approximation to a solution of Eq. (5.7). Therefore, there will be some deviations between $H_{od}^{\{1\}}$ and $\overline{H_{od}^{\{1\}}}$. We seek to exploit these deviations using gradient descent. Let

$$\delta H_{od}^{\{1\}} \equiv H_{od}^{\{1\}} - \overline{H_{od}^{\{1\}}} = \frac{H_{od}}{3!} + \frac{\left[\eta, H\right]_{od}}{3!} + \sum_{m=2}^{\infty} \left(\frac{1}{3! \times m!} \right) \left[\eta, H\right]_{od}^{(m)} \quad (\text{I.14})$$

Using gradient descent with step-size ds ,² we can extrapolate $H_{od}^{\{1\}}$

$$\begin{aligned} H_{od}^{\{1\} \text{ Extrapolated}} &\equiv H_{od}^{\{1\}} + ds \times \delta H_{od}^{\{1\}} \\ &= \left(\frac{1}{2!} + \frac{ds}{3!} \right) H_{od} + \left(\frac{1}{3!} + \frac{ds}{3!} \right) \left[\eta, H\right]_{od} + \sum_{m=2}^{\infty} \left(\frac{1}{(m+2)!} + \frac{ds}{3! \times m!} \right) \left[\eta, H\right]_{od}^{(m)} \\ &= \sum_{m=0}^{\infty} \left(\frac{1}{(m+2)!} + \frac{ds}{3! \times m!} \right) \left[\eta, H\right]_{od}^{(m)}. \end{aligned} \quad (\text{I.15})$$

²Step-size $ds = 1.0$ is sufficient for this work.

Revisiting Eq. (I.7), we can now solve

$$\begin{aligned}
-H_{od} &= \left[\eta, H_d + \left[\eta, H_{od}^{\{1\} \text{Extrapolated}} \right]_d \right]_{od} \\
&= \left[\eta, H_d + \sum_{m=0}^{\infty} \left(\frac{1}{(m+2)!} + \frac{ds}{3! \times m!} \right) \left[\eta, H \right]_d^{(m+1)} \right]_{od} \\
&= \left[\eta, H_d + \sum_{m=1}^{\infty} \left(\frac{1}{(m+1)!} + \frac{ds}{3! \times (m-1)!} \right) \left[\eta, H \right]_d^{(m)} \right]_{od} \\
&= \left[\eta, \sum_{m=0}^{\infty} a_m(ds) \left[\eta, H \right]_d^{(m)} \right]_{od} \\
&= \left[\eta, \underbrace{\sum_{m=0}^{\infty} a_m(ds) \left[\eta, H \right]_d^{(m)}}_{H^{RG}(\eta) \text{ ansatz}} \right]_{od}
\end{aligned} \tag{I.16}$$

$$a_m(ds) \equiv \left(\frac{1}{(m+1)!} + \frac{ds}{3! \times (m-1)!} \right), \quad \forall m \geq 0. \tag{I.17}$$

Some numerical values of $a_m(ds = 1.0)$ can be seen in Table I.1.³

Table I.1: First 7 series coefficients for $H^{RG}(\eta)$ ansatz

m	0	1	2	3	4	5	6
$a_m(ds = 1.0)$	1	2/3	1/3	1/8	13/360	1/120	1/630

³ $a_1(ds = 1.0)$ appears in Koide's formula. Coincidence??!!